Nuclear effects in Semi-Inclusive Deep-Inelastic Scattering off ^{84}Kr and other nuclei

Nuclear Effects in Semi-Inclusive Deep-Inelastic Scattering off ^{84}Kr and other nuclei

ACADEMISCH PROEFSCHRIFT

TER VERKRIJGING VAN DE GRAAD VAN DOCTOR
AAN DE UNIVERSITEIT VAN AMSTERDAM
OP GEZAG VAN DE RECTOR MAGNIFICUS
PROF. MR. P. F. VAN DER HEIJDEN
TEN OVERSTAAN VAN EEN DOOR HET COLLEGE VOOR PROMOTIES
INGESTELDE COMMISSIE, IN HET OPENBAAR TE VERDEDIGEN
IN DE AULA DER UNIVERSITEIT
OP VRIJDAG 14 MAART 2003, TE 12.00 UUR

door

Erika Garutti

geboren te Alfonsine (Italië)

Promotor: Prof. Dr. G. van der Steenhoven
Co-Promotor: Dr. J.J.M. Steijger

Faculteit der Natuurwetenschappen, Wiskunde en Informatica

The work described in this thesis is part of the research program of the 'Nationaal Instituut voor Kernfysica en Hoge-Energie Fysica' (NIKHEF). The author was financially supported by the 'Stichting voor Fundamenteel Onderzoek der Materie' (FOM).

Cover: Comics courtesy of the "De Nardo Super-Sisters Production", Ivana and Lara.
With the graphic support of: Marcello, Henning, Stefano.
The characters and events depicted in this picture are fictional. Any similarity to actual persons, living or dead, is purely coincidental.

Contents

Chapter 1

Introduction

The most beautiful experience we can have is the mysterious. It is the fundamental emotion which stands at the cradle of true art and true science. Whoever does not know it and can no longer wonder, no longer marvel, is as good as dead, and his eyes are dimmed.

Albert Einstein

The visible universe has a variety of structures composed of the same matter that is also at the basis of life. The understanding of the structure of matter is one of the most important and fascinating quests of modern physics. In particular *particle physics* is addressing this issue by searching for and investigating the most fundamental constituents of matter and their interactions.

Since the 1960s it was hypothesized that the constituents of atomic nuclei (protons and neutrons) and other strongly interacting particles (collectively known as *hadrons*) have an internal structure. The elementary constituents of a hadron were first referred to as *quarks* by M. Gell-Mann [1] and G. Zweig [2] in the *constituent quark model*, and later as *partons* by R. Feynman [3] who introduced the *parton model*. In both models the constituents of hadrons are point-like spin-1/2 particles carrying a fraction of the electric charge e, and are distinguished by different flavors. But while in the constituent quark model only 3 quarks share the total mass of a *nucleon* (proton or neutron), the parton model predicts a nucleon to be made of a huge number of quark-antiquark pairs of very small mass. These two models were subsequently merged into the *Quark-Parton Model*.

Starting from the late 1960s experiments have provided evidence in support of the existence of constituents of the nucleon by exploiting the high resolution of virtual photons probing nucleon structure in *deep-inelastic* electron *scattering*. As the experimental data [4] were in agreement with the kinematic dependencies predicted by Bjorken [5] and Callan & Gross [6] on the basis of the Quark-Parton Model, first compelling evidence for the existence of quarks came available. When investigated with a high resolution (corresponding to less than 1/10 of the nucleon size) the quarks behave as free particles, a phenomenon known as *asymptotic freedom*. But because quarks are only observed as composite particles, they are apparently kept together by a very strong force which prevents them from being observed as isolated particles, an effect known as *confinement*. To describe the very peculiar behavior of quarks at large and small distance scales a new theory was required, *Quantum Chromo-Dynamics* [7, 8], which describes the strong interactions between the quarks in terms of the exchange of a bicolor-charged particle, namely the *gluon*. The strength of the interaction is given by the strong coupling constant α_s, which as opposed to the electromagnetic coupling constant α, becomes weaker with decreasing distances. This behavior explains the asymptotic freedom of quarks [7, 8].

When choosing a less high resolution, corresponding to a larger distance scale, the onset of confinement is expected to become visible. Under these conditions α_s increases up to values close to unity and a perturbative treatment of QCD is no longer possible. While a lot is known about the perturbative (or short-distance) properties of QCD, the understanding of the non-perturbative (or long-distance) aspects of QCD and hadron structure is still very limited, and is therefore mostly based on phenomenological models. It is the purpose of this thesis to collect new data on hadronic structure in deep inelastic scattering to further our understanding of non-perturbative QCD.

In deep-inelastic electron scattering the interaction between an electron and a nucleon is mediated by the exchange of a virtual photon ($E^2 \neq c^2p^2$). If the virtuality of the photon (the square of its four-momentum Q) is high, the internal quark structure of the nucleon is probed. After absorbing the virtual photon, the quark is ejected from the nucleon with high kinetic energy. Because of the confinement property the kinetic energy of the quark is transformed into potential energy which increases with growing distance between the struck quark and the nucleon remnant. According to the "string model" description of this process a new quark-antiquark pair is created when the increase in potential energy is large enough, the string breaks eventually leading to the formation of a "jet" of hadrons. This is the common way to describe the process of hadron formation (or string fragmentation). However, the time evolution of the process cannot be calculated rigorously in this framework since it occurs on a large distance scale.

The detection of hadrons in the final state of a deep-inelastic scattering event (i.e. *semi-inclusive deep-inelastic scattering*) enables the experimental study of the fragmentation process. By embedding the formation of the hadron in the nuclear medium an additional degree of freedom becomes available to modify or influence the process at femtometer length scales. This idea was first explored in the 1980s with *inclusive deep-inelastic scattering* experiments on nuclear targets which led to the discovery of nuclear effects such as the EMC effect [9]. In a similar way, it will be shown how semi-inclusive deep-inelastic scattering on nuclear targets gives access to new information on hadron formation times and parton energy loss mechanisms by measuring the attenuation of hadrons (i.e. the reduction of the hadron multiplicity) on various targets.

Apart from their intrinsic interest, measurements of the hadron formation time and parton energy loss mechanisms in dense media are relevant for the relativistic heavy-ion collision experiments which try to identify a new state of matter, i.e. the quark-gluon plasma [10]. The hadron formation time needs to be known in order to estimate the amount of normal hadronic interactions occurring when the hadron traverses a dense nuclear medium. The amount of energy lost by a quark propagating through the static nuclear medium is expected to be much smaller than the energy lost in hot dens matter due to the expected higher gluon density. Hence, comparison of partonic energy loss mechanisms in semi-inclusive deep-inelastic scattering on nuclei, and relativistic heavy-ion collisions can be used to obtain evidence for the existence of the quark-gluon plasma.

The possibility to identify various hadron types allows one to make a distinction between the pion, kaon, proton and anti-proton formation times, and to use possible differences to disentangle formation time models and various energy loss mechanisms. In QCD it is predicted, for instance, that the dominant contribution to partonic energy loss is proportional to the square of the radius or $A^{2/3}$ (where A is the mass number), while traditional hadronic energy loss mechanisms lead to a proportionality of $A^{1/3}$. The experimental data presented in this thesis are used to distinguish between these two processes, by studying the A-dependence of semi-inclusive deep-inelastic scattering.

Aside from the study of relatively long-lived particles, such as π, K and p, also fast decaying particles or resonances carry information on hadron structure and non-perturbative QCD. One of the most fascinating topics in this field is the possibility to identify gluonic excitations of hadronic matter, also known as glueballs, predicted theoretically but not yet convincingly proven experimentally. Because the lowest mass glueball is predicted to have scalar quantum numbers ($J^{PC} = 0^{++}$) mixing effects are expected between the pure gluon state and the scalar $q\bar{q}$-mesons in the same mass range (0.9 - 1.8 GeV). It is, therefore, of great importance to have a very precise understanding of the structure of all scalar states in order to identify the scalar glueball.

For these reasons the production of the $f_0(980)$ scalar meson has been studied -for the first time- in deep-inelastic positron scattering on various nuclear targets. The A-dependence of the production is of particular interest as it offers a new degree of freedom in studying the structure of the $f_0(980)$ meson.

The work described in this thesis is thus meant to address two problems in non-perturbative QCD by studying hadron attenuation in the nuclear medium and the production of the lightest scalar meson, the $f_0(980)$, in semi-inclusive deep-inelastic scattering. The kinematic region covered by the HERMES experiment is particularly suited for this type of measurements because the hadron formation length at the HERMES incident positron energy (about 27 GeV) is on the order of 5 fm, which is comparable with nuclear dimensions. At higher energy the hadron is formed outside the nucleus therefore processes of hadron rescattering are suppressed, which are used as a filter for the hadron formation process.

In this work data are presented which are collected on various atomic nuclei. The nuclei chosen as target need to be gaseous in order to enable injection into the HERMES target cell. Among the heavy nuclei this limits the choice to noble gases such as helium, neon, argon, krypton and xenon. At HERMES data have been taken on ^{2}H, ^{3}He, ^{14}N, ^{20}Ne and ^{84}Kr nuclei. In this thesis the results obtained on various gases are shown, but the emphasis is on the krypton data. For that reason some additional information on this element is given below.

The element Krypton

Atomic Number:	36
Atomic Symbol:	Kr
Atomic Weight:	83.80

Krypton, from the Greek word *kryptos* (hidden), was discovered in 1898 by Ramsay and Travers in the residue left after liquid air had nearly boiled away. Krypton is present in the air at the level of about 1 ppm. The atmosphere of Mars has been found to contain 0.3 ppm of krypton. Solid krypton is a white crystalline substance with a face-centered cubic structure which is common to all the ”rare gases.” Krypton is one of the noble gases, it is characterized by its brilliant green and orange spectral lines.
In 1960 it was internationally agreed that the fundamental unit of length, the meter, should be defined in terms of the orange-red spectral line of ^{86}Kr. This replaced the standard meter of Paris, which was defined in terms of the length of a bar made of a platinum-iridium alloy. Krypton is used in certain photographic flash lamps for high-speed photography. Its use has thus far been limited because of its high cost. Krypton gas presently costs about 30 Euro/l. The most important use is in flashing stroboscopic lamps that outline airport runways.
In this thesis the krypton gas is always referred to as ^{84}Kr, but in nature the krypton gas is a mixture of six stable isotopes with atomic numbers between 78 and 86. Seventeen other unstable isotopes are known.
Naturally occurring krypton, in fact used in the present experiment, has the following natural abundances: 0.35% (78), 2.27% (80), 11.56% (82), 11.55% (83), 56.90% (84), 17.37% (86), where the isotope number is indicated between brackets. For the purpose of the present work this mixture is approximated by assuming that the single isotope ^{84}Kr is used. This is justified by the fact that the rms nuclear radius of ^{84}Kr is 4.237 fm [11], while the weighted average rms radius of the six isotopes is 4.236 fm. Since density and size are the relevant properties of the nucleus in the work described in this thesis, the negligible difference between these two values allows one to approximate the used isotope mixture by ^{84}Kr.

The outline of this thesis

In order to address the two major topics of this work, a theoretical introduction on inclusive and semi-inclusive deep-inelastic scattering is given in chapter 2, followed by a presentation of the theoretical models available to describe hadron formation in the nuclear medium. In

the same chapter the present knowledge on light scalar mesons is also reviewed with references to recent experimental findings at CERN. In chapter 4 the physics motivation, principle of operation and design of a new silicon detector, the Lambda Wheels, are presented. This detector will make it possible to extend the studies presented in this work to other hadrons in the future. For instance, studies of the Λ-hyperon will become possible thanks to the increased statistics which will be obtained with the Lambda Wheels. In chapter 4 a selection of studies which characterize a prototype module installed and operated at HERMES in the year 2000, is presented.
The evaluation of the hadron attenuation ratios requires a detailed study of inclusive deep-inelastic scattering, since the hadron multiplicities are defined with respect to the inclusive cross sections. For that reason chapter 5 is devoted to inclusive DIS studies on nuclear targets. The known EMC effect is reproduced by the HERMES data, which are found to be consistent with the world parameterization of inclusive cross section ratios after correction for radiative processes and for a serious detector inefficiency, which went previously unnoticed.
The main topics of this thesis are addressed in the next two chapters. Chapter 6 presents the results on nuclear attenuation on ^{84}Kr. The measurement of nuclear attenuation for pions, kaons, protons and anti-protons is achieved using a Ring Imaging Čerenkov detector. The formation time for the various particle types is extracted from phenomenological fits to the data. Combining the present analysis on ^{84}Kr with the published results on ^{14}N the A-dependence of the attenuation is determined and compared to various model predictions. In this way first evidence is found in favor of the QCD predicted $A^{2/3}$ dependence for the hadron attenuation.
In chapter 7 the reconstruction of the $f_0(980)$ scalar meson signal in the semi-inclusive two pion decay channel, $f_0(980) \rightarrow \pi^+\pi^-$ is described. The production of the $f_0(980)$ scalar meson is confirmed on various gas targets, and the A-dependence of its mass and yield is studied. The dependence of $f_0(980)$ leptoproduction on several kinematic variables is compared to the prediction of a deep-inelastic scattering based Monte Carlo generator. In the last chapter the main conclusions of this work are summarized.

Chapter 2

Deep-Inelastic Scattering

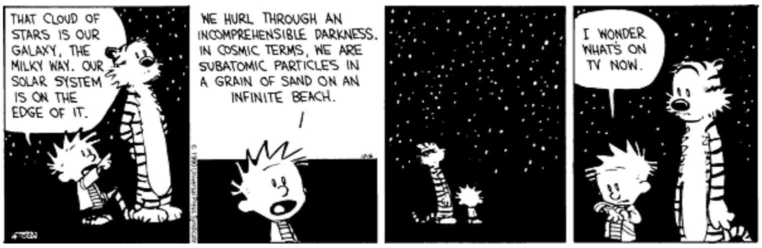

Calvin and Hobbes by Bill Watterson
©2003 Universal Press Syndicate

2.1 Inclusive Deep-Inelastic Scattering

In this section a review is given of the theoretical framework used to describe unpolarized inclusive deep-inelastic scattering of a lepton off a nucleon. The relevant kinematic variables are introduced, which are used to express the lepton nucleon cross section. The nucleon structure functions are interpreted within the framework of the Quark Parton Model with corrections given by the theory of Quantum Chromo-Dynamics.

2.1.1 Kinematic variables

In lepton-nucleon *Deep-Inelastic Scattering* (DIS), a high-energy lepton with momentum $\vec{\mathbf{k}}$ and energy E emits a virtual photon of four-momentum q. The photon is then absorbed by a target nucleon of four-momentum p, as shown in Fig. 2.1. The outgoing lepton with momentum $\vec{\mathbf{k}}'$ and energy E' is detected under an angle θ.
The hadronic final state X produced by the fragmentation of the target nucleon has a total invariant mass denoted by W and a four-momentum p_X. If the hadrons produced in the final state X are not differentiated, the type of reaction is called *inclusive*. The measurements of the incoming and outgoing lepton energy, E and E', and the scattering angle θ completely define the inclusive reaction. With the four-momentum transfer in the scattering process, i.e.

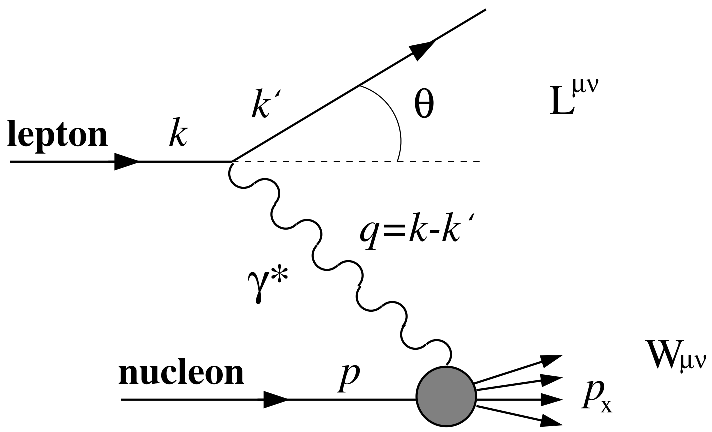

Figure 2.1: *Deep inelastic lepton nucleon scattering diagram in lowest order QED.*

the four momentum of the virtual photon, given by $q \equiv k - k'$ the invariant variable Q^2 and the energy transfer ν are defined as:

$$Q^2 \equiv -q^2 \stackrel{lab}{=} 4EE' \sin^2(\theta/2), \tag{2.1}$$

$$\nu \equiv \frac{p \cdot q}{M} \stackrel{lab}{=} E - E'. \tag{2.2}$$

It is useful to introduce two dimensionless variables x and y, referred to as the Bjorken scaling variables, expressed by the equations:

$$x = \frac{Q^2}{2p \cdot q} \stackrel{lab}{=} \frac{Q^2}{2M\nu}, \tag{2.3}$$

$$y = \frac{p \cdot q}{p \cdot k} \stackrel{lab}{=} \frac{\nu}{E}. \tag{2.4}$$

The energy transfer ν in the laboratory (lab) system is constrained between zero and E, therefore the kinematic range of y is $0 \leq y \leq 1$. Since both Q^2 and ν are positive, x has to be positive too. The other constraint on x comes from the invariant mass squared of the initial virtual photon nucleon system, which must be equal to or greater than the target nucleon mass square:

$$W^2 \equiv (p+q)^2 = M^2 + 2M\nu - Q^2 \geq M^2. \tag{2.5}$$

Using Eq. (2.3) this inequality gives $x \leq 1$, therefore $0 \leq x \leq 1$. In the case of elastic scattering ($W^2 = M^2$) from Eq. (2.5) it follows that $x = 1$.
For a fixed beam energy E (= 27.5 GeV at HERMES) the kinematics of inclusive DIS are determined completely by the measured variables (E', θ). This pair of variables is usually converted into (ν, Q^2). Fig. 2.2 illustrates the allowed range of these deep-inelastic scattering variables for the HERMES experiment. The dash-dotted lines represent the geometrical

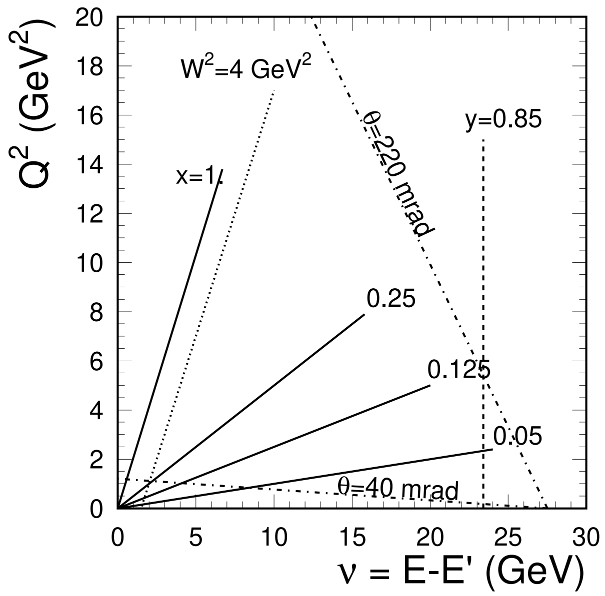

Figure 2.2: *Kinematic plane of deep-inelastic scattering at $E = 27.5$ GeV. For given Q^2 and ν values, all the other variables are defined. Lines of constant x, θ, W and y are shown.*

boundaries of the detector acceptance. The dotted line at $W^2 = 4$ GeV^2 sets the limit between the DIS and the nucleon resonance regions. The dashed line at y = 0.85 represents the cut used in the analyses presented in this thesis to exclude the kinematic region where QED radiative corrections become prohibitively large.

2.1.2 Unpolarized DIS cross section

A cross section is defined in order to describe the probability that a given scattering process is observed. For the photon exchange process illustrated in Fig. 2.1 the double differential cross section with respect to x and Q^2 is obtained by summing over all final states (including their spin) and averaging over the spin orientation of the initial particles [12],

$$\frac{d^2\sigma}{dxdQ^2} = \frac{2\pi\alpha^2}{(2ME)^2}\,\frac{1}{x^2Q^2}\,L^{\mu\nu}W_{\mu\nu}, \tag{2.6}$$

where $\alpha = 1/137$ is the electromagnetic coupling constant. The leptonic tensor $L^{\mu\nu}$ describes the leptonic vertex of the process, while the hadronic tensor $W_{\mu\nu}$ carries information on the hadronic structure of the nucleon.

The hadronic tensor cannot be calculated from our knowledge of the incoming and outgoing fermions, as the hadron does not represent an elementary point-like particle, which is at the basis of the expression for the leptonic tensor. However, using symmetry arguments and QED conservation laws the hadronic tensor can be expressed in terms of four scalar functions depending on ν and Q^2, which describe the electromagnetic structure of the nucleon. If the product is taken with the leptonic tensor, and the average over the incoming lepton helicity states is evaluated, the contributions of two out of these four structure functions vanish. By choosing to express $W_{\mu\nu}$ in two dimensionless structure functions F_1 and F_2 the differential cross section is given by [12]:

$$\frac{d^2\sigma}{dxdQ^2} = \frac{2\pi\alpha^2}{Q^4}\left[F_1(Q^2,x)\,y^2 + \frac{F_2(Q^2,x)}{x}\left(1-y-\frac{Mxy}{2E}\right)\right]. \tag{2.7}$$

Photo-absorption cross section

The optical theorem allows to extract the hadronic tensor $W_{\mu\nu}$ for lepton nucleon scattering from the imaginary part of the hadronic tensor $T_{\mu\nu}$ for Compton scattering using the relation $W_{\mu\nu}$ =Im$[T_{\mu\nu}]/2\pi$. A graphical expression of this theorem is shown in Fig. 2.3.

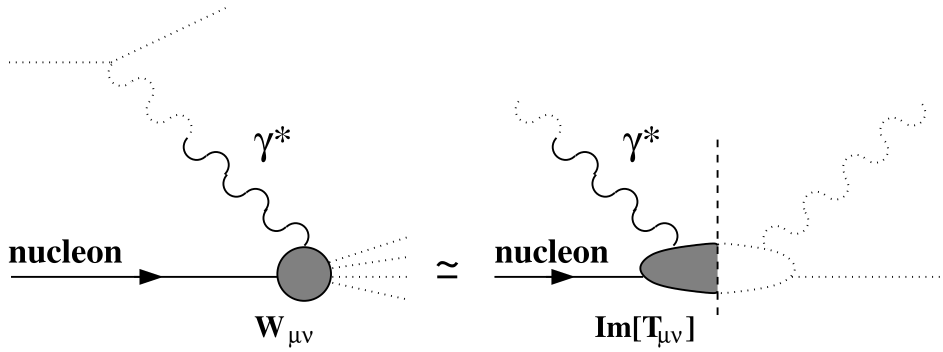

Figure 2.3: *Graphical representation of the optical theorem. The left diagram represents the DIS scattering process, the right one is the diagram for Compton scattering.*

When performing inclusive measurements the experimentally accessible quantity is in fact Im$[T_{\mu\nu}]$.

The cross section of Eq. (2.7) can alternatively be described in terms of absorption cross sections for longitudinally ($\sigma_{\rm L}$) and transversely ($\sigma_{\rm T}$) polarized photons:

$$\frac{d^2\sigma}{dxdQ^2} = \Gamma(\sigma_T(x,Q^2) + \epsilon\sigma_L(x,Q^2)), \tag{2.8}$$

where Γ describes the flux of virtual photons and ϵ their degree of polarization:

$$\epsilon = \frac{4(1-y) - \frac{Q^2}{E^2}}{4(1-y) + 2y^2 + \frac{Q^2}{E^2}} \tag{2.9}$$

with $\epsilon = 0$ corresponding to purely transverse polarization. Given the three possible photon polarization states

$$\varepsilon^{\mu}_{\pm} = \mp\frac{1}{\sqrt{2}}(0,1,\pm i,0), \quad \varepsilon^{\mu}_{0} = \frac{1}{\sqrt{Q^2}}(\sqrt{Q^2+\nu^2},0,0,\nu) \tag{2.10}$$

there are two spin-orientations of a target with spin $\pm\frac{1}{2}$ that contribute to the transverse cross section, and only one to the longitudinal:

$$\begin{aligned} \sigma_T &= \frac{1}{2}(\sigma^T_{1/2}+\sigma^T_{3/2}) \\ &= \pi(F_1+g_1-\gamma^2 g_2)+\pi(F_1-g_1+\gamma^2 g_2) = 2\pi F_1, && (2.11) \\ \sigma_L &= \sigma^L_{1/2} = 2\pi(-F_1+\frac{(1+\gamma^2)}{2x}F_2), && (2.12) \end{aligned}$$

with $\gamma^2 = \frac{Q^2}{\nu^2}$, and g_1 and g_2 the spin-dependent structure functions. The labels of the two cross section components can be understood as follows. "Transverse" refers to $\varepsilon^{\mu}_{\pm}$ (and $\varepsilon = 0$), implying that the direction of the electric and magnetic fields are transverse to the direction of motion, as for the real photon case, while "Longitudinal" refers to ε^{μ}_{0} implying that the electric and magnetic fields are oscillating in the direction of motion.
From Eq. (2.11) it can be seen that $F_1(Q^2,x)$ represents the transverse component of the cross section (modulo a constant), while the longitudinal component is proportional to the structure function $F_L(Q^2,x)$, defined as:

$$F_L(Q^2,x) = (1+\gamma^2)\;F_2(Q^2,x) - 2xF_1(Q^2,x). \tag{2.13}$$

The structure function $F_2(Q^2,x)$ is a mixture of the transverse and longitudinal component. The ratio of longitudinal to transverse photo-absorption cross sections, R is given by

$$\begin{aligned} R(x,Q^2) = \frac{\sigma_L}{\sigma_T} &= \frac{F_L(x,Q^2)}{2xF_1(x,Q^2)} && (2.14) \\ &= \frac{(1+\gamma^2)F_2(x,Q^2)}{2xF_1(x,Q^2)} - 1, && (2.15) \end{aligned}$$

where Eq. (2.15) is obtained from Eq. (2.14) using the relation (2.13). From Eq. (2.15) the relation between the two structure functions F_1 and F_2 is seen to be given by $F_1 = \frac{(1+\gamma^2)F_2}{2x(1+R)}$, which substituted in Eq. (2.7) gives the expression for the differential cross section as a function of F_2 and R:

$$\frac{d^2\sigma}{dxdQ^2} = \frac{2\pi\alpha^2}{Q^4}\,\frac{F_2(Q^2,x)}{x}\left(\frac{1+\epsilon R(x,Q^2)}{1+R(x,Q^2)}\right). \tag{2.16}$$

This expression is used in the analysis of inclusive DIS on nuclei presented in chapter 5.

2.1.3 Quark Parton Model

The *Quark Parton Model* (QPM) is used to describe the absorption of the virtual photon with the nucleon constituents. The quarks (partons) are assumed to be point-like particles carrying spin $\frac{1}{2}$. In the Bjorken limit of Q^2 and ν going simultaneously to infinity the structure functions F_1 and F_2 can be expressed as

$$F_2(x) = \sum_f e_f^2 x q_f(x), \tag{2.17}$$

$$F_1(x) = \frac{1}{2x} F_2(x), \tag{2.18}$$

with $q_f(x)$ the momentum distribution of a quark of flavor f and e_f the quark charge in units of electron charge. Eq. (2.18) is known as the Callan-Gross relation. In the QPM the structure functions are only dependent on the dimensionless variable x, which is interpreted as the fractional momentum carried by the struck parton. Increasing the spatial resolution of the scattering process by increasing Q^2 leaves the structure function unchanged, since the quarks in the QPM are assumed to be point-like.

This Bjorken scaling behavior has been confirmed experimentally in good approximation. Scaling violations are, however, observed for large and small values of Q^2, where $F_2(x)$ becomes Q^2 dependent.

In the QPM a value for R can be derived. Substituting the Callan-Gross relation into Eq. (2.15), it can be noted that in the Bjorken limit the structure function R goes to zero:

$$R = \frac{\sigma_L}{\sigma_T} \rightarrow \frac{F_2 - 2xF_1}{2xF_1} = 0. \tag{2.19}$$

The fact that R vanishes in the QPM can be traced to the spin $\frac{1}{2}$ character of the partons.

2.1.4 Scaling violations and pQCD

The scaling violations in the QPM are explained by *Quantum Chromo-Dynamics* (QCD) in terms of gluon radiation. A process which is better resolved when the photon wavelength becomes small, or alternatively Q^2 becomes large. The Q^2-dependence of $F_2(x)$ is calculable in QCD. When structure functions are known for a certain value of Q^2, they can be evolved to other Q^2 values using the Dokshitzer-Gribov-Lipatov-Altarelli-Parisi (DGLAP) equations [13, 14, 15].

At low Q^2 the wavelength of the virtual photon becomes so large that the partons inside the nucleon are not fully resolved any longer. As a result the nucleon is probed as a whole. The validity range for the QCD-extended QPM is not precisely known, but it is assumed to be valid for $Q^2 > 1$ GeV^2, which corresponds to a spatial resolution of about 0.2 fm. However comparison of experimental data to QCD analyses [16] suggests that the DGLAP equations can be applied down to a Q^2 of 0.3 GeV^2.

2.2 Semi-Inclusive Deep-Inelastic Scattering

In the previous section inclusive reactions have been considered where the only particle detected is the scattered lepton. If in addition to the scattered lepton also one of the produced hadrons is identified the event is called *semi-inclusive*. A schematic representation of a semi-inclusive event in lowest order QED is given in Fig. 2.4. The hadron carries information on the flavor of the struck quark. The flavor dependence of *Semi-Inclusive Deep-Inelastic Scattering* (SIDIS) can only be exploited for hadrons originating from struck quarks. These so-called *current fragments* must be separated from the ones originating from the target remnants (*target fragments*). The separation between the current and target fragmentation domains is accomplished by imposing requirements on the kinematics of the detected hadrons, e.g. by requiring that the hadrons are relatively fast in the laboratory frame. For this purpose

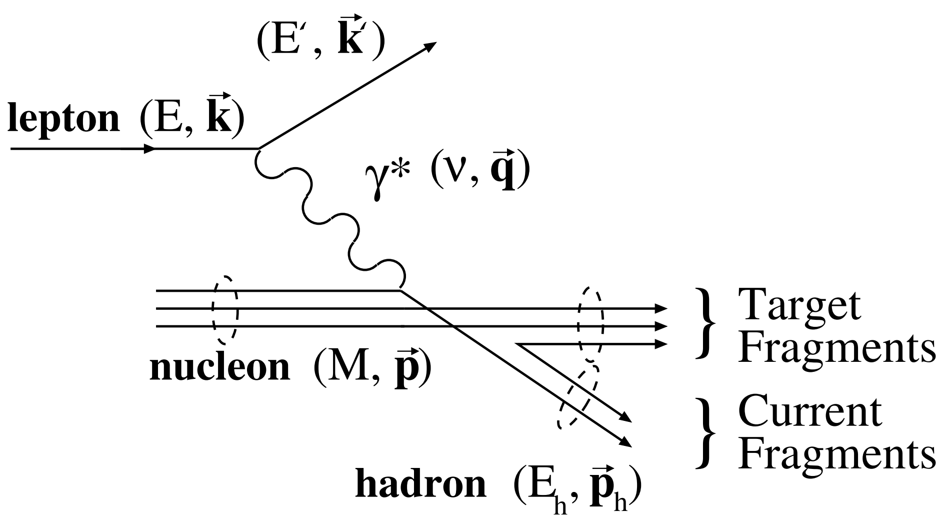

Figure 2.4: *Semi inclusive deep-inelastic lepton nucleon scattering diagram in lowest order QED.*

a lower limit is set on the fractional energy transferred from the virtual photon to the hadron, $z = E_h/\nu$.

The separation between current and target fragmentation can also be based on the Feynman scaling variable $x_F = p^h_{||}/W$, with $p^h_{||}$ the component of $\vec{p_h}$ parallel to the direction of the virtual photon. In general the requirement $x_F > 0$ selects the current fragmentation domain.

2.2.1 Semi-Inclusive DIS cross section

In semi-inclusive deep-inelastic scattering it is assumed that the timescale for the absorption of a virtual photon is very short as compared to the timescale needed for the quark to

fragment into a hadron. The fragmentation process is not calculable in pQCD since it involves long distance processes, and thus corresponds to very low Q^2 values where pQCD techniques cannot be used. Therefore, the fragmentation process in semi-inclusive scattering is parameterized by fragmentation functions $D_f^h(Q^2, z)$, which represent the probability that a quark of flavor f fragments in a hadron of type h with a fraction z of the virtual photon energy ($E_h = z\nu$). The kinematic dependence of the fragmentation function involves only Q^2, which represents the effect arising from gluon radiation of the struck quark, similar to the scaling violations discussed in section 2.1.4 for the structure functions.
In the QPM the cross section for the process $eN \to ehX$ is assumed to be the product of the differential inclusive cross section, already presented in Eq. (2.7), and the fragmentation probability to find a hadron h originating from a quark of any flavor f.

$$\frac{d^3\sigma(eN \to ehX)}{dxdQ^2dz} = \frac{d^2\sigma(eN \to eX)}{dxdQ^2} \frac{\sum_f e_f^2 q_f(x, Q^2) D_f^h(Q^2, z)}{\sum_f e_f^2 q_f(x, Q^2)}. \tag{2.20}$$

Here it is assumed that the quasi-free scattering process (related to the quark momentum distribution $q_f(x)$) and the fragmentation process (described by the fragmentation function $D_f^h(z)$) enter as two independent factors in the cross section (at the flavor level). This is known as *factorization*[1].
From Eq. (2.20) the hadron multiplicity per DIS event is obtained:

$$\mathcal{M}_h(Q^2, z) \equiv \frac{1}{\sigma} \frac{d^2\sigma(eN \to ehX)}{dQ^2dz} = \frac{\int dx \sum_f e_f^2 q_f(x, Q^2) D_f^h(Q^2, z)}{\int dx \sum_f e_f^2 q_f(x, Q^2)}, \tag{2.21}$$

where σ represents the differential inclusive DIS cross section $\frac{d^2\sigma(eN \to eX)}{dxdQ^2}$.

2.2.2 Hadronization in the nuclear medium

When embedded in a nuclear medium, the hadronization process is influenced by quark energy loss through gluon radiation and multiple quark-nucleon scattering as the quark propagates through the medium. Furthermore, hadron-nucleon interactions also affect the process if the hadron is formed while still inside the nucleus. The primary experimental observable to access the hadronization process is the multiplicity of hadrons produced on a dense nucleus as compared to the one produced on deuterium. In the absence of any kind of attenuation produced by interactions in the medium these two quantities would be identical (i.e. the ratio of the two multiplicities would be unity). This ratio of hadron multiplicities or attenuation ratio is defined as

$$R_{\mathrm{att}}^h(z, \nu) = \frac{\left(\frac{1}{\sigma} \frac{d^2\sigma(eN \to ehX)}{dzd\nu}\right)_{\mathrm{A}}}{\left(\frac{1}{\sigma} \frac{d^2\sigma(eN \to ehX)}{dzd\nu}\right)_{\mathrm{D}}}, \tag{2.22}$$

[1] A recent HERMES data has shown some evidence (see Ref. [17]) that the hadron multiplicity is also x-dependent at high z, which would represent a breaking of the factorization assumed in Eq. (2.20).

where the derivative with respect to Q^2 is substituted by the one with respect to ν because of the further application of this equation. The ν and z dependence of the attenuation ratio can be used to investigate the nature of the hadron formation mechanism.
The process of hadronization can be described in terms of the hadron formation time τ_f, the time between the moment that the quark is struck by the virtual photon and the moment that the final hadron is formed. Fig. 2.5 shows the quark propagating over a distance $l_f = c\tau_f$ before the hadron is formed. Hard partonic interactions are also drawn as gluon exchange lines. Not shown are possible interactions of the produced hadrons with the medium, subsequent to its formation.

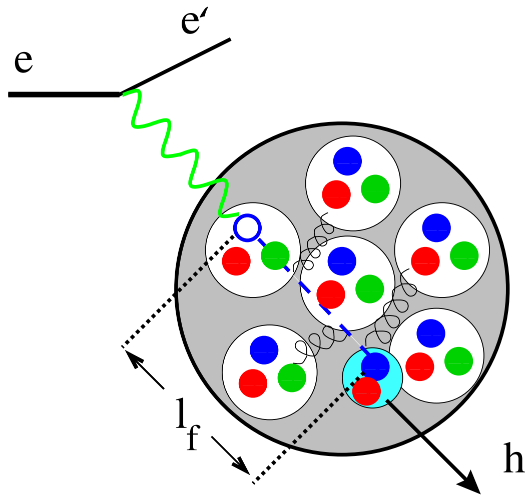

Figure 2.5: *Representation of the hadron formation process in the nuclear medium.*

Depending on the nuclear size and the formation length the hadron may still be formed inside the nucleus and therefore interact with the nucleons. These interactions are described by hadron-nucleus cross sections. This process is referred to as nuclear rescattering or absorption. While different theoretical models are used to describe the hadron formation process corresponding to different descriptions of the hadron formation time, the nuclear absorption of the formed hadron in the medium is always described by the same formalism which is discussed below. In subsections 2.2.3 and 2.2.4 a collection of theoretical models is presented which describe both the partonic and hadronic part of the hadronization process.

Nuclear absorption

After its formation in a nucleus A the hadron undergoes nuclear absorption if the formation time is short enough. The absorption can be factortorized out of the attenuation ratio R^h_{att} as expressed in Eq. (2.22), the factor is referred to as $\mathcal{N}_{\mathrm{A}}$. If no medium modification of the fragmentation or distribution function occurs, the attenuation ratio R^h_{att} is entirely

described by the nuclear absorption [18, 19] (i.e. $R^h_{\rm att} = \mathcal{N}_{\rm A}$). It has to be noted that both the fragmentation function and the nuclear absorption factor are phenomenological quantities. Therefore, more or less strength can be given to either one or the other in order to describe the effect of the nuclear medium on the hadron multiplicity, as it is shown in the following comparison of various models.
The factor $\mathcal{N}_{\rm A}$ can be evaluated according to the procedure given in Ref. [18][2]

$$\mathcal{N}_{\rm A} = \int d^2b \int_{-\infty}^{+\infty} dy\ \rho_{\rm A}(b,y)\ [S_{\rm A}(b,y)]^{A-1}, \tag{2.23}$$

where $\rho_{\rm A}(b,y)$ is the nuclear density normalized to 1 at transverse and longitudinal coordinates (b,y) [3]. The quantity $S_{\rm A}(b,y)$ is the survival probability of a hadron produced at (b,y). The exponent $A-1$ (with A the atomic number of the target A) accounts for the fact that the produced hadron can interact with the remaining $A-1$ nucleons in the nucleus. The survival probability is given by:

$$S_{\rm A}(b,y) = 1 - \sigma_h \int_y^{\infty} dy' \rho_{\rm A}(b,y') P_h(y'-y), \tag{2.24}$$

with $P_h(y'-y)$ the probability to find a hadron which had traveled a distance $(y'-y)$ in the nucleus. If τ_f is used to indicate the time after which the hadron is formed, and $l_f = c\tau_f$, $P_h(y'-y)$ is usually expressed as:

$$P_h(y'-y) = 1 - e^{-(y'-y)/l_f}. \tag{2.25}$$

Theoretical models for the hadronization process

Over the past 30 years a number of model predictions for the space-time behavior of hadronization has been developed. First phenomenological models were proposed to describe the formation time on the basis of the various interactions of the hadron constituents before the hadron is formed and the hadron interaction after formation (nuclear absorption). The two-timescale model based on the LUND string model is presented as an example in section 2.2.3. Moreover, attempts to model the attenuation effects in analogy to the Q^2-rescaling description of the EMC effect are presented as well in the same section, as the nuclear absorption part in this model is treated in the same phenomenological approach. Later QCD-based models were developed in an attempt to incorporate aspects of QCD in the description of the hadronization process. The gluon Bremsstrahlung and the fragmentation function modification models are examples discussed in section 2.2.4.

[2] Note that the exponent $A-1$ is used here instead of the more adequate exponential form for the survival probability suggested in Ref. [11]. This has been done in order to be able to compare the present analysis to the published results on ^{14}N [20].

[3] Typically, a Woods-Saxon shape is used for the nuclear matter density $\rho_{\rm A} = \rho_0/(1+e^{(r-r_{\rm A})/a_0})$, with $r_{\rm A}$ the nuclear radius parameter and a_0 the surface thickness parameter [18]. For a spherically symmetric nucleus the radius parameter is derived from the impact parameter b and the longitudinal coordinate y according to $r^2 = b^2 + y^2$.

2.2.3 Phenomenological models

Two-timescale model

In the string-fragmentation model a quark with sufficient kinetic energy moves away from an other constituent of the nucleon, and its potential energy increases with growing distance. When the potential energy is high enough to create a $q\bar{q}$ pair the string that connects it to the rest of the nucleon can break to form new quarks which subsequently become hadrons.
The formation of the hadron is divided into two phases (two-timescales), a time τ_c in which the first constituent of the hadron is formed, and a second phase in which a string is formed between the first and second constituent [19]. The first constituent is assumed to interact with the medium with a strength given by an unknown cross section σ_q. The string in the second phase propagates in the medium with an interaction cross section σ_s until the final hadron is formed after a total time period τ_f, known as the formation time. Fig. 2.6 sketches the two phases of the hadron formation process according to this model. The hadron will also interact with the medium, with a cross section σ_h representing the well known hadron-nucleon interaction. In this framework the formation time is given by the expression:

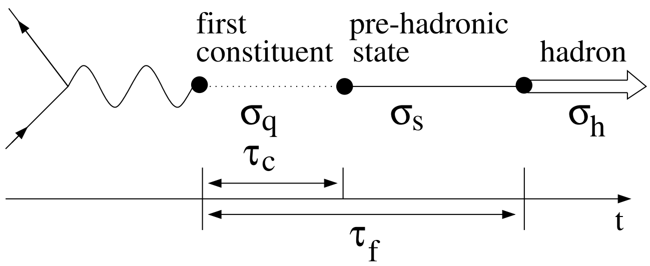

Figure 2.6: *Sketch of the two phases of hadron formation assumed in the two-timescale model.*

$$\tau_f - \tau_c = \frac{E_h}{k} = \frac{z\nu}{k}, \tag{2.26}$$

with the string tension given by k = 1 GeV/fm. In practice various expressions have been used for the hadron and constituent formation times [18, 19, 21, 22]. In the model there is a set of parameters (C_q) which control the form of the distribution of hadrons containing flavor q. Here, we present the expression for the constituent formation time obtained from Ref. [19] when setting $C_q = 1$, as it reproduces the z dependence of the existing data [19]:

$$\tau_c = \left(\frac{-\ln(z^2) - 1 + z^2}{1 - z^2} \right) \frac{z\nu}{k}. \tag{2.27}$$

The corresponding z-dependence of τ_f and τ_c is plotted in Fig. 2.7. It is noted that in the limit $z \to 1$, $\tau_c \to \frac{\nu}{k}\,(1 - z)$. The two unknown cross sections σ_q and σ_s are introduced in order

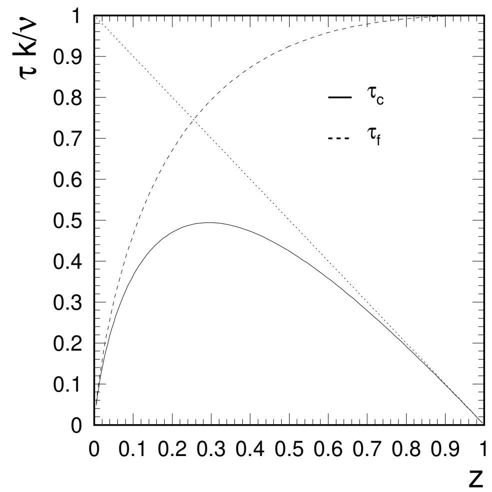

Figure 2.7: *The formation time (multiplied by k/ν) as a function of z as predicted by the two-timescale model [19] using Eq. (2.27). The total hadron (dashed line) and constituent (solid line) formation times are presented. For comparison the curve $\tau \propto (1-z)$ is plotted as a dotted line.*

to obtain the most general description of hadron attenuation phenomena. However, from the comparison to existing data [23] it turned out that the cross section of the pre-hadronic state σ_s could be taken as equal to the final hadronic cross section, thus restricting the effective hadron formation to time $\tau_f \approx \tau_c$. As a consequence, it follows that the formation time is expected to be proportional to $(1-z)$ for large values of z. Moreover, the value obtained from the comparison to the data for the quark-nucleon interaction cross section σ_q is consistent with zero [20]. In this way the two-timescale model effectively reduces to a one-timescale model, and nuclear absorption is responsible for the entire hadron attenuation. Also note that the model is taken to be flavor independent.

Flavor dependent string model

The flavor dependent string model is an expanded version of the two-timescale model for nuclear attenuation, which takes into account the flavor content of hadrons [24]. The model is applicable to all string-produced hadrons and is not only valid for the leading hadron as all the other models described in this subsection. The formalism is the same as that of the two-timescale model with the string tension k taken to be 1 GeV/fm and the total[4] hadronic cross sections for different particle types fixed by the experimental values:

[4]The total hadronic cross section is the sum of elastic and inelastic cross sections.

$$\sigma_{\pi^+} = \sigma_{\pi^-} = 25 \text{ mb}; \sigma_{K^+} = 17 \text{ mb}; \sigma_{K^-} = 23 \text{ mb}.$$

Differently from the two-timescale model the flavor dependent quark-nucleon cross section is assumed to be non-zero and is parameterized as a function of the constituent formation length (or time). The authors claim that their model is applicable in the domain $z > 0.2$ and $Q^2 > 0.3$ GeV^2. The z restriction is introduced to limit the maximum number of hadrons produced per string to three which is accounted for in the calculation. The requirement on Q^2 limits the model to a region in which the hadron-nucleon interaction is considered to be Q^2-independent. Hence, the Q^2-dependence of the model is restricted to the quark-nucleon interaction.

Rescaling model

In the rescaling model [25] (and its more recent update Ref. [26]) the nuclear absorption is treated in the same way as in the two-timescale model. Moreover, possible modifications of the distribution and fragmentation functions in nuclei are accounted for.
If distribution and fragmentation functions are modified in nuclei this is possibly caused by partial deconfinement effects. The confinement scale in nuclei, λ_A, is assumed to be effectively larger than the one in free nucleons, λ_0, due to the overlap of neighboring nucleons in the nucleus. A scale factor $\xi_\mathrm{A}(Q)$ can be defined to describe the change from λ_0 to λ_A for nucleus A. Moreover, in Ref. [25] it is assumed that the distribution and fragmentation functions at an arbitrary value of Q^2 can be obtained by means of the DGLAP evolution equations using $\xi_\mathrm{A} Q^2$ instead of Q^2, i.e. the Q^2 value is rescaled in the medium:

$$q_f^\mathrm{A}(x, Q^2) = q_f(x, \xi_\mathrm{A}(Q)Q^2), \tag{2.28}$$

$$D_f^{h|\mathrm{A}}(z, Q^2) = D_f^h(z, \xi_\mathrm{A}(Q)Q^2). \tag{2.29}$$

The scale factor $\xi_\mathrm{A}(Q) = \left(\frac{\lambda_\mathrm{A}}{\lambda_0}\right)^{\frac{\alpha_s(Q_0)}{2\alpha_s(Q)}} > 1$ is taken from the *partial deconfinement model* (PD) [27], where Q_0 is the physical threshold of hadron production.
Apart from deconfinement effects the rescaling model includes nuclear absorption which is implemented in roughly the same way as described above. In Ref. [25] only the inelastic cross sections were taken for the hadron-nucleon interaction σ_h, however, in the more recent Ref. [26] the total hadron-nucleon cross sections are used. The string (or pre-hadronic) cross section is set equal to the hadronic one, therefore the pre-hadronic state and the final hadron are treated essentially as the same object by the model. The formation time is given by Eq. (2.27). The string constant k is fixed to 0.4 GeV/fm, which is much smaller than the value used for k in the string model. Nuclear absorption is treated as a multiplicative factor applied to the multiplicity ratio calculated with modified distribution and fragmentation functions.
Given the above parameters, predictions are made using the rescaling model for the ν and z dependence of the attenuation ratio at the EMC kinematics which are compared to the published EMC data [23]. The results are shown in Fig. 2.8. The rescaling of fragmentation and

distribution functions describes the kinematic behavior of the ^{63}Cu data well, also without any nuclear absorption factor. However, it can also be seen that data at low ν and z are overestimated by the model, in this region the effect of nuclear absorption could be more relevant.

2.2.4 QCD inspired models

Gluon Bremsstrahlung model

The production of fast leading mesons in nuclei is described in terms of a modification of the fragmentation function in the medium due to energy loss caused by gluon radiation, in combination with hadron rescattering [22]. The approximation is made that the medium modification of the distribution function $q_{\mathrm{A}}(x, Q^2)$ is negligible. If it is also assumed that one flavor is dominant in the fragmentation process, the summation in Eq. (2.20) reduces to one term, and the attenuation ratio can be written as:

$$R^h_{\mathrm{att}} = \frac{D_f^{h|\mathrm{A}}(z)}{D_f^h(z)} \mathcal{N}_{\mathrm{A}}, \tag{2.30}$$

where the factor $\mathcal{N}_{\mathrm{A}}$ accounts for nuclear absorption and $D_f^{h|\mathrm{A}}$ is the nuclear modified fragmentation function. The modification is evaluated by calculating the energy loss due to gluon radiation, which is proportional to the energy of the virtual photon, the time during which the struck quark propagates freely before the hadron is formed and the fraction of energy

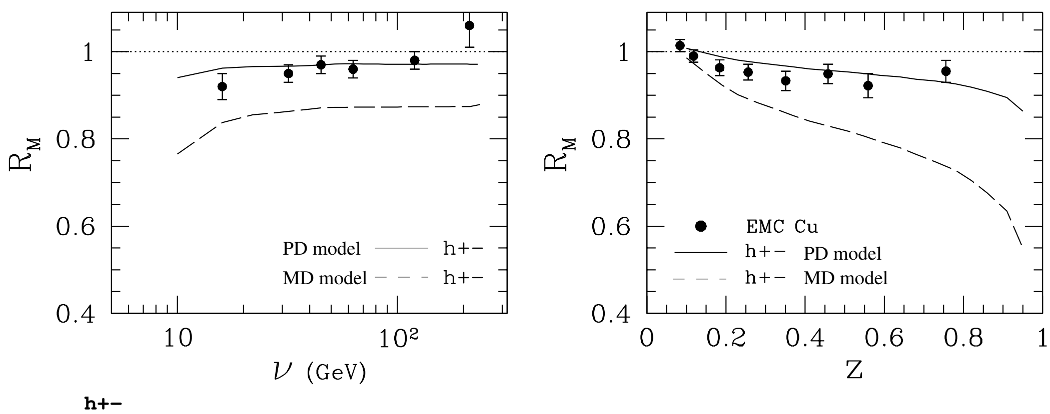

Figure 2.8: *Rescaling model predictions for the attenuation ratio as a function of ν (left) and z (right) without nuclear absorption, compared with the EMC results [23]. The solid curve are obtained in the partial deconfinement model (PM), while the dashed curves in the maximal deconfinement model (MD) overestimate the attenuation of the data. Plots from Fig. 3 of Ref. [26].*

carried by the hadron:

$$-\frac{dE}{dt} = \frac{\varepsilon\nu(1-z)}{t}. \tag{2.31}$$

where $\varepsilon = 4\alpha_s(k_T^2)/3\pi$ is calculated perturbatively, with the running QCD coupling constant $\alpha_s(k_T^2)$ fixed to $\alpha_s(k_0^2)$ for values of the quark transverse momentum $k_T \leq k_0$. The value of the gluon-gluon correlation radius $k_0 \approx 0.7$ GeV is chosen such that the amount of energy radiated per fm in this model is in agreement with the string tension used to describe the soft part of hadronization in the framework of color strings, $dE/dt \approx 1$ GeV/fm, [22]. From Eq. (2.31) the authors of Ref. [22] derive a distribution of formation times from which the following average formation time is derived:

$$\tau_f = c_h\,\nu(1-z) \tag{2.32}$$

with c_h the formation time constant expressed in fm/GeV. The dependence of the formation time on Q^2 is supposed to be small. The z dependence of Eq. (2.32) can be understood in terms of the following argument. The maximum energy which a hadron of observed total energy $E_h = z\nu$ may have lost by gluon radiation is $(1-z)\nu$. A high z hadron carries most of the virtual photon energy, and therefore has to be formed fast, otherwise gluon radiation would have reduced its energy. The hadrons formed early inside the nucleus have more time (length) to reinteract with the nuclear constituents, and therefore they get more strongly suppressed. This dependence suggests that a stronger attenuation at high z should

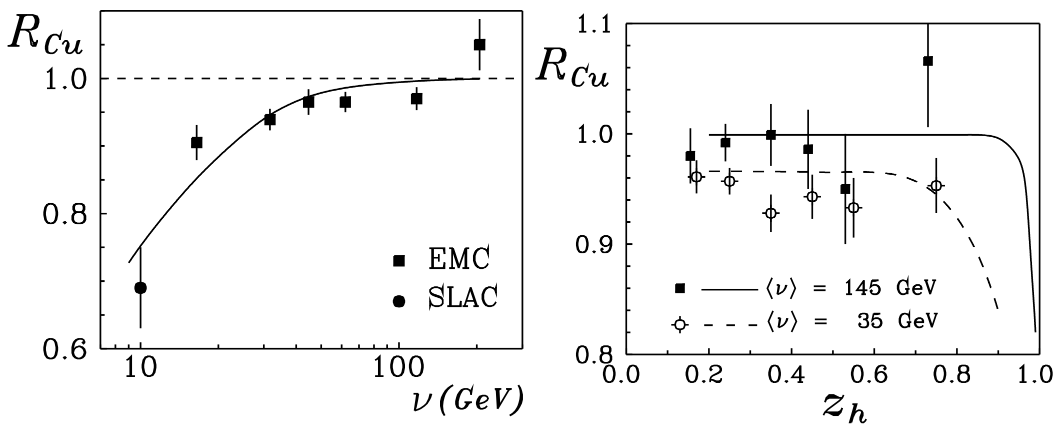

Figure 2.9: *Dependence of the Gluon Bremsstrahlung model [22], on ν (left) and z (right). The predictions for the attenuation ratio are compared with existing data [23, 28].*

be observed in the data.

The ν and z dependence of the attenuation ratio as predicted by this model are compared to existing EMC and SLAC data [23, 28] in Fig. 2.9. The decrease of the attenuation ratio R^h_{att} at large values of z is shown to be larger for smaller average energy. However, the absence of data above $z = 0.8$ makes it impossible to verify or falsify the predicted z dependence. Using the expression for the formation time as given by Eq. (2.32) the factor $\mathcal{N}_{\mathrm{A}}$ is evaluated using a similar approach as was discussed in section 2.2.2, assuming $\sigma_h \simeq 25$ mb. Nuclear absorption of formed hadrons is found to be the dominant mechanism of this model, while the energy loss due to gluon Bremsstrahlung has a small effect on R^h_{att} [29].

Fragmentation function modification model

In this model parton multiple scattering inside a nucleus is assumed to cause modifications of the fragmentation functions and of their perturbative QCD evolution [10]. When a parton is produced in the nuclear medium it undergoes multiple scattering and induced radiation which modifies the DGLAP evolution of the fragmentation functions. The in-medium modified fragmentation function becomes softer. This softening can directly be related to energy loss of the leading quark due to soft gluon emission. The dominant diagrams contributing to the modification are schematically shown in Fig. 2.10. Diagram (a) corresponds to rescattering of the struck quark from a gluon, but does not involve gluon radiation. This process causes the broadening of the momentum distribution of the leading hadron (or jet). The second diagram (b) is the rescattering with another quark, which causes the mixing of fragmentation processes originating from a (anti)quark or a gluon, i.e. $D^h_q(z)$ and $D^h_g(z)$, in the evolution equations. The last diagram (c) is a higher-twist correction of (a), which involves gluon radiation. The corresponding term gives the dominant higher-twist contribution in the QCD evolution of $D^h_q(z)$. Due to the fact that emitted gluons and leading quarks propagate coherently through the nucleus the last term is also affected by large interference effects. This effect is known as Landau-Pomeranchuk-Migdal (LPM) interference. The modified fragmentation function in a medium with atomic number A can be expressed in terms of the fragmentation function in vacuum plus a modification term,

$$D^{h|\mathrm{A}}_f(z, Q^2) \equiv D^h_f(z, Q^2) + \Delta D^h_f(z, Q^2). \tag{2.33}$$

The in-medium modification term is proportional to the square of the nuclear size $r_{\mathrm{A}} = r_0\, A^{1/3}$, according to

$$\Delta D^h_f(z, Q^2) \propto \frac{\tilde{C}\alpha_s^2}{x_{\mathrm{A}}^2} \Delta d_h(z, x, Q^2), \tag{2.34}$$

where $x_{\mathrm{A}} = \hbar c/m_p\, r_{\mathrm{A}}$, $\tilde{C}$ is the quark-gluon correlation strength parameter, and Δd_h is the nuclear size independent modification. As a result the model predicts that the fragmentation function depends on the nuclear medium as $A^{2/3}$. The quadratical dependence on the nuclear size comes from the LPM interference. Furthermore, the modification of $D^h_f(z)$ increases for small ν, or alternatively for increasing $x = Q^2/2M\nu$, as shown in Fig. 2.11, through the x dependence of $\Delta d_h(z, x, Q^2)$. The model accounts also for the in-medium modification of the parton distribution functions. The quark-gluon correlation strength is the only free parameter, which was tuned to reproduce the published HERMES ^{14}N data [20]. A value of

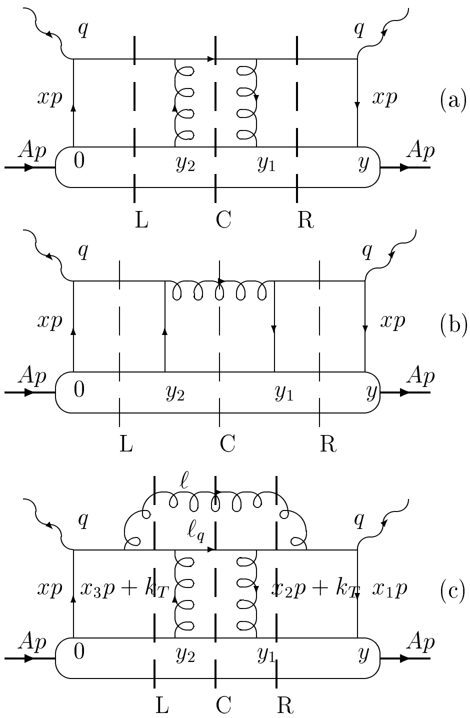

Figure 2.10: *Dominant terms in the modification of the fragmentation function, according to the model of Ref. [10].*

$\tilde{C}\alpha_s^2$ = 0.00065 GeV^2 was obtained [30].

Parton energy loss due to gluon radiation is the dominant mechanism of this model in accounting for the attenuation effects. The modification of the fragmentation function can be rewritten as an approximation in terms of the energy loss $\Delta E/E$ as:

$$\Delta D_f^h(z) \approx \frac{1}{1-\Delta E/E} D\left(\frac{z}{1-\Delta E/E}\right) \tag{2.35}$$

From the proportionality of the average energy loss to the quark-gluon correlation strength ($\Delta E \propto \tilde{C}\alpha_s^2$) the value of $dE/dx \approx 0.3$ GeV/fm has been extracted for the average energy loss by a quark propagating through the ^{84}Kr nucleus. This number can be directly related to the energy of radiated gluons, which is of great importance for studies in relativistic heavy-ion physics where the change of gluon density could be used as a possible probe for the existence of the quark gluon plasma. Furthermore, the parton energy loss per unit of length dE/dx is predicted to grow as the nuclear radius [10, 31]. Therefore, the total energy loss by gluon radiation ΔE scales with r_A^2, or alternatively with $A^{2/3}$.

All the models presented in this section give a reasonable description of the data available on hadronization in nuclei. Most of the calculations are yielding attenuation ratios which

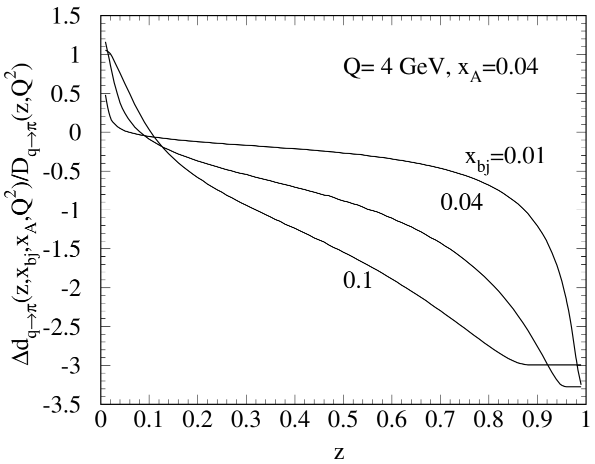

Figure 2.11: *Prediction of the fragmentation function modification model [10], for the modification term as a function of z for different values of Bjorken x.*

are close to each other, despite the fundamental differences in the physical mechanisms exploited to describe the same effect. A clear example is the contradiction between the gluon Bremsstrahlung model in which rescattering of formed hadrons is the dominant mechanism, and the fragmentation function modification model, in which the effect of nuclear attenuation is explained entirely by gluon radiation.
Predictions from these models for the hadron attenuation in ^{14}N and ^{84}Kr are compared to the HERMES data in chapter 6.

2.3 Hadron spectroscopy

The QCD structure of hadrons can be investigated using two complementary methods:

- in inclusive deep-inelastic scattering the short-distance (corresponding to high Q^2) dynamics of quarks and gluons is studied;
- the long-distance (or valence-like) structure of hadrons can be accessed with semi-inclusive deep-inelastic scattering as discussed in the previous section, or with hadron spectroscopy by studying the mass spectrum of hadrons.

A significant fraction of the hadrons observed in deep-inelastic scattering comes from the decay of a large variety of short lived particles, called resonances. The study of those meson and baryon resonances is hoped to reveal information on the structure of the resonances and their production mechanism. The most important issue in hadron spectroscopy is the search for missing resonances, such as hybrids and glueballs which are predicted theoretically but are still not conclusively observed experimentally[5]. Moreover, the structure of some states,

[5] For a recent overview of glueball searches see Ref. [32]

such as the scalar mesons, is not well understood. Hence, more experimental information is required.
The surprising development, which is reported in chapter 7 of this thesis, is that additional information on the structure of scalar mesons can be obtained from unpolarized DIS data on nuclear targets.
As an introduction to the data presented in chapter 7, in this section a sketch is given of theoretical models trying to explain and predict the properties of scalar mesons.
In the *Constituent Valence Model* [33] (CVM) the valence content of a meson is understood to be a quark and an anti-quark. Within this framework it is possible to describe meson mass spectra and various decays for almost all observed mesons. It is therefore understand-

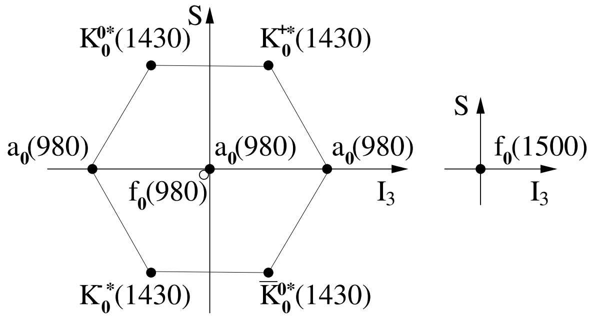

Figure 2.12: *Possible configuration for the lowest energy scalar mesons nonet.*

able that mesons which do not fit in the CVM description, like exotic hybrid mesons (with quantum numbers not possible in the CVM, i.e. $J^{CP} = 1^{-+}$) and glueballs ("pure gluonic" states) have attracted a lot of attention. In this respect the scalar mesons ($J^{CP} = 0^{++}$), are a continuous source of controversy, as their structure remains unclear. In order to characterize them it has been tried to find the candidates for a scalar meson nonet with masses below 1600 MeV in the framework of the CVM.
In the constituent valence model the total angular momentum ($J = 0$) of the ${}^3P_0$ $q\bar{q}$ state[6], which is the scalar meson, arises from oppositely oriented orbital momentum ($L = 1$) and spin ($S = 1$) components. Since the scalar mesons have a unit of orbital angular momentum, the mesons of this group are expected (by the CVM) to be heavier than the vector (${}^1P_1$) mesons. Hence, the mass of the $q\bar{q}$ scalar mesons was expected to lie in the domain 1.2-1.5 GeV. Here, the first controversy arises since experimental findings yield at least two 0^{++} mesons with masses below 1 GeV. One of the two isosinglets of this group is the $f_0(980)$. Also the isotriplet state $a_0(980)$ is found to be relatively light. Furthermore, if all the observed 0^{++} mesons with masses below 1600 MeV are used to construct a nonet as the one proposed in Fig. 2.12 [34], two observed resonances (see PDG) remain which do not fit in the classification, the $f_0(400 - 1200)$ and $f_0(1370)$ scalar mesons. These two resonances

[6]The notation reads: ${}^{2L+1}P_J$, where L is the orbital, P the spin, and J the total angular momentum.

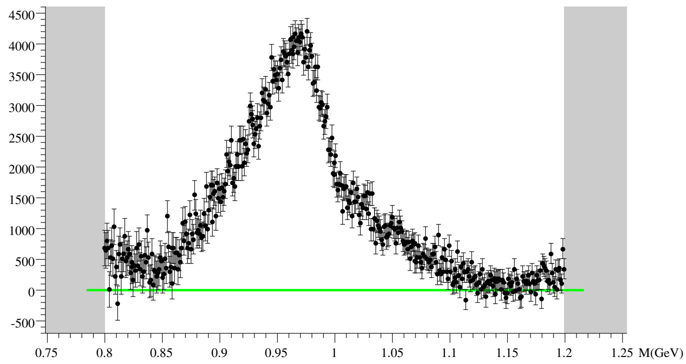

Figure 2.13: *Two-pion invariant mass spectrum observed in photoproduction on a beryllium target at an energy E_γ = 220 GeV [42]. The data are presented after the subtraction of a smooth polynomial background.*

are sometimes referred to as a broad "sigma" resonance [34] and some authors identify the $f_0(1370)$ as the lightest glueball [35], but this is by no means established.
These and other discrepancies from the CVM predictions led to various alternative interpretations for the structure of the light scalar mesons in terms of non-$q\bar{q}$ objects: like multi-quark states [36], glueballs mixed states [37], vacuum scalar state [38] or $K\bar{K}$ molecules [39].
In order to understand better the structure of the scalar mesons a much better knowledge is required on each of the observed mesons. In this sense the unexpected observation of the $f_0(980)$ in DIS data is very fortunate, as it enables us to obtain novel information on the structure of this scalar meson.
In the following subsection a part of the existing experimental data on the $f_0(980)$ meson is reviewed, including recently obtained data from e^+e^- collisions [40] and ν-scattering [41].

2.3.1 Production of the scalar meson $f_0(980)$

The main observed decay mode of the $f_0(980)$ is the two-pion channel: $f_0 \to \pi\pi$. No measurement of the branching ratio exists so far, but several observations of the $f_0(980)$ and of the kinematic dependence of the produced yields are available in the literature.
One of the first direct observations of the $f_0(980)$ scalar meson in a photoproduction experiment was reported in 1997 by the E687 collaboration at Fermilab [42]. Fig. 2.13 shows the two-pion invariant mass spectrum after subtraction of a smooth polynomial background in the $f_0(980)$ mass range. A Breit-Wigner fit has been used to extract a pole mass of 0.968 $\pm$ 0.0005 GeV and a width of 0.050 $\pm$ 0.0024 GeV.
In 1998 the OPAL collaboration published measurements of kinematic dependencies of the $f_0(980)$ yield from e^+e^- collisions with a center-of-mass energy corresponding to the Z^0

mass. The data were compared to JETSET 7.4 Monte Carlo calculations [40]. The good agreement with these LUND string-model based MC calculations is shown in Fig. 2.14. The kinematic dependencies of the $f_0(980)$ are compared to those of well established conventional mesons such as the $f_2(1270)$ and the $\phi(1020)$ with masses close to that of the $f_0(980)$. This led to the conclusion that the OPAL measurements are consistent with a conventional description of the f_0 meson in terms of a normal $^3P_0$ $q\bar{q}$ state.
More recently the NOMAD experiment has presented a more complete mapping of the kinematic dependencies of the $f_0(980)$ scalar meson as deduced from charged current interactions in neutrino-nucleon scattering. As an example the P_t^2 dependence is reproduced in the right panel of Fig. 2.15, while the left panel shows the $\pi^+\pi^-$ invariant mass spectrum with three distinct peaks corresponding to the positions of the $\rho^0(770)$, $f_0(980)$ and $f_2(1270)$ mesons. Also in the case of the NOMAD experiment a good agreement was found between most of

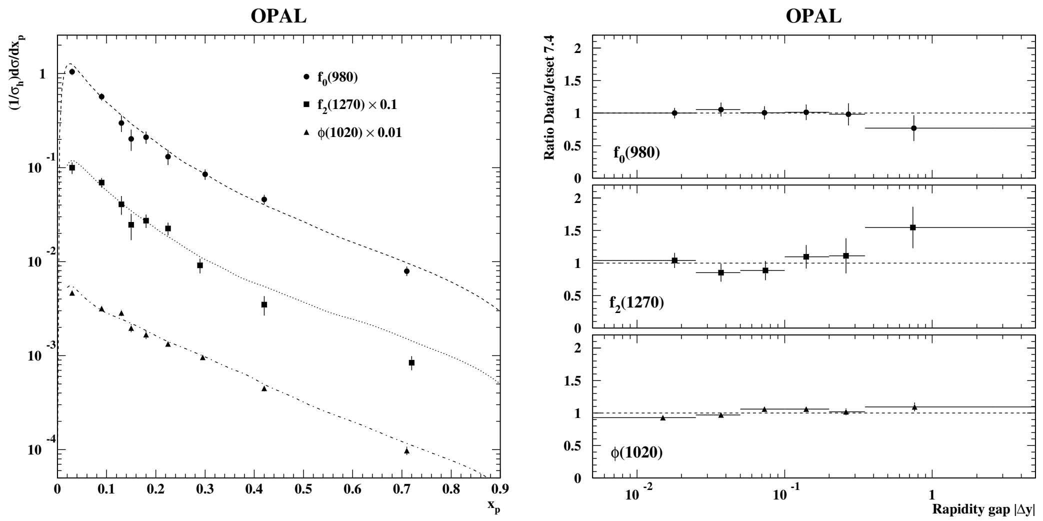

Figure 2.14: *Left: measured multiplicity distribution for f_0, f_2 and ϕ meson production at the OPAL experiment at CERN [40]. The data are plotted versus the scaled momentum of the two particles system x_p. Right: ratio of multiplicity distributions and JETSET 7.4 simulations as a function of the rapidity gap Δy. On the left the data are also compared to the JETSET 7.4 MC prediction.*

the measured distributions and the LUND Monte Carlo simulation. For future reference the slope of the P_t^2-distribution for $P_t^2 < 0.5$ GeV^2 is quoted here, b = (5.3 $\pm$ 0.2) GeV^{-2}.
Although the results from OPAL and NOMAD seem to show that the $f_0(980)$ is probably a normal $^3P_0$ $q\bar{q}$-state, the data cannot exclude other interpretations in the absence of MC generators based on the models from Ref. [36, 39], for instance. Recent data published by the KLOE collaboration ([43, 44]) instead, suggest that the f_0 nature could be consistent with a $q\bar{q}q\bar{q}$ model description as in Ref. [36]. Hence, the nature of the $f_0(980)$ remains an unre-

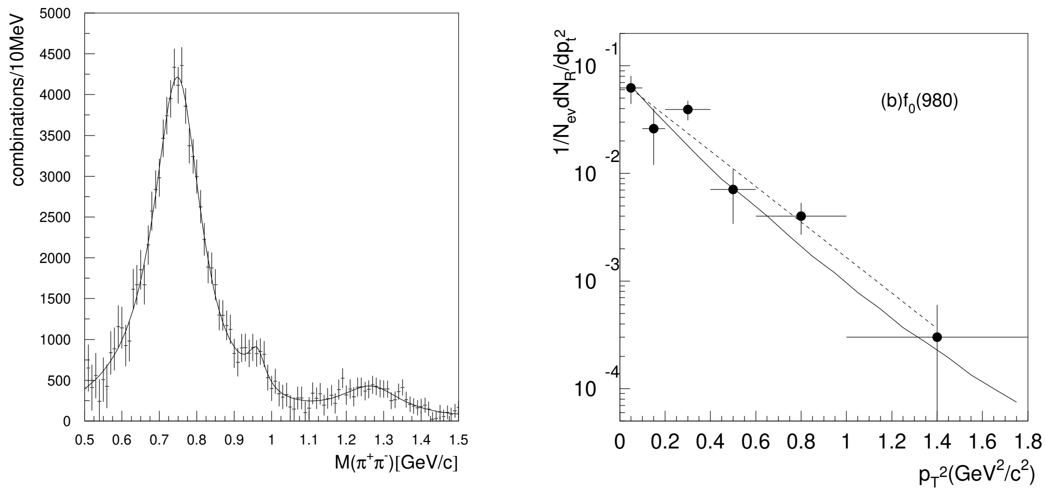

Figure 2.15: *Left:* NOMAD *data for the two-pion invariant mass spectrum as derived from ν-scattering at E_ν = 30-60 GeV on a target consisting mostly of carbon, [41]. Right: the P_t^2 dependence of the extracted f_0 yield is compared to the* LUND *simulation. The dashed line represents the result of the fit by the function $ae^{-bP_t^2}$.*

solved issue.
It has been suggested that the environment in which the $f_0(980)$ is produced can be used to determine some of its properties and may thus help to identify its dynamical structure [39]. By measuring the nuclear dependence of $f_0(980)$ leptoproduction, one can make a distinction between models assuming a relatively large size of the $f_0(980)$ -as would occur for a $K\bar{K}$ molecule- and other models. In the former case, Close has suggested that a large A-dependence should occur [39]. In the experimental results presented in chapter 7, this novel degree of freedom is used when studying the nature of the $f_0(980)$ scalar meson.

Chapter 3

The HERMES experiment

$'EPMH\Sigma$, in Greek mythology, messenger of the gods, the son of the god Zeus and of Maia, the daughter of the Titan Atlas. As the special servant and courier of Zeus, Hermes had winged sandals and a winged hat.

In order to perform at HERA MEasurements of nucleon Spin structure, the HERMES experiment was designed and built. The HERMES detector is located at one of the four experimental halls of the HERA electron-proton collider at DESY, as illustrated in Fig. 3.1. At HERA a polarized 27.5 GeV electron/positron beam and an unpolarized proton beam (920 GeV) are available. The proton beam passes unused through the HERMES detector. Instead a fixed polarized target is introduced into the electron/positron beam. Many different measurements can be carried out at HERMES on various properties of the nucleon related and unrelated to spin, such as the flavor asymmetry of the sea quarks [45], the exclusive vector-meson leptoproduction [46] and hadronization in nuclei [47]. For this purpose data are collected with polarized and unpolarized gaseous targets including ^{1}H, ^{2}H, ^{3}He, ^{4}He, ^{14}N, ^{20}Ne and ^{84}Kr. Because the physics analyses presented in this thesis are based on data obtained with unpolarized targets, no details are given on the polarized target or beam polarization techniques in the following sections. Details on the equipment needed for the polarized measurements can be found in [48, 49, 50]. In this chapter a brief description is given of the (unpolarized) target set-up at HERMES (sect. 3.1), and a more general description of the detector is presented. Some details are given on the techniques used to identify scattered and produced particles in deep-inelastic lepton scattering.

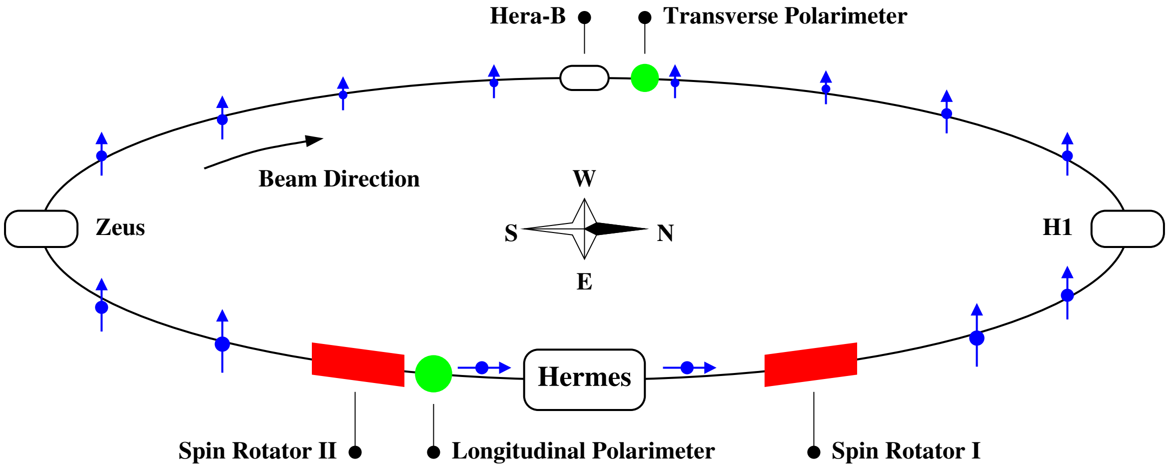

Figure 3.1: *The HERA storage ring with its four experimental sites. Only the electron beam is shown, with its spin direction symbolized by the small arrows. Two spin rotators ensure that the electron beam is longitudinally polarized at HERMES.*

3.1 The target

The HERMES target consist of an open ended storage cell [51] internal to the HERA positron ring. Using an *Unpolarized Gas Feed System* (UGFS) it is possible to deliver ^{1}H, ^{2}H, ^{4}He, ^{14}N, ^{20}Ne or ^{84}Kr gases with total areal densities between 10^{15} and 10^{16} nucl/cm^2 to the storage cell. The pressure in the UGFS is regulated via a diaphragm and a termo-valve in order to supply a constant density to the cell. The flow rate through the diaphragm can be measured with two barometers, by the pressure dependence of the diaphragm conductance. From the flow rate the target density for each gas can be evaluated given the cell conductance. Unfortunately this method gives an uncertainty on the absolute value of the target density of about 20%, mostly due to the uncertainty on the diaphragm and the cell conductances [52].

3.2 The spectrometer

The HERMES spectrometer is designed to perform asymmetry measurements in inclusive deep-inelastic scattering with high precision. In addition, hadronic products of the scattering processes can be reconstructed over a wide kinematic range, opening the possibility to carry out semi-inclusive measurements as well.
The HERMES spectrometer is a standard forward angle detector, symmetric about a central, horizontal shielding plate in the magnet. Both HERA beam pipes pass through the detector in the gap between the top and bottom part. A diagram of the spectrometer is shown in Fig. 3.2. The front tracking chambers are used to determine the polar (θ) and the azimuthal

(ϕ) scattering angles. The combination of the trajectories reconstructed by the chambers before and behind the magnet give the particle's momentum. In addition, three proportional chambers in the magnet help to merge front and back tracks and make it possible to track low momentum particles that do not reach the rear section of the spectrometer.
Particles with scattering angles within ± 170 mrad in the horizontal direction and between +(-)40 and +(-)140 mrad in the vertical direction are accepted. Together these boundaries lead to a polar angular acceptance of $40 < \theta < 220$ mrad.

3.2.1 Tracking

The first detector shown in Fig. 3.2, right after the target cell, with the name *Lambda Wheels* (LW) is the newly installed silicon detector. The LW are operational since 2001 but have not been used for measurements so far due to an extended period without beam at HERA which started in Sept. 2000. More information on this new detector is given in the next chapter.
After the LW in the drawing are shown the detectors of the front tracking system. The combined information from the micro-strip gas counters (VC1/2), drift vertex chambers (DVC) and front drift chambers (FC1/2) provide the reconstruction of the vertex position in the target, and the definition of the scattering angle[1]. The part of the track reconstructed in the back drift chambers (BC1/2 and BC3/4) add the information of the magnetic deflection to obtain the particle momentum. The back chambers also identify the hit in the particle identification detectors (PID) which can be associated with a particular track. The orientation of the wires of all tracking detectors is either vertical or tilted by 30° left or right. Like the rest of the spectrometer the tracking system is symmetric about the beam plane.
Momentum and angular resolution for positrons is limited by Bremsstrahlung and multiple scattering in the material of the target cell walls, as well as of the first tracking detectors. The momentum resolution is 0.7-1.25% over the entire kinematic range of the experiment, while the scattering angle resolution is better then 0.6 mrad [48].

3.2.2 Particle identification

The particle identification (PID) system at HERMES consists of four components and was designed to identify the DIS positron (or electron) with high efficiency and low hadron contamination.

Threshold and Ring Imaging Čerenkov detector

The Čerenkov detector is used for the separation of leptons from hadrons and for pion identification in the momentum range between 4 and 14 GeV. Electromagnetic radiation (Čerenkov

[1]In practice most analyses presented in this thesis are based on using either the FC1/2 alone, or a combination of VC1/2 and FC1/2.

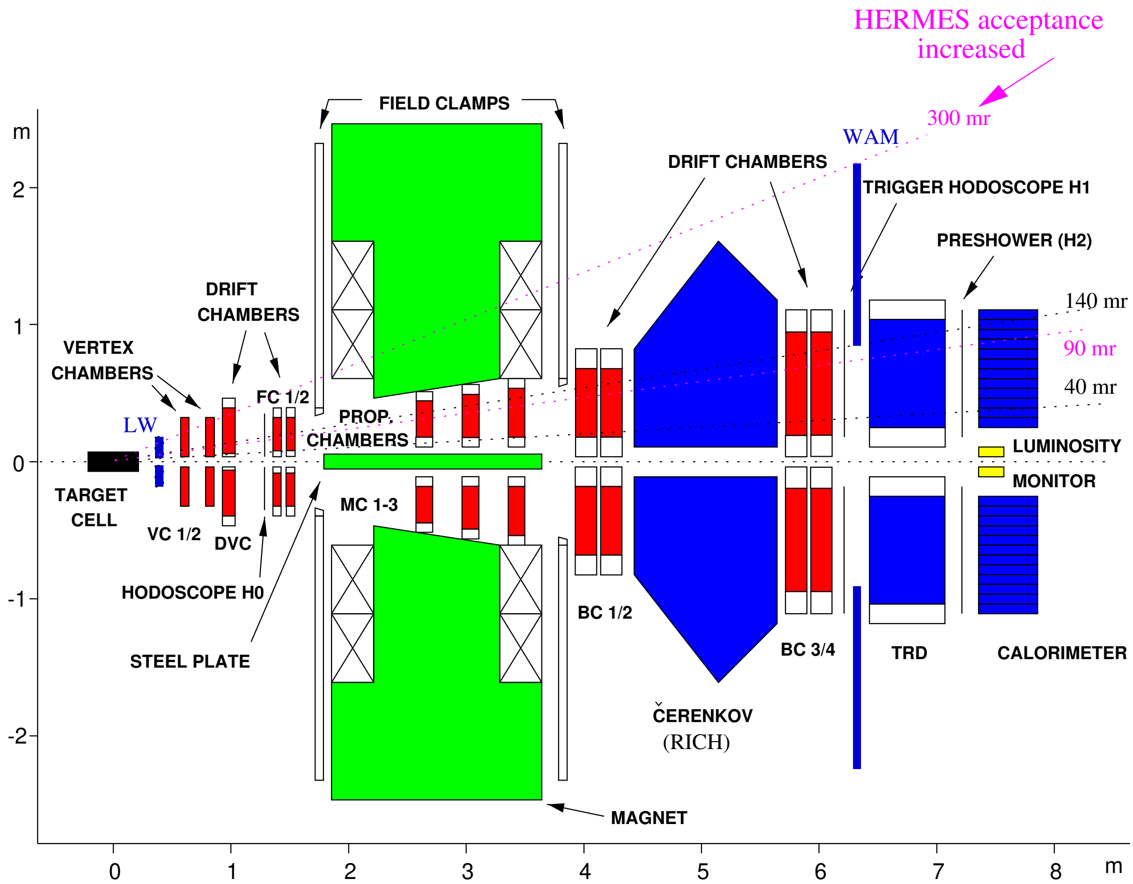

Figure 3.2: *Side view of the HERMES spectrometer. Both axes give the actual distance in meters with respect to the HERMES interaction point.*

light) is emitted when a particle traverses a medium with a velocity larger than the speed of light in that medium, $v > \frac{c}{n}$ with n the refraction index of the medium. The existing threshold Čerenkov detector was replaced in 1998 by a dual radiator Ring Imaging Čerenkov (RICH) to provide particle identification for pions, kaons and protons in the momentum range from 2 to 15 GeV [53]. The detector uses two radiators, a wall of silica aerogel tiles at the entrance of the detector, followed by a volume filled with C_4F_{10}, a heavy fluorocarbon gas. The photon detector consists of 1934 photomultiplier tubes (PMT) located above (below) the active volume for the top (bottom) part of the detector. The Čerenkov light cones are imaged onto the PMT by a spherical mirror array located at the rear of the radiator box. In Fig. 3.3 a schematic drawing of the main components of the (upper half of the) RICH are shown.

Different Čerenkov angles are produced in the aerogel and the heavy gas depending on the index of refraction as $\cos\theta_c = c/nv$. Moreover, the size of the angle has a different mo-

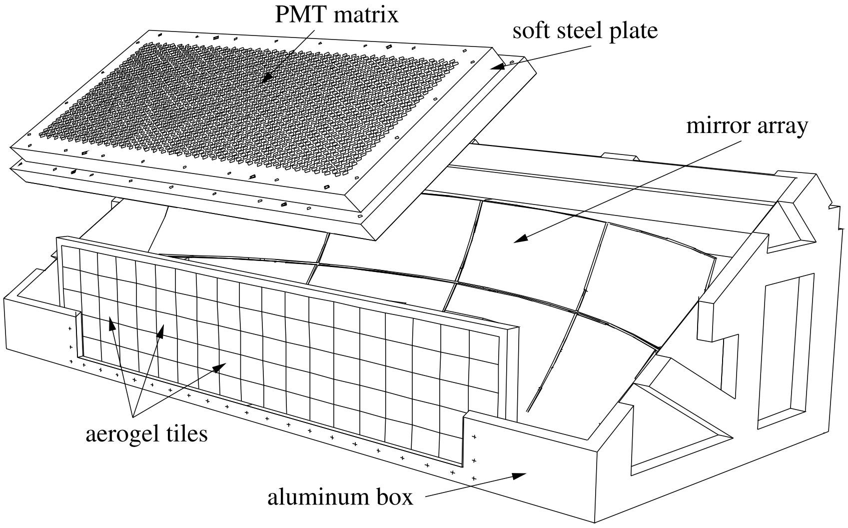

Figure 3.3: *A cut away schematic view of the (top) RICH counter.*

mentum dependence for pions, kaons and protons, as is shown in Fig. 3.4. These differences allow the identification of the different particle types with an efficiency of 98% for pions, 87% for kaons and 92% (82%) for protons (antiprotons)[2].

Transition Radiation Detector

The purpose of the *Transition Radiation Detector* (TRD) is to provide a pion rejection factor of at least 100 for electrons or positrons. The efficiency above 5 GeV for electron/positron detection is above 90%. Transition radiation is emitted when a charged particle crosses the boundary of materials with different dielectric constants. At 5 GeV the energy loss (dE/dx) of a pion in the detector is approximately 11 keV, while an electron deposits about twice as much energy due to transition radiation and the relativistic rise in dE/dx.
The detector consists of 2 halves of 6 sandwich modules alternating radiator material and X-ray detectors. The signal from the TRD is obtained by the combination of 5 out of 6 modules, where the one which received the largest signal is rejected. This method is called the *truncated-mean average*, and is meant to reduce proton-hadron signal overlap.

[2]The RICH efficiencies reported here are evaluated in the specific case of the analysis presented in chapter 6.

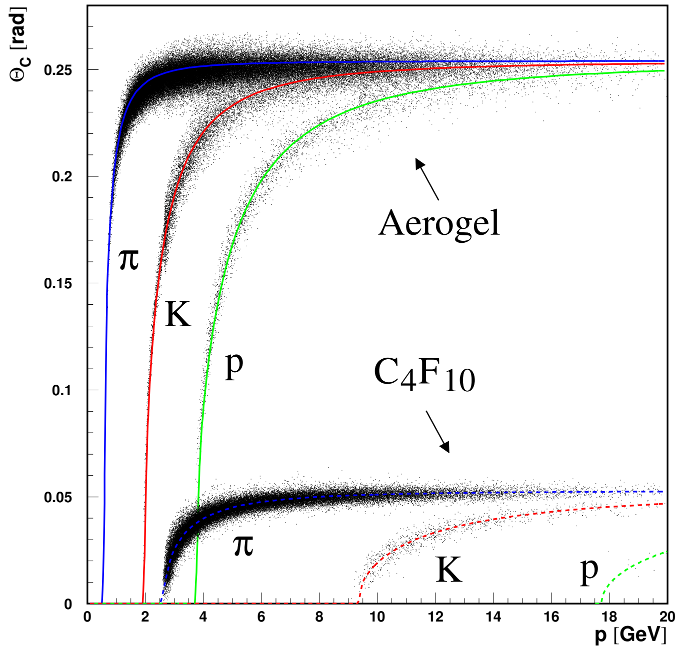

Figure 3.4: *The Čerenkov angle θ versus hadron momentum for the aerogel (upper band) and C_4F_{10} gas radiators (lower band). The data shown are based on a Monte Carlo simulation.*

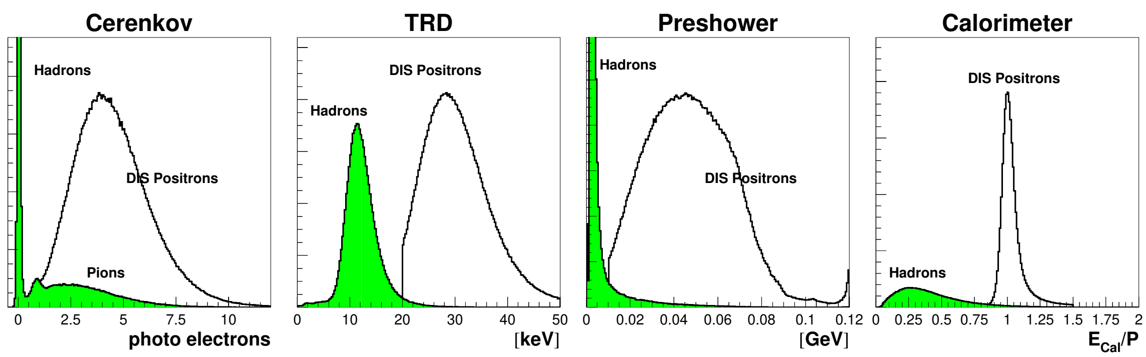

Figure 3.5: *Analogue signals from the four Particle Identification Detectors in HERMES. The Monte Carlo results of the separated signals of hadrons and DIS positrons are shown for each of the four detectors. In this simulation the threshold Čerenkov detector is used rather than the RICH which was installed in 1998.*

Pre-shower and Calorimeter

A lead glass calorimeter and a pre-shower hodoscope are used in the first level trigger to identify scattered positrons or electrons based on the difference between electromagnetic and hadronic shower in a localized energy region ($\geq$ 3.5 GeV for unpolarized targets). The calorimeter is also used to measure the energy of the scattered leptons, and photons from radiative decay of π^0 and η mesons. The energy resolution of the calorimeter is parameterized as [54]

$$\left(\frac{\sigma(E)}{E}\right)_{\text{calo}} = \frac{5.1 \pm 1.1}{\sqrt{E[GeV]}} + (2.0 \pm 0.5)[\%]. \tag{3.1}$$

The depth of each of the 9×9×50 cm^3 glass blocks corresponds to 18 radiation lengths. The electrons therefore will lose all their energy in the calorimeter while the hadrons will deposit only a fraction of their energy. The ratio E/p can be used to distinguish electrons from hadrons, where E is the deposited energy in the calorimeter and p the momentum determined by the spectrometer.
The pre-shower detector consists of a 1.1 cm Pb layer in front of the hodoscope denoted by H2 in the diagram. The passive radiator initiates electro-magnetic showers that deposit more energy for leptons in the scintillator than other minimum ionizing particles (hadrons). While pions deposit only 2 MeV, positrons are distinguished by a broad distribution with a mean deposited energy of about 20-40 MeV. The pre-shower resolution adds to the calorimeter once resulting in the total energy resolution given by [54]

$$\frac{\sigma(E)}{E} = \left(\frac{\sigma(E)}{E}\right)_{\text{calo}} + \frac{10.0 \pm 2.0}{E[GeV]}[\%]. \tag{3.2}$$

Particle identification scheme

In order to discuss the overall particle identification properties of the HERMES spectrometer, the results of a Monte Carlo simulation of the yield of each PID detector for hadrons and leptons separately are given in Fig. 3.5. The signals from the four detectors are usually combined using a likelihood method, which allows to convert the observed signal strengths into true probabilities for hadron or lepton identification using Bayes' theorem:

$$\mathcal{P}^i = \frac{\Phi^i \mathcal{L}^i}{\sum_j \Phi^j \mathcal{L}^j}, \tag{3.3}$$

where Φ^i is the flux of particles of type i which is (generally) a function of momentum and scattering angle, and $\mathcal{L}^i$ is the likelihood for observing a particle of type i for which the amplitude of the signal in a given detector is taken. The PID function which is used in practical data analyses, is evaluated according to:

$$\text{PID} = \log_{10} \frac{\mathcal{P}^e}{\mathcal{P}^h} = \log_{10} \frac{\mathcal{L}^e}{\mathcal{L}^h} + \log_{10} \frac{\Phi^e}{\Phi^h}, \tag{3.4}$$

where $\mathcal{P}^{e(h)}$ is the probability that the reconstructed particle is a lepton(hadron), and $\mathcal{P}^e + \mathcal{P}^h = 1$. For the ratio of likelihoods $\frac{\mathcal{L}^e}{\mathcal{L}^h}$ the signals from the various PID detectors are combined as follows [55]:

$$\begin{aligned}
\log_{10}\frac{\mathcal{L}^e}{\mathcal{L}^h} &= \log_{10}\frac{\mathcal{L}^e_{\mathrm{Cal}}\cdot\mathcal{L}^e_{\mathrm{Pre}}\cdot\mathcal{L}^e_{\mathrm{Cer}}}{\mathcal{L}^p_{\mathrm{Cal}}\cdot\mathcal{L}^p_{\mathrm{Pre}}\cdot\mathcal{L}^p_{\mathrm{Cer}}} + \log_{10}\frac{\mathcal{L}^e_{\mathrm{TRD}}}{\mathcal{L}^h_{\mathrm{TRD}}} \\
&\equiv \mathrm{PID}_3 + \mathrm{PID}_5,
\end{aligned} \tag{3.5}$$

where PID_3 indicates the sum of the 3 likelihoods of Čerenkov, Pre-shower and Calorimeter and PID_5 the sum of the 5 likelihoods of the TRD modules according to the truncated-mean method. In the analysis performed after the year 1998 the Čerenkov likelihood is removed from the PID scheme and a new function called PID_2 is defined containing only the calorimeter and pre-shower information, while the RICH information is analyzed separately as explained in the next subsection. In order to be able to select well defined regions of the yield of all PID detectors the electron efficiency ϵ and hadron contamination h can be calculated from the probability functions defined in Eq. (3.3) as follows:

$$\epsilon = \frac{\displaystyle\int_{\mathrm{PID}_{cut}}^{\infty} d\mathrm{PID}\;\; \mathcal{P}^e\;\; N}{\displaystyle\int_{-\infty}^{\infty} d\mathrm{PID}\;\; \mathcal{P}^e\;\; N}, \tag{3.6}$$

$$h = \frac{\displaystyle\int_{\mathrm{PID}_{cut}}^{\infty} d\mathrm{PID}\;\; \mathcal{P}^h\;\; N}{\displaystyle\int_{\mathrm{PID}_{cut}}^{\infty} d\mathrm{PID}\;\; N}, \tag{3.7}$$

where the integrals are evaluated using only the PID variables implicitly defined in Eq. (3.5), and N is the number of particles at a given PID value. With this method it has been found that electrons and positrons can be identified with an efficiency of more than 98% and a hadron contamination of less than 1%.

RICH particle identification

The RICH PID combines the information from the reconstructed angles and the unknown threshold behavior of the response of both radiators, the aerogel and the C_4F_{10} gas. Two methods are used to combine all this information into a particle identification response: Inverse Ray Tracing (IRT) and Direct Ray Tracing (DRT) [53]. For the purpose of the present analysis only the IRT method is applied, which is further described in Ref. [56].
For each hit in the PMTs one aerogel Čerenkov angle and one gas Čerenkov angle is reconstructed. The average angles resulting from the IRT method are compared to the simulated curves of Fig. 3.4 at the measured momentum with a likelihood analysis to obtain the probability that a given hadron produced the track. The likelihood algorithm defines for a known particle flux Φ_t, a set of probabilities P_t^i for a true particle of type t to be identified as a

particle of type i (i.e. π, K, p, or X) if the average angle reconstructed with the IRT method is $< \theta >$. This set of identification probabilities is a 4×3 matrix since it includes also the probability that a particle of type t is not identified by the RICH (type X, or unknown):

$$P(\pi, K, p) = \begin{bmatrix} P_\pi^\pi & P_K^\pi & P_p^\pi \\ P_\pi^K & P_K^K & P_p^K \\ P_\pi^p & P_K^p & P_p^p \\ P_\pi^X & P_K^X & P_p^X \end{bmatrix}. \tag{3.8}$$

However, what is needed in an analysis in order to extract the information of the true particle type is the complementary matrix of true type probabilities Q_t^i that a particle is identified as type i if it is truly of type t:

$$Q(\pi, K, p) = \begin{bmatrix} \mathbf{Q}_\pi^\pi & Q_\pi^K & Q_\pi^p & Q_\pi^X \\ Q_K^\pi & \mathbf{Q_K^K} & Q_K^p & Q_K^X \\ Q_p^\pi & Q_p^K & \mathbf{Q_p^p} & Q_p^X \end{bmatrix}. \tag{3.9}$$

The diagonal terms of the left 3×3 matrix are the purities for a certain data sample, the off-diagonal terms are the contaminations. The columns of the P and the Q matrices are normalized to unity. The relation between the P and the Q matrices is given by the Bayes' theorem:

$$Q_t^i = \frac{P_t^i \cdot \Phi_t}{\sum_s P_s^i \cdot \Phi_s}, \tag{3.10}$$

where Φ_t is the relative flux of hadrons of type $t = \pi, K, p$ and i is the identified type ($i = \pi, K, p, X$). For each kinematic interval in momentum of the data sample in which the fluxes are calculated, the relation between the vectors of the numbers of true $\vec{N}$ and identified $\vec{I}$ particles is given by:

$$\vec{N} = Q \cdot \vec{I} \tag{3.11}$$

or in terms of a matrix product,

$$[N_\pi, N_K, N_p] = \begin{bmatrix} Q_\pi^\pi & Q_\pi^K & Q_\pi^p & Q_X^\pi \\ Q_K^\pi & Q_K^K & Q_K^p & Q_X^K \\ Q_p^\pi & Q_p^K & Q_p^p & Q_X^p \end{bmatrix} \cdot \begin{bmatrix} I_\pi \\ I_K \\ I_p \\ I_X \end{bmatrix} \tag{3.12}$$

Eq. (3.12) is applied to the data in chapter 6 to identify pions, kaons and protons. Currently the P matrices used for the HERMES RICH detector are binned in momentum and also in track multiplicity to account for events with overlapping rings. While the P matrices are only dependent on the detector response, the Q matrices combine the performance of the detector to the relative particle fluxes of a data sample and therefore are analysis dependent. Q matrices are binned in momentum, track multiplicity and particle charge, to account for differences in the fluxes of opposite charges.

3.2.3 The luminosity monitor

A measurement of the integrated luminosity recorded during a certain time period is needed as a relative normalization factor to compare cross sections from different data sets, i.e. different spin states or different target gases. The luminosity accounts for differences in target thickness, beam intensity and beam position. The measurement is based on elastic scattering of beam positrons from atomic target gas electrons (Bhabha scattering). However, it should be noted that the named process $e^+e^- \rightarrow e^+e^-$ is indistinguishable from processes involving the annihilation of an electron and positron into two photon pairs $e^+e^- \rightarrow \gamma\gamma$ because the luminosity monitor cannot separate electrons from photons. The coincidences of scattered particles are detected in two arrays of 3×4 calorimeter blocks placed at z = 7.2 m from the center of the target and positioned at 3 cm left and right from the center of the beam pipe during standard data taking. During injection and dumping of the beam the luminosity detector is moved to a larger distance. The hit distribution in the calorimeters is shown in Fig. 3.6. Coincident pairs are selected requiring two signals with energy above 5 GeV in both the left and right calorimeter. An average rate of about 150 Hz provides a statistical accuracy of the luminosity measurement of 1% for every 100 s. It is noted that due to geometry and calibration differences care should be taken when data from different years are normalized by means of the luminosity monitor (see section 5.2.4).

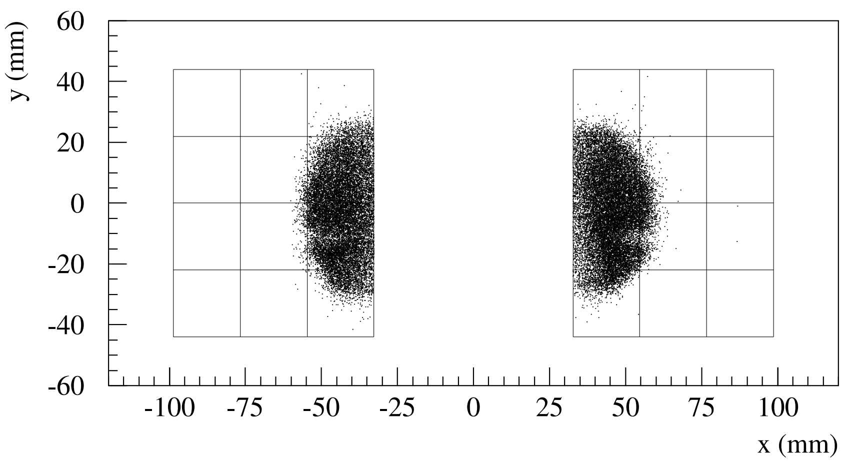

Figure 3.6: *Hit distribution in the calorimeter blocks of the luminosity monitor. The zero position in x and y indicates the center of the beam pipe*

3.3 Data acquisition

3.3.1 Trigger

The HERMES first level trigger consists of discriminated signals from the hodoscopes plus a column-wise summed calorimeter signal and, in the years before 1998, the Čerenkov counter signal. The decision to initiate digitization and readout of an event is made within about 400 ns. In this way various triggers are constructed such as one for DIS events, photo-produced hadrons, etc.

The DIS trigger is the one most relevant for the analyses presented in this thesis. It requires a hit in each of the three hodoscopes H0, H1 and H2, plus energy deposition in one of the calorimeter columns above threshold. As a clock to synchronize the trigger the HERA electron bunch timing is taken. The calorimeter threshold for unpolarized data taking is set to 3.5 GeV, which equals a cut at $y < 0.87$. Such a setting suppresses the charged hadronic background by a factor of more than 10 in the trigger. The pre-shower threshold is set below the level of minimum ionizing particle to suppress hadronic showers depositing enough energy. The requirement of a signal in the hodoscope H1 ensures a complete track behind the spectrometer magnet and helps to suppress neutral particle background. A time window set around the HERA clock signal works efficiently to suppress the background from protons coming from the HERA proton ring passing through the detector in the opposite direction.

3.3.2 Data acquisition system

The HERMES *Data AcQuisition system* (DAQ) consists of two separated parts, the front-end electronics located in a trailer close to the experimental area and the online workstation cluster. The connection between the two is realized with optical fibers. The maximum DAQ throughput is 1.5 Mbyte/s. Raw events are collected online and separated in *runs*, of about 450 Mbyte recorded data. During the time needed for the digitization and readout of the detector, no new trigger can be accepted, leading to a trigger *dead time*. For each trigger a dead time fraction δ_i is defined as:

$$\delta_i = 1 - \frac{T^i_{acc}}{T^i_{gen}}, \tag{3.13}$$

where T^i_{acc} and T^i_{gen} are the number of accepted and generated triggers of type i respectively. The dead time fraction is dependent on the trigger rate. For each trigger a value of δ_i is given every 10 seconds, the period of time (chosen arbitrarily) referred to as a *burst*. Data are normally analyzed which have δ_i above 0.5, but a typical value for the dead time is higher (i.e. for the DIS trigger dead time around 0.9).

Chapter 4

Silicon detector at HERMES

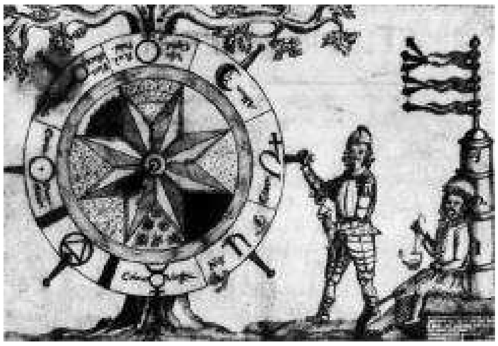

Mercurio gira la Ruota ad Otto Raggi, che rappresenta
la Grande Opera. Regge in mano il Telum Passionis.
(Speculum veritatis, XVII sec.)

During the year 2001 a new detector has been installed in the front region of the HERMES spectrometer as part of a general upgrade project. A wheel-shaped array of silicon counters was placed right after the target chamber and before the standard tracking detectors. The aim is to increase the detector acceptance and in particular to augment by a factor of four the yield of reconstructed Λ-hyperons. The increase of events containing Λ-hyperons is needed to obtain additional and qualitatively new information on the spin structure of the nucleon and some other baryons. The motivation of the project is briefly summarized in section 4.1.
An increase of the Λ statistics is also of interest for the study of nuclear effects at HERMES. As discussed in detail in chapter 6 the study of nuclear attenuation effects for different hadron types, has provided evidence that baryons have longer formation times than mesons. At present the only baryons for which such an evidence exists are protons and anti-protons. The possibility to extend these studies of possible meson-baryon differences with measurements on hyperon (Λ, Σ^*, Ξ) formation times is a very attractive perspective for the nearby future.

The bulk of this chapter is devoted to a description of the Lambda Wheels detector system. Details on the chosen double-sided silicon strip detector are given in section 4.2, which also contains a description of the general working principle of silicon detectors. In section 4.3 the design of the Lambda Wheels themselves is presented, whereas some results obtained with a prototype of a single module which was operated in the year 2000, are the subject of the last section of this chapter.
It is noted that the design, construction and commissioning of the Lambda Wheels silicon detector at HERMES is a large collaborative effort involving several institutions (NIKHEF, PNPI, University of Nürnberg-Erlangen). In this chapter only those studies are presented which were carried out by the author of this thesis. Related results describing other aspects of this work can be found in the PhD thesis of J. Visser [57] (Silicon test counter), D. Heesbeen [58] (Tracking and efficiency) and A. Reischl [59] (Commissioning).

4.1 Physics motivation

The observation of hyperons in deep-inelastic scattering gives access, due to their strangeness content, to novel aspects when studying the spin structure of baryons. Moreover, experimental evidence in the past 30 years has shown that the Λ-hyperon, as well as other hyperons (e.g. Σ, Ξ), is a self-analyzing particle [60, 61, 62]. A particle is self-analyzing when its polarization can be measured from the angular distribution of its decay products. The polarization of the Λ particle can be measured from its dominant hadronic decay: $\Lambda \rightarrow p+\pi^-$ and $\bar{\Lambda} \rightarrow \bar{p} + \pi^+$. Because of the parity-violating nature of the weak decay, the proton is preferentially emitted in the direction of the spin of the Λ. Defining θ_0 as the angle between the proton momentum and the Λ-polarization vector P_Λ, the angular distribution of the emitted protons can be expressed by

$$\frac{dN}{dcos\theta_0} = N_0(1 + \alpha P_\Lambda \; cos\theta_0), \tag{4.1}$$

where $\alpha = 0.642 \pm 0.013$ is the asymmetry parameter of the parity-violating weak decay of the Λ-hyperon [63] and N_0 is a normalization constant.
Both the strangeness content and its self-analyzing nature make the Λ-hyperon a unique tool in spin physics. It allows studies of various subjects, such as the strangeness polarization in the nucleon, the polarization of the sea quarks, gluon polarization, the spin structure of the Λ-hyperon, charm threshold production and transversity. It goes beyond the scope of this thesis to discuss all these subjects. In the following subsections only two have been selected: transversity and Λ_c threshold production.

4.1.1 Transversity

Apart from the structure functions $F_{1,2}(x)$ and $g_{1,2}(x)$ already introduced in chapter 2, there is a third leading twist structure function $h_1(x)$ known as *transversity* distribution. At present no data are available on $h_1(x)$, but theoretical predictions suggest that the tensor charge $\delta\Sigma_q$ is considerably larger than the longitudinal quark spin contribution $\Delta\Sigma_q$. This is due to the absence of gluon-splitting in the transverse case, which also results in a relatively weak Q^2 dependence of $h_1(x)$.
Because of its chiral-odd nature the $h_1(x)$ structure function can be accessed in semi-inclusive DIS only if combined with a chiral-odd fragmentation function. The transverse spin transfer from a u quark to the Λ, δD_q^Λ is such a function.
In the QPM the spin of the Λ is entirely due to the strange quark, while the up and down quark polarizations are zero. Assuming instead SU(3) flavor symmetry, up and down quarks also contribute to the Λ polarization. This is important as, due to the larger charge factor, the up quark will dominate interactions in which spin is transfered to the Λ.
Assuming u-quark dominance [64] the measurement of P_Λ with an unpolarized target and a *longitudinally* polarized beam gives direct information on the longitudinal spin transfer from a u-quark to a Λ-hyperon,

$$\vec{P_\Lambda} \simeq \hat{p}_B \; P_B \; D(y) \, \frac{\Delta D_u^\Lambda}{D_u^\Lambda}, \tag{4.2}$$

where $D(y)$ is the depolarization factor, P_B the beam polarization, and $\hat{p}_B$ the beam direction. Measurements (at HERMES [65]) have shown that $\frac{\Delta D_u^\Lambda}{D_u^\Lambda} \approx 0$, but the precision of these data is still very modest. Here future LW-data will certainly contribute.
In the case of unpolarized beam and *transversely* polarized target instead, the Λ polarization is expressed by [64]:

$$\vec{P_\Lambda^\perp} \simeq \vec{P_T}^\perp (1 - D(y)) \, \frac{\delta u}{u} \, \frac{\delta D_u^\Lambda}{D_u^\Lambda}. \tag{4.3}$$

If the fragmentation function $\frac{\delta D_u^\Lambda}{D_u^\Lambda}$ can be estimated from other sources this expression gives access to the transverse spin distribution of u-quarks in the nucleon ($\frac{\delta u}{u}$), which is the dominant contribution to the transverse structure function $h_1(x) = \delta q(x) \equiv \frac{1}{2}(\frac{4}{9}\delta u(x) + \frac{1}{9}\delta d(x) + \frac{1}{9}\delta s(x))$.
It is noted that the observation of $\frac{\Delta D_u^\Lambda}{D_u^\Lambda} \approx 0$ does not imply that $\frac{\delta D_u^\Lambda}{D_u^\Lambda}$ is small as well, since the longitudinal result may well be caused by a subtle cancellation between various heavy hyperons (that decay in a Λ) involving different gluon contributions that are absent in the transverse case.
Transverse polarization data collected using the LWs will thus give access to transversity through Eq. (4.3).

4.1.2 Open charm production

In the production of open charm the $c\bar{c}$ pair in which the virtual photon fluctuates gives rise to two charmed baryons (e.g. $\gamma^* \rightarrow c\bar{c} \rightarrow D^-\Lambda_c^+$). The large mass of the c-quark sets the hard scale of the process. Therefore, it is possible to describe photo-production of open charm with a perturbative expansion in the QCD framework, while the same does not apply to photo-production of lighter quarks. The HERMES energy domain for charm photo-production is relatively low, and covers the threshold region. At threshold all the constituent quarks of the target must act coherently, as all available energy must be used in the heavy quark production process, but the precise mechanism is at present not understood. If the dominant production mechanism of open charm production near threshold is photon-gluon fusion [66], this process is sensitive to the gluon polarization in the nucleon $\left(\frac{\Delta G}{G}\right)$ provided that the measurement is performed with polarized beam and target. However, other mechanisms may also contribute to open charm production near threshold, such as multi-quark, gluonic, or hidden-color correlations in hadronic or nuclear wave functions [67]. The large anticipated yield of Λ_c^+-hyperons using the Lambda Wheels at HERMES will make it possible to shed some light on its production mechanism, and possibly extract information on $\left(\frac{\Delta G}{G}\right)$ [58].

4.2 Silicon detectors: principle of operation

Detection of charged particles and electromagnetic radiation is made possible by their interaction with matter. Charged particles and electromagnetic radiation can ionize atoms and produce free electric charge carriers. The current induced by the drift of such carriers can be measured. The application of semiconductors for the measurement of position and energy is motivated by the high electron density, low ionization energy (3.6 eV compared to 30 eV for Ar detectors), and high mobility for both electrons and holes. All these characteristics ensure a high precision and fast response in a detector. This section summarizes the basic semiconductor physics, and introduces the elementary structure of semiconductor devices.

4.2.1 Basic semiconductor physics

The physical principle applied in a semiconductor detector is the fact that a charged particle traversing a material ionizes and produces electron-hole pairs along its track, in number proportional to the energy loss. If an electric field is present in the ionization region the produced charges are separated before they recombine and they drift in opposite directions towards the electrodes where they are collected. The collected charge produces a current pulse of a few ns on the electrode, the integral of this pulse signal equals the total charge generated by the incident particles.

In a silicon detector the p$^+$n diode is reversed-biased by a high voltage V applied to the junction side of a silicon layer of thickness d, such that an active area of thickness l is depleted of all mobile charge carriers. In the depleted region an electric field E is present which has its maximum at the junction side and it linearly decreases to zero at the ohmic contact. The electric field determines the speed of the positive (negative) electric charges $v_{drift}^{p(n)}$ in a given material. The basic structure of a silicon detector is shown in Fig. 4.1. The readout electron-

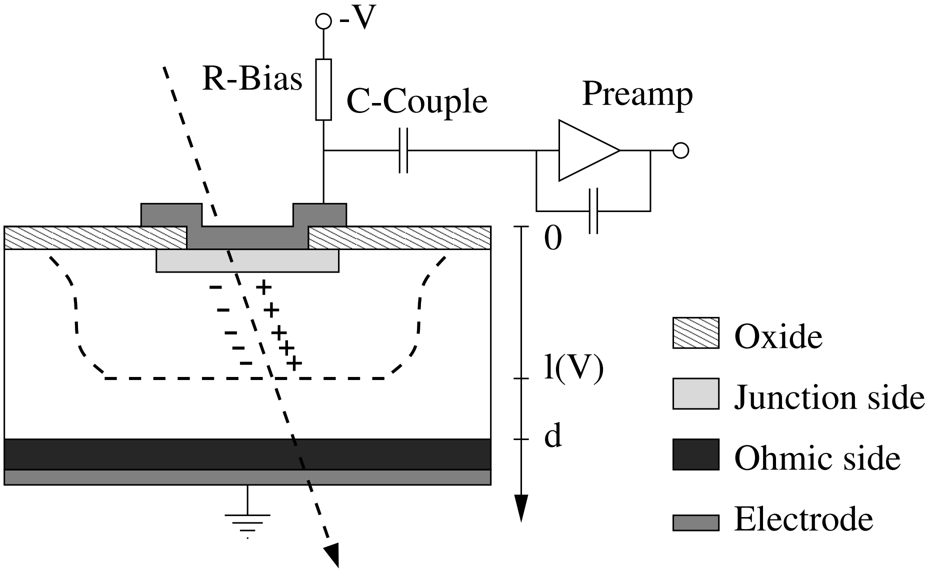

Figure 4.1: *Schematic representation of the basic operation of a silicon detector. The electron-hole pair created in the depleted region is collected and converted into a signal by the readout electronic.*

ics consist of a charge integrating amplifier followed by a shaping amplifier.
Three parameters can be optimized when choosing a semiconductor: the average ionization energy E_{ion} necessary to produce one electron hole pair, the mobility of charges in the material $\mu^{p(n)}E = v_{drift}^{p(n)}$, and the size of the region where the electric field E can be generated $l \leq d$. Silicon is considered to be a good semiconductor, with low average E_{ion} = 3.6 eV and a mobility of the same order for electrons and holes ($\mu^n = 1350$ cm^2/Vs, $\mu^p > 480$ cm^2/Vs). The number of collected charges depends on the thickness l of the depleted region, which needs to be maximized for a better performance of the detector. The size of the depleted region is a function of the bias voltage [68],

$$l(V) = d \cdot \left(\frac{V + V_0}{V_{dep} + V_0} \right)^{1/2} \qquad V < V_{dep} \tag{4.4}$$

$$= d \qquad V \geq V_{dep} \tag{4.5}$$

with V_0 the contact potential and V_{dep} the depletion voltage for which $l = d$. In general, the bias voltage and depletion voltage are much larger than the contact potential and the approximation $V_0 \approx 0$ can be used. In this approximation the size of the depletion is proportional to $\sqrt{V}$. A bias voltage smaller than the depletion voltage causes a reduction of the signal.
If the signal becomes too small with respect to the noise of the electronics the operation of the detector becomes impossible. Hence, an important parameter in the construction and operation of a silicon detector is the ratio of the signal to noise amplitudes. The amount of noise is related to the detector capacitance, the readout amplifier, and the leakage current generated in the silicon layer under the influence of the bias potential. An increase of leakage current and capacitance generally implies an increase of noise. Attention should be given to the design of a detector in order to minimize the noise level of the electronic circuit. Moreover, during the operation of the detector the optimal value for the bias voltage and working temperature need to be chosen.

Characterization of silicon

The characterization of silicon detectors consists of three basic measurements: backplane capacitance, interstrip capacitance, and leakage current. First the detector capacitances are addressed.
The total capacitance of a detector is given by the sum of backplane and interstrip capacitance. The interstrip capacitance is larger, and it is found to be a linear function of the strip width and pitch [69]. The capacitance of the metal strip to the backplane is discussed in more detail since it is the dominant contribution in describing the voltage dependence of the total capacitance in the range of interest for the operation of the detector. Assuming a plane capacitor with parallel electrodes of area A, the backplane capacitance is defined as:

$$C_{back}(V) = \epsilon_r \epsilon_0 \frac{A}{l(V)}, \tag{4.6}$$

where ϵ_r = 11.9 is the permittivity of silicon. For large bias voltages one has $C_{back}(V) \propto 1/\sqrt{V}$. As illustrated in Fig. 4.2 the relation between the capacitance and the voltage is linear. For $V > V_{dep}$ the thickness of the depleted region becomes constant and therefore also the capacitance. Small additional contributions can cause a deviation from the constant behavior which are not addressed here (see for instance Ref. [68]). While for $V = 0$ the value of the capacitance is determined by the contact potential.

Leakage current

The total current generated in a detector is the sum of various contributions. Because of the large depletion volume usually the largest current source is the generation of electron-hole pairs in absence of an ionizing particle traversing the active volume. Defects close to the

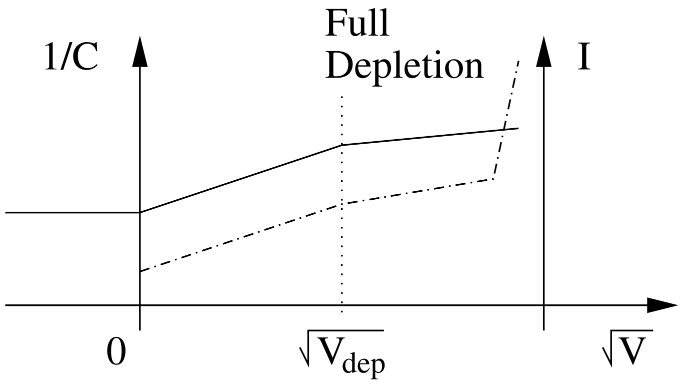

Figure 4.2: *Schematic view of the voltage dependence of capacitance (solid line) and leakage current (dot-dashed line).*

middle of the band gap are efficient electron-hole generation centers. The volume component of the leakage current can be expressed as a function of voltage and temperature [68]:

$$I_{Vol}(V,T) = q_0 A n_i \frac{l_g(V)}{\tau_g} \quad (4.7)$$

$$= \left(q_0 A \frac{l_g(V)}{\tau_g}\right) \sqrt{N_C N_V}\, exp\left(-\frac{E_g}{2k_B T}\right), \quad (4.8)$$

with τ_g and $l_g(V)$ the generation lifetime and width respectively. In general the generation width is not equal to the whole depletion width, only for high voltages they approach each other: $l_g(V) \approx l(V)$ and therefore $I_{Vol} \propto \sqrt{V}$, as shown in Fig. 4.2. There is a limit for the increase of the bias voltage above depletion which is defined as the breakdown voltage. When the bias voltage gets close to the breakdown voltage the slope of the leakage current curve becomes steeper. Normally it is preferable to operate a detector below this point.
The intrinsic carrier concentration n_i is proportional to the effective density of states in the conduction (N_C) and in the valence (N_V) bands, and to the band gap energy, E_g, defined to be the minimum energy needed to excite an electron from the valence into the conduction band. In the literature, [70], values for the band gap energy are given at room temperature (20°C) where E_g=1.12 eV. It is seen that the leakage current increases with the silicon temperature according to the exponential term in Eq. (4.8).

4.2.2 Basic detector structure

The basic detector configuration was already presented in Fig. 4.1. The diode consists of a highly doped p^+ region, connected to a very low-doped n^- one and a highly doped n^+ layer which gives the possibility to create a metallic contact with the electrode. The semiconductor is sandwiched between two aluminum electrodes and the whole detector is operated in reverse bias mode. The electron-hole pairs generated by charged particles or radiation passing through the depleted region are separated by the electric field, and drift towards the electrodes.

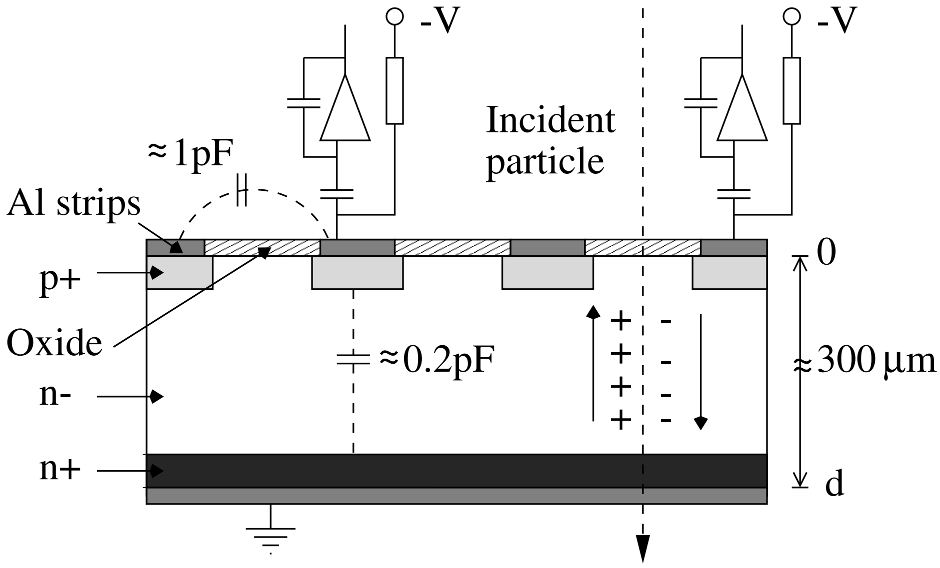

Figure 4.3: *Basic structure of a DC p-n junction detector, of which the junction side is split up in strips.*

Strip detectors

Semiconductors play an important role in modern high precision tracking measurements. To obtain information on the track of a single particle passing the detector the p side of a p-n junction detector as the one described above can be divided into narrow strips. The width of each strip can vary between 20 and 5000 μm. In the case of the HERMES Lambda Wheels detector a strip width of 160 μm was chosen, and each strip has a separate analogue read out. In a detector with strips of this size the position of the particle's track can be determined by interpolating the signals deposited in adjacent strips. A schematic view of a widely used silicon micro-strip detector is given in Fig. 4.3. This type of detector only uses the information of the p-strips for position determination. If also the n^+-doped backside of the detector is equipped with a strip shaped read out, a second coordinate can be obtained by interpolating also the signal induced on the ohmic side. A p-doped conductor (called a p-stop, not shown) is needed to separate two adjacent n^+-strips which would otherwise be short-circuited by the electron accumulation.
A further improvement in the 2D position reconstruction can be obtained by using pixel de-

tectors. As an example the ATLAS pixel detector will have pixel sizes of $50 \times 300\ \mu\text{m}^2$ [71]. This configuration resolves the ambiguities that occurs in double sided strip detectors when more than one track per event hits the same detector.

4.3 Detector description

The Lambda Wheels are a detector system for minimum ionizing particles, with the main purpose of reconstructing tracks of decay products of slowly decaying particles through the determination of the secondary vertex of processes like $\Lambda^0 \rightarrow p\pi^-$ or $K_s^0 \rightarrow \pi^+\pi^-$.
The wheels are located inside the same vacuum vessel as the beam, just downstream of the target chamber, as presented in Fig. 4.4. The beam (going from left to right in the figure) is separated from the main volume by the target cell, the target extension-piece, the *Wake-Field Suppressor* (WFS) and the beam-pipe. The pumping holes in the WFS are covered by a fine-mesh gauze, and the pumping cross is separated from the target chamber by a similar screen. Two detector layers are placed at z = 45 cm and z = 50 cm from the center of the target. The overall acceptance of the HERMES spectrometer is increased such that now 75-80% of all Λ particles resulting from the decay of a Λ_c^+-particle, for instance have a decay pion traversing the Lambda Wheels.
Silicon counters were chosen because their size, granularity and vacuum properties match the requirements for this detector. The particular shape of the wheels and the design as an assembly of identical modules is meant to fit the pre-existing pumping cross chamber. The thickness of the silicon is chosen to be 300 μm. All electronic and mechanical structures are located on the outside periphery, out of the acceptance of the rest of the spectrometer. The available radius for the silicon detectors was limited to about 17 cm. The inner radius of 4.5 cm is fixed by the size of the silicon wafers from which the detectors are cut (6 inches).
In Fig. 4.5, the Lambda Wheels acceptance is compared with the box acceptance of the spectrometer calculated at different z values starting from the beginning to the end of the target cell. The increase in acceptance achieved with the installation of the new silicon detector shifts the limit of the vertical opening angle from $\theta_y < 140$ mrad to $\theta_y < 270$ mrad.
The silicon is cut in a trapezoidal shape, with an apex of 30°, a base of 85.3 mm, and a top of 23.2 mm. This detector is cut out of a 6 inch n-type silicon wafer. Both sides of the detector have a strip pitch of 160 μm and the strips are oriented parallel to the oblique sides of the trapezoid. This configuration was chosen so that all the strips could be electrically connected from the outside ring, with the disadvantage that it causes a little variation in position resolution across the detector surface. The strips on the front and back of one detector cross each other under the angle of 30°, creating a grid for the position reconstruction of a track. The strips are biased via 2 MΩ resistors and 499 strips per side are AC-coupled to the read-out electronics, creating a total active area of 93%. The strips on the n-side are isolated from each other by p-stops around each strip individually, and a single p-strip around all strips.

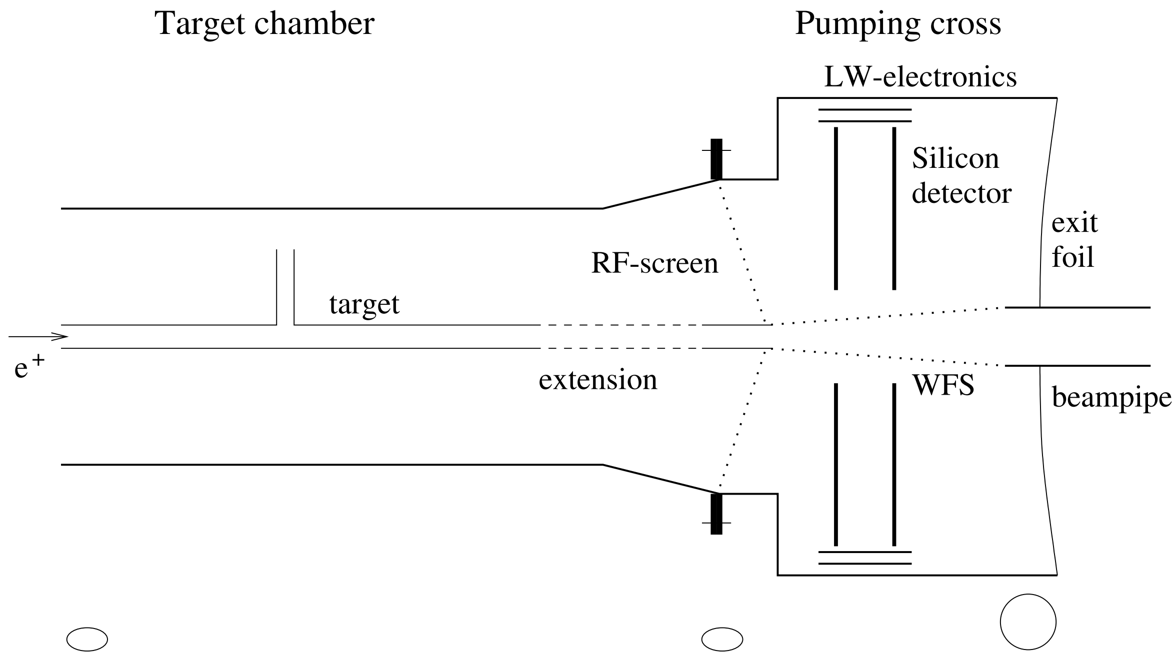

Figure 4.4: *Schematic diagram showing the position of the Lambda Wheels detector in the HERMES target area. On the bottom of the figure the cross-sections of the parts closest to the beam are shown on the same scale.*

The finished detector was passivated with a 2 μm thick silicon-oxide layer.

4.3.1 Cooling system

The cooling system for the silicon detector is located in a secondary vacuum and connected to the ultra-high vacuum of the accelerator. It is capable of removing up to 100 W of heat from the LW detector at a temperature of -35°C. The system consists of two loops. The first one is a closed internal loop which cools the detectors and front-end electronics. In this loop, which crosses the vacuum envelope, alcohol is flowing, cooled by an open external loop which uses a water cooling line. The flow of alcohol is maintained by a rotary pump positioned at the top of the closed loop. The heat pump between the internal loop operating at low temperature, and the external one which is operating just below 10°C, consists of a set of Peltier modules. The cooling power of these modules is controlled by the current passed through them, which gives the possibility to stabilize the temperature of the detector. The Peltier modules are housed in a secondary vacuum to reduce the dispersion of heat due to the contact with the environment. A schematic diagram of the cooling system is presented in Fig. 4.6.

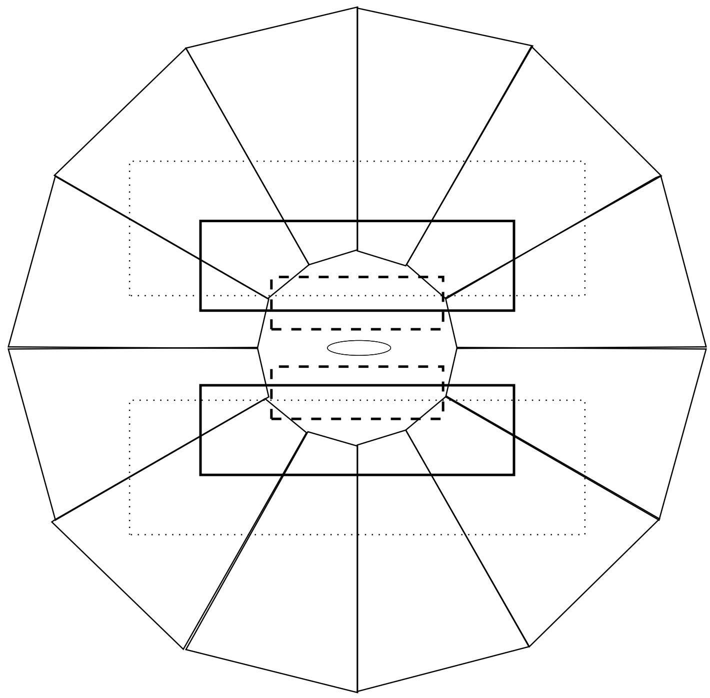

Figure 4.5: *Comparison of the size of the Lambda Wheels detector at z=45 cm, with the standard* HERMES *acceptance. Solid box: acceptance from the center of the target (z=0 cm), dashed box: from the upstream end of the target (z=-20 cm), and dotted box: from the downstream end of the target (z=20 cm). The target density drops linearly to zero from the center of the target to z=20 cm. The ellipse in the center shows the size of the target extension-piece at z=45 cm.*

Peltier elements

Peltier elements consist of two different materials through which an electric current is passed. In this circuit heat is absorbed or generated at the contact area of the two unlike materials, depending on the direction of the electric current. This phenomenon is known as the Peltier effect. Depending on the relative directions of the electric and heat currents a small amount of heat is absorbed (electric current parallel to heat flow) or generated (anti-parallel). This second effect is known under the name Thomson effect. Both effects are proportional to the current. Finally, the electric resistance of the materials causes the generation of Joule heat, which is proportional to the square of the current. The Peltier effect removes heat from one end of the module, which is used to cool the internal loop. The same amount of heat is produced at the other side which is cooled by the cooling water line. The amount of heat removed is 11.5 WA^{-1} for a single Peltier module. Part of this cooling is used to compensate the Joule heating, which is divided almost equally between the hot and cold ends of the module, and the heat conducted through the module when a temperature difference between

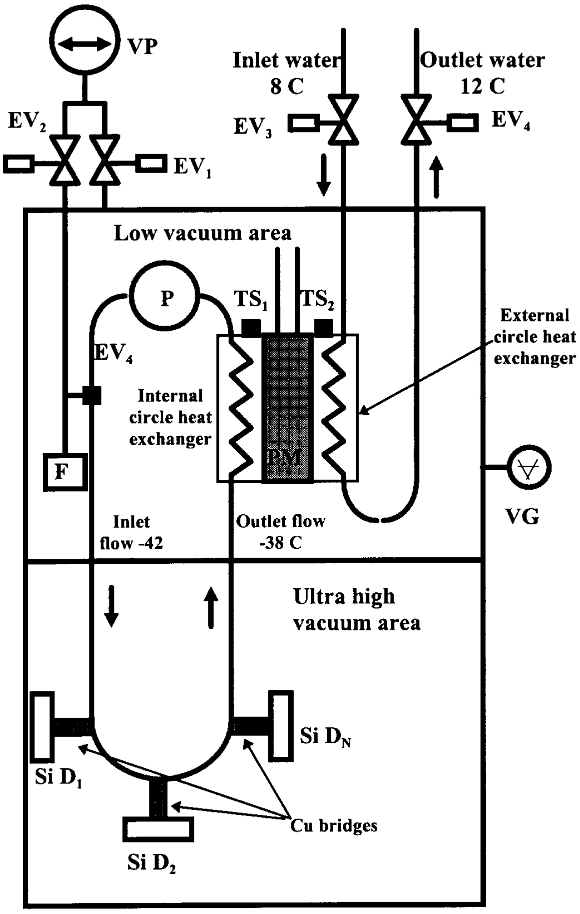

Figure 4.6: *General layout of the cooling system. The two vacuum volumes are shown, the ultra-high vacuum connected to the pump cross chamber and the secondary vacuum where the rotary pump (P) and Peltier elements (PM) are located.*

the two sides is maintained. The conductance is about 0.42 WK^{-1}, and the electric resistance of the module about 2.6 Ω. In the operating conditions about 25 W of cooling power (at -10°C) per Peltier module is available. In that case 160 W of power must be removed by the cooling water. This requires a flow of about 0.35 m^{3}hr^{-1} for a temperature rise of 4 K (for a total of ten Peltier elements).

4.4 Detector studies

In the year 2000 a prototype Lambda Wheels module was installed in the HERMES vacuum vessel. The performance of this module was studied with the aim of extracting information

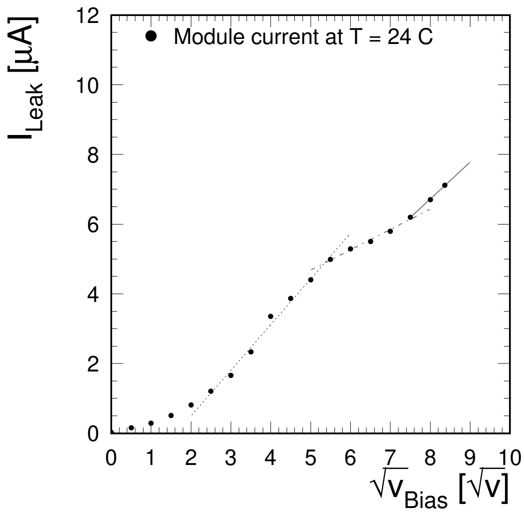

Figure 4.7: *Leakage current versus square root of bias voltage, for one (prototype) silicon module. The lines represents linear fits to the data below and above the depletion voltage, and below the breakdown voltage.*

on the properties of the silicon wafer. The results of a limited number of studies are presented in separate subsections below. From the dependence of the leakage current and the detector capacitance on the bias voltage the depletion voltage is extracted. Also reported is the dependence of the leakage current on the module temperature. The radiation damage of the silicon is discussed in terms of an increase of leakage current with time. In the last subsection a measurement of the signal to noise ratio is given.

4.4.1 Capacitance and leakage current measurements

The expected dependence of the leakage current on the bias voltage below depletion is expressed by Eq. (4.7). On the prototype module the leakage current is measured as a function of the square root of the bias voltage at a fixed temperature of 24°C. The resulting data are plotted in Fig. 4.7. The change in slope at about 30 V shows the transition to the fully depleted zone. By raising the bias voltage above this value another transition can be seen as a second change of the slope of the data above 50 V. This is a hint of the breakdown voltage. The precise value of the depletion voltage of a detector can be extracted from the dependence of the measured capacitance on the bias voltage (see Fig. 4.2). Such a measurement was performed on the two silicon wafers constituting one module. The highest of the two measured values of the depletion voltage was used for the entire module. An example of the extracted data for one wafer is given in Fig. 4.8 where the depletion voltage is found at 38.6 V.

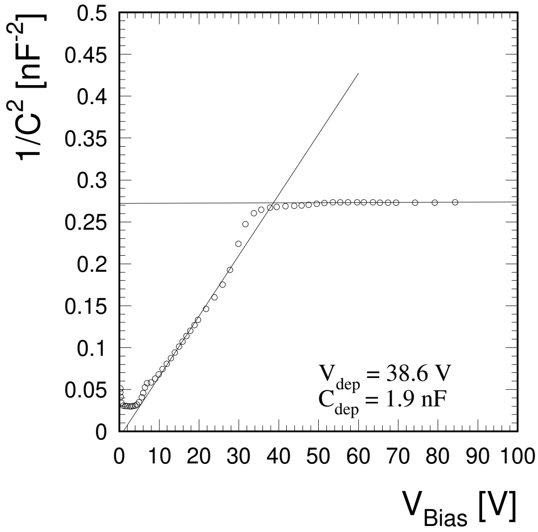

Figure 4.8: *Backplane capacitance versus bias voltage for one wafer of the prototype silicon module. The lines represent linear fits to the data below and above the depletion voltage. The measured depletion voltage is represented by the crossing point of the fits at 38.6 V.*

4.4.2 Temperature dependence of the leakage current

The temperature dependence of the leakage current can be used to extract the value of the energy gap E_g in the silicon. If the leakage current is plotted versus temperature at a fixed bias voltage (see left panel in Fig. 4.9), an exponential fit using Eq. (4.8) allows to extract values for the band gap energy E_g and the leakage current at infinite temperature, $I_0 = q_0 A \frac{l_g(V)}{\tau_g}$. The values of E_g extracted from temperature scans of the leakage current on the prototype module are shown in the right panel of Fig. 4.9 for various values of the bias voltage. The extrapolated value at $V_{Bias} = 0$ V is $E_g = 1.02$ eV. Once the parameters for the temperature dependence are fixed, the leakage currents can be evaluated at a reference temperature and the voltage dependence at that fixed temperature given by Eq. (4.7) can be used to extract the generation lifetime τ_g. An example is given in the left panel of Fig. 4.10 for $T = 0\ °C$. The slope of the line represents the ratio $q_0 A n_i/\tau_g$, which is reported in the right panel for various values of temperature. The typical exponential dependence on the temperature is shown by the data in the right panel of Fig. 4.10.
The generation lifetime is the average time between the production of two subsequent electron-hole pairs from one defect in the silicon, and is defined as $\tau_g = n_i/G$ where n_i is the intrinsic carrier concentration and G is the generation rate of electron-hole pairs in a region completely depleted of carriers (such as a depletion region under reverse bias)[1]. The higher the

[1] τ_g has some relation with, but is usually quite different from, the recombination lifetime.

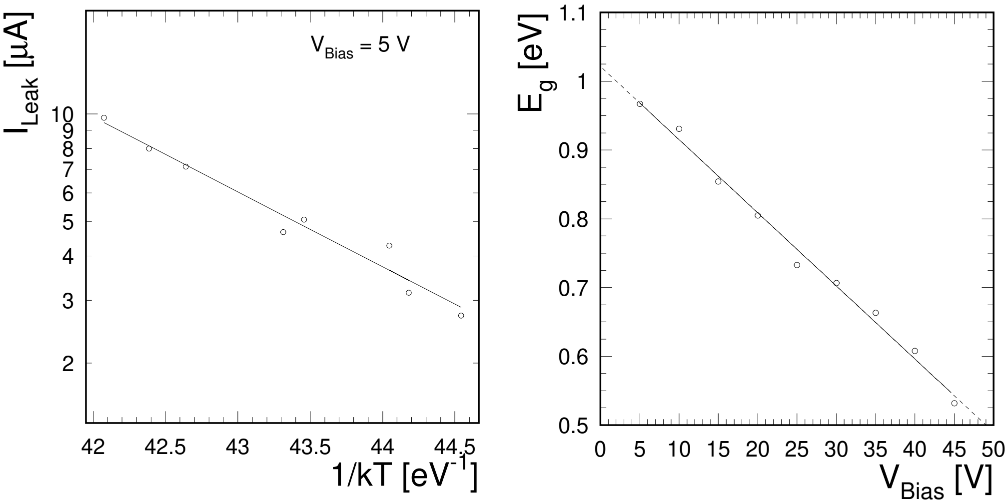

Figure 4.9: *Extraction of the band gap energy E_g from the temperature dependence of the leakage current at a fixed value of the bias voltage (left panel). The curve is an exponential fit to the data using Eq. (4.8). In the right panel, the values of E_g extracted at various values of V_{Bias} are fitted with a line to obtain the extrapolated value of E_g at zero V_{Bias}.*

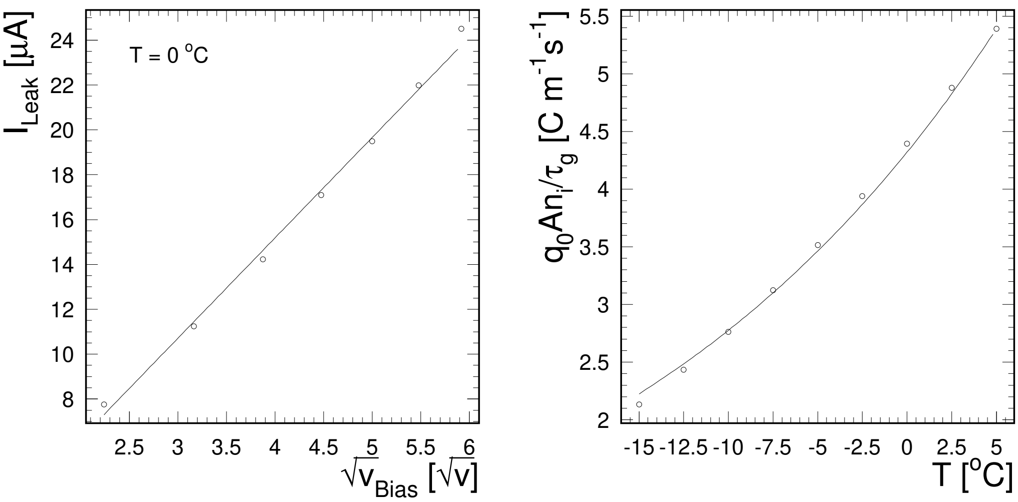

Figure 4.10: *Left panel: extraction of τ_g from the voltage dependence of the leakage current evolved at a fixed value of temperature using E_g and I_0 as obtained from Fig. 4.9. Right panel: various values of the ratio $q_0 A n_i / \tau_g$ extracted from the linear fit to the voltage dependence at different temperatures.*

electron-hole pair production rate the higher is the leakage current, which means that comparing different silicon wafers, the ones with larger τ_g should be chosen for the detector construction.

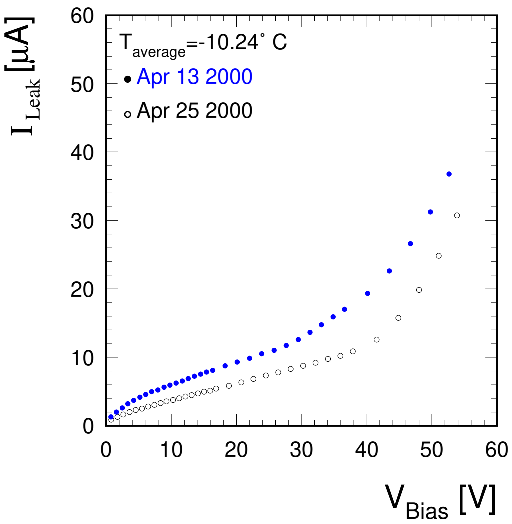

Figure 4.11: *Leakage current measured as a function of bias voltage of the prototype module, right after an involuntarily loss of the HERA positron beam in the vicinity of the HERMES target cell (April 13, 2000) and, a few days later (April 25, 2000).*

4.4.3 Radiation damage

The high radiation dose received by a semiconductor detector operated in the vicinity of a high-energy electron beam may alter the characteristics of the silicon. Two types of radiation damage can be distinguished [72]: displacement effects and long-term ionization effects. The first kind occurs when atoms in the crystal lattice are displaced from their normal sites by radiation. This may cause long-lived changes of some of the semiconductor properties, which may disappear again after some time if the silicon is kept at a higher temperature (annealing). Long-term ionization effects are provoked by radiation on insulating material, e.g. SiO_2 used as the dielectric in the coupling capacitor. Radiation can cause electron-hole pairs to be trapped changing the state of the material permanently. These mutations can affect the electric properties of the semiconductor adjacent to the insulator through the modification of the electric field.

As mentioned in section 4.2 the leakage current defines the limits of the performance of the detector. An increase of the leakage current due to collected radiation on the silicon would reduce the signal to noise ratio of a silicon counter depleted with a fixed bias voltage. In order to estimate the time evolution of this kind of radiation damage, measurements of the leakage current were performed on the prototype module during its time of operation. As a result of these studies it was noticed that a high dose of radiation concentrated in a short time (i.e. an accidental beam loss in the HERMES target area) causes an increase of the leakage current which recovers within a few days. Fig. 4.11 shows one example of such an event. The beam was lost in the vicinity of the target cell on April 13th. The leakage current was measured right after the beam loss event, and the current was found to be higher than normal. After a few days the leakage current was back to the nominal values as shown by the data

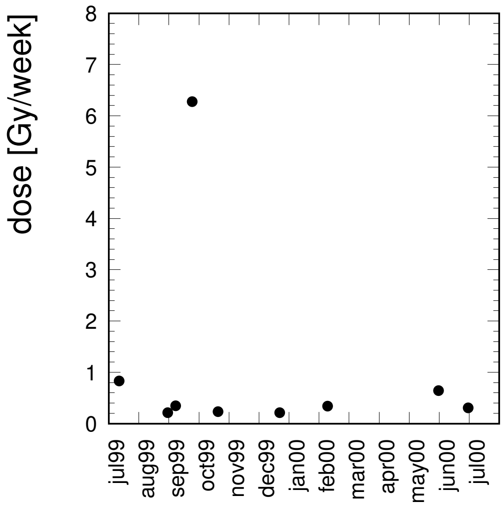

Figure 4.12: *Collected radiation dose in the vicinity of the Lambda Wheel prototype module accumulated over one year of data taking at* HERMES.

obtained from measurements on April 25th at the same module temperature.
The radiation dose collected in the vicinity of the prototype module was monitored for a period of one year using glass dosimeters sensitive to photons and neutrons. A set of dosimeters was left in the beam area for about 1-2 months. Fig. 4.12 shows the integrated radiation dose collected by each set in units of Gy/week as a function of time. An almost constant dose of about 0.5 Gy/week is seen in the whole period apart from one event where a very high dose was collected in a short period of time (mid September 1999). This high dose was related to several subsequent beam losses in the HERMES area. Unfortunately the high dose collected during the April beam loss is not visible, since the radiation dose was averaged over a much longer period of time (from the beginning of March to the end of May) due to the impossibility to access the experimental area and collect the dosimeters.
To prevent accidental losses of the beam a system was developed, which triggers a controlled dump of the beam in case of equipment failures or high induced radiation levels due to an unexpected beam loss. The *Beam Loss Monitor* (BLM) [73] is a set of ionization chambers which measure radiation in the vicinity of the LW detector. If the signal exceeds a fixed threshold, a trigger is transmitted to the dump-kicker, which is located in the West-area of the HERA ring, and the beam is dumped. The operation of the BLM and dump kicker prevents most accidental beam losses which otherwise could have caused a high radiation level leading to (reversible) radiation damage, and enhanced noise levels. The long-term (or permanent) radiation damage due to the constant dose of radiation collected over time during normal data taking cannot be prevented. This radiation determines the life time of the detector (which is presently estimated to be larger than the duration of the HERMES run II (2002-2006)).

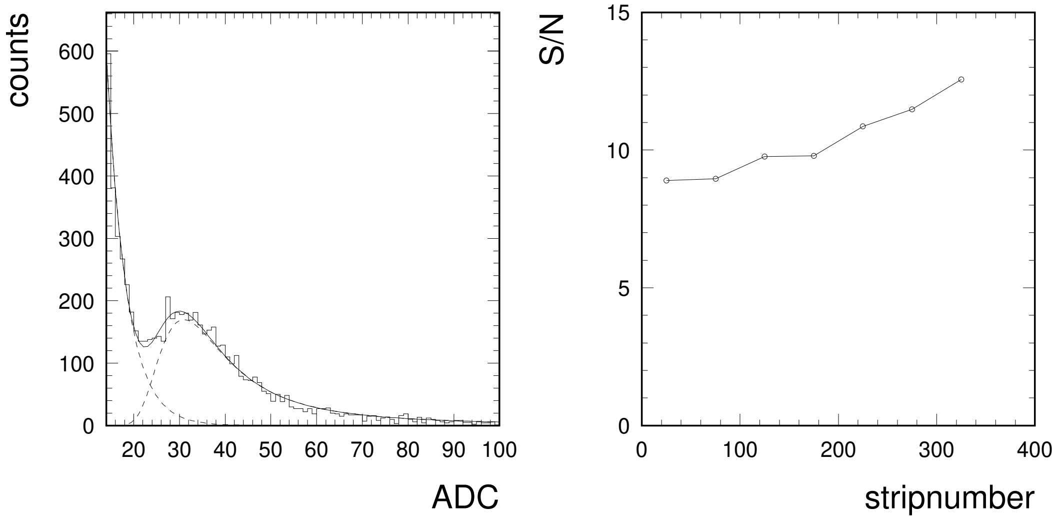

Figure 4.13: *Left: pulse height spectrum of the LW prototype detector. The solid line is a fit using an exponential shape for the background and a Landau curve for the high ADC data. Only data from the long strips have been used. Right: measured signal-to-noise ratio for the LW prototype detector. The data are plotted versus the strip number. Higher strip numbers correspond to short strip lengths.*

4.4.4 Signal to noise ratio

Using the ADC data collected with the prototype module the pulse height distribution containing both signal and noise events is illustrated in the left panel of Fig. 4.13. The noise of the system has been measured calculating the RMS value of the signal using a random trigger instead of the physics trigger. In that case the readout is triggered during the period not in coincidence with the time slots in which the beam is colliding with the gas stored in the target cell. The resulting signal-to-noise ratio is shown as a function of strip number in the right panel of Fig. 4.13. On average the signal-to-noise ratio is consistent with 10 which is in accordance with the design specifications. The rise of the signal-to-noise ratio with increasing strip number is related to the decrease of the strip length (and hence a decreasing capacitance) across the module.

4.5 Outlook

In parallel with the test of the prototype module the construction of the remaining 12 modules (plus 2 spares) for the complete LW detector was completed in the year 2001. At the beginning of 2002 the complete array of modules was installed at HERMES together with the BLM. Since then the commissioning of the detector has continued with the development of the tracking and slow-control software. The full scale data taking is expected to begin in the year 2003.

Chapter 5

Inclusive DIS on nuclei

Se la prudenza dunque e' tanto necessaria in questioni scientifiche, dove spesso il riprovare ci permette di correggere gli sbagli del provare, indirizzandoci ad una giusta conclusione, ben maggiore circospezione occorre nel trarre le conseguenze, allorquando il raziocinio si protrae sulla base di fatti poco accertabili, di opinioni, di congetture, di analogie e sotto l'influenza di sentimenti assai variabili.

Achille Sclavo

5.1 Introduction

The multi-GeV energy length scale at which deep-inelastic scattering (DIS) is typically employed to study the partonic structure of nucleons greatly differs from the multi-MeV length scale relevant to the atomic nucleus. Hence, the A-dependence observed in the structure function $F_2(x)$ [9] was unexpected and thus stimulated the search for similar behavior in its longitudinal and transverse components, $F_L(x)$ and $F_1(x)$. As expressed by Eq. (2.15), these structure functions are related to the ratio R of longitudinal to transverse photo-absorption cross sections. Previous measurements at HERMES seemed to indicate a nuclear dependence of R in deep inelastic positron scattering on ^{14}N and ^{3}He [74]. In order to further study a possible A-dependence of R, data on heavier nuclei are required. During a dedicated run in October 1999 data were collected at HERMES on an unpolarized natural Kr target. This chapter reports the analysis of these data and the reanalysis of the previously taken ^{14}N data. These analyses led to the conclusion that the previously observed A-dependence of R was caused by an instrumental effect. In fact, by combining the newly analyzed HERMES data on inclusive DIS off nuclei with existing NMC data on neighboring nuclei [75, 76, 77] it is found that $R_A \approx R_D$ down to $Q^2 = 0.5$ GeV^2.

In section 5.2 the data quality and kinematic restrictions used in this analysis are presented. The most important corrections that were applied to the data are explained in subsection 5.2.1 (photon shower correction) and subsection 5.2.2 (radiative corrections), respectively. A summary of the systematic studies performed on the data sets can be found in subsection 5.2.3. The systematic uncertainties on the inclusive cross section ratios are listed in section 5.3 and the actual results of the analysis are presented in section 5.4. Data are shown for the cross section ratios $\sigma_{\rm Kr}/\sigma_{\rm D}$, $\sigma_{\rm N}/\sigma_{\rm D}$ and $\sigma_{\rm He}/\sigma_{\rm D}$. Values for the ratio R are extracted using the method described in [78], i.e. by using a two parameter fit of the ϵ dependence of $\sigma_{\rm A}/\sigma_{\rm D}$ at constant values of x.

5.2 Cross section ratio $\sigma_{\rm A}/\sigma_{\rm D}$

The ratio of inclusive DIS cross sections on a nucleus A and deuterium D (=^{2}H) follows from Eq. (2.16) and is given by:

$$\frac{\sigma_{\rm A}}{\sigma_{\rm D}} = \frac{F_2^{\rm A}}{F_2^{\rm D}} \frac{(1+\epsilon R_{\rm A})(1+R_{\rm D})}{(1+R_{\rm A})(1+\epsilon R_{\rm D})} \tag{5.1}$$

with $R_{\rm A}$ and $R_{\rm D}$ the ratio of longitudinal to transverse photon absorption cross sections for nucleus A and for deuterium. Inclusive DIS events on ^{84}Kr, ^{14}N, ^{3}He and D are used to extract the cross section ratios $\sigma_{\rm Kr}/\sigma_{\rm D}$, $\sigma_{\rm N}/\sigma_{\rm D}$ and $\sigma_{\rm He}/\sigma_{\rm D}$. It is noted that ^{84}Kr and ^{3}He are non-isoscalar nuclei, i.e. nuclei with a number of neutrons different from the number of protons. All the cross sections are defined as cross sections per nucleon, and are therefore corrected for the difference in the number of the two nucleon types in the nucleus:

$$\frac{\sigma_{\rm A}}{\sigma_{\rm D}} \equiv \frac{\sigma_{\rm A}^{nucleus}}{Z\sigma_p + (A-Z)\sigma_n}, \tag{5.2}$$

where σ_p and σ_n are the DIS cross sections for proton and neutron. In practice the measured cross section ratio is multiplied by the following factor to correct for non isoscalarity:

$$\frac{\sigma_{\rm A}}{\sigma_{\rm D}} = \left(\frac{\sigma_{\rm A}}{\sigma_{\rm D}}\right)_{meas} \cdot \frac{\frac{A}{2}\sigma_p + \frac{A}{2}\sigma_n}{Z\sigma_p + (A-Z)\sigma_n}, \tag{5.3}$$

where Z = 36 for ^{84}Kr and Z = 2 for ^{3}He, and σ_n/σ_p is obtained from the known cross section ratio $\sigma_{\rm D}/\sigma_p$ [79].
In this section all aspects of the data analysis are discussed, including event selection, radiative corrections, normalization, and systematic studies.

Event selection

Data collected on ^{14}N, ^{3}He and D in the year 1997 and on ^{84}Kr and D in the year 1999 are used in this analysis. Starting from a few million DIS events for each target type, the final

number of analyzable events is obtained by filtering out the ones that are corrupted due to malfunctioning spectrometer components, voltage interrupts or other causes leading to missing or incorrect information for the event reconstruction.
The analysis is based on two data sets: the cross section ratio $\sigma_{\mathrm{N}}/\sigma_{\mathrm{D}}$ is evaluated using events selected from the μDSTs[1] of the 97b4 production for both gases, ^{14}N and D, while events were selected from the μDSTs of the 99b2 production for both ^{84}Kr and D to obtain $\sigma_{\mathrm{Kr}}/\sigma_{\mathrm{D}}$. Since the ^{14}N data were collected in three different periods during the year 1997 at different target densities, a more detailed study on the consistency of these three periods is presented in one of the following subsections. Data on ^{84}Kr were collected in a dedicated high density run of three days during which the detector performance was carefully monitored. Therefore, almost no data had to be rejected due to some detector component failure. It would have been natural to use the already analyzed deuterium data set also to measure the cross section ratio $\sigma_{\mathrm{Kr}}/\sigma_{\mathrm{D}}$. However, inconsistencies in the data sets, which are discussed in a dedicated subsection, indicated that data from different years could not be used. Therefore, the deuterium data from the standard polarized data taking before and after the dedicated ^{84}Kr run were used. The data quality criteria for this analysis are presented in the next paragraph followed by a description of the kinematic requirements imposed on the data.

Data-quality

The target was required to be either polarized or unpolarized deuterium, unpolarized nitrogen or unpolarized krypton (as determined from the target type information in the field labeled `g1Unpol.iGasType` of the μDSTs). In order to define a good event the DIS trigger (trigger 21, as defined in subsection 3.3.1) must have fired and the event was contained in a burst that passed the following burst-level data quality requirements:

- the burst was part of a run which was marked as analyzable in the logrun.new file (*i.e.* the data-quality was marked to be good in the log-book);
- the burst was not affected by HV trips in the tracking chambers;
- the GMS[2] indicated that the calorimeter, the luminosity monitor, and the pre-shower detectors were fully operational during the burst;
- the TRD was fully operational during the burst;
- the burst length was between 0 and 11 seconds;
- the DAQ live-time for trigger 21 was greater than 0.5.

[1] μDST refers to micro *Data Summary Tape* which are tables in ADAMO format containing information of the triggered events synchronized with the detector status after a preliminary off-line analysis has been performed.
[2] GMS is the *Gain Monitor System* which measures the stability of the response of the various particle detectors.

Constraints on the positron kinematics

Each event contained at least one e^+, as identified by a cut on the value of the PID variable (see section 3.2.2). The exact value of the cut depends on the kinematics. While PID > 1 is appropriate for ^{84}Kr, PID > 2 has to be used for the other two datasets. The following constraints on the scattering angle and the vertex position are imposed:

- The origin of the reconstructed track has to be within the target cell: $|z_L(e^+)| < 18$ cm and $|z_T(e^+)| < 0.75$ cm, with z_L the longitudinal and z_T the transverse vertex coordinate with respect to the interaction point.
- Fiducial cuts are chosen such as to require that the e^+ track is inside the HERMES box acceptance.

Kinematic requirements are imposed on Q^2, on W^2 to exclude the resonance region, and on y to limit the size of the radiative corrections:

- $Q^2 > 0.3\ GeV^2$
- $W^2 > 4\ GeV^2$
- $y < 0.85$
- The energy of the cluster of hits (i.e. non-zero ADC values) in the calorimeter must correspond to $E_{calo}(e^+) > 3.5$ GeV to enforce a common trigger threshold between the unpolarized and polarized data.

The result of this event selection procedure is presented in table 5.1, where the remaining number of DIS events (in units of 10^6) for each target gas is presented.

	^{14}N	^{84}Kr	D
1997	3.1	-	3.6
1999	-	1.5	1.1

Table 5.1: *Number of DIS events in units of 10^6 that remain for each gas type after application of the data quality and kinematic requirements.*

5.2.1 Photon shower corrections

In order to extract deep inelastic lepton scattering cross sections radiative processes and local inefficiencies that may contribute to the total measured DIS cross section need to be discussed. Radiative background and their correction is the subject of the next subsection, while the present subsection deals with a detector inefficiency caused by the radiated photons. In inelastic processes such photons are mostly emitted in the direction of either the

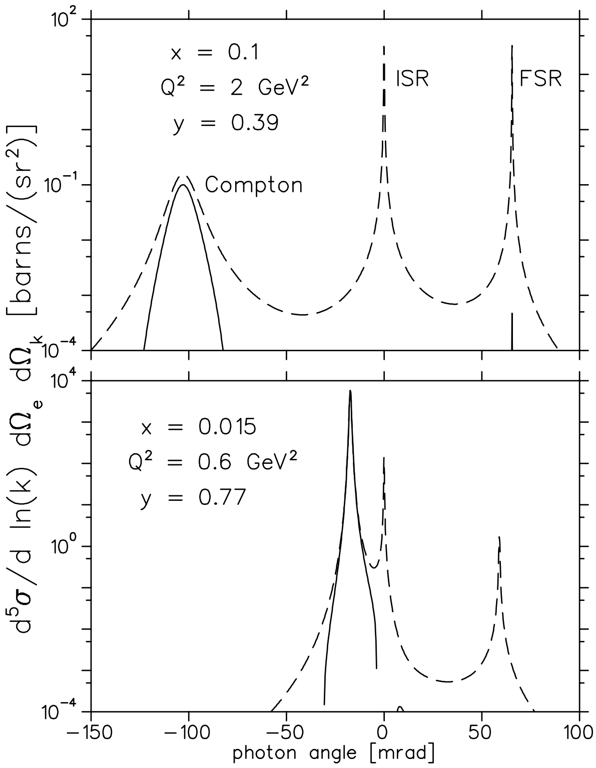

Figure 5.1: *The Bethe-Heitler cross section for ^{14}N in two different coplanar kinematic conditions labeled by the values of x, Q^2 and y. The continuous curves include the effects of the nuclear form factor.*

beam lepton (*initial state radiation*, ISR) or the scattered lepton (*final state radiation*, FSR). On the other hand hard photons associated with nuclear elastic scattering, i.e. Compton scattering, are emitted typically at very small angles. The Bethe-Heitler cross section for radiative elastic processes predicts that in kinematic conditions corresponding to quite small values of x, the Compton peak becomes much more prominent compared to ISR and FSR, simply because smaller values of Q^2 become kinematically available, and the cross section is proportional to a factor $1/Q^4$. This is illustrated in Fig. 5.1, which shows the Bethe-Heitler cross section in two different kinematic situations, assuming that the emitted photon lies in the lepton scattering plane. When multiplying the Bethe-Heitler cross section by the nuclear form factor only the Compton peak is left. At low x and Q^2 the Compton photons are emitted at very small angles as can be seen from Fig. 5.1. These energetic photons from nuclear targets have a high probability of hitting the detector frames surrounding the beam line in front of the spectrometer magnet, and may produce extensive electromagnetic showers. In such a case the high multiplicity seen by the tracking detectors makes it impossible to perform track reconstruction. This will result in a large inefficiency in particular in the kinematic region

where these photons are emitted, i.e. corresponding to small values of x and Q^2.
Corrections for these process-specific inefficiencies must be applied, since they increase in severity as the Z of nuclear targets increases. A Monte Carlo simulation is needed to estimate the inefficiency due to event losses. A GEANT-based Monte Carlo was set up that includes a detailed geometry description of the detector frames and the beam pipe. The probability of photon emission is modeled following the description of Mo and Tsai [80], and has been carefully compared to other calculations of radiative processes. The resulting reconstruction efficiencies ξ_A for target nucleus A compared to that for deuterium are shown in Fig. 5.2 as a function of x for the different target materials used in this analysis. The reconstruction

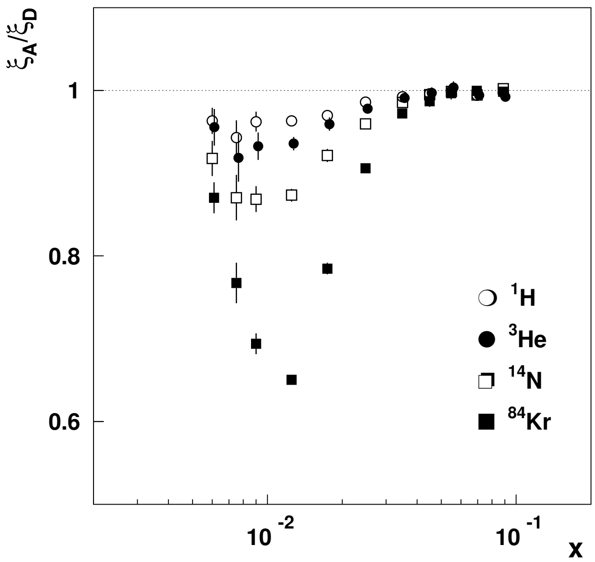

Figure 5.2: *Ratio of track reconstruction efficiencies in ^{1}H, ^{3}He, ^{14}N and ^{84}Kr with respect to that in deuterium as a function of x.*

losses are strongly dependent on target material and on y, and consequently on x and Q^2. Note that these reconstruction efficiencies, which have been determined from a Monte Carlo simulation, include not only the tracking efficiency but also geometric acceptance effects.
The Monte Carlo was tuned to reproduce the efficiency observed in a sub-sample of the data which was reconstructed by comparing the yield in the detector halves above and below the beam pipe using them as independent detectors. For about 50% of the events with a hard radiated photon the resulting electromagnetic shower is contained in one detector half while the scattered electron is found in the other. Such events are normally rejected at HERMES as it is required that the maximum number of tracks (MAXMUL cut) is below 22. This event topology can be extracted from the data by applying requirements on the number of tracks in the top or in the bottom detector separately. This method has been applied both to the data and the Monte Carlo, and thus provides a good measure of the quality of the simulation.

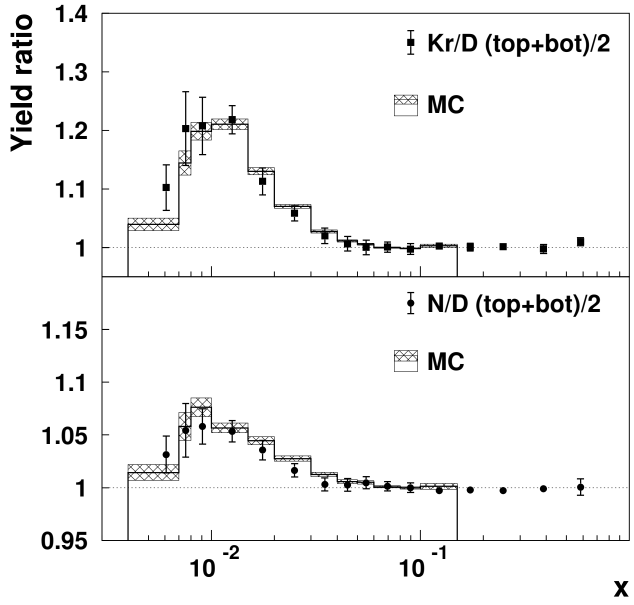

Figure 5.3: *Comparison between data (points) and MC simulation (histogram) for the fractional change in the yield ratios due to the photon shower effect when treating the upper and lower HERMES detector halves independently. The hatched area represents the statistical error in the MC simulation.*

Reasonable agreement between the data and the simulation is found for all target materials if the yields from the two detector halves is averaged, as shown in Fig. 5.3 for ^{14}N and ^{84}Kr. If instead of the average the absolute yield ratios for upper and lower detector are compared to the Monte Carlo results, a difference is observed between the yields in the two detector halves which is attributed to a relative misalignment between the two detectors. The effect of this misalignment is discussed in section 5.2.3.

5.2.2 Radiative corrections

The radiative correction needs to account for three different processes in which a photon is radiated. The elastic scattering of the positron on the nucleus as a whole, the quasi elastic interaction of the positron with one of the nucleons inside the nucleus, and the inelastic scattering of the positron on a single quark. These contributions are calculated using the TERAD code, a code based on the method outlined in Ref. [81, 82, 83]. The elastic form factors, which are different for different nuclei, were taken from the literature [84, 85, 86, 87]. For the quasi-elastic tails, the nucleon form factor parameterization of Gari and Krümpelmann [88] was used. The reduction of the bound nucleon cross section with respect to the free nucleon

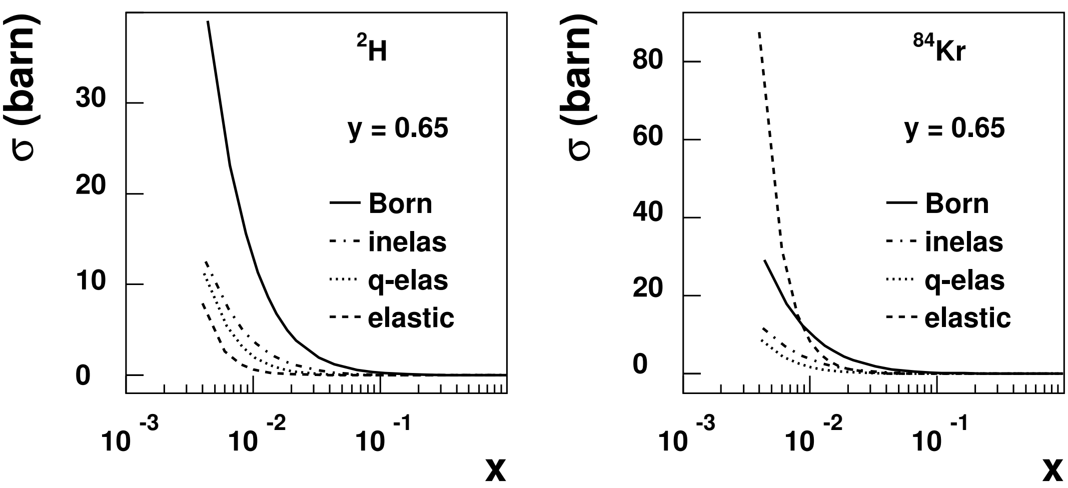

Figure 5.4: *Radiative background cross sections (elastic: full circles, quasi-elastic: open squares, inelastic: full triangles) compared to the Born DIS cross section (stars) for D (left) and ^{84}Kr (right), evaluated for $E = 27.5$ GeV at a fix value of y.*

one (quasi-elastic suppression) was evaluated using the results of a calculation by Bernabeu [89] for deuterium, and a non-relativistic Fermi gas model for ^{3}He, ^{14}N and ^{84}Kr [90].
The evaluation of the inelastic QED processes comprising the full radiative correction requires the knowledge of both F_2 and R over a wide range of x and Q^2. The structure function $F_2^{\mathrm{D}}(x, Q^2)$ was described by a Regge motivated parameterization of the proton structure function $F_2^p(x, Q^2)$ [91] multiplied by the NMC measurement of F_2^{D}/F_2^p [79]. For the structure function $R_{\mathrm{D}}(x, Q^2)$ the Whitlow parameterization [92] was used. The nuclear structure functions $F_2^{\mathrm{A}}(x, Q^2)$ were taken from phenomenological fits to the NMC [75, 76, 77] and SLAC [93, 94] data, while $R_{\mathrm{A}}(x, Q^2)$ was assumed to be equal to $R_{\mathrm{D}}(x, Q^2)$. To get an impression of the relative importance of the various contributions to the radiative background cross sections, the elastic, quasi-elastic and inelastic cross sections are presented as a function of x for a fixed y value and compared to the respective Born DIS cross section for two different nuclei (D and ^{84}Kr) in Fig. 5.4. As can be seen from Fig. 5.4 radiative corrections do not cancel in the ratio $\sigma_{\mathrm{A}}/\sigma_{\mathrm{D}}$ because the yield of radiative events associated with elastic scattering scales nonlinearly with Z^2. At small values of x and Q^2, corresponding to large values of y, the contribution from radiative elastic scattering becomes large. In this kinematic region, some of the associated energetic photons are radiated at small scattering angles which can produce electromagnetic showers responsible for the large detector inefficiencies treated in the previous subsection.
Since elastic and quasi-elastic tails are an additive background to the Born DIS cross sections, they need to be subtracted from the measured cross section. The treatment of the

inelastic tail is more complicated. An unfolding procedure would be needed to properly correct each x-bin for both the loss of inelastic events due to migration to lower x-bins and for the gain of events due to the migration of events from higher x-bins into the bin of interest. In order to further understand this point, it is useful to identify the three main components making up the difference between the Born and the measured DIS cross section on a proton, which are illustrated in Fig. 5.5:

a) Schwinger correction [80],
b) loss of cross section due to radiation of photons after the positron interaction,
c) increase of cross section due to radiation before the positron interaction,

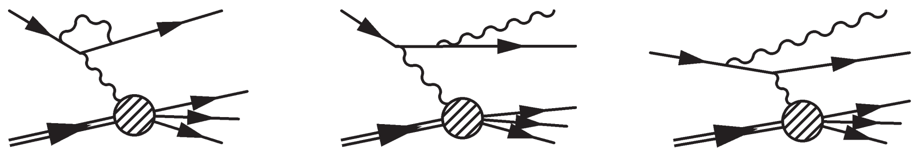

(a) Schwinger correction (b) final-state radiation (c) initial-state radiation

Figure 5.5: Most important DIS processes contributing to the radiative corrections.

The contributions a) and b) are directly proportional to the Born cross section, while c) corresponds to x, Q^2 values different from, but close to the x, Q^2 values measured for a given data point. The latter contribution is proportional to the Born cross section at somewhat lower x, Q^2 values, which on average leads to an increase of the cross section. This is the part which should be treated with an unfolding approach. This procedure requires a quite complicated mathematical exercise, which was considered to be unnecessary since the effect on the results would not be larger than the quoted systematic uncertainties. Instead a simplified method was adopted where all the radiative backgrounds actually "seen" in the experiment are subtracted from the measured yield. Two equations can be written to link the measured yields to the Born cross sections for each target gas:

$$\begin{aligned} Y^{\mathrm{A}} &= (\xi^{\mathrm{A}}_{\mathrm{Born}}\sigma^{\mathrm{A}}_{\mathrm{Born}} + \xi^{\mathrm{A}}_{\mathrm{bg}}\sigma^{\mathrm{A}}_{\mathrm{bg}}) \\ Y^{\mathrm{D}} &= (\xi^{\mathrm{D}}_{\mathrm{Born}}\sigma^{\mathrm{D}}_{\mathrm{Born}} + \xi^{\mathrm{D}}_{\mathrm{bg}}\sigma^{\mathrm{D}}_{\mathrm{bg}}), \end{aligned} \tag{5.4}$$

where the yield $Y = N/L$ is given by the number of DIS events divided by the (dead time corrected) integrated luminosity, and $\xi^{\mathrm{A(D)}}_{\mathrm{Born}(bg)}$ are the reconstruction efficiencies for Born and background events of target material A and D, respectively, as described in the previous subsection. The terms $\xi^{\mathrm{A(D)}}_{\mathrm{bg}}\sigma^{\mathrm{A(D)}}_{\mathrm{bg}}$ in the Eq. (5.4) have to be replaced by $\xi^{\mathrm{A(D)}}_{\mathrm{el}}\sigma^{\mathrm{A(D)}}_{\mathrm{el}} + \xi^{\mathrm{A(D)}}_{\mathrm{qel}}\sigma^{\mathrm{A(D)}}_{\mathrm{qel}} + \xi^{\mathrm{A(D)}}_{\mathrm{inel}}\sigma^{\mathrm{A(D)}}_{\mathrm{inel}}$, if each contributing term is made explicit. The remaining small

radiative contributions (vacuum polarization, electroweak interference term and hadronic vertex contributions) are treated in the same way as the inelastic radiative contribution. For simplicity these contributions are simply included in $\sigma_{\mathrm{inel}}^{\mathrm{A(D)}}$.
Defining

$$R_{\mathrm{meas}} = \frac{Y^{\mathrm{A}}}{Y^{\mathrm{D}}} = \frac{\xi_{\mathrm{Born}}^{\mathrm{A}}\sigma_{\mathrm{Born}}^{\mathrm{A}} + \xi_{\mathrm{bg}}^{\mathrm{A}}\sigma_{\mathrm{bg}}^{\mathrm{A}}}{\xi_{\mathrm{Born}}^{\mathrm{D}}\sigma_{\mathrm{Born}}^{\mathrm{D}} + \xi_{\mathrm{bg}}^{\mathrm{D}}\sigma_{\mathrm{bg}}^{\mathrm{D}}}, \tag{5.5}$$

the ratio of Born cross sections can be derived with simple algebra,

$$\frac{\sigma_{\mathrm{Born}}^{\mathrm{A}}}{\sigma_{\mathrm{Born}}^{\mathrm{D}}} = \frac{R_{\mathrm{meas}}}{\xi_{\mathrm{Born}}^{\mathrm{A}}}\left(\xi_{\mathrm{Born}}^{\mathrm{D}} + \frac{\xi_{\mathrm{bg}}^{\mathrm{D}}\sigma_{\mathrm{bg}}^{\mathrm{D}}}{\sigma_{\mathrm{Born}}^{\mathrm{D}}} - \frac{1}{R_{\mathrm{meas}}}\frac{\xi_{\mathrm{bg}}^{\mathrm{A}}\sigma_{\mathrm{bg}}^{\mathrm{A}}}{\sigma_{\mathrm{Born}}^{\mathrm{D}}}\right). \tag{5.6}$$

This expression has been used in the actual evaluation of the cross section ratio. More details can be found in Appendix A.
For high-Z targets such as krypton, the probability for the exchange of more than one-photon becomes non-negligible. The corresponding amplitudes lead to a destructive interference with the leading one photon exchange amplitudes. For the dominant contribution to the radiative correction - the elastic radiative tail - this effect has been estimated using the distorted wave function method [95], resulting into a 5-10% reduction of the radiative elastic tail. Other contributions, which are proportional to $Z \cdot \alpha$, might not be negligible but could not be estimated.

5.2.3 Systematic studies

As part of the analysis, several systematic studies were performed on the data to verify that the observed cross section ratio is not biased by other detector effects. The results of these studies are reported in the following paragraphs.

Comparison of top and bottom detectors

A misalignment in the relative position of the two halves of the detector with respect to the beam pipe was already known to exist from previous HERMES analyses [96]. This effect has also been investigated for the present data. The separate extraction of the yield ratio $Y_{\mathrm{A}}/Y_{\mathrm{D}}$ for top and bottom detectors shows a large difference in the low x region. This is illustrated in Fig. 5.6 were the ratio of yield ratios $Y_{\mathrm{Kr}}/Y_{\mathrm{D}}$ for bottom to top detector half is displayed as a function of x. It is seen that the effect of the misalignment increases as x decreases. This can be explained from the configuration of the HERMES spectrometer as being due to a different lower θ limit in the two data samples, since low x is strongly correlated to low θ. A misalignment of 1 mm in the vertical direction of one half of the detector could lead to an effect on the yield ratio of the size displayed in Fig. 5.6 [97]. Because a correction of the misalignment would lead to very large systematic uncertainties in the low x domain (thus hiding any possible physics information), it was decided to restrict the analysis to x

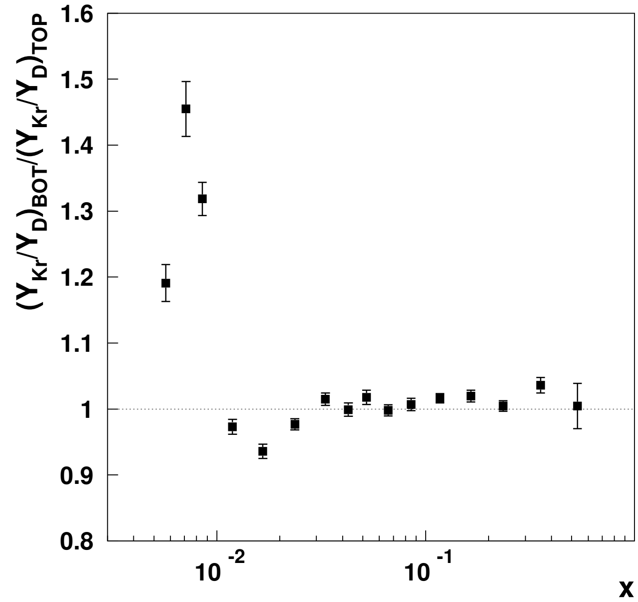

Figure 5.6: *Ratio of yield ratios of* ^{84}*Kr to D for top and bottom detector halves versus* x.

values greater than 0.01. Above this limit the difference between top and bottom yield ratios is much smaller and the effect can be included in the calculation of the uncertainties. To account for the error introduced by the misalignment the statistical uncertainty of the data is scaled with the square root of the χ^2 value calculated assuming that the top and bottom detector measurements of the cross section ratios should be consistent (see Appendix A).

Variation of the z_L cut

Since the collimators in front of the target cell generate events which contribute to the background of the DIS sample, it was verified that the resulting cross section ratios were independent of the cut on the longitudinal vertex coordinate (z_L). This study was a leading-lepton analysis performed with a PID cut of 2.0. The negative z_L cut (from the side of the collimator) was changed in steps from -5 to -18 cm. The result of this study shows that to a level of less than 0.9% there is no contamination from the collimators in the chosen sample.

Variation of the PID cut

Since the hadron contamination can be large in the low-x bins of interest, the cross section ratios were evaluated for various values of the PID cut. In this leading-lepton analysis the standard cuts were used. The PID cut was raised from 1 to 4. The results show that there is a difference of about 0.1% if the value of the PID cut is varied in this range.

Charge symmetric background contribution

In the standard analysis only leading leptons which pass the DIS cuts are counted. In this way no correction is made for positrons originating from the $\gamma \rightarrow e^+e^-$ processes. This background contribution can be corrected for by counting all electrons and then subtracting them from the total number of positrons. The numbers obtained with and without the charge conjugate background subtracted were compared. The result of this comparison indicates that the two extracted ratios are consistent with each other at the 0.1% level.

Variation of calorimeter threshold

Since the calorimeter threshold used in collecting the polarized D and unpolarized ^{84}Kr data differed, the knee of the threshold efficiency curve for the two datasets differed as well. This difference may alter the ratio of DIS events in the (x, Q^2)-bins which contain a significant amount of low momentum events. To check that this difference is not affecting the cross section ratio, the analysis was repeated with a higher threshold settings by imposing a lower y cut of 0.83 instead of 0.85. This cut corresponds to a calorimeter energy cut of 4.68 GeV. Previous studies have shown that the trigger is nearly 100% efficient for particles with momenta of more than 1.0 GeV above the threshold setting. The reduced efficiency below this value does not affect the deduced cross section ratios to more than a 0.2%, as emerged from the analysis with the two different y cuts.

5.2.4 Normalization issues

Nitrogen to deuterium ratio

The analysis of the nitrogen data was previously presented in Ref. [78]. There an overall normalization correction of 1.014 was quoted to account for the disagreement at mid-x between the cross section ratio σ_N/σ_D measured at HERMES and previous measurements. During the review of the ^{14}N/D analysis, special attention was given to the understanding of this disagreement. The dependence of the yield on the rates in the luminosity monitor shows a decrease of about 2% of the yield going from low rate corresponding to low target densities (10^{+13} nucl/cm^2) to high rates obtained with a target density of about $7 \cdot 10^{+14}$ nucl/cm^2. In addition to this linear drop of the yield, two periods were identified with a significant normalization deviation as compared to the bulk of the data. In Fig. 5.7 the rate dependence of the yield is shown for the deuterium data, and for three different periods in which nitrogen data were collected at different target densities. The three periods are separated in time by a few months during the year 1997. Period 2 shows two different normalization levels, and was therefore divided into two separate periods: 2a and 2b. For period 2a a normalization factor of 1.054 is needed to be in agreement with the rest of the data, while for period 2b the deviation is much larger, i.e. a factor of 1.14 is necessary. One possibility to explain

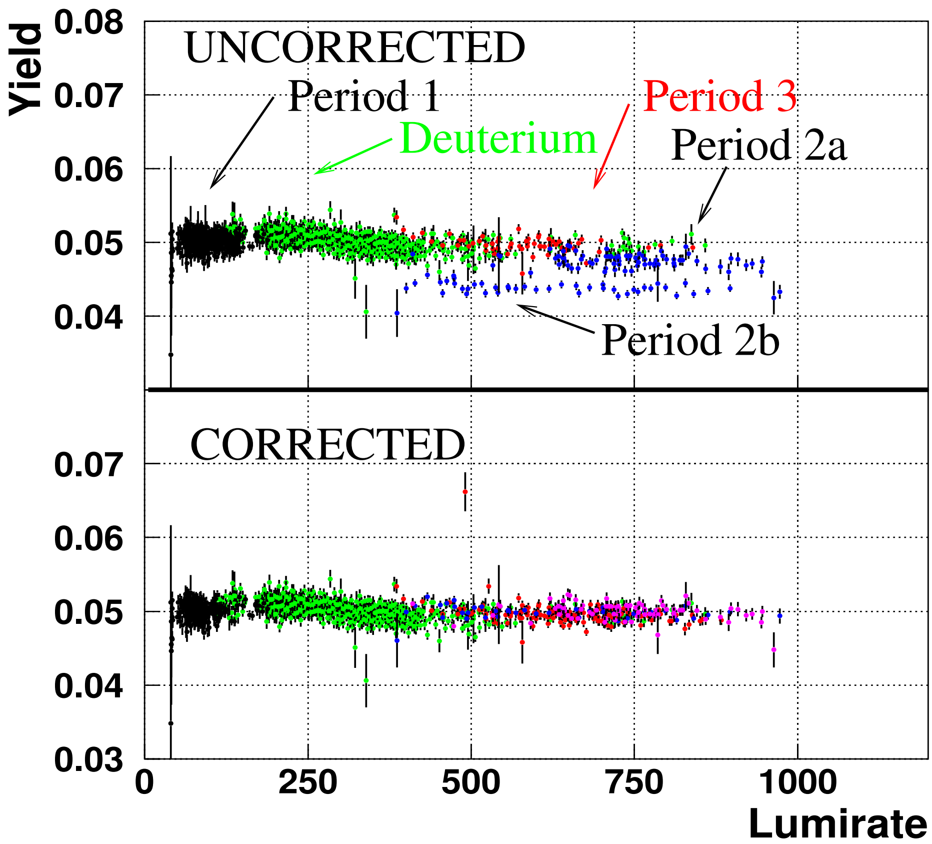

Figure 5.7: *Deep inelastic scattering yield of nitrogen and deuterium versus the rate observed in the luminosity monitor. In the top panel the uncorrected data are presented (since the symbols are indistinguishable the different periods as indicated by the arrows have different shades of gray), while a normalization factor of 1.054 (1.14) for period 2a (2b) is applied to obtain the data shown in the bottom panel.*

such a deviation is a hydrogen gas contamination of the nitrogen gas. This would result in a different kinematic dependence of sample 2 with respect to the other samples. Such a dependence is observed only for period 2b as reported in Fig. 5.8, where the uncorrected cross section ratio is presented for the three different periods as a function of x. The entire period 2 was removed from the nitrogen sample because of the supposed gas contamination, which could not be verified by independent checks, such as an analysis of the content of the gas bottle used. A total of 125 runs were rejected leaving a total of 2.4 million DIS events to be analyzed.

After rejection of the contaminated period the nitrogen and helium data both exhibit a somewhat lower normalization with respect to existing data. Most likely the remaining effect has to be attributed to the calibration of the luminosity monitor. As discussed in more detail in the next section, for the year 1997 a MC study would be needed to properly recalibrate the response of this device. Instead, in the present work a normalization factor of 1.009 was used for both the ^{14}N and ^{3}He cross section ratios, which is obtained from the comparison to the NMCdata in the region $0.1 < x < 0.3$.

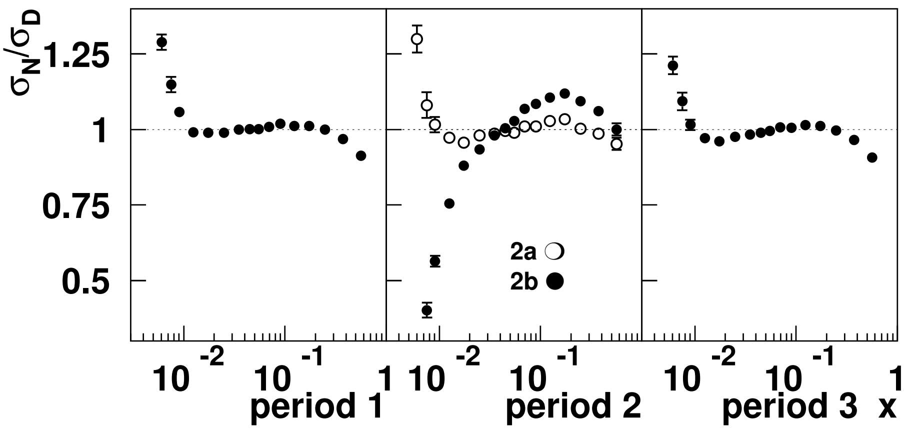

Figure 5.8: *Nitrogen to deuterium cross section ratio (without radiative corrections) for data collected in 3 different periods. Period 2a is multiplied by a normalization factor of 1.054, period 2b by a factor of 1.14.*

Krypton to deuterium ratio

The 1997 unpolarized deuterium dataset was the one first used to evaluate the cross section ratio $\sigma_{\rm Kr}/\sigma_{\rm D}$, because it was also used when evaluating the cross section ratio $\sigma_{\rm N}/\sigma_{\rm D}$. The results obtained for the uncorrected yield ratio of ^{84}Kr to D versus x are shown in the left panel of Fig. 5.9, where the 1997 dataset for deuterium was used (production 97b4)[3]. A non-isoscalarity correction is applied to the ^{84}Kr data in Fig. 5.9 (and in the following figures) according to Eq. (5.2) to account for the difference in proton-neutron content of the ^{84}Kr nuclei. This correction increases the data by up to 5% in the high x region. The HERMES data are compared to published data on ^{56}Fe, ^{108}Ag and ^{119}Sn from other experiments. A 5-7% difference in the overall normalization with respect to the existing data is observed in the mid-x range. For comparison the uncorrected ^{14}N to D yield ratio, normalized by a factor of 1.009, is shown in the right-hand panel of Figure 5.9. While the nitrogen data are

[3]In this plot as in the two to follow, data are presented for completeness also in the region $x < 0.01$. Even though in the section presenting the results of the analysis (section 5.4) these points are rejected as explained in section 5.2.3

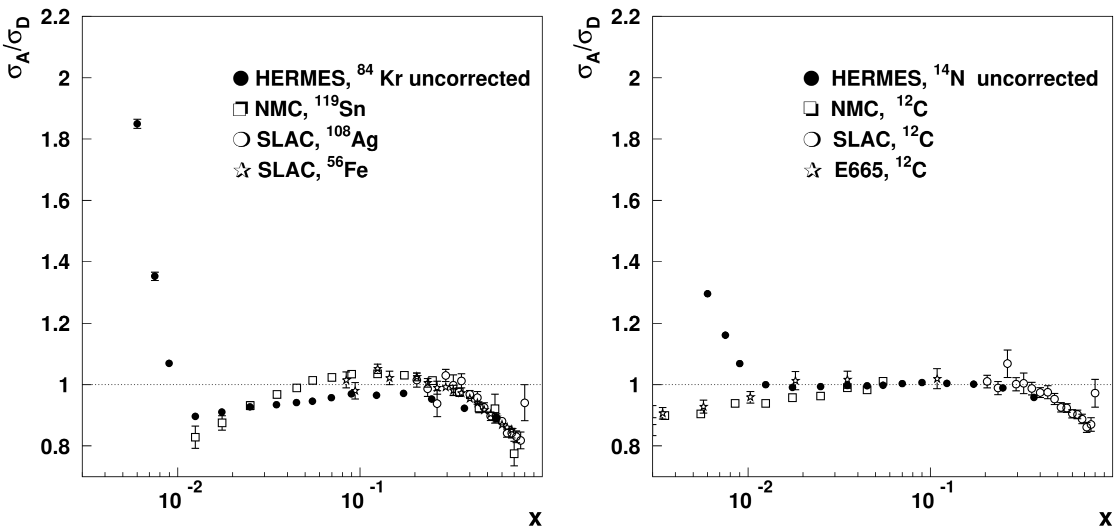

Figure 5.9: *Left: krypton to deuterium (1997) yield ratio (full circles) compared to the existing data on similar targets. Right: nitrogen to deuterium (1997) yield ratio (full circles) compared to existing data on ^{12}C. The $\sigma_{\mathrm{N}}/\sigma_{\mathrm{D}}$ data are normalized by a factor of 1.009. No efficiency nor radiative correction is applied to the data.*

in agreement with existing high-x data, this is not the case for the krypton data. The cause of the difference in the normalization of data collected in different years was attributed to the behavior of the luminosity monitor. A detailed series of systematic studies of the behavior of the luminosity detector was performed, including an estimate of a possibly required acceptance correction. It was concluded that there are two possible effects which may give rise to different acceptance corrections for the luminosity detector in different years:
1) The luminosity rate may depend on the x and y position of the beam which on average were different in the two years;
2) The luminosity monitor may have had a different position with respect to the beam due to a misalignment of the detector (year to year correction).
Separate correction factors need to be evaluated for these effects. Correction 1) was obtained from explicit measurements of the x and y dependence of the rates in the luminosity detector. The effect of changes in beam slope is corrected for by using two separate functions for variations of the x- and y-beam slope. While the variation of the x-slope during standard high density data taking is normally about $100\ \mu$rad, it was 300 μrad for the krypton data. This accounts for a total shift of the yield of about 1%. The y-slope correction was found to be less significant, since the variation during data taking was <50 μrad. In the case of the 1999 (polarized) deuterium data, the beam position was kept at a stable position. The correction on the yield is thus negligible. When applying these corrections and evaluating the $\sigma_{\mathrm{Kr}}/\sigma_{\mathrm{D}}$ ratio by taking data consistently from the same year (1999), the raw cross section

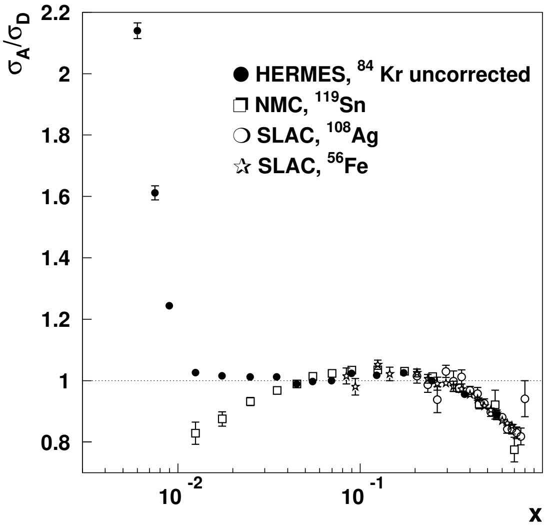

Figure 5.10: *Comparison of the krypton to deuterium (1999) yield ratio (full circles) to published data on: Sn (NMC, open squares), Ag (SLAC, open circles) and Fe (EMC, open stars). No efficiency nor radiative correction is applied to the data.*

ratios are found to agree with existing data for $x > 0.03$ (see Fig. 5.10). Below this x-value the photon shower correction is very important and thus needs to be applied before the data can be compared.
For the calculation of the second correction (2) a Monte Carlo simulation is needed which is under development at the moment. Since the position of the luminosity monitor changed between 1997 and 1998, it is presently impossible to get the correct relative normalization for the data taken in these two periods. The same problem is not encountered when comparing the D and ^{84}Kr data both collected in 1999. For this reason the 1997 dataset was not used to obtain the ratio $\sigma_{\mathrm{Kr}}/\sigma_{\mathrm{D}}$.

5.2.5 PID flux factors

Using two different target gases (^{84}Kr and D) a flux factor correction to the PID value is necessary. As discussed in section 3.2.2 the likelihood for properly identifying a particle in the different detectors has to be corrected by a factor which accounts for the actual particle fluxes (see Eq. (3.4)). The flux factors ϕ are calculated from the data as:

$$\log_{10}\phi \equiv \log_{10}\frac{\Phi^e}{\Phi^h} = \log_{10}\frac{n_e}{n_h} \tag{5.7}$$

with n_e the number of leptons and n_h the number of hadrons. From the obtained flux factor values the PID for each particle was recalculated as:

$$\mathrm{PID} = \mathrm{PID}_2 + \mathrm{PID}_5 + \log_{10}\phi. \tag{5.8}$$

From the new PID distributions the efficiencies and contaminations for ^{84}Kr and D were calculated for different PID cuts using Eq. (3.6) and Eq. (3.7). The table below shows the result for the efficiencies and contaminations for two values of this cut. The chosen PID cut used for both polarized deuterium and krypton is PID > 1.

	ϵ_{Kr}	ϵ_{D_2}	h_{Kr}	h_{D_2}
PID>2	0.95	0.92	0.001	0.009
PID>1	0.98	0.98	0.004	0.01

Table 5.2: *Calculated lepton efficiency (ϵ) and hadron contamination (h) for ^{84}Kr and D using two different PID cuts.*

After applying the flux factor corrections in the PID scheme the cross section ratios change less than 2% in the low x region and considerably less for higher value of x.

5.3 Uncertainty in the cross section ratio

The main source of systematic uncertainty is the correction for radiative effects, which is addressed in the second part of this section. The other main uncertainty stems from the photon shower correction, which is related to the detector misalignment as the MC statistics is not a limiting factor. The detector misalignment contribution was already described in section 5.2.3. The corresponding uncertainty is included in the statistical error. An additional source of systematic error in the data is the rate dependence of the yield of the luminosity monitor. After correcting for the luminosity acceptance the ^{84}Kr dataset still contains a small rate dependence: at higher luminosity rates the ^{84}Kr yield is lower with respect to that at lower rates. The overall variation amounts to 2%, which gives a systematic uncertainty contribution $\delta L = \pm 1\%$ for the ^{84}Kr data. Similar variations are seen also in the ^{14}N data sample while for ^{3}He the quoted normalization uncertainty is about 0.5%. The polarized deuterium data were all collected at standard ABS density, corresponding to low rates in the luminosity detector, which leads to no relevant variation in the yield.

Systematic uncertainties on radiative corrections

The systematic uncertainty due to radiative corrections is estimated using the upper and lower limit of the used parameterizations and also alternative parameterizations [92, 98, 99]

for all the input parameters to the TERAD code, such as the parameterizations for $R_{\rm D}$ and $F_2^{\rm A}/F_2^{\rm D}$. No uncertainty could be assigned to the missing radiative correction contributions from multi-photon exchange (Coulomb distortion).
The resulting uncertainty on the cross section ratio $\sigma_{\rm Kr}/\sigma_{\rm D}$ is about 6% at small x, quickly falling to values smaller than 1% for $x > 0.06$. Since the radiative corrections are smaller for ^{14}N and ^{3}He, the uncertainties due to radiative corrections for $\sigma_{\rm N}/\sigma_{\rm D}$ and $\sigma_{\rm He}/\sigma_{\rm D}$ are also smaller, i.e. about 3% at the lowest x value. Table 5.3 summarizes the sources of systematic uncertainties and their average effect on the ratio R, separately for ^{84}Kr, ^{14}N and ^{3}He. A complete list of the total systematic uncertainty in each x bin can be found in Appendix B, in tables B.1 - B.3 (more complete tables for (x,Q^2) bins can be found in http://www.nikhef.nl/~erikag/Analysis/inclusive.html).
It is concluded that the average systematic uncertainty on R amounts to 2.5% for $\sigma_{\rm Kr}/\sigma_{\rm D}$, 1.6% for $\sigma_{\rm N}/\sigma_{\rm D}$ and 0.9% for $\sigma_{\rm He}/\sigma_{\rm D}$.

Source	Error in %		
	$\sigma_{\rm Kr}/\sigma_{\rm D}$	$\sigma_{\rm N}/\sigma_{\rm D}$	$\sigma_{\rm He}/\sigma_{\rm D}$
Radiative correction	1.4	0.6	< 0.1
Photon shower corr.	0.4	0.4	< 0.1
Top/Bottom alignment	1.4	0.4	< 0.3
Luminosity monitor	1.0	1.0	0.5
PID cut	< 0.3	< 0.3	< 0.1
Charge symmetric bg.	0.1	< 0.1	< 0.1
Calorimeter threshold	< 0.2	-	-
Total	2.5	1.6	0.9

Table 5.3: *Sources of systematic uncertainties for $\sigma_{\rm He}/\sigma_{\rm D}$, $\sigma_{\rm N}/\sigma_{\rm D}$ and $\sigma_{\rm Kr}/\sigma_{\rm D}$. The numbers given are the average over the x and Q^2 range covered by the present analysis.*

5.4 Results

For completeness the studies presented in the previous sections (with the exception of section 5.3) were based on the entire x range covered by the HERMES experiment, $0.003 < x < 0.7$. The results discussed in this section only cover the x-region above 0.01 to avoid the region where the detector misalignment effect (see section 5.2.3) is not under control. The results for the cross section ratios $\sigma_{\rm Kr}/\sigma_{\rm D}$, $\sigma_{\rm N}/\sigma_{\rm D}$ and $\sigma_{\rm He}/\sigma_{\rm D}$ are presented in Fig. 5.11 as a function of x. The expressions used to extract these data and those presented in the remainder of this section, and evaluate the corresponding error bars are described in full detail in Appendix A. These formulae include all effects discussed in the previous sections. Also shown are the results of the NMC [75, 76, 77], and SLAC [93, 94] measurements for $\sigma_{He}/\sigma_{\rm D}$, $\sigma_C/\sigma_{\rm D}$ and $\sigma_{Sn}/\sigma_{\rm D}$, where the NMC values for $\sigma_{Sn}/\sigma_{\rm D}$ have been obtained from the measurements of σ_{Sn}/σ_C and $\sigma_C/\sigma_{\rm D}$. The $\sigma_{\rm N}/\sigma_{\rm D}$ and $\sigma_{\rm He}/\sigma_{\rm D}$ results have been renormalized by 0.9% to match the NMC and SLAC data at mid-x (i.e x = 0.1) as described in subsection 5.2.4. For x values below $x = 0.1$ the present data on ^{14}N/D and ^{84}Kr/D are slightly below the NMC data, but consistent within the present statistical and systematic uncertainties.

Q^2 and ϵ dependence of $\sigma_{\rm Kr}/\sigma_{\rm D}$ and $\sigma_{\rm N}/\sigma_{\rm D}$

To understand better the small discrepancy between the HERMES and NMC data at low values of x the Q^2 dependence of the cross section ratios is displayed in Fig. 5.12 for $\sigma_{\rm N}/\sigma_{\rm D}$, and in Fig. 5.13 for $\sigma_{\rm Kr}/\sigma_{\rm D}$ for fixed small ranges in x. Also shown are the data from NMC on ^{12}C and ^{119}Sn. It is noted that the HERMES data for $x < 0.08$ show an edge effect at the highest Q^2 values in each bin. This effect is believed to be due to an imperfect correction for the photon shower inefficiencies. In the case of ^{84}Kr/D the difference from the NMC measurements is accentuated by the positive small Q^2 dependence of the ^{119}Sn/D data. While no significant Q^2 dependence is observed in the cross section ratio of ^{14}N/D, the large uncertainty on the ^{84}Kr/D data does not allow to discriminate between a flat Q^2 dependence and an extrapolation of the positive Q^2 dependence as indicated by the NMC $\sigma_{Sn}/\sigma_{\rm D}$ measurements.
In order to extract the longitudinal to transverse cross section ratio $R(x, Q^2)$, the ϵ dependence of the cross section ratio has been evaluated as well.
Fig. 5.14 shows the ϵ dependence of the cross section ratio for ^{14}N/D, while the ϵ dependence of the ^{84}Kr/D data is shown in Fig. 5.15. Note that the ϵ dependence is not independent from the Q^2 dependence, i.e. small ϵ values correspond to large Q^2 values and vice versa.
The solid curves in Fig. 5.14 and Fig. 5.15 represent a two-parameter fit of the ϵ dependence based on Eq. (5.1), where the free parameters correspond to $F_{\rm A}/F_{\rm D}$ and $R_{\rm A}/R_{\rm D}$. The parameterization for $R_{\rm D}$ from Ref. [92] has been used. In general, the cross section ratios are well described by the fits.
Fig. 5.16 shows the extracted F_2 ratio for ^{14}N/D (top panel) and ^{84}Kr/D (bottom panel) in comparison with the parameterization of the NMC data for ^{12}C/D and ^{119}Sn/D. The parameterizations are in good agreement with the F_2 ratios extracted from the HERMES data.
The super ratio $R_{\rm A}/R_{\rm D}$ extracted from the same fit is presented in Fig. 5.17, where the HERMES results are compared to other published results. Existing data are usually represented in terms of $\Delta R = R_{\rm A} - R_{\rm D}$. The published values of ΔR [93, 101, 100] have been converted to $R_{\rm A}/R_{\rm D}$ using a parameterization for $R_{\rm D}$ [92]. The systematic uncertainty on the extracted ratios $F_2^{\rm A}/F_2^{\rm D}$ and $R_{\rm A}/R_{\rm D}$ is determined by the variation of the fit results when performing the fit on $\sigma_{\rm A}/\sigma_{\rm D}$ plus and minus the systematic uncertainty described in section 5.3. The re-

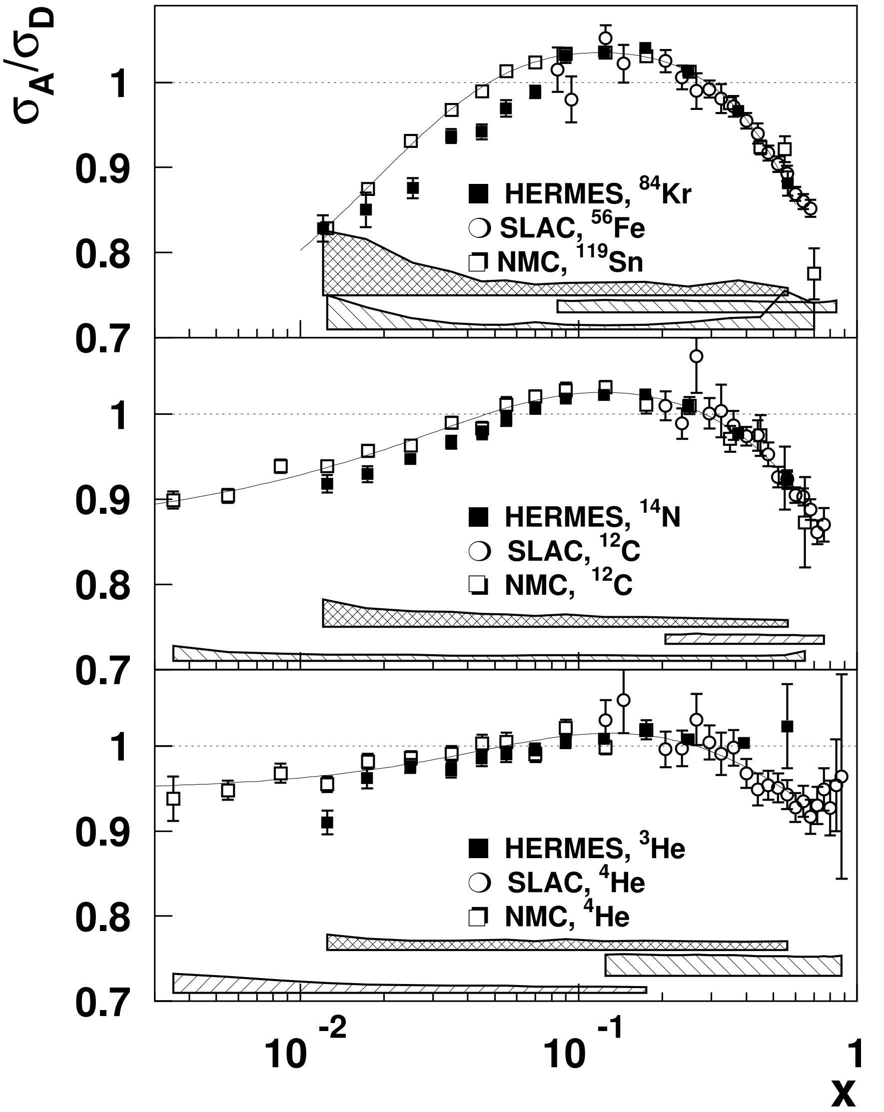

Figure 5.11: *Ratio of inclusive cross sections per nucleon for deep-inelastic lepton scattering from nucleus A and D versus x. The data have been corrected for radiative effects, photon shower inefficiencies and other detector effects described in section 5.2. The error bars represent the statistical uncertainties. The systematic uncertainties are given by the error bands (ordered according to the legend). The curves represent a parameterization of the* NMC *data. Also shown are the results of the* NMC *[75, 76, 77], and* SLAC *[93, 94] measurements.*

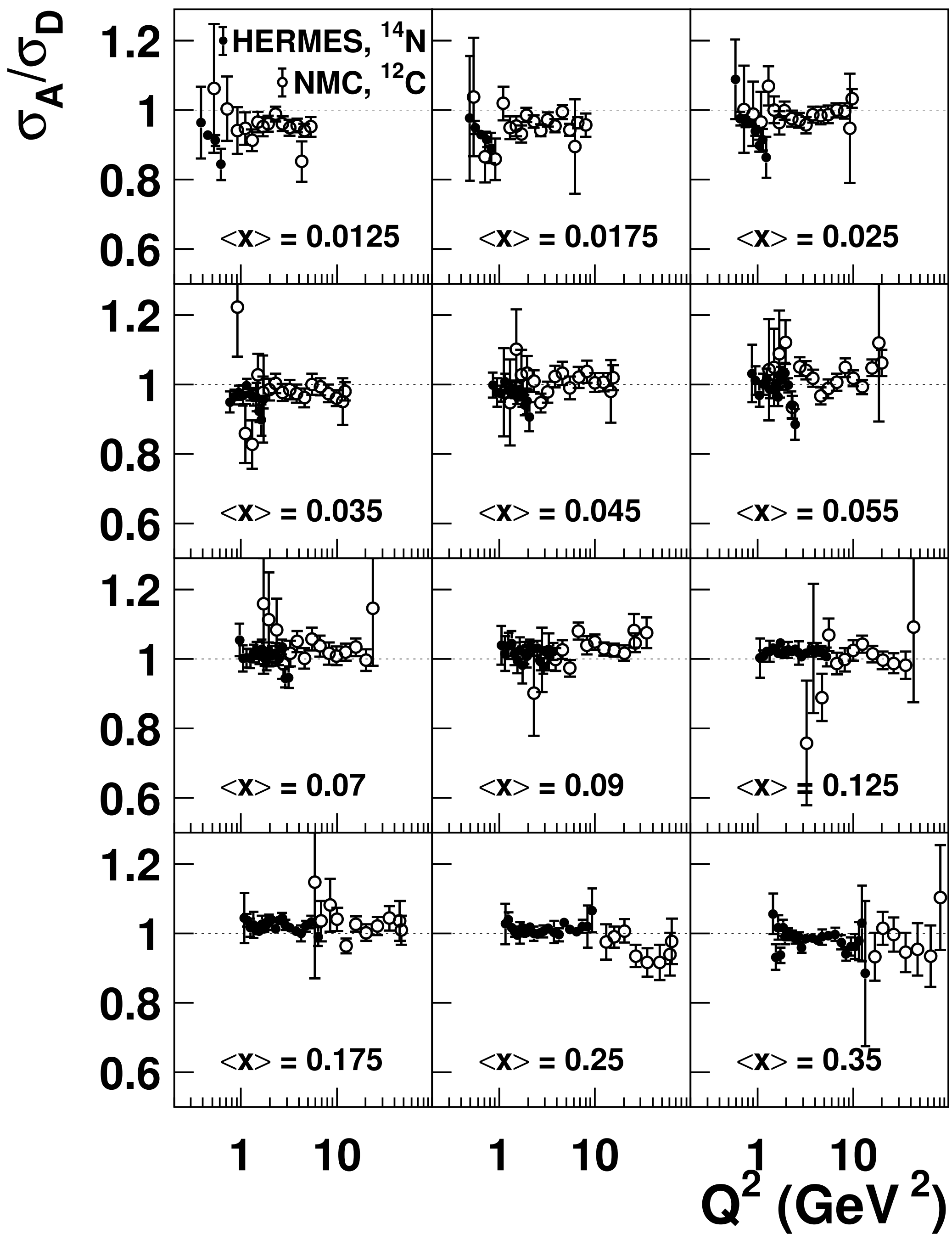

Figure 5.12: *Q^2 dependence of the cross section ratio $\sigma_{\mathrm{N}}/\sigma_{\mathrm{D}}$ for small ranges in x. The corrections applied to the data are listed in the caption of Fig. 5.11. The average x value for each x bin is listed in each panel. The* HERMES *^{14}N data have been normalized by a factor 1.009. The* NMC *^{12}C data are taken from Ref. [76].*

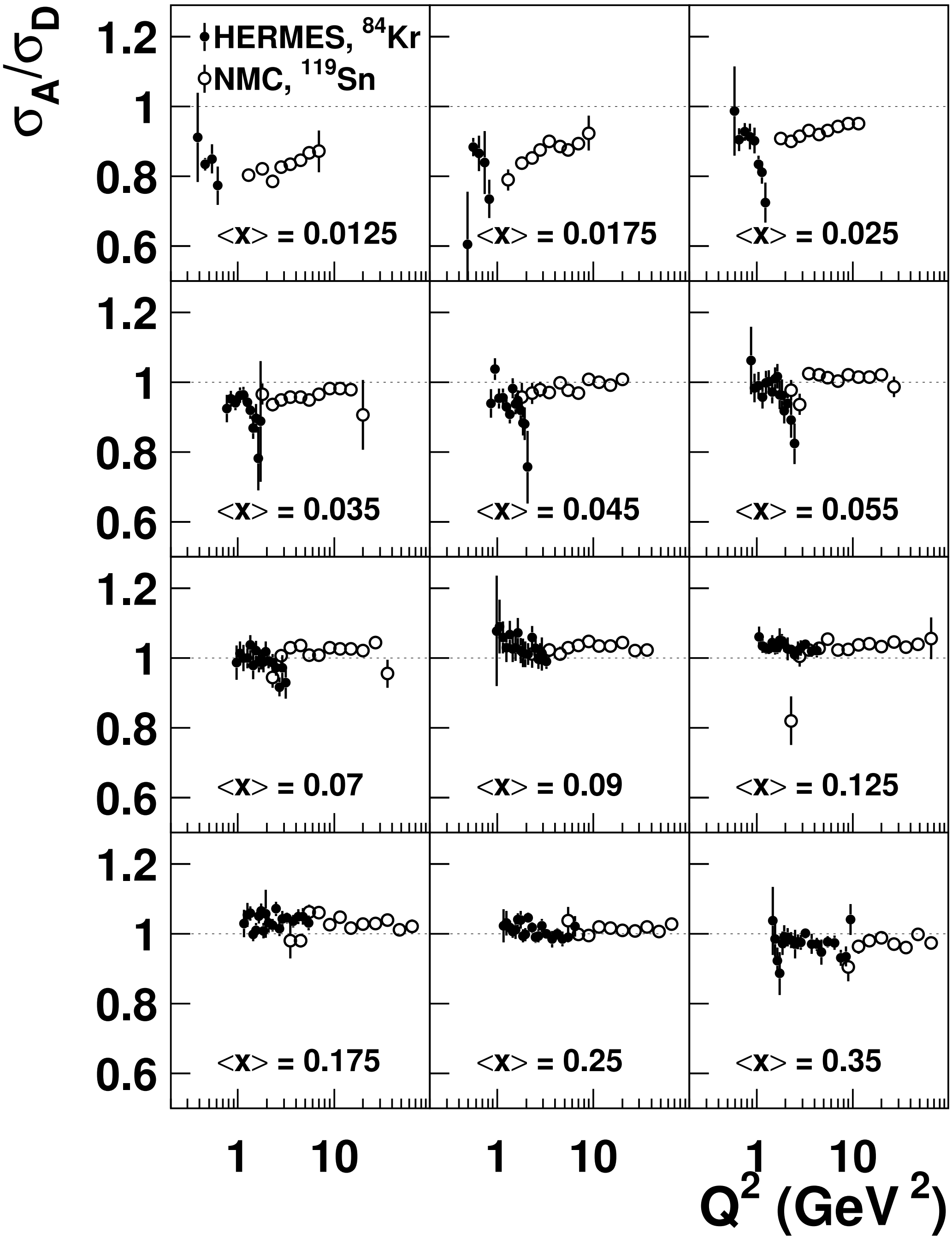

Figure 5.13: *Q^2 dependence of the cross section ratio $\sigma_{\rm Kr}/\sigma_{\rm D}$ for small ranges in x. The corrections applied to the data are listed in the caption of Fig. 5.11. The average x value for each x bin is listed in each panel. The NMC ^{119}Sn data are taken from Ref. [77].*

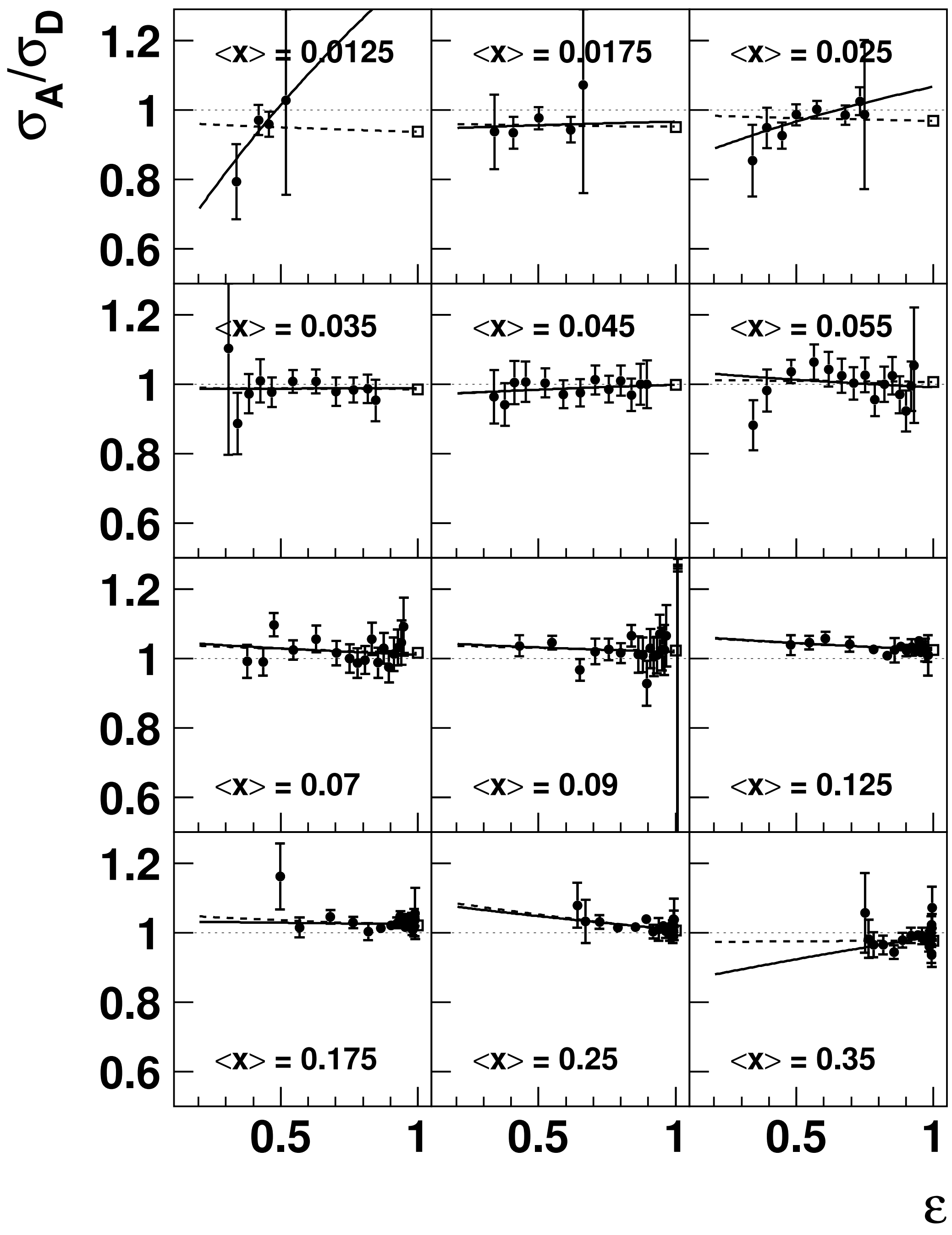

Figure 5.14: *ϵ dependence of the cross section ratio σ_N/σ_D for small ranges in x. The average x value is listed in each panel. The HERMES ^{14}N data have been normalized by a factor 1.009. The curves represent two-parameter fits based on Eq. (5.1) while the dashed curves represent one-parameter fits based on the same equation where the parameter F_2^A/F_2^D is fixed to the NMC value for ^{12}C (shown as an open square at ϵ=1).*

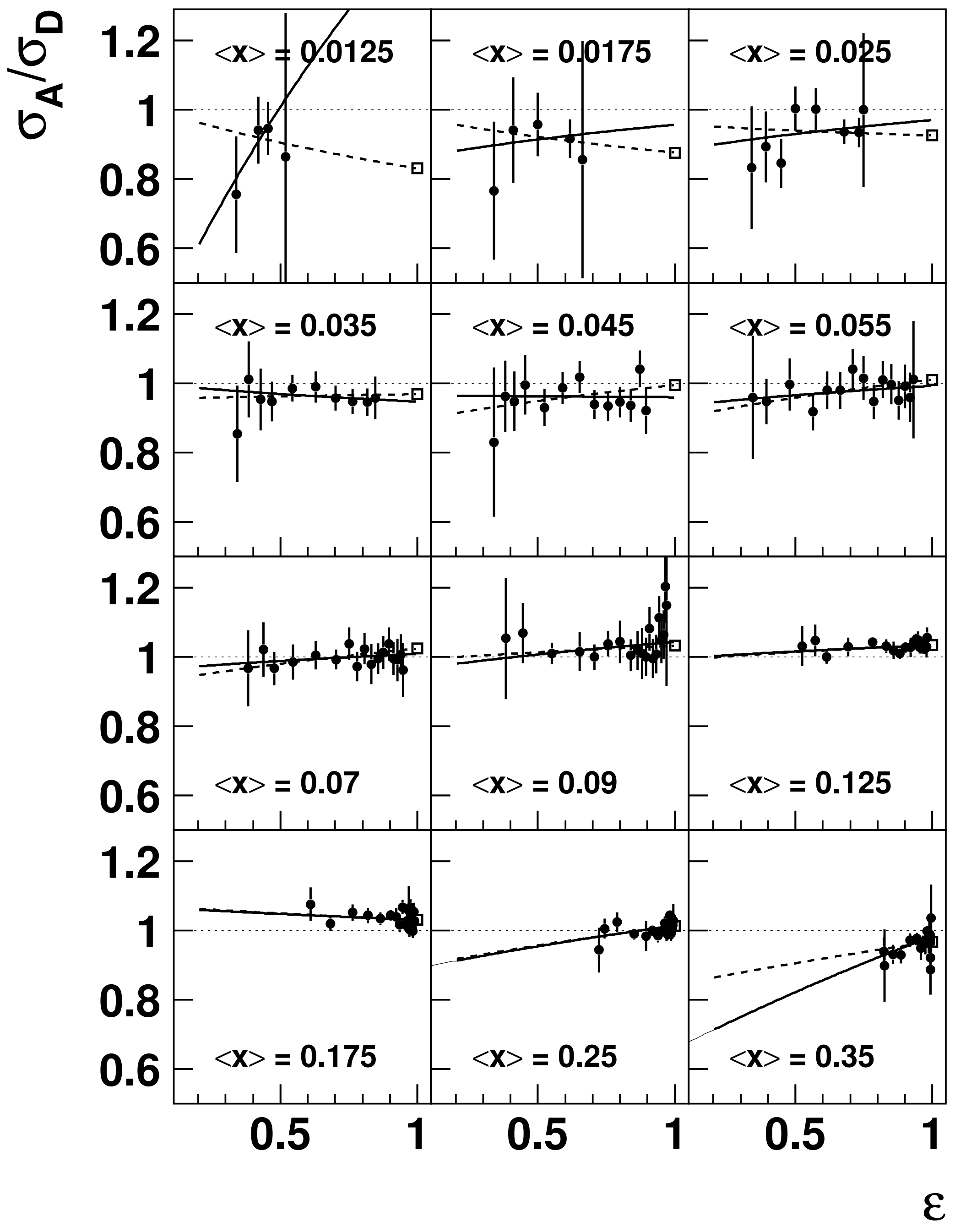

Figure 5.15: *ϵ dependence of the cross section ratio $\sigma_{\rm Kr}/\sigma_{\rm D}$ for small ranges in x. The average x value is listed in each panel. The curves represent two-parameter fits based on Eq. (5.1) while the dashed curves represent one-parameter fits based on the same equation where the parameter $F_2^{\rm A}/F_2^{\rm D}$ is fixed to the* NMC *value for ^{119}Sn (shown as an open square at ϵ=1).*

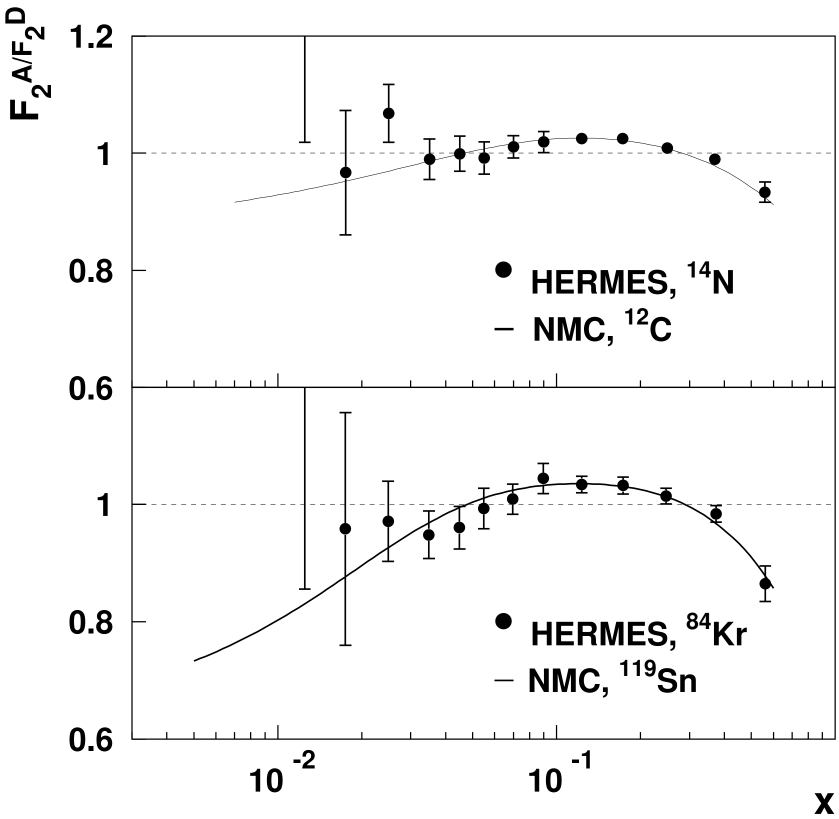

Figure 5.16: *Top panel: the ratio $F_2^{\rm A}/F_2^{\rm D}$ extracted from a fit to the HERMES ^{14}N/D data compared to NMC parameterization of the ^{12}C/D data (solid line). Bottom panel: the ratio $F_2^{\rm A}/F_2^{\rm D}$ for the HERMES ^{84}Kr/D data compared to NMC parameterization of the ^{119}Sn/D data (solid line). The error bars represent the statistical (including the correlated error in $R_{\rm A}/R_{\rm D}$) and systematic uncertainty added in quadrature.*

sulting uncertainties have been included in the error bars shown in Fig. 5.16 and 5.17. Their numerical values are listed together with the values of $F_2^{\rm A}/F_2^{\rm D}$ and $R_{\rm A}/R_{\rm D}$ in table B.4 in Appendix B. All data for R_A/R_D are found to be consistent with unity within errors.
The uncertainty in the extraction of the super ratio $R_{\rm A}/R_{\rm D}$ can be reduced by fixing the value of the ratio $F_2^{\rm A}/F_2^{\rm D}$ in the fitting function given by Eq. (5.1) to the corresponding NMC value for each bin in x. From the evidence shown in Fig. 5.16, the ratio $F_2^{\rm A}/F_2^{\rm D}$ is seen to be consistent with the parameterization of existing data. Since the F_2 ratio is considered to be Q^2 independent, the $F_2^{\rm A}/F_2^{\rm D}$ NMC data (open squares) plotted in Fig. 5.14 and 5.15

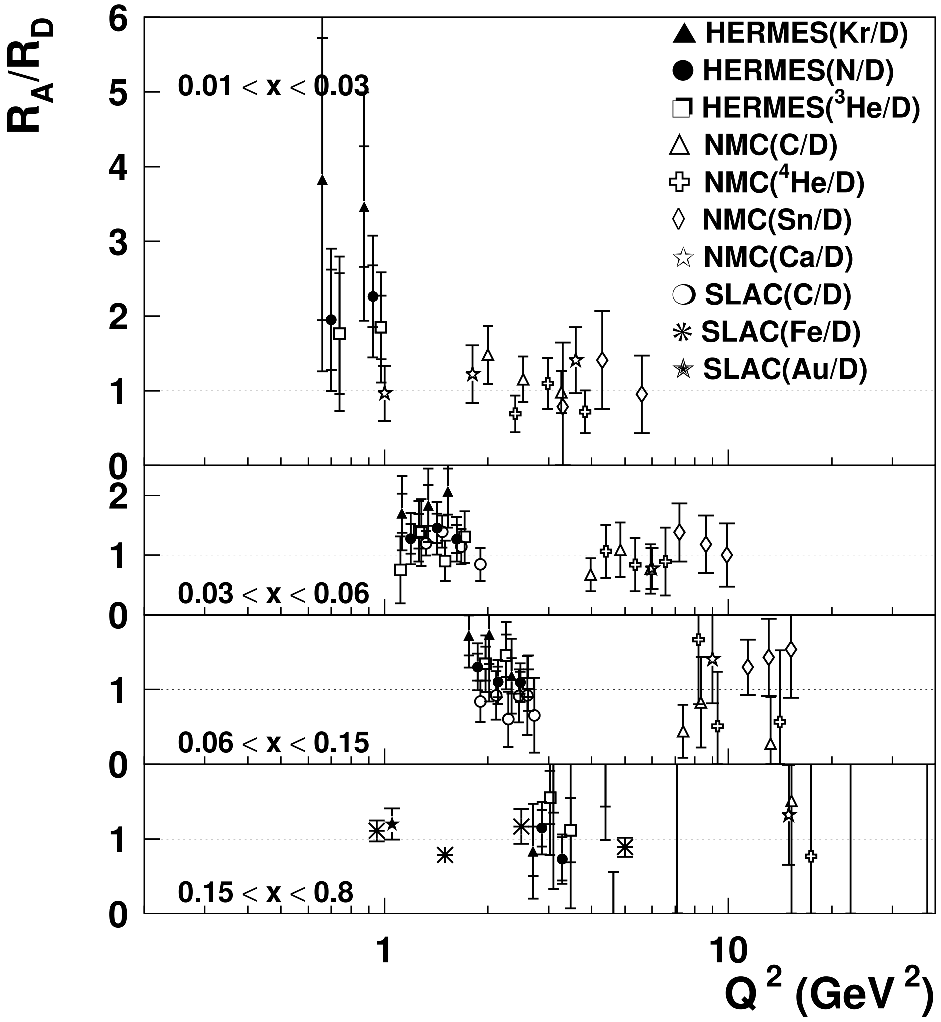

Figure 5.17: *The super ratio $R_\mathrm{A}/R_\mathrm{D}$ for ^{84}Kr, ^{14}N and ^{3}He, as extracted from a two parameter fit of the HERMES $\sigma_\mathrm{A}/\sigma_\mathrm{D}$ data. The open triangles (^{12}C) and crosses (^{4}He) have been derived from the NMC data using Eq. (5.1). The SLAC [93] and other NMC data [100] displayed have been derived from published values of $\Delta R = R_\mathrm{A} - R_\mathrm{D}$ and a parameterization [101] for R_D. The inner error bars represent the statistical uncertainty and include the correlated error in $F_2^\mathrm{A}/F_2^\mathrm{D}$. The outer error bars represent the quadratic sum of the statistical and systematic uncertainties.*

have been evaluated at the average Q^2 value of HERMES. This allows to perform a fit with only one free parameter, thus increasing the precision on the extracted ratio $R_\mathrm{A}/R_\mathrm{D}$. The results of the new fit to the HERMES data with the value at $\epsilon = 1$ fixed to the NMC value

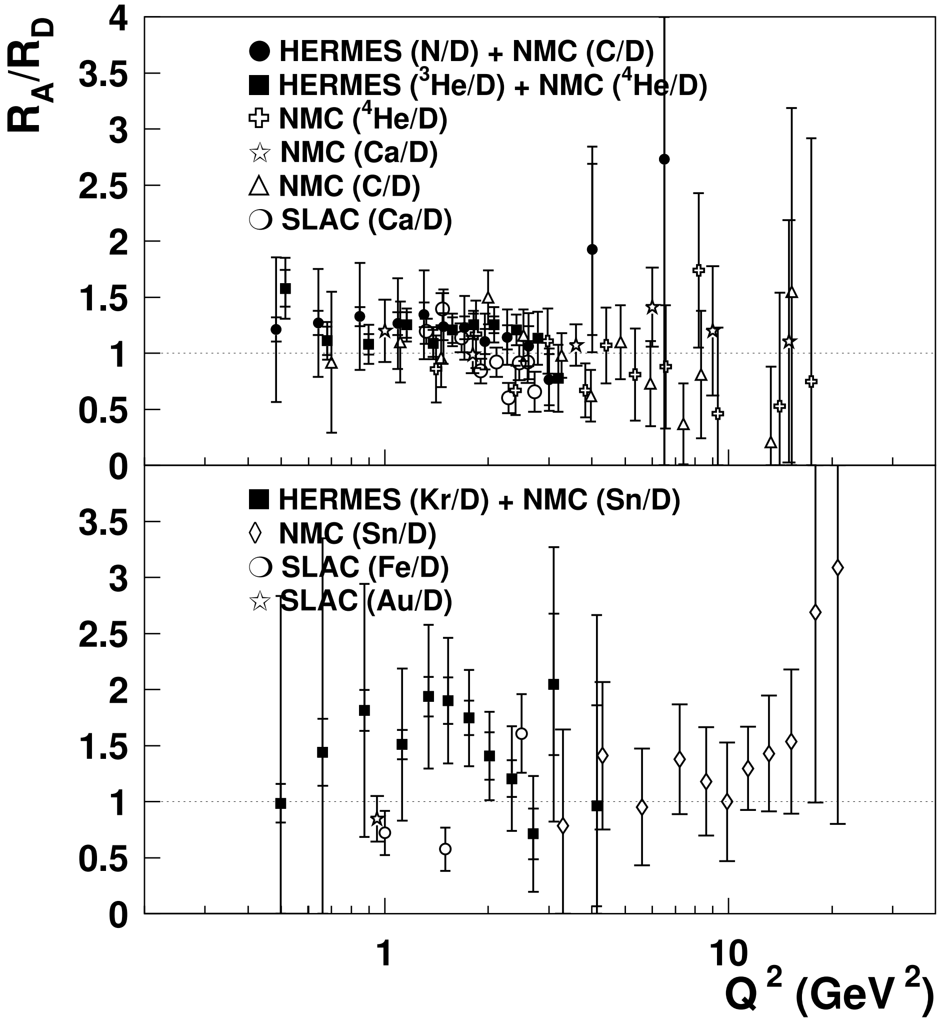

Figure 5.18: *The super ratio $R_\mathrm{A}/R_\mathrm{D}$ for ^{14}N and ^{3}He (top panel), and ^{84}Kr (bottom panel) as extracted from a one-parameter fit of the HERMES $\sigma_\mathrm{A}/\sigma_\mathrm{D}$ data. Existing data from other experiments are presented as well; the description is found in the caption of Fig. 5.17. The inner error bars represent the statistical uncertainty. The outer error bars represent the quadratic sum of the statistical and systematic uncertainties.*

are displayed in Fig. 5.14 and 5.15 as dashed lines. The resulting values for $R_\mathrm{A}/R_\mathrm{D}$ are shown as a function of Q^2 in Fig. 5.18. In the 1-parameter fit effectively information on $\sigma_\mathrm{A}/\sigma_\mathrm{D}$ obtained by NMC at high ϵ is combined with information obtained at lower ϵ values in the present experiment. Also in this case the value of R_A/R_D is found to be consistent with unity, but the uncertainties involved in the data on heavy nuclei are still very large.

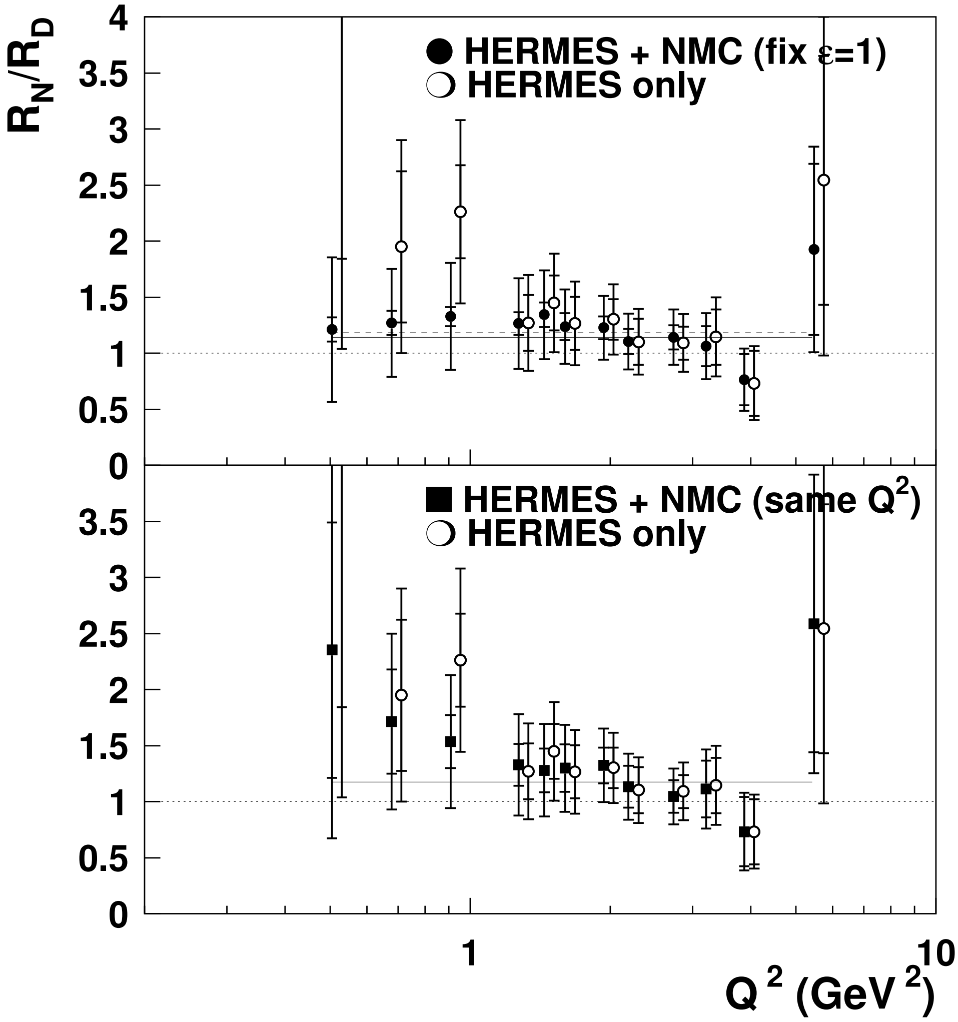

Figure 5.19: *Comparison between different extraction methods for the super ratio $R_{\rm A}/R_{\rm D}$ on ^{14}N. Top: results obtained using either the one (solid circles) or two (open circles) parameter fit shown in Fig. 5.14. Bottom: the solid squares represent the result of the Rosenbluth-type of analysis.*

An alternative method to combine HERMES and NMC data is a Rosenbluth separation: only using NMC $\sigma_{\rm A}/\sigma_{\rm D}$ data obtained in (x, Q^2) bins also covered by the HERMES measurements. As the HERMES measurements at a given average value of x cover a range in Q^2, the Q^2 values of the NMC data must be restricted to the same Q^2 range (for each x bin). In Fig. 5.12 the NMC and HERMES data with overlapping (x, Q^2)-values can be identified. On average the NMC data cover higher ϵ values of course. In order to carry out this alternative (Rosenbluth like) analysis the NMC and HERMES data covering the same (x, Q^2) range are plotted

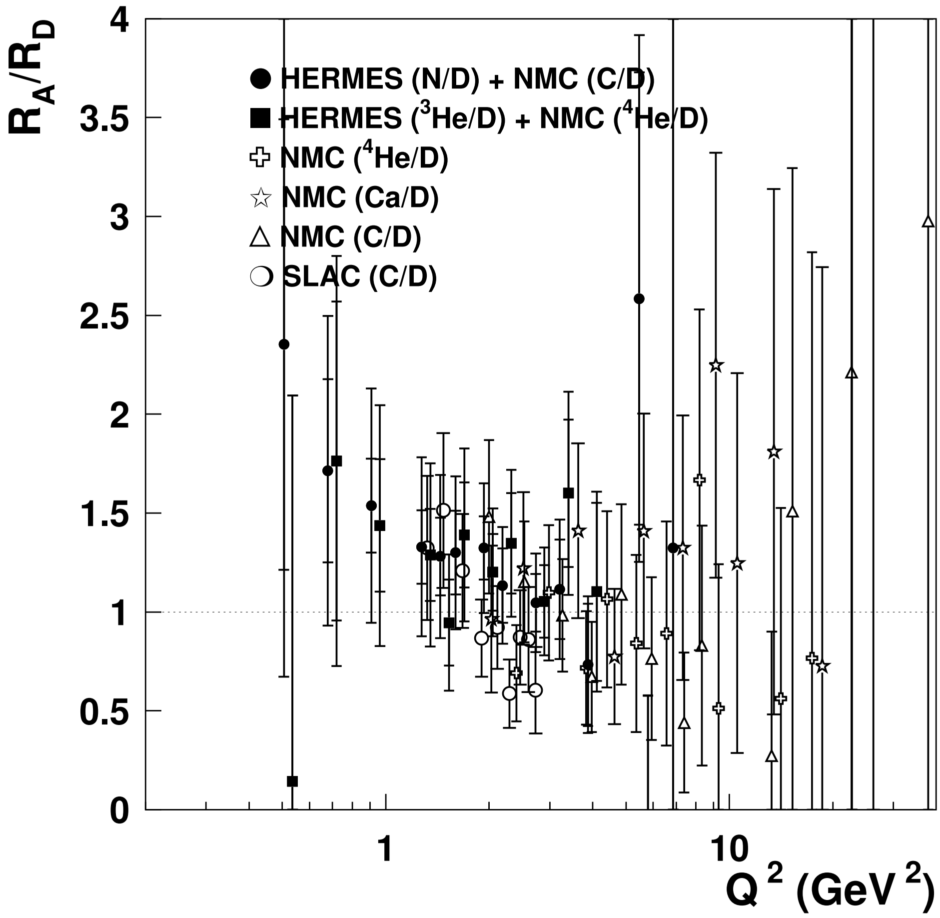

Figure 5.20: *The super ratio R_A/R_D for ^{14}N and ^{3}He as extracted from a Rosenbluth separation of the HERMES and NMC combined σ_A/σ_D data. Existing data from other experiments are presented as well; the description is found in the caption of Fig. 5.17.*

versus ϵ and fitted using Eq. (5.1). The fit performed to the combined set of data yields values for R_N/R_D which are compared in Fig. 5.19 to the other two results for R_N/R_D, i.e. the ones from the fit to the HERMES data only, and the ones from the fit to HERMES data with the value of the cross section ratio at ϵ =1 fixed to the NMC value for F_2^A/F_2^D. In both cases the additional information of NMC reduces the error bars. It should be noted that the large lever arm in ϵ created by using both NMC and HERMES data is particularly effective in reducing the uncertainties. The combined fits constrain the results to an average value of $R_A/R_D = 1.17 \pm 0.11$, which is very close to the value obtained using the HERMES data alone which is 1.18 $\pm$0.11. As expected the fit performed in which the cross section ratio is fixed at ϵ =1 has the smallest uncertainty. But in this case it is implicitly assumed that $F_2^{\rm A}/F_2^{\rm D}$ is Q^2 independent. This assumption does not enter in the Rosenbluth-type analysis. The resulting average $R_{\rm A}/R_{\rm D}$ with this method is 1.14 $\pm$ 0.10. The Rosenbluth separation cannot be applied to the combined ^{84}Kr and ^{119}Sn data, since there is insufficient overlap in (x, Q^2) between the HERMES and NMC data, in particular at low x (see Fig. 5.13). The results on the Rosenbluth separation performed on the helium and nitrogen (carbon) HERMES and NMC data are presented in Fig. 5.20 as a function of Q^2 together with all other measurements of $R_{\rm A}/R_{\rm D}$ on light and medium heavy nuclei. For Q^2 values between 0.5 and 20 GeV^2 and nuclei from ^{3}He to ^{40}Ca, $R_{\rm A}$ is found to be consistent with the Whitlow parameterization [92], which is dominated by data on the proton and the deuteron. A more recent parameterization of R from Abe et al. [93] exists, which is significantly influenced by the nuclear data. The influence of the choice in the R parameterization is however very small. The average value of $R_{\rm A}/R_{\rm D}$ for light targets (Fig. 5.20) is 0.96 $\pm$ 0.03, which does not change if the heavier targets are included in the average.

5.5 Concluding remarks

The cross section ratios for deep-inelastic scattering from a nucleus A as compared to deuterium are evaluated from data collected at HERMES on natural Kr, ^{14}N and ^{3}He targets. In a previous analysis of the HERMES data on ^{14}N a nuclear dependence of R was reported. In this chapter the reanalysis of those data has been presented and newly analyzed data on ^{84}Kr have been included with the aim to confirm or refute this effect. Furthermore, a precise measurement of the inclusive cross section ratios was needed for the normalization of the semi-inclusive data on nuclei which are presented in chapter 6. It has been shown that the extracted cross section ratios, properly corrected for radiative processes and a previously unnoticed detector inefficiency, have the well known behavior of shadowing, anti-shadowing and EMC effect [9, 102] in the various x regions. In addition, the data are found to be consistent with previously published measurements by NMC and SLAC over the entire x range covered by the present analysis. Hence, these results supersede the previous ones on ^{14}N, in which the effect of the photon shower was not corrected.
The Q^2 dependence of the cross section ratios is studied for separate x bins and found to be negligible for light targets (^{14}N and ^{3}He), while the ^{84}Kr data possibly show a weak Q^2 dependence in the lowest x bins. The ongoing analysis of ^{84}Kr data collected at HERMES with a beam energy of 12 GeV will enable us to verify this observation by extending the measurement of the inclusive cross section ratios to lower Q^2 values.
From the ϵ dependence of the cross section ratios the value of $R_{\rm A}/R_{\rm D}$, with R =$\sigma_{\rm L}/\sigma_{\rm T}$, is extracted using three different methods. With a two parameter fit to the HERMES cross

section ratio, the values of $R_{\mathrm{A}}/R_{\mathrm{D}}$ and $F_2^{\mathrm{A}}/F_2^{\mathrm{D}}$ are determined simultaneously. From this fit the super ratio $R_{\mathrm{A}}/R_{\mathrm{D}}$ is found to be compatible with unity, and $F_2^{\mathrm{A}}/F_2^{\mathrm{D}}$ is shown to be in good agreement with the NMC parameterization of existing data. In a second approach the NMC data are used to fix $F_2^{\mathrm{A}}/F_2^{\mathrm{D}}$ at ϵ =1, and the ϵ dependence is fitted with only one free parameter, yielding a better precision for $R_{\mathrm{A}}/R_{\mathrm{D}}$. This method can only be applied if the ratio $F_2^{\mathrm{A}}/F_2^{\mathrm{D}}$ is assumed to be Q^2 independent, which is supported by the ^{14}N data shown in Fig. 5.12. With this assumption a good fit of the ^{14}N data is obtained as illustrated in Fig. 5.14 (dashed lines). For the ^{84}Kr cross section ratio the weak Q^2 dependence mentioned above makes it impossible to perform a 1-parameter fit. This Q^2 dependence might be the cause of the deviation from unity of the values of $R_{\mathrm{A}}/R_{\mathrm{D}}$ extracted for the lower x bins (see bottom panel of Fig. 5.18).

Because of their large kinematic coverage the NMC ^{12}C (^{4}He) data overlap the ^{14}N (^{3}He) HERMES ones in certain (x, Q^2) regions. These data are used for a Rosenbluth separation to extract $R_{\mathrm{A}}/R_{\mathrm{D}}$. This (third) procedure avoids the assumption of $F_2^{\mathrm{A}}/F_2^{\mathrm{D}}$ being Q^2-independent, while still allowing to reduce the uncertainty by exploiting the large lever arm between the HERMES and the NMC data in ϵ. The resulting $R_{\mathrm{A}}/R_{\mathrm{D}}$ ratio is close to unity and is in good agreement with the result obtained by fixing the value of the cross section ratio at ϵ =1, although the errors are larger. The average value for the ratio $R_{\mathrm{A}}/R_{\mathrm{D}}$ for ^{14}N is in agreement with unity within 20% in the Q^2 range between 0.5 and 10 GeV^2, independent from the extraction method applied, as it can be seen from Fig. 5.19. Within the quoted uncertainty the HERMES data are consistent with the most recent calculation of possible medium effects on R at medium and high values of x discussed in Ref. [103].

This analysis has extended the range in which R_{A} is found to be consistent with R_{D} down to Q^2 = 0.5 GeV^2 (for x = 0.01). Furthermore, it has added significance to the NMC observation of a possible Q^2 dependence of the inclusive cross section ratio for heavy targets.

Chapter 6

Attenuation of hadrons in ^{84}Kr

Volvitur tempus rata quidem lege, sed per obscurum: quid autem ad me an naturae certum sit quod mihi incertum est?

Lucius Annaeus Seneca
Epistularum moralium ad Lucilium

6.1 Introduction

Besides studies of the internal structure of the nucleon, deep-inelastic scattering offers a direct way of studying the space-time development of the hadronization (or fragmentation) process, which is the process by which final-state hadrons are formed from the quark struck in a hard scattering event. The hadron formation time or the corresponding hadron formation length can be determined by measuring the effect of secondary reactions of the final state particles in the nuclear medium. In fact, both the propagating quark and the electroproduced hadrons can reinteract in the nucleus, leading to dissipation of a fraction of their energy. Hence, such measurements can also give information on the energy loss $\frac{dE}{dl}$ of partons in cold nuclear medium, which is most relevant as a benchmark for studies of relativistic heavy-ion collisions searching for evidence of the Quark-Gluon Plasma.

As an aside, it is of interest to note that there is currently a growing interplay between the physics of hadrons in dense matter, the physics of relativistic heavy-ion collisions, and also the physics of compact objects in astrophysics (which need as input the information gained from the other two fields). This last connection is mostly related to the study of kaons in the nuclear medium [104].

Semi-inclusive deep inelastic scattering on nuclear targets gives access to quantitative information on secondary partonic or hadronic reactions in cold nuclear matter. By measuring the multiplicity of hadrons produced on a heavy nucleus as compared to that on deuterium, the effect of the secondary interactions is observed as an attenuation of the hadron multiplicity.

In phenomenological approaches of hadron attenuation in nuclei it is assumed that hadrons are absorbed with a probability that depends on their inelastic cross section and on their formation time. The reinteraction probability for hadrons inside the nucleus and the energy dissipated by the hadron itself is thus reduced if the formation length is comparable to the size of the nucleus. However, the hadronization process itself when embedded in a nuclear medium, may also be influenced by quark energy loss through multiple scattering and gluon radiation as the quark propagates through the medium. The nucleus in these examples thus acts as a kind of passive 'detector' for any possible reinteraction at the scale of a few femtometer.

The various interactions within the nucleus result in a depletion (i.e. nuclear attenuation) of the energetic hadrons as compared to interactions with an elementary target. Hence, the fast forward hadron multiplicity is reduced, an effect which increases with the size of the nucleus.

At present the formation time of a hadron is not calculable in QCD, as the hadronization process takes place at a scale where perturbative field theoretical techniques are not applicable. Therefore, at the moment, the distribution of hadrons produced in deep-inelastic scattering and a possible modification of this distribution in nuclear matter can only be calculated with help of phenomenological models.

As was already mentioned before, the hadronization process in the medium needs to be understood in order to be able to interpret certain aspects of relativistic heavy-ion collisions. A modification of hadronic spectra is believed to be one of the expected signatures of the transition from cold nuclear matter to a deconfined Quark-Gluon Plasma.

Semi-inclusive deep-inelastic lepton-nucleus scattering provides a clean tool for the study of quark and hadron propagation effects. In contrast to hadron scattering, in DIS no deconvolution of the distributions of projectile and target fragments has to be made. Therefore, the comparison of hadron multiplicities extracted from DIS of leptons on various nuclei offers the best way to obtain information on the formation time of hadrons and the associated parton energy loss [105, 106].

In this chapter results are presented of semi-inclusive DIS experiments on ^{14}N and ^{84}Kr, which are used to study the attenuation of various (identified) hadrons in nuclear matter. The results are compared to various model calculations to extract information on parton energy loss and hadron formation times. The chapter is organized as follows. In section 6.2 the definition of the attenuation ratio is given together with the description of the extraction procedure. In the same section also the event selection and kinematic restrictions are addressed, followed by the treatment of the radiative and photon shower corrections. In order to obtain separate data for pions, kaons and protons a Ring Imaging Čerenkov detector (RICH) is used for particle identification, which is the subject of subsection 6.2.4. The systematic uncertainties on the attenuation ratios are evaluated in section 6.3 and the results are presented in section 6.4. In section 6.5 phenomenological models are used to fit the data and extract information on the formation times of various hadrons. Next, in section 6.6 existing QCD based model predictions are compared to the results of this analysis, and the A-dependence of the attenuation effects is discussed. Conclusions are drawn in section 6.7.

6.2 Attenuation ratio

The attenuation ratio is a function of four variables: the leptonic ones (x,Q^2) and the hadronic ones (z,p_T^2). As the data are only weakly dependence on Q^2 and p_T^2 the attenuation ratio R^h_{att} is integrated over these two variables and it is expressed as a function of (x,z) (or equivalently (ν,z)) as already shown in Eq. (2.22)

$$R^h_{\text{att}}(\nu, z) = \left[\frac{1}{\sigma_{\text{DIS}}(\nu)}\frac{d^2\sigma_{\text{SIDIS}}}{d\nu dz}\right]_{\text{A}} \cdot \left[\frac{1}{\sigma_{\text{DIS}}(\nu)}\frac{d^2\sigma_{\text{SIDIS}}}{d\nu dz}\right]^{-1}_{\text{D}} \tag{6.1}$$

can be separated into two terms: the ratio of inclusive DIS cross sections, which is calculated according to Eq. (5.6), and the ratio of SIDIS cross sections expressed as

$$\frac{\sigma_{\text{A}}^{\text{SIDIS}}}{\sigma_{\text{D}}^{\text{SIDIS}}} = \left(\frac{Y_{\text{A}}^{\text{SIDIS}}}{Y_{\text{D}}^{\text{SIDIS}}}\right)_{\text{meas}} \cdot \frac{\eta^A_{\text{inel}}}{\eta^D_{\text{inel}}}, \tag{6.2}$$

where $Y_{\text{A}}^{\text{SIDIS}}$ represents the luminosity-normalized yield for SIDIS on nucleus A, and the term $\eta_{\text{inel}} = \frac{\sigma_{\text{Born}}+\sigma_{\text{bg}}^{\text{inel}}}{\sigma_{\text{Born}}}$ accounts for the inelastic radiative background only, since elastic and quasi-elastic radiative processes do not contribute in semi-inclusive DIS. The ratio of inclusive DIS cross sections as expressed by Eq. (5.6) already includes the proper treatment for the subtraction of radiative effects. In the semi-inclusive case a multiplicative term is used for the radiative correction. This is due to the absence of a proper parameterization of the semi-inclusive Born cross section, which is needed as input of the TERAD code to extract the value of the radiative contributions. For the inclusive case, parameterizations for targets of similar atomic number from other experiments are used, but for the semi-inclusive cross section $\sigma_{\text{A}}^{\text{SIDIS}}$ no such parameterization exists. The best knowledge on radiative corrections for semi-inclusive processes is therefore obtained by using a relative value of the radiative correction factor, i.e. η_{inel}, as used in Eq. (6.2). The evaluation of the multiplicative factor η_{inel} is discussed in section 6.2.2.

6.2.1 Event selection

The analysis of the SIDIS data presented in this chapter is based on the sample of unpolarized ^{84}Kr and polarized D data described in section 5.2. The same data quality criteria have been applied as for the inclusive analysis. The kinematic constraints on the DIS lepton and the PID requirements are also the same as those presented in section 5.2, except for the Q^2 range which is limited to values above 1 GeV^2 for the present analysis to ensure the applicability of various models when interpreting the results. The virtual photon energy ν is required to be

sufficiently high (> 7 GeV) to avoid correlations between the values of the variables ν and z (see section 6.4). The restrictions on Q^2 and ν imply a limit on the value of the Bjorken scaling variable x, i.e. $x > 0.02$.
The analysis has been performed for charged hadrons, which are identified with the PID detectors by requiring PID $<$ -1, and for charged pions, kaons and (anti)protons using the RICH unfolding procedure (see section 6.2.4). Hadrons are required to have a sufficiently large fraction of the virtual photon energy to increase the probability that they carry the struck quark, $z > 0.2$. This limit sets the lower momentum of identified hadrons to $P_h > 1.4$ GeV, while for the separation of pions, kaons and (anti)protons the momentum range is limited by the RICH momentum thresholds[1]: $2.5 < P_{\pi,K} < 15$ GeV and $4 < P_{p(\bar{p})} < 15$ GeV. The semi-inclusive kinematic constraints for hadrons are summarized in the following list:

- $PID < -1$
- $z > 0.2$
- $\nu > 7$ GeV

For hadrons which are identified as charged pions, kaons or (anti)protons, the following additional selection criteria apply:

- RICH unfolding identification
- `smRICH.rQp` > 0 (see section 6.2.4)
- $2.5 < P_{\pi,K} < 15$ GeV
- $4 < P_{p(\bar{p})} < 15$ GeV

The total number of events that remain after the application of these requirements is given in table 6.1. It is noted that the selection criteria presented in this section for semi-inclusively produced hadrons on ^{84}Kr are similar but not identical to those used in Ref. [20] for hadrons produced on ^{14}N. An additional restriction was imposed on the x range of the ^{14}N data, i.e. $x > 0.06$, in order to avoid the region where the photon shower inefficiency cannot be neglected. Furthermore, in the ^{14}N sample pions could only be identified in the momentum range of $4 < P_{\pi,K} < 13.5$ GeV since the threshold Čerenkov detector was installed at that time in the HERMES spectrometer instead of the RICH. Therefore, no identification of kaons and (anti)protons was possible on ^{14}N. For these reasons the comparison of ^{14}N and ^{84}Kr results is limited to multiplicity ratios for hadrons and identified pions[2].

[1] After the completion of this analysis it has been shown that the pion momentum range can be extended down to 0.6 GeV [107].

[2] It has to be noted that the pion momentum range and x cut are different for the two data sets.

	^{84}Kr	D
DIS	804599	628577
h	174647	176894
π	111482	118408
K	18702	18224
$p+\bar{p}$	10546	9307

Table 6.1: *The number of DIS and SIDIS events that are used in the present analysis after the application of data quality criteria and kinematic constraints. The numbers of pions, kaons and (anti)protons have been obtained with the RICH unfolding procedure described in section 6.2.4.*

6.2.2 Radiative corrections

The evaluation of radiative corrections for the inclusive DIS cross section ratio (Eq. (5.6)) is addressed in section 5.2.2. It is noted that due to the more restricted kinematic range of the semi-inclusive data the inclusive radiative corrections that need to be applied in this case are smaller than the corrections applied in the inclusive case discussed in the previous chapter.
The measured ratio of SIDIS yields also has to be corrected for radiative processes using Eq. (6.2). These corrections are also calculated with the TERAD code, which is a code developed for inclusive DIS, and therefore it does not account for the z dependence of the radiative corrections. Due to the requirement that a produced hadron is also detected the phase space of the radiated photon can be slightly different from that in the inclusive case and may thus depend on z. To account for this effect, an additional multiplicative correction is calculated using the SIRAD code [108], which was specifically developed for the evaluation of radiative corrections in semi-inclusive deep inelastic scattering on hydrogen. This code properly treats the z dependence of the radiative correction. The total radiative correction of the semi-inclusive cross section ratio is obtained by multiplying the TERAD based correction already presented in Eq. (6.2) by the one resulting from SIRAD (η_{SIRAD})

$$\frac{\sigma_{\mathrm{A}}^{\mathrm{SIDIS}}}{\sigma_{\mathrm{D}}^{\mathrm{SIDIS}}} = \left(\frac{Y_{\mathrm{A}}^{\mathrm{SIDIS}}}{Y_{\mathrm{D}}^{\mathrm{SIDIS}}}\right)_{\mathrm{meas}} \cdot \frac{\eta_{\mathrm{inel}}^{\mathrm{A}}}{\eta_{\mathrm{inel}}^{\mathrm{D}}} \cdot \eta_{\mathsf{SIRAD}}. \tag{6.3}$$

The value of the attenuation ratio R_{att}^{h} is obtained by taking the ratio of Eq. (6.3) and Eq. (5.6). The values of the SIRAD corrections range between 2.3% and 0.2% for $R_{\mathrm{att}}^{h}(\nu)$, and between 3.1% and 2.5% for $R_{\mathrm{att}}^{h}(z)$.

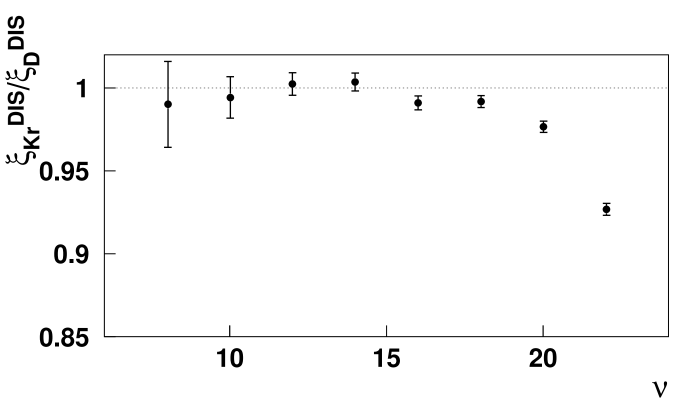

Figure 6.1: *Ratio of efficiencies for the detection of DIS events on krypton and deuterium in the ν range covered by the semi-inclusive analysis.*

6.2.3 Photon shower corrections

As discussed in section 5.2.1, the DIS cross section has to be corrected for the inefficiency caused by the photon shower effect. As for the radiative corrections also the photon shower corrections are much smaller in the present semi-inclusive analysis, reaching a maximum of 7% in the highest ν-bin (which corresponds to the lowest x value). The photon shower correction for each ν-bin of the present analysis has been calculated separately and is shown in Fig. 6.1.

The topology of the photon shower effect is such (as explained in section 5.2.1) that the resulting inefficiency only affects elastic and quasi-elastic events. Therefore, the number of hadrons (inelastic events) reconstructed in the detector does not suffer from this inefficiency. However, there is the possibility that semi-inclusive events in which a π^0 meson decays into two photons cause similar inefficiencies for the number of hadrons reconstructed. This effect has been investigated using the special μDST production used to tune the Monte Carlo for the photon shower correction. In this special production the lost events in one half of the detector are partially recovered by considering the two detector halves independently as described in section 5.2.1. When requiring a hadron to be found in coincidence with the scattered positron (hadron tagging method) the data selected are by definition inelastic. The inefficiency for this data set has been studied in the x range covered by the semi-inclusive analysis (0.02 $< x <$ 0.9) for both the deuterium and krypton targets by taking the ratio of semi-inclusive yields used in the present analysis and those derived from the aforementioned special μDST production. The resulting inefficiencies, plotted in Fig. 6.2, are about 10% for each gas target. The ratio ξ_{SIDIS} of hadron-tagged (inelastic) events has an average value of 1.0099 ± 0.0076, which implies that the inefficiencies cancel at the 1% level. This additional inefficiency is treated as a contribution to the systematic uncertainty, as the size of the correction is similar to the uncertainty by which it can be evaluated.

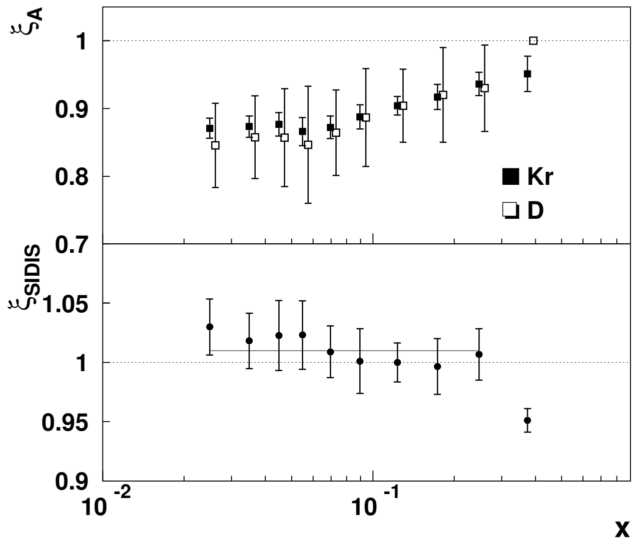

Figure 6.2: *Efficiency for the detection of hadrons produced on deuterium or krypton (top panel) and the ratio of hadron detection efficiencies on ^{84}Kr and D (bottom panel) in the x range covered by the semi-inclusive analysis. The effect of the two inefficiencies cancels in the ratio at the 1% level.*

6.2.4 RICH unfolding procedure

The separation of charged pions, kaons and (anti)protons is obtained with the RICH unfolding procedure using the Inverse Ray Tracing (IRT) method as described in subsection 3.2.2. To each identified track a vector of probabilities is associated. The components of the vector represent the probability that the identified particle is either a true pion, kaon or (anti)proton, depending on the average reconstructed Čerenkov angles in the gas and the aerogel radiators. In order to explain better the adopted procedure an example is given for the particular case of an identified pion: if the RICH identifies a pion (`smRICH.iType` = 3) the vector $\vec{I}$ of Eq. (3.12) becomes

$$\begin{bmatrix} I_\pi \\ I_K \\ I_p \\ I_X \end{bmatrix} = \begin{bmatrix} 1 \\ 0 \\ 0 \\ 0 \end{bmatrix} \tag{6.4}$$

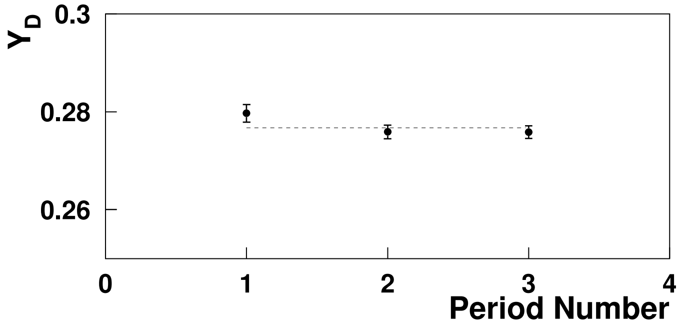

Figure 6.3: *Semi-inclusive hadron yield on deuterium in three different periods of data taking, which correspond to about 1500 runs each. The yield is found to be constant to within 1%.*

and the product $Q \cdot \vec{I}$ of Eq. (3.12) only yields 3 non-zero matrix elements, which correspond to the probabilities for the identified pion to be a true pion, kaon or (anti)proton,

$$[N_\pi, N_K, N_p] = [Q^\pi_\pi, Q^\pi_K, Q^\pi_p]. \tag{6.5}$$

The same vector is calculated for each track and the total number of pions in a given data sample results from evaluating the sum $\sum_i N^i_\pi$ over all tracks.
To ensure a good performance of the RICH identification procedure a quality parameter is defined (`smRICH.rQp`) as the logarithm of the likelihood ratio between the most likely hadron and the second most likely hadron identified. For a good hadron identification this parameter is required to be larger than zero.

6.3 Systematic uncertainty

Most of the systematic uncertainties related to the detector acceptance, reconstruction efficiencies and the particle identification procedure cancel in the ratio $R^h_{\rm att}$. Due to the different calorimeter thresholds used when collecting the ^{84}Kr and D data (3.5 GeV for ^{84}Kr and 1.4 GeV for D) an identical threshold of 3.5 GeV has been applied in the present analysis for the two targets. Increasing the threshold from 3.5 GeV to 5 GeV has an effect of only 0.2% on the extracted value of $R^h_{\rm att}$.
A reproducibility check has been performed on the D sample which was collected over a longer period of time. The total data sample has been divided in three subsamples of about 1500 runs each. The variation of the deuterium yield over these 3 periods is about 1%, as shown in Fig. 6.3. This systematic uncertainty accounts for possible variations of the detector acceptance and the detector efficiency with time.
The uncertainty of the radiative corrections associated with the use of the TERAD code was

evaluated in section 5.2.2 to be 1.4%. An additional systematic uncertainty comes from the application of the SIRAD code connected to the differences found when different fragmentation function and distribution function parameterizations are used in the code (0.6%). The evaluation of the photon shower effect on the attenuation ratio brings an uncertainty of 0.4%. The effect of the hadron detection efficiency on the ratio is 1%, as shown in Fig. 6.2.
Moreover, there is a contribution to the total systematic uncertainty due to decay pions from diffractive ρ_0 production which contaminates the hadron and pion attenuation ratios. This uncertainty has been estimated to be about 2.0%. From all the contributions described above the total systematic uncertainty has been calculated to be (on average) 3.3%. Table 6.2 summarizes the individual systematic uncertainties and their average effect on the attenuation ratio R^h_{att}.

Source	Single	Sum
	error in %	
Diffractive ρ_0	2.0	2.0
RC (TERAD)	1.4	
RC (SIRAD)	0.6	
		2.0
Photon shower effect	0.4	
Hadron eff. ratio	1.0	
		1.4
Reproducibility	1.0	1.0
Total		3.3

Table 6.2: *Sources of systematic uncertainties on R^h_{att}. The numbers given have been averaged over the entire ν and z coverage of the present data. The second column gives singular contributions; in the third column the correlated ones are summed linearly.*

In addition to the sources of systematic uncertainties mentioned above, the uncertainty related to the RICH unfolding procedure needs to be added (when the RICH information is used). To estimate this contribution two methods have been used: propagation of the error from the P to the Q-matrix, and comparison of attenuation ratios extracted with and without unfolding procedure. The total systematic uncertainty due to the RICH unfolding is taken to be the largest of these two contributions. In the first method, the statistical Monte Carlo based error is taken for the elements of the P-matrix, which is propagated to the Q-matrix for ^{84}Kr and D, respectively. The systematic uncertainty on the attenuation ratios of pions, kaons and anti(protons) has been evaluated using the errors on the Q-matrix. In the second method the uncertainty is evaluated by taking the ratio of the results for R^h_{att} obtained with and without the unfolding procedure. The two methods lead to similar uncertainties, and the largest is assigned as systematic error for each particle type. The total systematic uncertainty is 3.9% for pions, 4.2% for kaons and 3.9% (7.2%) for protons (antiprotons). This number is the sum in quadrature of the RICH systematic uncertainty and the total uncertainty on R^h_{att} of 3.3% described above.

6.4 Results

The results for the multiplicity (or attenuation) ratio R^h_{att} on ^{84}Kr are presented in Fig. 6.4 as a function of ν. The data are shown separately for positive and negative pions and kaons, and for protons and anti-protons. The separation between different particle types is achieved by unfolding the RICH information in the momentum range between 2.5 and 15 GeV for mesons, and 4 to 15 GeV for baryons.

Within errors the multiplicity ratios for positive and negative pions are found to be equal implying that there is no charge dependence of the pion attenuation ratio. Also, it is observed that the attenuation for negative kaons is similar to that of the pions, while the positive kaons are seen to be somewhat less attenuated.

The observed attenuation of protons is much smaller than the one of anti-protons, i.e. $R^p_{\mathrm{att}} > R^{\bar{p}}_{\mathrm{att}}$. This can be partially explained by noting that the interaction cross sections $\sigma(\bar{p}d)$ and $\sigma(pd)$ differ by about a factor 3 at the energies of interest. If the hadron is formed well inside the nucleus the interaction probability for a proton is smaller than that of an anti-proton, resulting in substantially more nuclear absorption or rescattering, and thus a smaller value of $R^{\bar{p}}_{\mathrm{att}}$. Alternatively, the data may indicate different modifications of the quark and anti-quark fragmentation functions in nuclei [109].

The bottom panel of Fig. 6.4 shows the variation of the average values of Q^2 and z in the ν range covered by the data. Note that the different values given for z for either (anti)protons or mesons arise from the different average energies of mesons and baryons.

Fig. 6.5 shows the z dependence of the same data sample[3]. It is seen that pions and negative kaons have the same z dependence. The values for the multiplicity of positive kaons are systematically above the ones of negative kaons. According to Ref. [110, 111, 104] (and others) positive and negative kaons are subject to opposite in-medium effects: in nuclear matter the K^+ feels a weak repulsive potential, whereas the K^- feels a strong attractive potential. As a result the K^+ mesons are less sensitive to rescattering effects in dense matter. For this theoretical prediction supportive evidence is found from the heavy-ion experiment described in Ref. [112]. This effect might also be at the origin of the observed difference in the multiplicity ratios for K^+ and K^- presented in Fig. 6.4 and Fig. 6.5, but explicit calculations applied to the present experiment are not available.

[3]Tables reporting the values of R^h_{att} in Fig. 6.4 and Fig. 6.5 can be found on the web site: http://www.nikhef.nl/∼erikag/Analysis/hadron-attenuation.html.

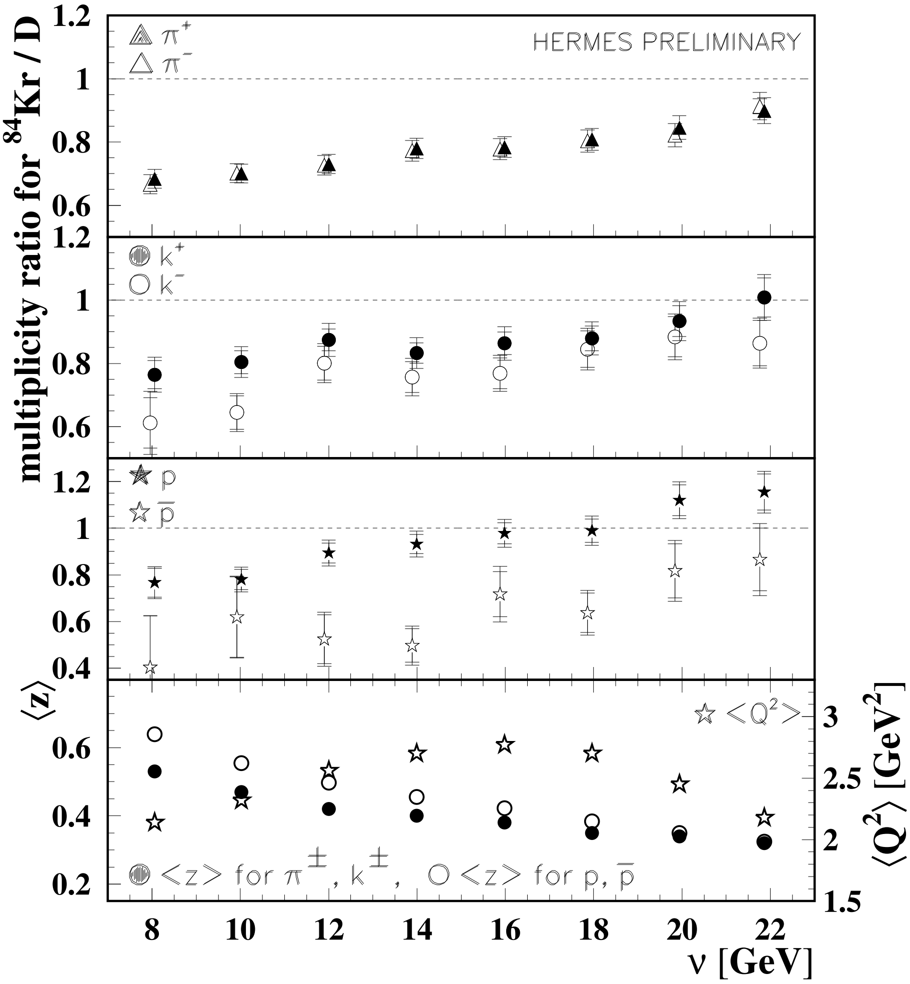

Figure 6.4: *Multiplicity ratio for identified positive and negative pions and kaons, and for protons and anti-protons versus ν for ^{84}Kr compared to D. The outer error bands are the sum in quadrature of statistical (inner bands) and systematic uncertainties. The bottom panel shows the average values for the other two kinematic variables (z and Q^2) governing the hadronization process.*

Protons and anti-protons have a quite different z dependence. The anti-proton attenuation ratio is almost constant in z, while the proton attenuation ratio rises above unity at low z. Possible causes of this rise are addressed below.

At high z ($z > 0.5$) the hadron is most likely to carry the struck quark (leading hadron). In the case of an anti-proton the struck quark must be an anti-quark. Under the assumption that factorization holds for the HERMES kinematics, the multiplicity distribution of anti-protons thus gives direct information on the essentially unknown fragmentation function of

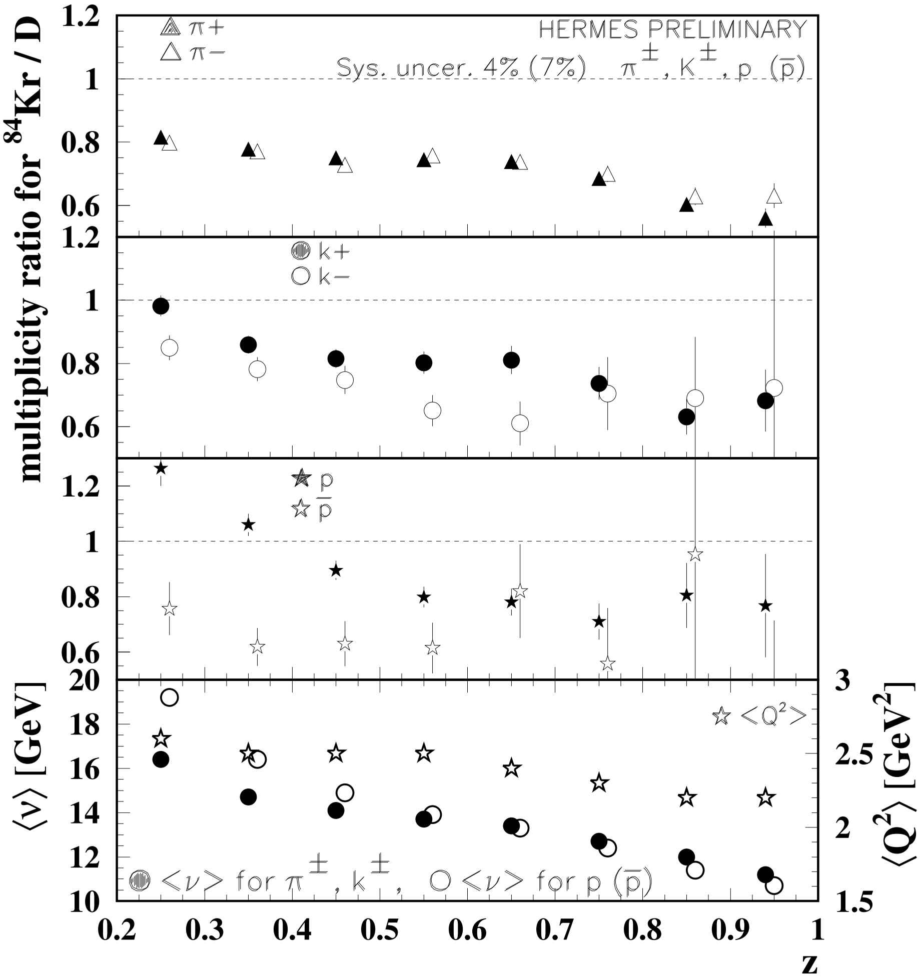

Figure 6.5: *Multiplicity ratio for identified positive and negative pions and kaons, and for protons and anti-protons versus z for ^{84}Kr compared to D. The outer error bands are the sum in quadrature of statistical (inner bands) and systematic uncertainties. The bottom panel shows the average values for the other two kinematic variables (ν and Q^2) governing the hadronization process.*

anti-quarks forming anti-protons, $D_{\bar{q}}^{\bar{p}}(z)$ [10]. This subject is not further pursued as the determination of absolute multiplicities is beyond the scope of this analysis.

Proton rescattering

To understand better the behavior of the proton multiplicity ratio in the region where $R^p_{\rm att}$ becomes larger than unity, the corresponding ν and z dependence are also evaluated with different kinematic restrictions. For the ν dependence the lower z limit is changed from 0.2 to 0.5. This requirement selects fast forward hadrons only, implying that the detected proton most likely contains the struck quark. The result is plotted in the left panel of Fig. 6.6, and shows that the attenuation of fast protons does not exceed unity. On the other hand, limiting the virtual photon energy range to $7 < \nu < 16$ GeV gives the same proton attenuation ratio as in the range $7 < \nu < 23$ GeV, as shown in the right panel of Fig. 6.6. These results strongly

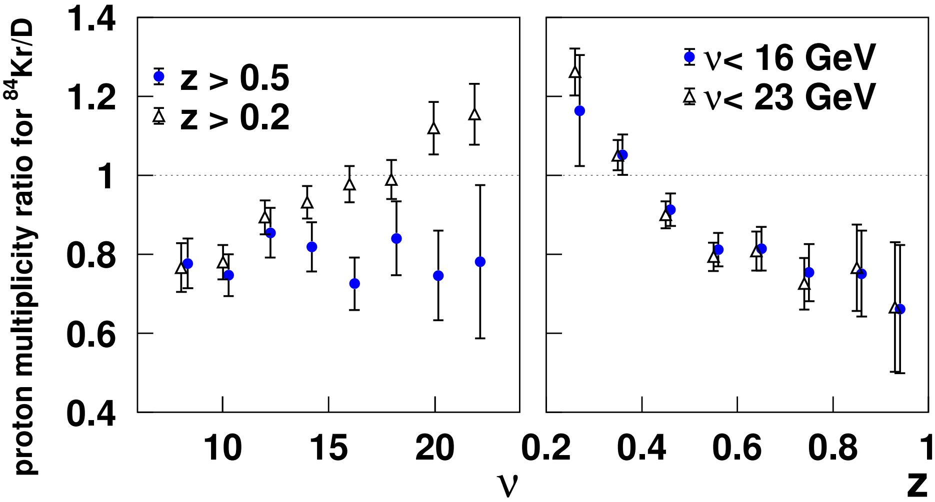

Figure 6.6: *Proton multiplicity ratio versus ν (left) for different z cuts, and versus z (right) for different ν cuts.*

suggest that the enhancement of $R^p_{\rm att}$ at low z and high ν is indeed related to possible rescattering contributions, leading to additional low z protons also showing up at high ν.
Another possibility for selecting leading hadrons is offered by increasing the lower limit on the invariant mass squared of the proton-lepton system W^2 from 4 GeV^2 to a higher value such as 10 GeV^2. However, as 98% of the DIS events anyhow have $W^2 > 10$ GeV^2 this requirement is not very effective. For the same reason it is not possible with the HERMES data to investigate the attenuation ratio in the resonance region ($1 < W^2 < 4$ GeV^2).
The processes responsible for the values of $R^p_{\rm att} > 1$, could be inelastic rescattering of primary hadrons (i.e. pions) on the target protons. Processes of this kind are clearly more likely to happen in a heavy nucleus since in deuterium there is only one proton available for such a rescattering process.

6.5 Formation time fits

As discussed in sections 2.2.3 and 2.2.4, essentially two types of models are available to describe the phenomenon of hadron attenuation. In the first type, the interactions of the hadron constituents and of the formed hadron with the nuclear medium are modeled in a semi-classical phenomenological approach, in which the nuclear absorption is the dominant mechanism. As a result the attenuation is expected to scale with the nuclear radius, i.e. $A^{1/3}$. On the other hand there are models which are based on a QCD description of the hadronization process in which parton energy loss induced by gluon radiation is the dominant mechanism. This class of QCD based models predict a dependence of the attenuation on the square of the nuclear radius, i.e. $A^{2/3}$.
In this section the phenomenological approach is used to fit the attenuation ratios, while in the next section available calculations from both types of models are compared to the HERMES data. At the end of that section the dependence of the attenuation on the nuclear mass A is evaluated as a further means to distinguish between the two proposed mechanisms.
Under the assumption that nuclear absorption is the dominant cause of attenuation for leading hadrons, the formation time constants for the various hadrons can be determined by fitting the measured multiplicity ratios for $z > 0.5$ using Eq. (2.23). These fits serve various purposes: they provide a convenient parameterization of the data, and they enable us to investigate the validity of the assumption that nuclear absorption is the dominant (if not the only) contribution to the hadron attenuation. This assumption is confirmed if the same formation time constants (c_h, or k and σ_s) are found for different nuclei. The third purpose of the fits is to provide a -model dependent- estimate of the average hadron formation time which is a useful number for other applications.
When evaluation the formation time fits, two different approaches are considered when describing the data. These two approaches, which correspond to different assumptions often used in model calculations, are discussed separately below.

One-timescale model

In the first approach the hadron formation time is parameterized by a one-timescale model where τ_f is the time needed to form an object which interacts with a cross section σ_h with the nucleons in the nucleus. For the expression of the formation time τ_f, which is needed to evaluate the survival probability in Eq. (2.23), the following form is taken (suggested by many theoretical models describing the hadron formation at high z [18, 19, 22, 26]):

$$\tau_f = c_h \, \nu(1 - z), \tag{6.6}$$

where the formation time constant c_h (expressed in fm GeV^{-1}c^{-1}) is the only free parameter in the fit. In this approach the quark-nucleon cross section σ_q is set equal to zero, as was also assumed by previous analyses [78, 113].

	c_h [fm GeV^{-1}c^{-1}]	sys
π^+	1.49 $\pm$ 0.09	$\pm$ 0.30
π^-	1.68 $\pm$ 0.13	$\pm$ 0.30
K^+	1.23 $\pm$ 0.21	$\pm$ 0.25
K^-	0.73 $\pm$ 0.19	$\pm$ 0.10
p	3.34 $\pm$ 0.60	$\pm$ 0.50
$\bar{p}$	2.13 $\pm$ 0.77	$\pm$ 0.30

Table 6.3: *Fitted values of the formation time constant c_h using a one-timescale model fit with a 3pG parameterization of the ^{84}Kr matter density. Only leading hadrons (i.e. with $z > 0.5$) are used in the fit. The third column reports the systematic errors.*

As it is often assumed in string model calculations that the string cross section is equal to the hadron cross section σ_h, the present approach does not distinguish between string-like and hadron-like interactions with the nuclear medium. For σ_h different values are used for the different hadron types:

$$\sigma_{\pi^+} = \sigma_{\pi^-} = 25 \text{ mb}; \sigma_{K^+} = 17 \text{ mb}; \sigma_{K^-} = 23 \text{ mb}; \sigma_p = 35 \text{ mb}; \sigma_{\bar{p}} = 60 \text{ mb}.$$

The ^{84}Kr density distribution which is needed in these fits (see Eq. (2.24)), has been derived from existing electron scattering data off the neighboring nuclei ^{76}Ge and ^{88}Sr. The ^{84}Kr matter density is extracted by interpolating between the two known charge distributions, correcting for different core polarization distributions [11]. The obtained distribution is described with a *3-parameter Gaussian* (3pG) function

$$\rho_{3pG}(r) = \rho_0 \frac{1 + w\left(\frac{r}{c}\right)^2}{1 + e^{(r^2 - c^2)/z^2}}, \tag{6.7}$$

in which the radial distance $r = \sqrt{b^2 + y^2}$ is determined by the transverse and longitudinal coordinates (b, y). The values obtained for the free parameters are respectively: c = 4.47 $\pm$ 0.49 fm, z = 2.52 $\pm$ 0.10 fm and w = 0.26 $\pm$ 0.41, implying a matter density of ρ_0 = 0.163 $\pm$ 0.015 fm^{-3} [11]. Note that the normalized matter density is actually used in the fits: ρ_0' = ρ_0/84 fm^{-3}. As an alternative a *2-parameter Fermi* (2pF) function has also been used to fit the nuclear matter density distribution:

$$\rho_{2pF}(r) = \rho_0 \frac{1}{1 + e^{(r - r_{\mathrm{Kr}})/a_0}}. \tag{6.8}$$

The values obtained for the nuclear radius and the surface thickness parameter for ^{84}Kr are [11]: r_{Kr} = 4.86 $\pm$ 0.07 fm and a_0 = 0.53 $\pm$ 0.03 fm, respectively, implying an integrated matter density of ρ_0 = 0.157 $\pm$ 0.005 fm^{-3}. The formation time constants c_h extracted using

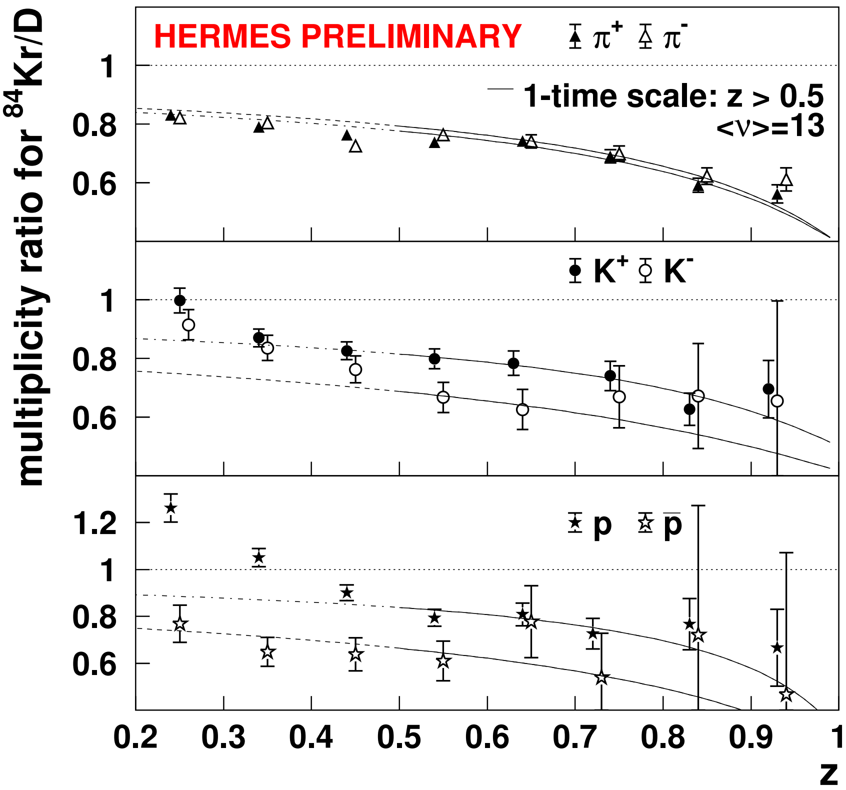

Figure 6.7: *Multiplicity ratios for pions, kaons and (anti)protons as a function of z for ^{84}Kr. The data are compared to curves obtained using the values reported in table 6.3 at an average ν value of 13 GeV in a one-timescale model. Only data above $z > 0.5$ have been included in the fit (solid lines). In each panel the dash-dotted (dashed) line is the extrapolation to low z values of the fit for the positive (negative) hadron type represented by the closed (open) symbols.*

these two parameterizations are in agreement to within 1%. In table 6.3 the values for c_h extracted with the 3pG function are reported. The systematic uncertainty in the third column of table 6.3 is obtained by repeating the fit with all the data simultaneously increased or decreased by their total systematic uncertainty.

The curves corresponding to the fits obtained with the matter density represented by Eq. (6.7) are presented in Fig. 6.7. The fits describe the z dependence of all data above $z = 0.5$ well. By extrapolating the fits to lower z values it is observed that the fit agrees with the pion data, while for kaons and especially for protons the fit clearly underestimates the data at low z. As was argued in section 6.4 the relative enhancement of $R^p_{\rm att}$ for low-z protons is possibly caused by rescattering effects in the nucleus. However, as the formation time fits can only account for loss of strength, an extension of the model is needed to account for any low-z enhancement.

The high-z results can be used to study the effect of nuclear absorption on the various hadrons and make relative statements. It is observed that the values of c_{π^+} and c_{π^-} are in good agreement with each other and are slightly higher than (but within errors in agreement with) the values found in a previous analysis of hadron attenuation on ^{14}N: $c_{\pi^+} = 1.37 \pm 0.18$ fm GeV^{-1}c^{-1} and $c_{\pi^-} = 1.38 \pm 0.21$ fm GeV^{-1}c^{-1} [20]. The agreement found for c_π as derived from two very different nuclei is an important result, since it seems to support the (relatively simple) treatment of the hadron attenuation effects in terms of nuclear absorption. Moreover, these numbers are also in agreement with the theoretical calculation of c_π in the framework of the gluon Bremsstrahlung model for high-z pions: $c_\pi = 1.35$ fm GeV^{-1}c^{-1} [29]. It is noted, however, that in the model calculation of Ref. [29] the dominant source of attenuation is nuclear absorption rather than gluon Bremsstrahlung.

The results for the K^- and K^+ mesons are seen to have on average somewhat smaller formation time constants as compared to those of the pions. Although the large statistical uncertainty of the K^- sample does not lead to a well constrained fit, the results suggest a lower value for c_{K^-} than for c_{K^+}. This difference might be related to the previously mentioned nuclear medium effects on the K^+N and K^-N interactions, i.e. the possibility that the values of σ_{K^+} and σ_{K^-} are medium dependent, as suggested by the GSI observation of Ref. [112]. However, the difference between the values of c_{K^-} and c_{K^+} is only about 2.5σ.

The values of c_p and $c_{\bar{p}}$ indicate a longer formation time for these baryons than for the mesons, which would confirm, at least qualitatively, the speculations on such formation time differences mentioned in [20]. It is noted that a value of c_h which is larger for baryons than for mesons is certainly in contrast to the first pioneering estimates of τ_f which assumed a $1/m_h$ dependence [21]. More data are needed to confirm this result and enlarge the significance of the difference between c_p and c_π.

If protons have a longer formation time, the effect could also be visible for other baryons, such as the Λ-hyperon. A first indication of the Λ attenuation was obtained in a preliminary analysis of HERMES data [114] on the Λ yields on D, ^{3}He and ^{14}N target as compared to ^{1}H. The results are shown in the middle panel of Fig. 6.8. Unfortunately, the limited statistics enforced an integration over ν and z. Moreover, the small A coverage of the data does not allow to make conclusive statements on the subject. The same applies to the slight increase of the K_s and $\bar{\Lambda}$ multiplicity ratios with A shown in the top and bottom panel of Fig. 6.8. More statistics are needed before firm conclusions can be drawn. At HERMES it will be possible to obtain a considerable improvement of the statistics of Λ hyperons with the new Lambda Wheels. If such data are collected with heavy target gases such as ^{40}Ar and ^{131}Xe, a detailed study of Λ attenuation in nuclei can be performed, thereby also increasing the statistics for kaons and (anti)protons.

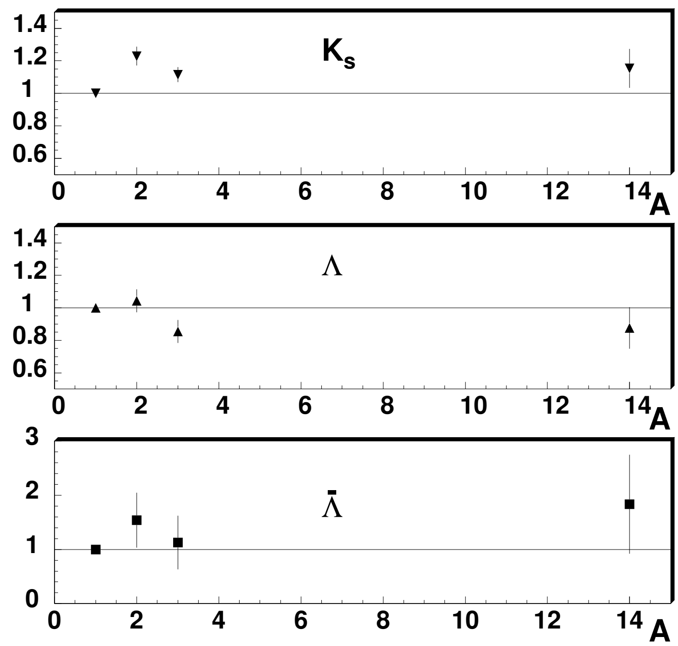

Figure 6.8: *A-dependence of the multiplicity ratio for identified Λ and $\bar{\Lambda}$-hyperons, as extracted from the analysis reported in [114].*

One-timescale model with string interaction

The one-timescale model fits discussed on the previous pages are based on the assumption that the pre-hadronic string-like state interacts with the same cross section as the hadronic state, while the initial quark-like state has a vanishing interaction cross section. The formation time obtained can be interpreted as the time needed until the pre-hadronic string-like state is formed, but there is no distinction between the pre-hadronic state and the final hadron. As the initial quark-like interaction is set to zero, the observed hadron attenuation is entirely attributed to conventional nuclear absorption processes. However, it can be argued that this is an extreme case, as the quark and string-like contributions need not be zero. In fact, it is very important to study this aspect in more detail since at least one theoretical model [30] attributes essentially all of the observed attenuation to partonic interactions. For that reason a second type of fit has been performed assuming that the pre-hadronic state interacts with the medium with a cross section σ_s different from zero[4].
Differently from the string model described in section 2.2.3, in the present approach the pre-

[4]Ideally one could even assume separate values for σ_s and σ_q, but the statistics of the data are not sufficient to obtain uncorrelated values for more than 2 parameters.

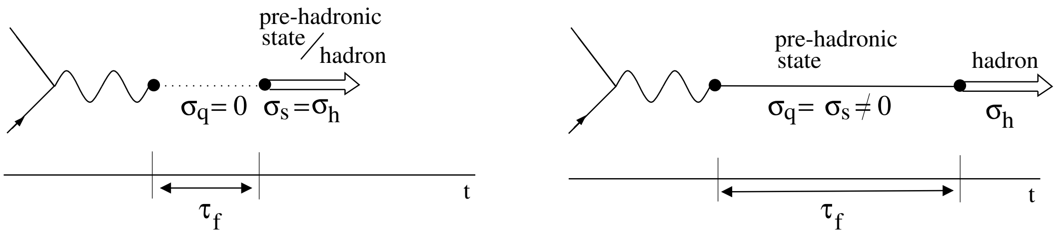

Figure 6.9: *Representation of the parameters used in the one-time model fits without (left) and with (right) a pre-hadronic state interaction.*

hadronic state (or string) is supposed to be formed immediately after the quark is struck (at a time τ_c = 0 in the LUND string model language). The string interacts with a cross section σ_s, and after a total time τ_f the hadron is formed. After its formation the hadron is subject to nuclear absorption which is evaluated using the same description as previously. The present approach is an extreme case as well, in which the interaction of the struck quark is neglected (or -equivalently- set equal to the string interaction). In this framework the formation time is expressed in terms of the string constant k (expressed in GeV c fm^{-1})

$$\tau_f = \frac{\nu}{k}(1 - z), \tag{6.9}$$

to reproduce the z dependence of the data. Using this expression a two-parameter fit can be performed with k and σ_s as free parameters, which can be extracted from the HERMES data. Fig. 6.9 summarizes the parameters involved in this type of fit as compared to the ones of the fit previously described. This approach cannot be directly compared to the LUND string model described in section 2.2.3, since in the approximation τ_c = 0 the model of Ref. [19] gives a different z dependence, i.e. $\tau_f \sim z$. Here, it has been chosen to use Eq. (6.9) instead to ensure a reasonable description of the data.
According to the string model the value of the effective string constant should be the same for all mesons, while it should be different for baryons. The same should be true for the string cross section. Therefore, a combined fit to the ^{84}Kr data is performed using either all meson or all baryon data together. The two resulting curves are compared to the data for mesons and baryons, respectively, in the top and bottom panel of Fig. 6.10. Again, while for $z > 0.5$ the curves describe the data fairly well, the extrapolation of the fit to lower values of z shows the limitation of this leading hadron analysis. It is noted that the fit to the mesons is entirely governed by the pion data[5], while the baryon fit is strongly driven by the proton data. It is still preferable to combine the data in the way suggested by the string model in view of the physical meaning of the extracted quantities.

[5]Separate fits to the pion and kaon data were also performed. The results are k_π = 0.28 ± 0.06 GeV c fm^{-1} and σ_s^π = 4.1 ± 0.7 mb for the fit to the pion data; and for the kaon data k_K = 0.17 ± 0.27 GeV c fm^{-1}, and σ_s^K = 4.1 ± 2.0 mb.

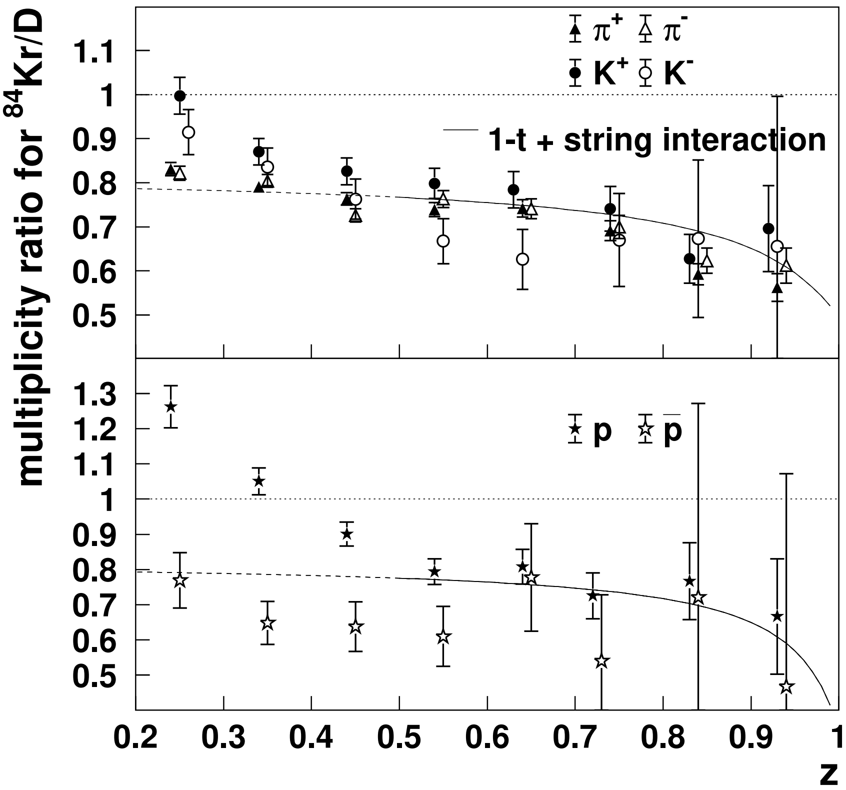

Figure 6.10: *Multiplicity ratios for pions, kaons and (anti)protons as a function of z. The solid lines are fits obtained with the one-timescale model with string interaction for different hadron types. Only data above $z > 0.5$ are used in the fit. The dashed lines are extrapolations of the fits to lower values of z.*

The extracted values for k and σ_s are listed in table 6.4. For the string cross section σ_s there is good agreement between the meson and baryon data, even if σ_s is not expected to be equal in the two cases. The string constant k for mesons is seen to be larger than the value of k for baryons, which is related to the observed shorter formation time of the mesons as compared to that of the baryons. In fact in the limit of $\sigma_s = 0$ the string constant k is equal to $1/c_h$.
A mass dependence of k is foreseen by the LUND model: it is expected that baryons have a longer formation time than mesons [115], corresponding to a smaller string constant. The latter prediction is confirmed by the fitted values of the string constants presented in table 6.4.
For comparison the same fit has also been performed for the published ^{14}N data [20] both for pions and for all hadrons combined. The results of these two fits are also reported in

^{84}Kr			^{14}N		
	k [GeV c fm^{-1}]	σ_s [mb]		k [GeV c fm^{-1}]	σ_s [mb]
Mesons	0.28 ± 0.06	4.2 ± 0.7	Pions	0.12 ± 0.04	2.7 ± 0.6
Baryons	0.11 ± 0.04	4.3 ± 1.5	Hadrons	0.11 ± 0.04	2.1 ± 0.5

Table 6.4: *Values for the string tension k and the string cross section σ_s for mesons and baryons as extracted from a fit using the one-timescale model with string interaction and the ^{84}Kr data shown in Fig. 6.10. On the right the results for pions and all hadrons as extracted from a similar fit to the HERMES ^{14}N data [20] are listed. Only leading hadrons (i.e. with $z > 0.5$) are used in both fits.*

table 6.4. The results for mesons on ^{84}Kr and pions on ^{14}N can be directly compared and are expected to be the same if the effect of the nuclear medium is properly accounted for, and k and σ_s only characterize the hadronization process. Instead, a significant difference for both the value of the string constant and the string cross section are observed between the two gas targets. This result provides first evidence that phenomenological models based on nuclear absorption do not reproduce the A-dependence of the HERMES attenuation data. This point is further discussed at the end of the next section when the A-dependence of the R_{att} data is discussed explicitly.

Comparing the results of the two types of formation time fits presented in this section, and in particular the values extracted for c_h and k, it is seen that these type of fits only yield model dependent values for the hadron formation time. By comparing, for instance, the value of c_π from table 6.3 to the value of $1/k$ = 3.6 GeV c fm^{-1} for mesons from table 6.4, a factor of about 2.5 is found between the pion formation time τ_f as calculated with Eq. (6.6) and the value obtained with Eq. (6.9) for fixed values of ν and z. It is important to note, however, that the large difference between the pion and proton formation times remains, which indicates that independent from the sophistication of the model, the proton formation time is about twice as long as that of the pion. This result represents new information which is not yet available from any previous analysis. It is also important to point out that the A-dependence of the data does not seem to be well reproduced by these type of fits, and therefore a different approach is needed in order to arrive at a consistent description of the ^{14}N and ^{84}Kr data.

6.6 Comparison to model calculations

In this section the two types of models for which published calculations exist are compared to the HERMES data for hadron attenuation. Most of the theoretical models available at the time of this work only describe the z or ν dependence of the attenuation (or multiplicity) ratios for charged hadrons or mesons, without a separation for the particle type as achieved experimentally by HERMES. Therefore, the attenuation ratio has also been extracted from the data for positive and negative hadrons combined in order to enable a comparison to various theoretical predictions. The combined hadron attenuation data have the advantage of extending the available momentum range of the data to $1.4 < P_h < 15$ GeV, since the RICH information is not required as the hadrons are identified by the other PID detectors using the PID scheme described in section 3.2.2. Furthermore, the various models also contain specific predictions for the A dependence of $R^h_{\rm att}$. For that reason the published ^{14}N data [20] are also included in the plots together with the corresponding model predictions[6].

Phenomenological models

Three phenomenological models were briefly described in section 2.2.3. A modification of the first model, the two-timescale model, has been used in the previous section to fit the data and extract information on the string constant k. From the other two models (Ref. [26] and [24]) calculations have been made available by the authors, which are compared to the ^{84}Kr data in Fig. 6.11 and Fig. 6.12, respectively. As was already mentioned in section 2.2.3 in the rescaling model the string constant k is set equal to 0.4 GeV c fm^{-1}. This value is similar to the result obtained from the second fit described in section 6.5, where k is found to be 0.28 ± 0.06 GeV c fm^{-1}. The results of the rescaling model with nuclear absorption (shown in Fig. 6.11) give an adequate description of the ν and z dependence of $R^h_{\rm att}$ for both positive and negative pions, and positive kaons, while negative kaons are less well reproduced. The influence of nuclear absorption on the calculations is made explicit by showing calculations with (lower pair of curves) and without (upper pair of curves) this effect. The effect is seen to be crucial as rescaling alone would not be enough to describe the hadron attenuation data on ^{84}Kr. Apparently, the rescaling effect is quite small as compared to the nuclear absorption effect for a heavy target. In Ref. [26] the authors argue that the major contribution to the attenuation in this model originates from pre-hadron absorption (rather than from hadron absorption). This is illustrated by fixing the hadronic cross section to zero and the pre-hadronic one equal to the hadron cross section in the calculation, as is represented by the dotted line in the upper right plot of Fig. 6.11. However, as we already discussed in the previous section experimentally it is not possible to discriminate between pre-hadronic (string-like) and hadronic interactions if both are assumed to be governed by the same interaction cross section. In both cases the first quark-like interactions (governed by small cross sections) are followed by stronger hadron-like interactions. For that reason all these results are very similar to the one-timescale model fits discussed in the previous section.

The separate predictions for positive and negative pions and kaons from the flavor dependent

[6]Since all the model calculations were made using the kinematic restrictions of the published ^{14}N data [78], the same cut of $x > 0.06$ is also used here for the ^{84}Kr data with all hadrons combined.

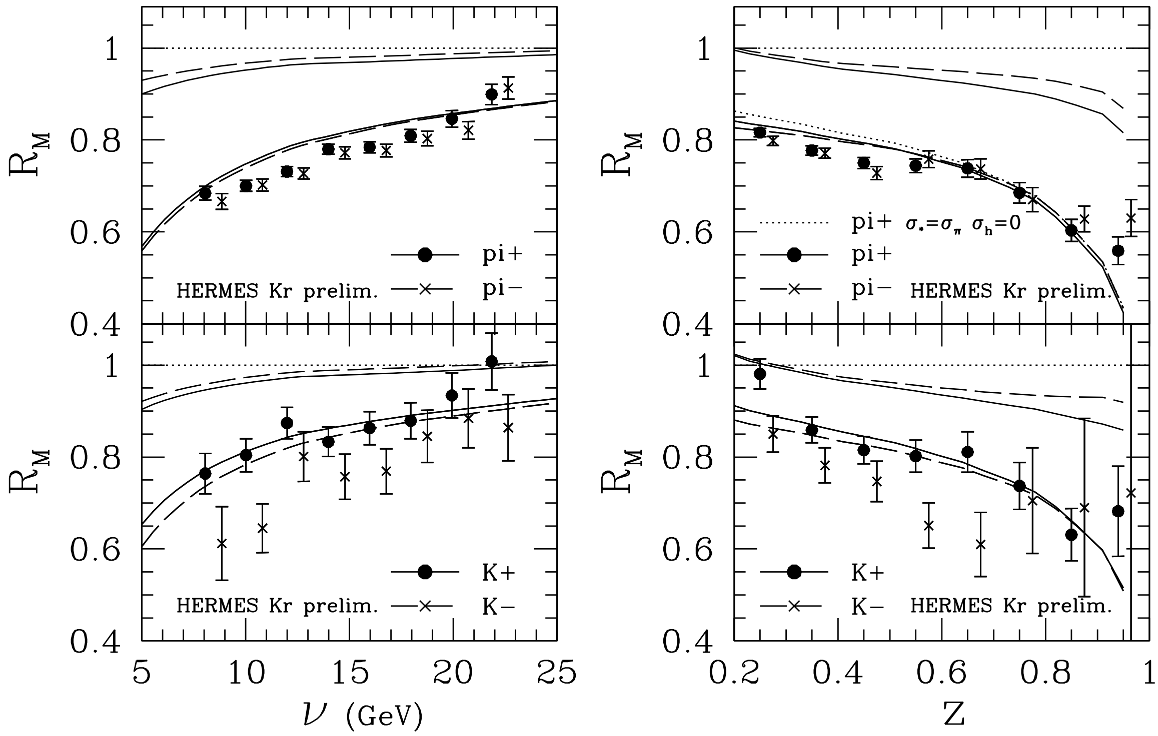

Figure 6.11: *Multiplicity ratio for identified pions and kaons produced on ^{84}Kr versus ν (left-hand panel) and z (right-hand panel) compared to the predictions of the rescaling model of Ref. [26]. In the upper pairs of curves the contribution of nuclear absorption in the model has been turned off.*

model of Ref. [24] is compared to the ^{84}Kr data in Fig. 6.12. While the equal attenuation of π^+ and π^- mesons is well described by the calculation, for K^+ and K^- mesons the model does not reproduce the difference implied by the data. This may indicate that either the flavor dependence implemented in the model is too weak, or that another mechanism has to be used to explain the difference between positive and negative kaons. Once more it is emphasized that also according to this model the attenuation is largely caused by nuclear absorption of an object interacting with the hadron-nucleon cross section. In this model, however, no distinction is made between the pre-hadronic and the hadronic state.

Gluon Bremsstrahlung model

In the left panel of Fig. 6.13 the multiplicity ratios for pions produced on ^{14}N and ^{84}Kr are shown separately. The pions were identified in the momentum range from 4 to 15 GeV using the HERMES RICH detector for the ^{84}Kr data and using a threshold Čerenkov detector for the older ^{14}N data. The data are compared to the gluon Bremsstrahlung model of Ref. [22], in which the main source of hadron attenuation is also hadronic rescattering (or nuclear

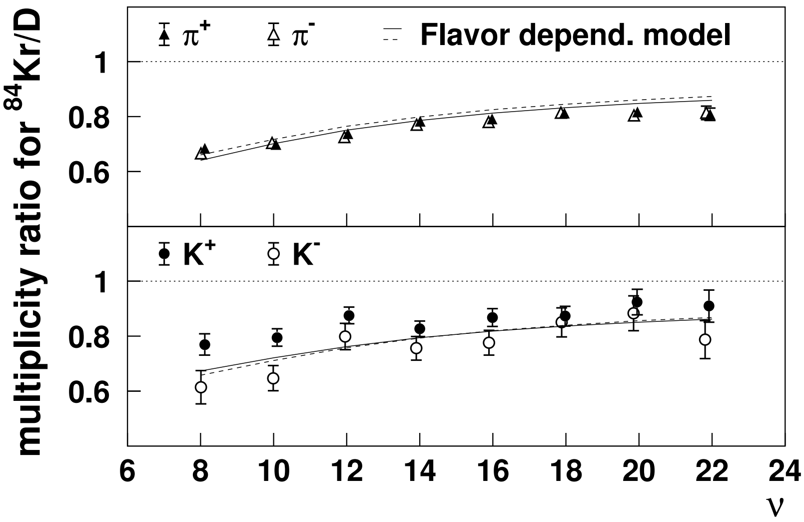

Figure 6.12: *Multiplicity ratio for identified pions and kaons in ^{84}Kr versus ν as compared to the predictions of the model of Ref. [24].*

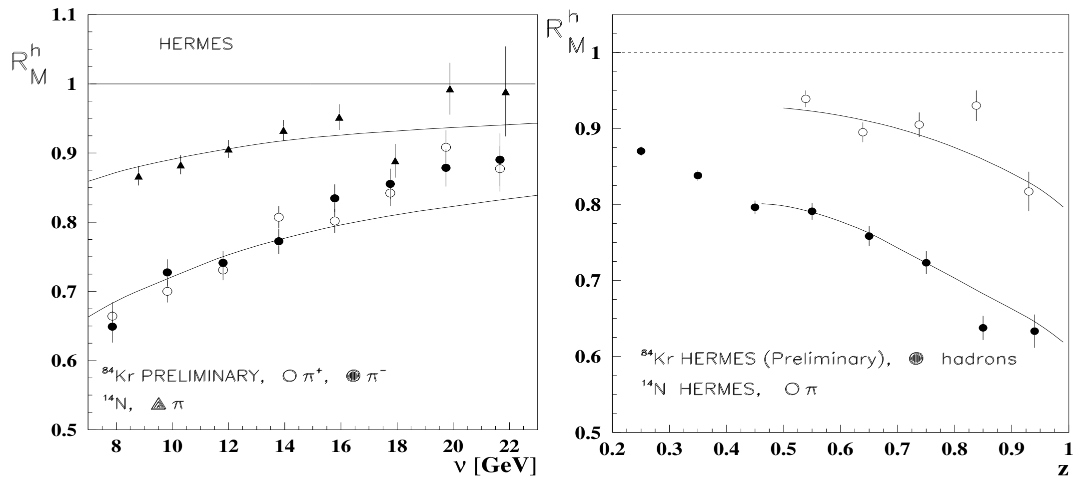

Figure 6.13: *Multiplicity ratio for identified pions (hadrons) versus ν and z for ^{14}N and ^{84}Kr targets. The curves represent the predictions of the gluon Bremsstrahlung model of Ref. [22].*

absorption) after the pion is formed, while the gluon Bremsstrahlung itself causes only a small attenuation. Calculations in this model are only available for leading pions and kaons, which restricts the comparison to $z > 0.5$. This may explain why the ν dependence is better described for low ν-values which correspond on average to higher z values. In the right panel of Fig. 6.13 the model calculation is compared to the z-dependence of $R^h_{\rm att}$ and seen to agree well with the data at high z. In fact, the calculation can be represented by a simple parameterization involving a single timescale expressed as $\tau_f = c_h\nu(1-z)$ similar to the one used in the previous section. The value of the proportionality constant c_h as obtained from the model calculation ($c_h = 1.35$ fm GeV^{-1}c^{-1} [29]) agrees well with the value of c_π derived from the fit to the HERMES data presented in the previous section. From the gluon Bremsstrahlung model of Ref. [22] also predictions for the attenuation of π^+ and K^+ mesons are available [29], which are presented in Fig. 6.14 together with the ^{84}Kr data. Also in this case the model shows a good agreement with the data confirming once more that the nuclear absorption description of hadron attenuation is adequate to account for the data.

Fragmentation function modification model

As opposed to the previously described models, the fragmentation function modification model [10] attributes the attenuation effect largely to partonic energy loss which is predicted to scale quadratically with the nuclear radius.

The results of the model calculation of Ref. [10] are compared to the charged-hadron multiplicity ratio $R^h_{\rm att}$ in Fig. 6.15 as a function of ν and z, for $\nu > 7$ GeV and $x > 0.06$. In the model calculations the attenuation ratio is expressed in terms of a ratio of modified fragmentation functions, where the modification arises from multiple parton scattering and induced gluon radiation. The ν and z dependence of the data is reproduced quite well by the model. Also, the observed attenuation of fast hadrons is considerably stronger for ^{84}Kr than for ^{14}N,

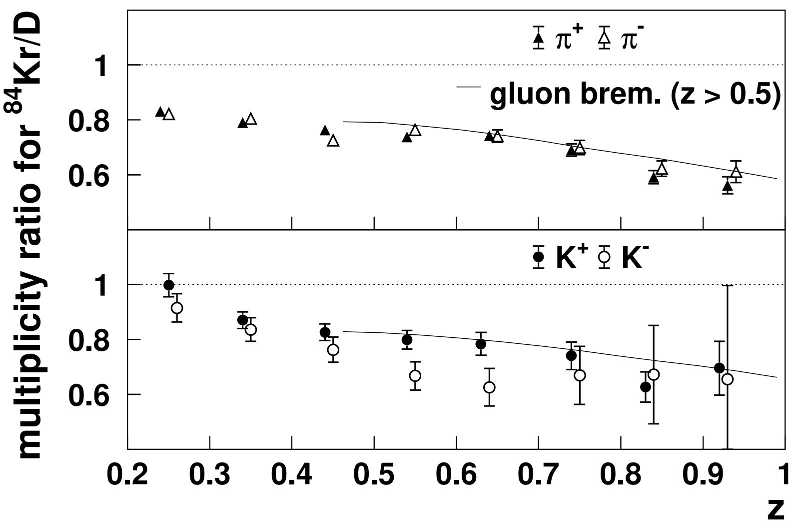

Figure 6.14: *Multiplicity ratio for identified pions and kaons in ^{84}Kr versus z as compared to the predictions of the gluon Bremsstrahlung model of Ref. [22].*

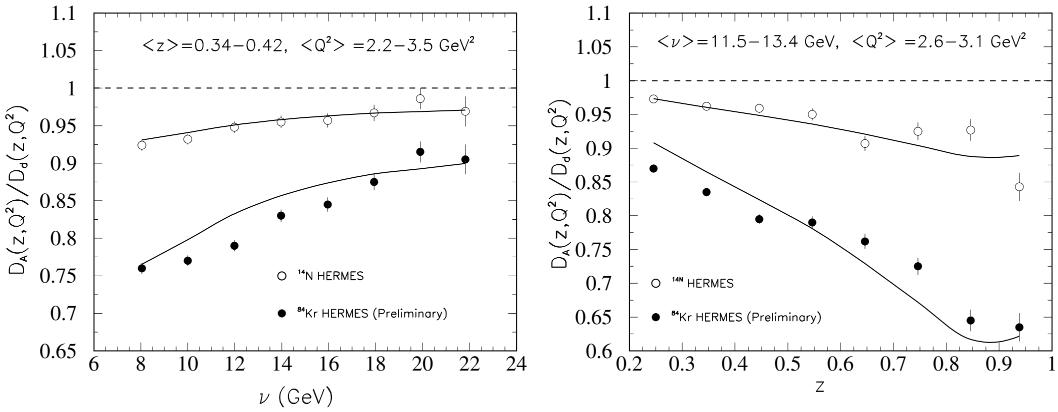

Figure 6.15: *Multiplicity ratio for charged hadrons versus ν and z for ^{14}N and ^{84}Kr targets. The curves are predictions of the fragmentation function modification model of Ref. [10].*

although it has to be noted that the prediction for ^{84}Kr at low and medium ν is systematically above the data. More details on the A-dependence of the data are given below.
In the context of this same model, the average parton energy loss in the nuclear medium was evaluated from the ^{14}N data [30]. The obtained value of $dE/dx \approx$ 0.3 GeV/fm for krypton ("cold" nuclear matter) can be compared to estimates of dE/dx for hot nuclear matter as extracted from recent PHENIX data [116] on relativistic heavy-ion Au-Au collisions. The average energy loss derived from the heavy-ion data (0.5 GeV/fm) needs to be corrected for the rapid expansion of the dense medium after the collision, which yields $(dE/dx)_0 \approx 7.3$ GeV/fm in a static medium [117]. This value is 15 times larger than that derived from the attenuation data in ^{14}N, and has been quoted as possible evidence for a gluon density at the early stages of the PHENIX Au-Au collisions which is 15 times higher than in cold nuclear matter.

After having seen the comparison of the various models to the data, a word of caution is appropriate. In Ref. [10] the entire hadron attenuation is attributed to gluon Bremsstrahlung and parton rescattering, while the effect of hadron rescattering is not included in the calculation. On the other hand, on the previous pages we have seen that nuclear absorption can also account for the attenuation observed in the data. This is demonstrated by the fits presented in section 6.5, and is also confirmed by the good agreement of calculations like that of the rescattering model and the gluon Bremsstrahlung model with the data (Fig. 6.11 and Fig. 6.13).
A possible way to distinguish between the partonic energy loss mechanism of Ref. [10] and the nuclear absorption processes proposed by others, is the study of the A-dependence of the attenuation. As was mentioned before and as explained in section 2.2.4, the LPM interference term in the fragmentation function modification model depends on $A^{2/3}$ [30]. On

the other hand, in models based on nuclear absorption the attenuation is proportional to the distance traversed in the nucleus, and therefore an $A^{1/3}$ dependence is expected. Hence, the extraction of the A-dependence of $R^h_{\rm att}$ from the data can offer a way to distinguish between the models.

6.6.1 A-dependence

The HERMES data for $R^h_{\rm att}$ on ^{14}N and ^{84}Kr offer the possibility to extract the A-dependence of nuclear attenuation effects in semi-inclusive deep-inelastic scattering. In order to investigate the actual A-dependence of the $R^h_{\rm att}$ data, it is assumed that the attenuation itself depends on an arbitrary power of A:

$$1 - R_{\rm att} \propto A^{\alpha}. \tag{6.10}$$

The parameter α can be obtained in each ν-bin[7] from the expression

$$\alpha = \ln\left(\frac{1 - R^{\rm N}_{\rm att}}{1 - R^{\rm Kr}_{\rm att}}\right) / \ln\left(\frac{14}{84}\right). \tag{6.11}$$

A set of values has been evaluated for the exponent α which are plotted in Fig. 6.16 as a function of ν for the available samples of positive and negative hadrons and pions. The data corresponding to ν = 20 and ν = 22 GeV are omitted from the positive hadron plot (top left plot in Fig. 6.16) since for these data the value of the nitrogen attenuation ratio $R^{\rm N}_{\rm att}$ is equal to 1, and therefore α is undefined. The systematic uncertainty, shown as a shaded area in Fig. 6.16, is obtained by moving the ^{14}N and ^{84}Kr points by their systematic uncertainty of 2.5% and 3.5%, respectively. Since the largest contribution to the systematic uncertainty is the same for both gases, i.e. radiative corrections and diffractive ρ_0 contamination, the data are moved up or down simultaneously. In the figure the values of α = 1, 2/3 and 1/3 (shown as dashed lines) indicate the three possible A-dependencies for medium effects: volume, surface and radial effects. It is emphasized that the values α = 2/3 and α = 1/3 correspond to the two values for the A-dependence suggested by the model calculations of Ref. [10] and Ref. [18, 19], respectively. The average values of α for the various particle types are reported in table 6.5 together with the average statistical and systematic errors.
The values of α obtained for charged pions and negative hadrons are in agreement with the value of 2/3 characteristic of the interference LPM term in the fragmentation function modification model. The data differ from the value of $1/3$ suggested by the nuclear absorption model by more than 2σ (3σ if only the pions are considered). This observation is in line with the conclusions derived from the one-timescale model fit with pre-hadronic interaction which led to different parameters for ^{84}Kr and ^{14}N. In both cases a nuclear absorption based model does not provide a consistent description of all available HERMES data.

[7] It has to be noted that the same calculation can equivalently be performed for the z-bins and the results for the obtained values of α are in very good agreement with the values presented in table 6.5.

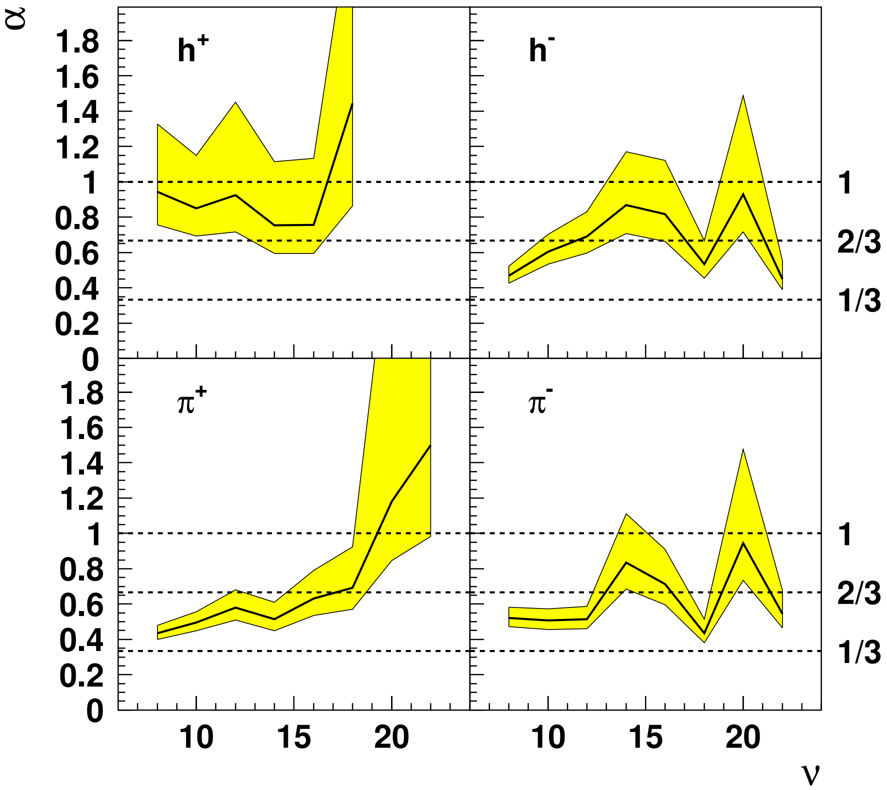

Figure 6.16: *Values of the exponent α versus ν for various particle types obtained using Eq. (6.11). The shaded area represents the systematic uncertainty on the value of α in each bin. The dashed lines indicate the values of α = 1, 2/3 and 1/3 for comparison.*

The values of α obtained for positive hadrons are above 2/3. As was already mentioned before the positive hadron sample has a strong contribution from protons. The corresponding attenuation ratio is shown to have a much steeper ν-dependence (see Fig. 6.4). The value for the parameter α extracted for the positive hadron sample can be simply due to a different contribution of protons in the hadron sample in ^{14}N as compared to ^{84}Kr, or alternatively it can be an indication that the proton A-dependence is stronger than that of pions.
Data collected on other nuclei after the installation of the RICH detector will enable to also determine the A-dependence of $R^h_{\rm att}$ for kaons and (anti)protons, separately.

	$< \alpha > \pm stat \pm sys$
h^+	$0.91 \pm 0.05\ ^{+0.47}_{-0.22}$
h^-	$0.68 \pm 0.06\ ^{+0.19}_{-0.11}$
π^+	$0.65 \pm 0.07\ ^{+0.28}_{-0.11}$
π^-	$0.63 \pm 0.08\ ^{+0.17}_{-0.09}$

Table 6.5: *Average value of the exponent α as extracted from the values reported in Fig. 6.16. The asymmetric systematic uncertainty is explained in the text.*

6.7 Concluding remarks

Semi-inclusive deep-inelastic scattering has been studied on ^{84}Kr and D nuclei so as to study the effect of the nuclear medium on the hadronization process. In these experiments the nuclear target acts as a filter to investigate processes at the femtometer length scale. From the hadron multiplicities measured on the two targets the attenuation ratio R^h_{att} is determined as a function of the kinematic variables ν and z. Using the HERMES RICH it was possible for the first time to obtain separated information on the attenuation of charged pions, kaons, protons and anti-protons.

Simple models can be used to describe the attenuation of the produced hadrons in terms of nuclear absorption. A value for the formation time constant for each hadron type has been determined in this framework, which however, was shown to be model dependent. Nevertheless, novel information can be extracted from this type of phenomenological fits, namely that the proton formation time is about twice as long as that of pions. More data on kaon attenuation and especially new data on other baryons (i.e. the Λ hyperon) are needed to confirm the observed difference between meson and baryon formation times.

The new hadron attenuation data on ^{84}Kr/D and the previously published data on ^{14}N/D are used to compare two different types of model calculations: the ones in which the hadron rescattering (nuclear absorption) is the dominant (if not the only) contribution to the hadron attenuation, and the one in which parton rescattering and gluon radiation account for the entire effect. Both these apparently contradicting approaches give an adequate description of the kinematic dependence of the attenuation ratio on both gas targets (^{14}N and ^{84}Kr). But when fitting the ^{84}Kr and ^{14}N multiplicity ratios with a one-timescale model, which also accounts for the pre-hadronic state interaction, different results are obtained for the string constant and string cross section on the two nuclei. This result suggests that nuclear absorption models cannot consistently reproduce the A-dependence of the data, while they do provide a reasonable description of the individual kinematic dependencies.

At this point same remarks are necessary concerning the various models. The phenomenological models only describe leading hadrons, i.e. with $z > 0.5$, therefore they cannot be compared to the HERMES data over the full kinematic range. The fragmentation function modification model can be used over a larger z range, but its prediction for ^{84}Kr is systematically higher than the data at mid and low ν values (see left-hand plot of Fig. 6.15). This fact may indicate that some nuclear absorption contribution is required to describe the hadron attenuation of heavy targets. The rescaling model supports this last statement, since it shows that in order to describe the attenuation of the ^{84}Kr data well, both nuclear absorption and some others process (parameterized by rescaling in this case) are required. It has to be noted, though, that the models are compared to the sum of positive and negative hadrons which need not have the same A-dependence.

The two types of models presented above have two distinct A-dependencies. In the phenomenological models in which nuclear absorption is dominant the hadron attenuation is expected to scale as $A^{1/3}$, while the parton rescattering interference with gluon radiation predicts a $A^{2/3}$ dependence. From the available ^{14}N and ^{84}Kr data the power α of the A^{α} dependence of the hadron attenuation is found to be consistent with $2/3$ for charged pions and negative hadrons, while it is even larger than $2/3$ for positive hadrons. The latter fact may be attributed to possible differences in the A-dependence of protons as compared to that of pions.

Unfortunately, the experimental results on the A-dependence of the attenuation ratios, which are crucial in order to make progress in this field, rely on only two targets at present and only provides information for pions. Data on several gas targets are required to better determine the power of α of the A-dependence. This may make it possible to rule out one approach as compared to the other, or may suggest that a combination of the two approaches is needed to describe the data. Data on ^{4}He and ^{20}Ne have already been collected at HERMES after the installation of the RICH detector and will soon be analyzed. Furthermore, HERMES has the possibility to collect data on ^{40}Ar and ^{131}Xe, which will extend the A coverage and thus provide for a better determination of α. The present analysis is performed on a sample of about one million DIS events, if the data will be collected on another nucleus it is desirable to increase the statistics by a factor of 5 at least, to be able to map the z dependence of various ν ranges.

Finally, the importance of understanding the nature of parton propagation and hadron formation in the nuclear environment is probably best illustrated with reference to the energy loss determinations of Wang et al. [116] based on the HERMES ^{14}N data. A possible role of nuclear absorption in addition to the fragmentation function modification used in this reference would influence the value of the parton energy loss extracted from the semi-inclusive deep-inelastic lepton scattering data. Fixing a precise value of ΔE for cold matter will serve as a reference for relativistic heavy-ion collision experiments aimed at discovering possible evidence for a new state of matter.

Chapter 7

The $f_0(980)$ scalar meson

Nu chilo d'annecchia, nu chilo e mmezzo 'e spezzatino, iammoncello, tracchia 'e locena, punt'e natica, pettola 'e spalla, due nervi, fianchetti e corazza.

Sofia Loren

7.1 Introduction

In this chapter the first observation of the $f_0(980)$ scalar meson in semi-inclusive deep-inelastic positron scattering is presented. Production of the $f_0(980)$ scalar meson is of particular interest because its precise nature has long been uncertain. In section 2.3 a brief survey is given of possible models of the $f_0(980)$ meson, and some recent experimental results are summarized.
The data sets presented in this chapter enable the study of the A-dependence of $f_0(980)$ electroproduction. It has been suggested by F. Close et al. [39] that the propagation of the $f_0(980)$ through the nuclear medium could be a sensitive tool to distinguish between various models for its structure. Moreover, the present studies make it possible to determine for the first time various kinematic dependencies of $f_0(980)$ electroproduction. It is hoped that these data will help to clarify the structure and production mechanism of this scalar meson.
As was already mentioned in section 2.3 the $f_0(980)$ scalar meson is accessible through its decay into two charged pions, $f_0(980) \to \pi^+\pi^-$. The $\pi^+\pi^-$ channel also gives access to the $\rho_0(770)$ and $f_2(1270)$ mesons, which are a background when identifying the $f_0(980)$ scalar meson.
The sets of data and kinematic restrictions used in this analysis are summarized in section 7.2. The method used to identify the $\rho_0(770)$, $f_0(980)$ and $f_2(1270)$ mesons in the $\pi^+\pi^-$ channel is described in section 7.3. Results are given at the end of this section leading to preliminary conclusions on the A-dependence of $f_0(980)$ electroproduction. In section 7.4 various kinematic dependencies of $f_0(980)$ and $f_2(1270)$ production (on hydrogen) are pre-

sented, and compared to Monte Carlo simulations. In section 7.5 the multiplicity distribution for $f_0(980)$ and $f_2(1270)$ electroproduction is evaluated. Finally, conclusions are drawn in section 7.6.

7.2 Event selection and kinematic restrictions

Data collected on a natural Kr target in the year 1999 and on ^{1}H, ^{2}H and ^{20}Ne targets in the year 2000 are used in this analysis. While for the year 1999 the μDST production 99b2 could be used, at the time of this analysis only the first calibrated production for the year 2000 (00b1) was available. The same data quality criteria have been applied as for the analyses described in the previous two chapters. A reconstructed DIS lepton is required in order to fix the kinematics of the event, therefore events are selected in which the DIS trigger (trigger 21) has fired. The kinematic constraints on the DIS lepton and the PID requirements on both the scattered lepton and the produced hadrons are the same as those described in sections 5.2 and 6.2.1. (As a reminder we mention the DIS cuts which have been applied to the data: $W^2 > 4$ GeV^2, $y < 0.85$, $E_{calo}(e^+) > 3.5$ GeV). However, no restriction has been imposed on Q^2 in order to enable a study of the Q^2-dependence of f_0 electroproduction over the largest possible range.
Apart from the positron track, the presence in the event of two identified pions and an additional track through the detector is required to reduce the exclusive ρ^0 background. The identification of the two pions is made with the RICH detector. Therefore, the pion momentum is restricted to $2.5 < P_\pi < 15$ GeV, (see section 6.2.1).
In addition it is required that the positron and each of the two pion tracks originate from the same vertex ($|z^i_{pos} - z^j_{pos}| < 2.5$ cm). This requirement reduces the combinatorial background.
The data collected in the year 1997 on ^{3}He and ^{14}N targets by the HERMES experiment have not been used in the present analysis as pion identification with the Čerenkov threshold detector used in 1997 covers a smaller momentum range and has a different efficiency than that obtained with the RICH detector (used from 1998 on). The data collected on these two targets are therefore omitted from this part of the analysis.

7.3 Identification of the $f_0(980)$ scalar meson

In order to identify the $f_0(980)$ scalar meson from the decay channel $f_0 \to \pi^+\pi^-$ the invariant mass of the two pion final state is reconstructed. The first surprising observation which triggered this analysis was the appearance of a small peak or shoulder in the $\pi^+\pi^-$ invariant mass spectrum. The position and width of the peak has been determined using a Breit-Wigner function to fit the resulting mass distribution. The expression for a Breit-Wigner

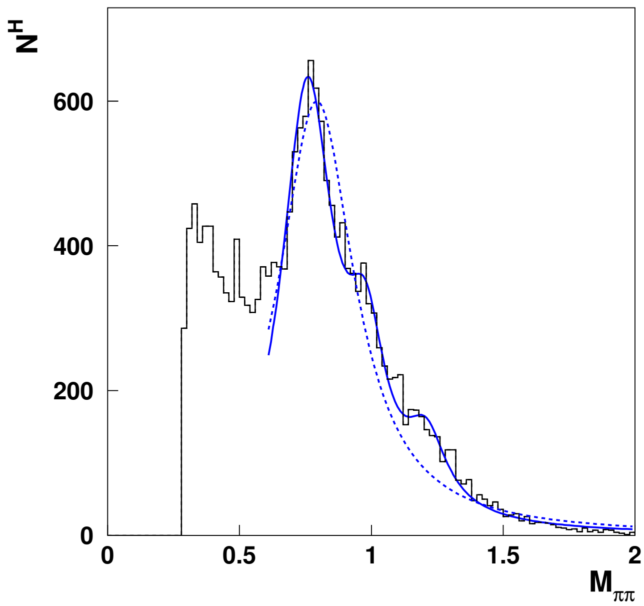

Figure 7.1: *Reconstructed $M_{\pi\pi}$ invariant mass spectrum derived from the hydrogen data sample, expressed as number of counts N^H. The number N^H is not normalized to the number of DIS events. The dashed line is a fit to the data using a single Breit-Wigner function, while the solid line represents a fit using the sum of 3 Breit-Wigner functions.*

representing a resonance a decaying into two pions is given by:

$$BW_a(M_{\pi\pi}) = h_a \frac{\Gamma_a}{2\pi[(M_{\pi\pi} - M_a)^2 + (\Gamma_a/2)^2]} \tag{7.1}$$

with h_a, Γ_a and M_a being respectively the height, width and mass of the resonance a, and the running variable $M_{\pi\pi}$ the two pion invariant mass. If more than one resonance appears in an invariant mass spectrum several Breit-Wigners have to be added.

7.3.1 The $M_{\pi\pi}$ distribution

The invariant mass of the $\pi^+\pi^-$ system has been evaluated in the kinematic region defined above for 4 different gas targets: ^{1}H, ^{2}H, ^{20}Ne and Kr. An example of a $M_{\pi^+\pi^-}$ spectrum is presented in Fig. 7.1, for the case of a hydrogen target. The ρ^0 peak is clearly visible at $M_{\pi^+\pi^-} \approx 0.8$ GeV, and in fact small shoulders are noticed at about 1 and 1.2 GeV. The dashed curve superimposed on the data shows that a fit with only one Breit-Wigner does not give a good description of the data in the region above 0.9 GeV, while a superposition

of three Breit-Wigner functions (solid line) yields a much better description of the invariant mass spectrum.
If no constraints are imposed, 9 parameters are needed to define three Breit-Wigner functions: the height, the position and the width of each resonance. A description of the $M_{\pi^+\pi^-}$ spectrum in terms of three Breit-Wigners serves the purpose of trying to obtain qualitative evidence supporting the observation of the $f_0(980)$ scalar meson. The results of such 9-parameter fits applied to each of the four gas targets show that for each target it is possible to identify the three peaks, $\rho^0(770)$, $f_0(980)$ and $f_2(1270)$, but the position of the resonances resulting from the fit appears to be shifted to lower values than indicated by the PDG for each of the three peaks. From the fits the mass of the ρ^0 meson is found between 0.757 GeV (in ^{1}H) and 0.731 GeV (in Kr). For the f_0 peak the centroid values range from 0.976 down to 0.923 GeV, and for the f_2 the fitted position goes from 1.213 GeV (in ^{1}H) to 1.186 GeV (in Kr). All these values have a statistical uncertainty of about 2-3% but a much higher systematic uncertainty as is discussed below. For comparison the positions and widths of each of the three states, as taken from the PDG [63], are listed below:

$$
\begin{aligned}
M_{\rho_0} &= 0.771 \pm 0.001 \ \text{GeV}, \quad \Gamma_{\rho_0} = 0.149 \pm 0.001 \ \text{GeV},\\
M_{f_0} &= 0.980 \pm 0.010 \ \text{GeV}, \quad \Gamma_{f_0} = 0.040 - 0.100 \ \text{GeV},\\
M_{f_2} &= 1.275 \pm 0.001 \ \text{GeV}, \quad \Gamma_{f_2} = 0.185 \pm 0.003 \ \text{GeV}.
\end{aligned}
$$

The f_0 peak position is in reasonable agreement with the PDG values for ^{1}H and ^{2}H, while for heavy nuclei some difference is observed. The f_2 peak positions, for ^{1}H and heavy nuclei, is found to have lower values in comparison to the PDG one. The differences are likely to be caused by the fact that the background at this stage has not yet been subtracted from the data. This may also explain why the fitted widths are found to be larger than those listed in the PDG. Hence, a background subtraction is required to properly extract information on the $f_0(980)$ position and width, which is the subject of the next subsection.

7.3.2 Background subtraction

In order to obtain an estimate of the DIS background contained in the $M_{\pi^+\pi^-}$ spectrum a set of semi-inclusive *Monte Carlo* (MC) events has been analyzed, which were previously produced with the LEPTO 6.5.1 event generator [118]. In the MC simulation the fragmentation parameters have been tuned such as to reproduce the hadron multiplicity distributions measured at HERMES [17]. In the MC the production of scalar and tensor mesons is turned off. The $M_{\pi\pi}$ MC spectrum is obtained by using the same kinematic restrictions as were applied in the f_0 search. In the MC spectrum the relative strength of ρ^0 and K_s mesons production does not match the data, as is illustrated in Fig. 7.2 in the case of a hydrogen target. This is likely due to the fact that in the MC only DIS events are simulated while in the data there are also events coming from other processes such as non-resonant $q\bar{q}$-production. A stronger cut on the missing mass like $M_x^2 > 25$ GeV^2 for instance, reduces the relative height of the ρ^0

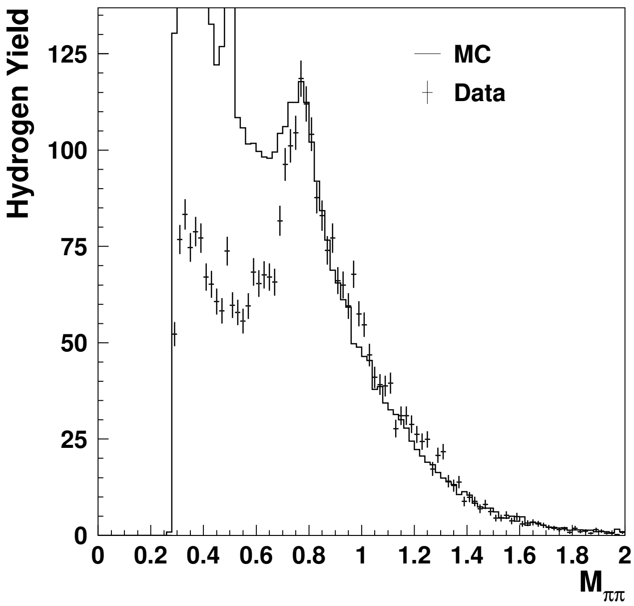

Figure 7.2: *$M_{\pi\pi}$ spectrum on a hydrogen target (data) compared to the MC generated background (histogram) normalized to the data at the ρ^0 peak.*

peak in the data with respect to the K_s one, yielding a good agreement between data and MC background in the whole invariant mass region. However, a strong M_x^2 cut would also reduce the f_0 yield without improving the signal to background ratio. Therefore, it was decided to normalize the background MC spectrum to the $\rho^0(770)$ peak, while disregarding the part of the spectrum below 0.7 GeV. As the K_s peak is very narrow, the overestimated K_s strength should not influence the generated $M_{\pi\pi}$ spectrum above 0.8 GeV.
Above the ρ^0 peak the MC generated spectrum describes the data fairly well, showing some evidence for remaining strength at the location of the $f_0(980)$ and possibly of the $f_2(1270)$ meson. The normalization of the MC is the largest source of uncertainty in the determination of the f_0 peak and needs to be optimized. A χ^2 minimization method is used to obtain the best normalization for each target gas presented in Fig. 7.3[1]. The method used is the following. A χ^2 parameter is defined by the difference between data and MC in the region above the ρ^0 peak (starting from $M_{\pi\pi}$ = 0.77 GeV). Two regions of the spectra with a width of Γ_{f_0} (or Γ_{f_2}) and centered around the fitted position of the f_0 and f_2 peaks (using the above mentioned 3 Breit Wigner's fit) are excluded from the definition of χ^2. The excluded regions are those bordered by the dotted lines in Fig. 7.3. The χ^2 is then minimized varying the normalization of the MC with respect to the data spectrum.

[1]The spectra presented in Fig. 7.3 and Fig. 7.5 are normalized to the total number of DIS events for the various data sample as it is described below.

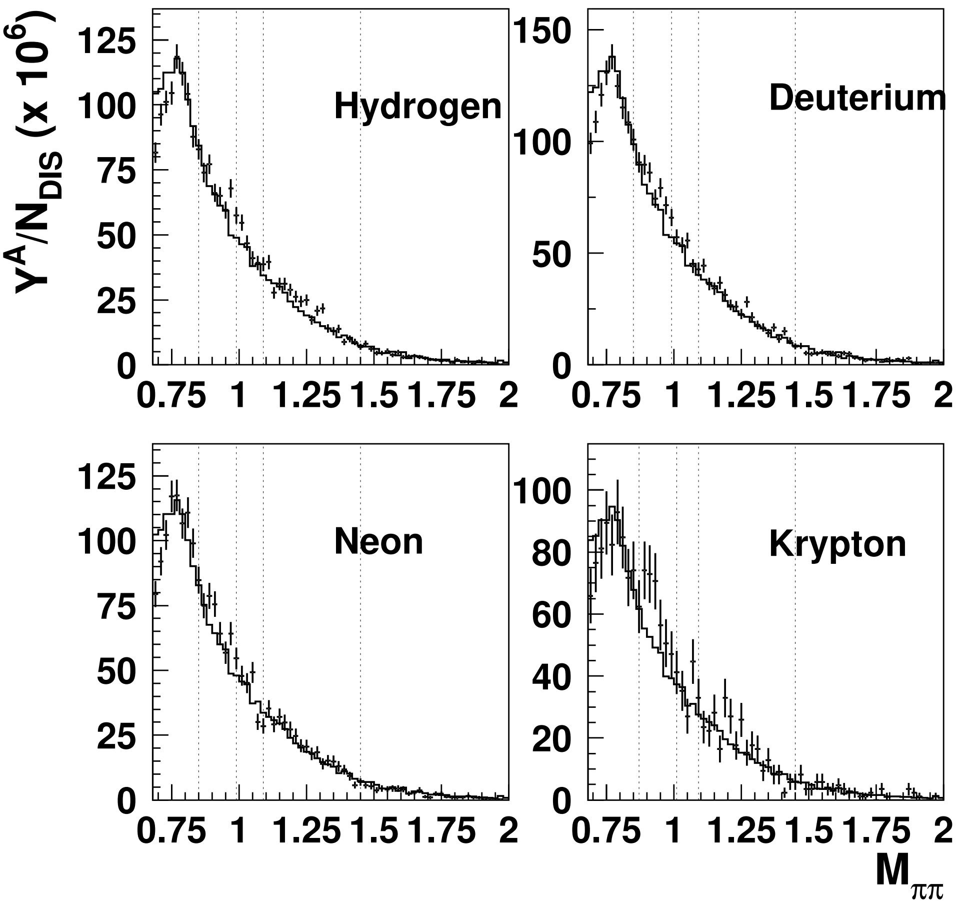

Figure 7.3: *Measured $M_{\pi\pi}$ spectrum for four gas targets (data) compared to the MC generated background (histogram) normalized to the data. The normalization is optimized in the region of the spectra outside the region identified by the dotted lines, which correspond to the one-Γ widths of the f_0 and f_2 mesons centered at the fitted position.*

The significance of the signal with respect to the background is defined, within the one Γ region of each peak, by the quantity $(Y_{\rm data} - Y_{\rm MC})/\sqrt{\Delta Y_{\rm data} + \Delta Y_{\rm MC}}$, where the denominator represents the one σ fluctuation of the signal, and $Y_{\rm data}$ and $Y_{\rm MC}$ represent the yield of data and MC histogram, respectively. The significance obtained for each gas target at the minimum χ^2 gives the number of σ's by which the signal can be separated from the normalized background. In Fig. 7.4 the minimization of the χ^2 is plotted as a function of the significance for the f_0 and f_2 peaks for each of the four gas targets. The vertical dotted line

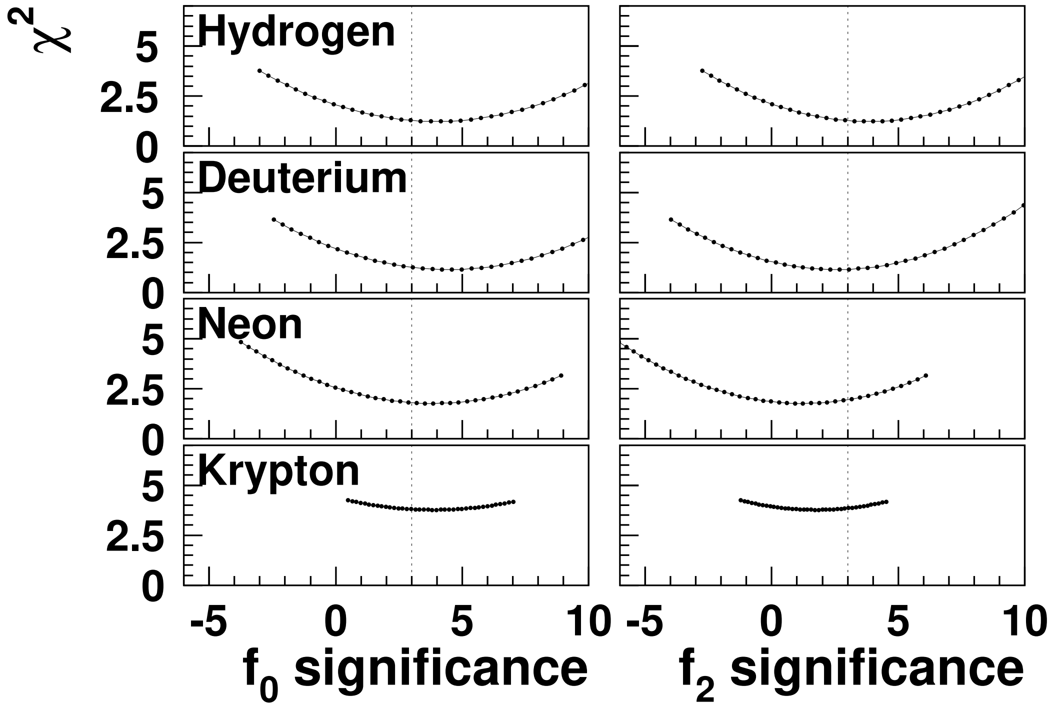

Figure 7.4: *Minimization of the χ^2 value measuring the difference between data and MC background versus the statistical significance of the f_0 (left) and f_2 (right) peaks on ^1H, ^2H, ^{20}Ne and Kr targets.*

at a significance of 3 sets the conventional lower limit for claiming an observation. A value below this line is considered to be below statistical significance. The best χ^2 for the normalization of the background to the data is found to be 1.2, 1.1, 1.8 and 3.7 respectively for ^{1}H, ^{2}H, ^{20}Ne and Kr. At these minima the corresponding significances of the f_0 peak are found to be 4.1, 4.5, 3.8 and 3.9, while the values for the f_2 significance are: 4.0, 2.6, 1.2 and 2.0, respectively. From these values it is concluded that the f_0 scalar meson is observed in each of the 4 data samples, while the f_2 tensor meson is observed with more than 3σ significance only on hydrogen with only hints of its presence in the other data samples.

When the properly normalized MC histogram is subtracted from the data, the remaining structure clearly indicates the presence of the f_0 peak in all targets, and possibly the f_2 peak on the lighter ones, as shown in Fig. 7.5. As explained above the subtracted spectrum is limited to $M_{\pi\pi} > 0.7$ GeV because of the bad reproduction of the data by the background MC below this value. The remaining spectra are fitted with a combination of two Breit-Wigner functions. Because of the limited statistics the widths of the two resonances are fixed to the central values obtained from the fit on ^{1}H: Γ^H_{f0} = 0.070±0.004 and Γ^H_{f2} = 0.185±0.030. In this way only 4 free parameters are left in the fitting function. The resulting values are re-

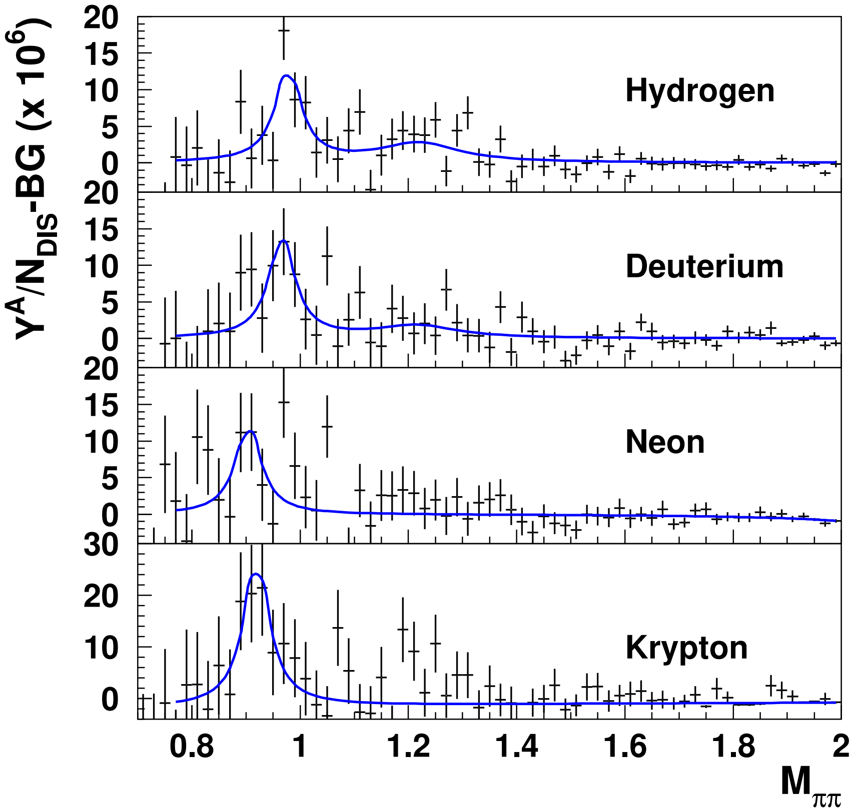

Figure 7.5: *Two pion invariant mass spectrum after background subtraction containing evidence for the production of the $f_0(980)$ and $f_2(1270)$ mesons. The data are described with a 4 parameter fit keeping the widths fixed.*

	^{1}H	^{2}H	^{20}Ne	^{84}Kr
h_{f0}	1.160 ±0.238	1.262 ±0.285	0.959 ±0.287	2.837 ±0.584
M_{f0}	0.978 ±0.014	0.965 ±0.020	0.973 ±0.020	0.919 ±0.020
h_{f2}	0.751 ±0.197	0.489 ±0.210	not found	not found
M_{f2}	1.219 ±0.046	1.215 ±0.100	not found	not found

Table 7.1: *Results of the 4 parameter fit to the $M_{\pi\pi}$ spectra, after subtraction of the MC generated background spectrum, for both the $f_0(980)$ and $f_2(1270)$ mesons.*

ported in table 7.1. The combination of two Breit-Wigner functions describes the data quite well (the χ^2's of the fits are between 1.0 and 1.5 for the 4 fits). In the ^{20}Ne and Kr samples the fitting procedure does not converge for the f_2 peak. In the ^{20}Ne case the reason is the low significance of only 1.5, while in the Kr case the fact that the fit does not converge might be related to the large χ^2 obtained from the minimization of the background normalization, i.e. 3.9.

In order to also compare the relative yields of $f_0(980)$ electroproduction in various gas targets, the mass spectra have been normalized to the total number of DIS events collected in the same set of runs (multiplied by 10^6) for each data sample before the fit is performed. The number of DIS events is corrected for radiative effects by a multiplicative correction calculated at the average x and y of each DIS sample ($< x > \approx 0.05$ and $< y > \approx 0.73$), for these average values the contribution of the photon shower correction (addressed in section

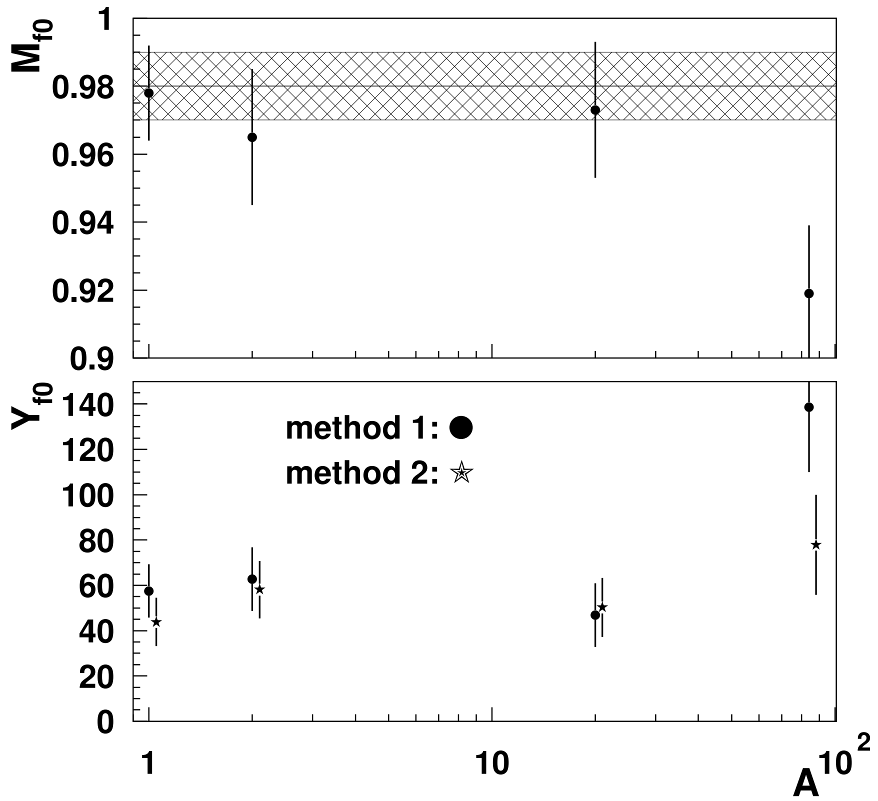

Figure 7.6: *Top: fitted mass values of the f_0 meson plotted as a function of the atomic number A. The hatched band represents the position and margin of uncertainty assigned to the f_0 scalar meson according to the PDG. Bottom: f_0 yields (normalized to the number of DIS events) on the 4 targets obtained with two different methods as discussed in the text.*

5.2.1) is negligible. Thereafter the integral of the Breit-Wigner has been evaluated using the position parameters given in table 7.1 and the f_0 width quoted before (this method is referred to as 'method 1').
The values of the f_0 peak position and f_0 yields found on the various targets are plotted as a function of the atomic number A in Fig. 7.6. The peak of the f_0 meson as observed on the various targets is in agreement with the PDG value represented by the hatched band in the top panel of Fig. 7.6. No significant A-dependence is observed within the available statistics neither in the peak position nor in the yield. Only the values found on the Kr target differ somewhat from the average over the other targets, but the discrepancies are only on the 2σ level.
It is not possible to study the A-dependence of the f_2 meson since a significant peak is not seen on heavier targets. It is noted however that the f_2 position as found on hydrogen is about 1σ below the value quoted in the PDG.
Theoretical calculations exist [119] predicting possible nuclear effects on meson masses, but up to now only few measurements are available to support these predictions. Especially, for scalar mesons there are at present no predictions for a possible A-dependence. As no significant A-dependence has been observed within the statistics of the present experiment no medium effect on the f_0 mass can be determined.
In Fig. 7.6 an alternative method to calculate the f_0 yield is also presented (labeled 'method 2') which does not involve the fitting of the resonances. In this case the MC background is subtracted from the two pion invariant mass spectrum for each gas target. From the remaining histogram the yield of f_0 and f_2 is obtained by counting the number of events in a one-Γ width range centered at the corresponding peak position as determined with method 1. This alternative method has the advantage that it does not require the integration of the fitted Breit-Wigner functions. It is therefore more directly related to the statistical significance of the observed peaks. In fact, the central value is obtained in method 2 as $(Y_{\text{data}} - Y_{\text{MC}})$ while the error is evaluated from $\sqrt{\Delta Y_{\text{data}} + \Delta Y_{\text{MC}}}$. As already mentioned the ratio of these two numbers is defined as the significance of the signal.
The values obtained with method 2 for the f_0 yields are in agreement with those obtained with method 1 within 30% for hydrogen, 8% for deuterium and neon and 70% for krypton. These percentages are used as an estimate of the systematic uncertainty on the f_0 yield. Method 2 will be used in the next section to study the kinematic dependence of f_0 and f_2 yields.
In conclusion, from the results presented on f_0 electroproduction for various gas targets no significant indication is found for a possible A-dependence of either mass or yield of the peak.

7.4 Kinematic dependencies

The hydrogen target offers both a high significance for the $f_0(980)$ meson and the evidence of the $f_2(1270)$ signal, therefore this data sample is chosen in order to study several kinematic dependencies of the yield. For these studies the invariant mass spectrum is evaluated for 3 ranges of a given kinematic variable while integrating over the other parameters. Four dependencies are addressed in this section: the dependencies on Q^2, z, P_t^2 and $-t$.
If the f_0 resonance is a conventional ${}^3P_0$ meson, its kinematic dependencies are expected to be similar to those of the nearby ρ^0 vector meson or the ${}^3P_2$ $q\bar{q}$-meson of similar mass, i.e. the $f_2(1270)$ tensor meson.
The f_0 (or f_2) yield is evaluated as the number of counts in the mass range 0.91 $< M_{\pi\pi} <$ 1.04 GeV (or 1.13 $< M_{\pi\pi} <$ 1.33 GeV, respectively) after subtraction of the normalized MC background, for each of the kinematic bins of interest. The applied procedure is illustrated in Fig. 7.7, where the $M_{\pi\pi}$ spectrum is divided in three different Q^2 regions. As for method 2 introduced previously the MC background spectrum (histogram) in each Q^2 bin is first normalized to the data excluding the regions in the vicinity of the f_0 and f_2 mesons. The normalized background is then subtracted from the signal (data). The yields obtained with this method in the three Q^2 bins are listed in table 7.2, together with the yield in the z, P_t^2 and $-t$ bins. The statistical errors are also listed in the table, which are evaluated as the sum of the absolute errors of signal and background counts.
Before discussing the yield dependence an acceptance correction needs to be evaluated to account for the limited angular acceptance of the HERMES spectrometer with respect to the entire solid angle. A Monte Carlo simulation is required to determine the relative number of particles produced outside the detector acceptance as compared to those generated inside the acceptance. This is the subject of the next subsection.

7.4.1 Monte Carlo simulation

For the simulation of f_0 photoproduction the PYTHIA [120] generator package as implemented in the HERMES MC is used. PYTHIA is a LUND-model based MC within which the f_0 is treated as a scalar meson composed of $u\bar{u}$ and $d\bar{d}$ pairs. The currently used version is PYTHIA 6.2. The MC parameters have been tuned to reproduce the pion multiplicity distributions observed at HERMES [17]. As compared to the normal HERMES Monte Carlo simulations, only the production of scalar and tensor mesons had to be turned on in order to compute an acceptance correction for f_0 and f_2 electroproduction in HERMES. The relevant parameters enabling the production in PYTHIA of scalar ${}^3P_0$ mesons (`PARJ(15)` = 0.08), and tensor ${}^3P_2$ mesons (`PARJ(17)` = 0.185) have been set according to the values given in Ref. [41]. The HERMES MC is used to generate events of the type $ep \to e\pi\pi X$ in 4π. Subsequently, the generated events are tracked through the detector geometry to obtain a sample of accepted events, thus enabling the evaluation of the required acceptance correction factor.

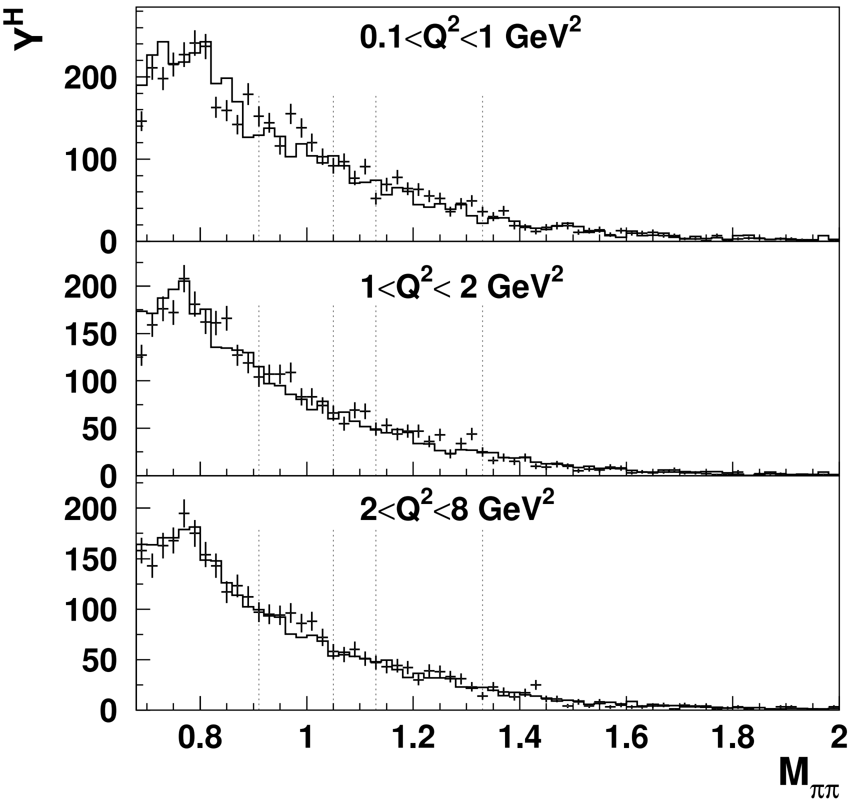

Figure 7.7: *Yield of two pion final state in three Q^2 bins. The background MC (histogram) is normalized to the data using the region outside the f_0 and f_2 peaks. The f_0 and f_2 yields are determined by subtracting the histogram from the data.*

The uncorrected yields for each kinematic bin have been normalized by the total number of f_0 (or f_2) events. In Fig. 7.8 and Fig. 7.9 these normalized yields are compared to the MC prediction for the distribution of accepted f_0 and f_2 mesons respectively. The MC gives a fairly good account of the yield for both mesons for all four kinematic dependencies. The Q^2 distributions are well reproduced, while the agreement of the P_t^2 distributions with the MC is in both cases less good. The z distribution of the f_0 meson shows a similar peak at medium z values as the data, but low-z and high-z bins are not correctly reproduced by the MC simulation. The dependencies for the f_2 production are slightly better reproduced, but this does not apply to the low P_t^2 bins. Hence, it is concluded that the production mechanism assumed by PYTHIA is sufficiently adequate to describe the production of both the $f_0(980)$ scalar meson and the $f_2(1270)$ tensor meson in the HERMES kinematics. Higher statistics data are needed to judge whether the observed deviations are significant.

Variable	Range	Y_{f0}	Y_{f2}
Q^2	[0.1 - 1]	100.8 ± 42.4	74.5 ± 32.3
	[1 - 2]	51.4 ± 31.7	61.1 ± 24.5
	[2 - 8]	57.6 ± 28.4	15.7 ± 21.3
z	[0 - 0.4]	61.8 ± 15.0	6.4 ± 6.2
	[0.4 - 0.6]	185.8± 48.7	68.9 ± 34.5
	[0.6 - 1]	0.0± 26.1	72.6 ± 25.9
P_t^2	[0 - 0.07]	148.4 ± 28.1	46.0 ± 20.9
	[0.07 - 0.17]	76.1 ± 27.7	34.6 ± 20.7
	[0.17 - 0.5]	46.8 ± 33.7	92.8 ± 26.9
$-t$	[0 - 0.15]	126.9 ± 28.4	54.3 ± 22.5
	[0.15 - 0.35]	57.8 ± 25.0	29.3 ± 19.0
	[0.35 - 1.0]	46.6 ± 35.4	77.1 ± 27.9

Table 7.2: *Number of counts obtained in electroproduction of $f_0(980)$ and $f_2(1270)$ mesons in different kinematic bins, as extracted from the $M_{\pi\pi}$ spectra after the subtraction of the MC background. The values are not normalized to the number of DIS events in the hydrogen sample.*

In the absence of a better MC for $f_0(980)$ production the present simulation is also used to extract the number of generated particles outside the HERMES acceptance to determine the -model dependent- acceptance corrections $\varepsilon^a_{\text{acc}}$:

$$\varepsilon^a_{\text{acc}}(x) = \frac{N^a_{\text{acc}}(x)}{N^a_{\text{gen}}(x)}, \quad x = (Q^2, z, P_t^2, -t) \quad \text{and} \quad a = (f_0, f_2). \tag{7.2}$$

The value of $\varepsilon^a_{\text{acc}}(x)$ has been evaluated separately for each x-bin, while integrating over the other variables. The normalized yields that are used in the next section to evaluate the multiplicity distributions, are corrected for detector acceptance effects by dividing the uncorrected yields by ε_{acc}.

7.5 Multiplicity Distributions

Dividing the acceptance corrected yields by the total number of DIS events recorded in the same data sample (which are corrected for radiative effects), the multiplicity distribution for the production of f_0 and f_2 mesons is evaluated

$$\mathcal{M}_a(x) = \frac{1}{\sigma_{\text{DIS}}}\frac{d\sigma_a}{dx} = \frac{1}{N_{\text{DIS}} \cdot \eta_{RC}}\frac{dN_a(x)}{dx}\frac{1}{\varepsilon^a_{\text{acc}}(x)}, \tag{7.3}$$

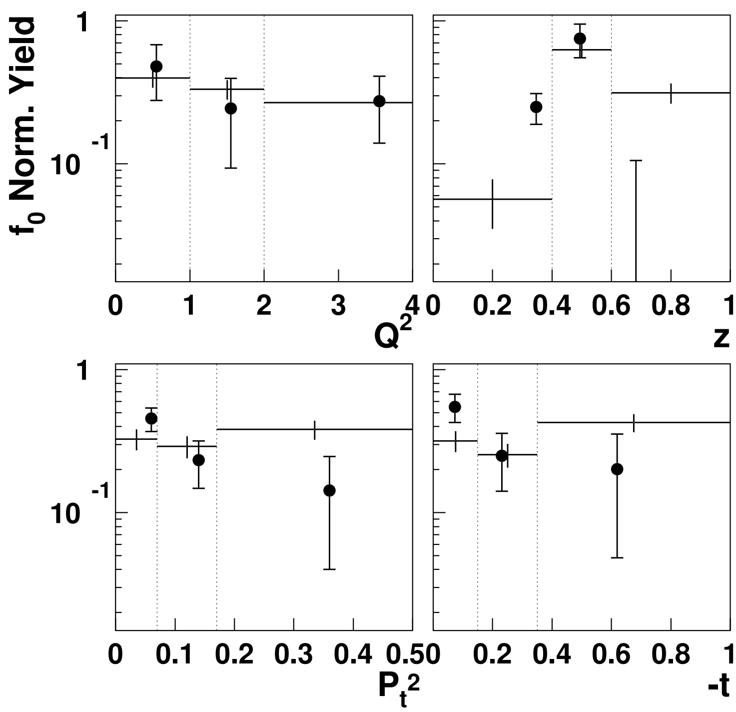

Figure 7.8: *Comparison of normalized f_0 yields to MC predictions for 4 different kinematic variables. The solid lines represent the MC predictions, while the data yields are represented by the closed symbols. The normalized yields only represent events accepted by the* HERMES *detector. No acceptance corrections have been applied.*

where $x = (Q^2, z, P_t^2, -t)$. The radiative correction factor η_{RC}, as calculated at the average values of x and y of the DIS sample is found to be 0.68. As discussed in the previous section the corrections for the photon shower effect is negligible at these values of $< x >$ and $< y >$. The acceptance correction $\varepsilon^a_{\rm acc}$ has been discussed in the previous section. Note that the multiplicity distribution is defined here with respect to the *total* number of DIS events, which is different from the definition used in chapter 6.
The resulting multiplicity distribution for f_0 electroproduction is shown in Fig. 7.10 as a function of the four kinematic variables Q^2, z, P_t^2 and $-t$. The errors bars are the sum in quadrature of the statistical error and the systematic uncertainty of 30% quoted in section 7.3.2.
The decrease of $\mathcal{M}_{f_0}(Q^2)$ with Q^2 is investigated to gain information on the f_0 production mechanism. If the f_0 is directly produced in a DIS process the Q^2-dependence of its multiplicity should be proportional to $1/Q^4$. On the other hand according to F. Close[2] the f_0 could

[2]private communication.

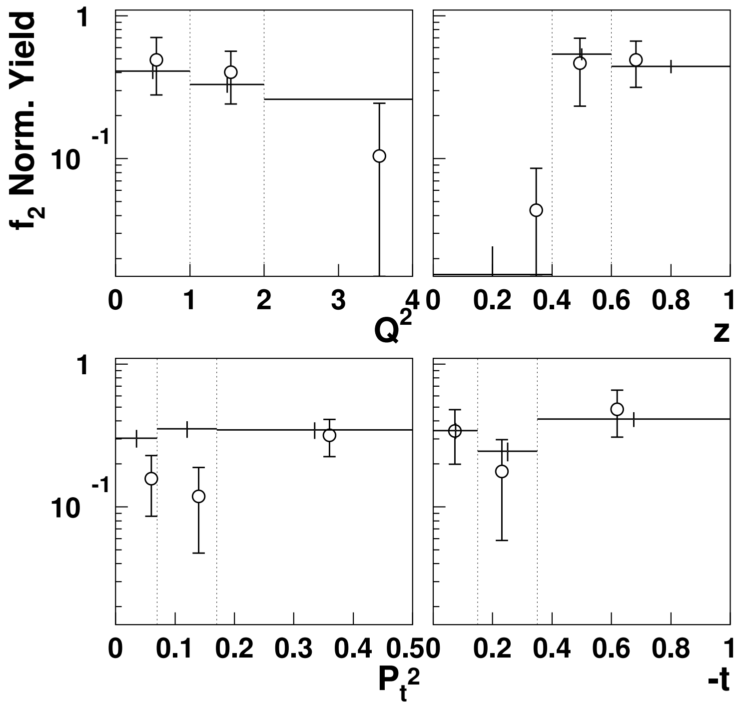

Figure 7.9: *Comparison of normalized f_2 yields to MC predictions for 4 different kinematic variables. The solid lines represent the MC predictions, while the data yields are represented by the open symbols. The normalized yields only represent events accepted by the* HERMES *detector. No acceptance corrections have been applied.*

also be a decay product of diffractive ρ' production, in which case the Q^2-dependence of its multiplicity should be described by the *Vector Meson Dominance* (VMD) model [121]:

$$\frac{d\sigma}{dQ^2} \propto \left(\frac{M_{\rho'}^2}{Q^2 + M_{\rho'}^2} \right)^{\alpha}, \tag{7.4}$$

with $\alpha = 2$. The solid line in the top left panel of Fig. 7.10 is the result of a fit in which α is used as a free parameter. The obtained parameter α is equal to (4.5 $\pm$ 1.5) which indicates that a VMD description of the f_0 production is not favored by the data. If instead the parameterization $\frac{d\sigma}{dQ^2} \propto \left(\frac{1}{Q^2}\right)^{\alpha}$ is used, the value of α obtained by fitting the data is (2.2 $\pm$ 0.5), which is in good agreement with $\alpha = 2$ expected for a DIS direct production mechanism.
The t-dependence is also investigated in order to verify the possibility that the f_0 is produced in the decay of a diffractively produced ρ'. If the $-t$ dependence of the multiplicity distribution is fitted with an exponential shape, the slope (or impact) parameter is found to be (5.5 $\pm$ 2.4) GeV^{-2}. This value is similar (within the large uncertainty) to the one quoted for

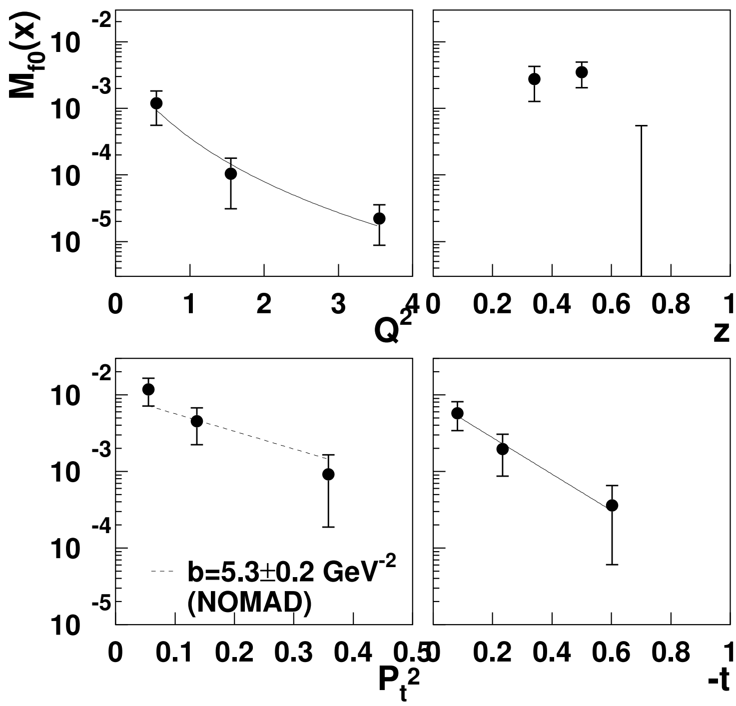

Figure 7.10: *Multiplicity distribution for f_0 production as a function of the variables Q^2, z, P_t^2 and $-t$, while integrating over the other kinematic variables. The errors bands are the sum in quadrature of statistical and systematic errors. The curves are described in the text.*

diffractive ρ^0 production (6.39 $\pm$ 0.13) [122]. The error bars are such large, however, that no clear conclusion can be drawn from the $-t$ dependence.
From the z dependence of the multiplicity distribution it is concluded that the data are sitting at low/medium-z, with a peak at $z \approx 0.5$, suggesting that it is likely that the f_0 is produced in combination with another meson of similar mass (e.g. the ϕ), each taking half of the virtual photon energy, as suggested in Ref. [42].
In the bottom left panel the P_t^2 dependence of the multiplicity distribution is described with an exponential function:

$$\frac{d\sigma}{dP_t^2} \propto C\, e^{-bP_t^2}, \tag{7.5}$$

where the slope parameter b is fixed to the value quoted by the NOMAD collaboration [41] for neutrino induced f_0 production at $P_t^2 < 0.5$ GeV^2, i.e. b = (5.3 $\pm$ 0.2) GeV^{-2}. The P_t^2 slope derived from the NOMAD data provides a good description of the HERMES data.
For comparison the multiplicity distributions for the $f_2(1270)$ production are presented in

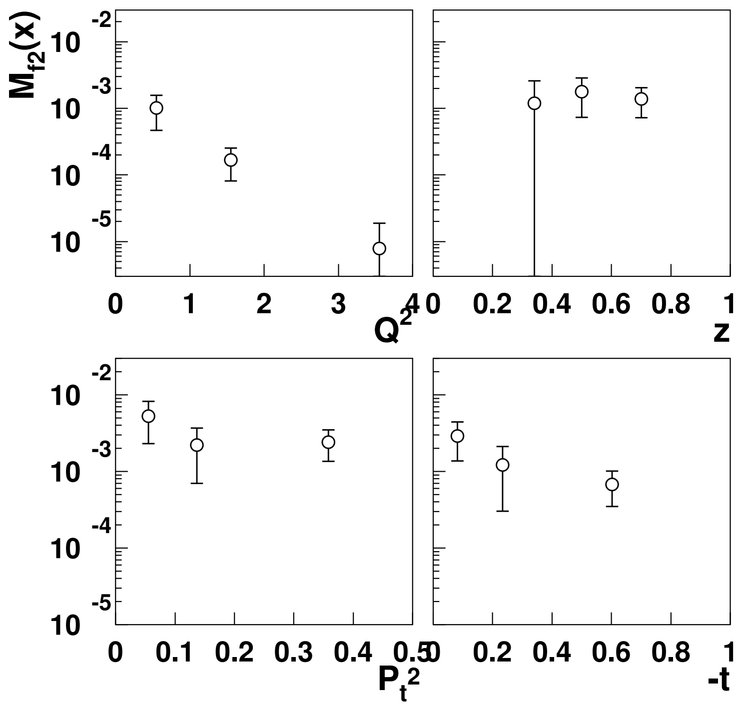

Figure 7.11: *Multiplicity distribution for f_2 production as a function of the variables Q^2, z, P_t^2 and $-t$, while integrating over the other kinematic variables. The errors bands are the sum in quadrature of statistical and systematic errors.*

Fig. 7.11, which are found to be similar to those for the f_0 scalar meson.
The values for the integrated multiplicities of f_0 scalar meson electroproduction are shown in table 7.3. Since all four values of $\mathcal{M}_{f_0}(x)$ in table 7.3 are obtained by integrating over the full data set, and thus cover the same kinematic range, the 4 results should be the same. Hence, the variation in the values obtained is an indication of the systematic uncertainty on the value of the multiplicity, which amounts to about 15%. However, the variation is smaller than the overall systematic uncertainty on the yield of 30%, which is considered to be the dominant source of systematic uncertainty.
The averaged values for the integrated multiplicities of the f_0 and f_2 mesons obtained in this analysis are shown in table 7.4 together with the multiplicities obtained by the NOMAD collaboration, which are also normalized to the total inclusive DIS rate. The values obtained by the OPAL collaboration, which are also listed in table 7.4, have to be taken with caution since the multiplicity in this case is normalized to the total hadronic yield.
From the results reported in table 7.4 it can be seen that there is a factor of 10 between the integrated multiplicity measured by the OPAL and NOMAD experiments and another factor

	f_0	f_0
$\mathcal{M}_{f_0}(Q^2)$	0.0014 ± 0.0003	0.0012 ± 0.0003
$\mathcal{M}_{f_0}(z)$	0.0018 ± 0.0004	0.0014 ± 0.0003
$\mathcal{M}_{f_0}(P_t^2)$	0.0016 ± 0.0003	0.0014 ± 0.0002
$\mathcal{M}_{f_0}(t)$	0.0015 ± 0.0002	0.0011 ± 0.0001

Table 7.3: *Values of the integrated multiplicity of f_0 and f_2 electroproduction obtained by integrating over the entire kinematic range covered by the data. The errors are statistical only.*

	HERMES (e^+)	NOMAD (ν)	OPAL (e^+e^-)
$\mathcal{M}_{f_0}$	0.0016 ± 0.0006	0.018 ± 0.004	0.141 ± 0.007
$\mathcal{M}_{f_2}$	0.0013 ± 0.0005	0.038 ± 0.009	0.155 ± 0.011

Table 7.4: *Values of the integrated multiplicity of f_0 and f_2 production as extracted from the present analysis, and the NOMAD [41] and OPAL [40] experiments. The OPAL multiplicity is normalized to the total hadronic yield, while the HERMES and NOMAD multiplicities are normalized to the DIS yield.*

of 10 between NOMAD and HERMES. These differences may be related to the difference in the center-of-mass energies in the three experiments: about 6 GeV at HERMES, 7-10 GeV at NOMAD and 91 GeV at OPAL. The multiplicities for both f_0 and f_2 productions are shown to increase with the center-of-mass energy in a similar way.

7.6 Concluding remarks

In this chapter the first experimental evidence for the production of the $f_0(980)$ scalar meson in a deep-inelastic positron scattering experiment is presented. A resonance with a mass of 0.978 ± 0.014 GeV and a width of 0.070 ± 0.004 GeV is observed, after background subtraction, in the $\pi^+\pi^-$ invariant mass spectrum on a hydrogen target with a significance of 4.1σ. These numbers are in good agreement with those quoted in the PDG. The presence of the same resonance is confirmed on ^{2}H, ^{20}Ne and Kr targets each with a statistical significances above 3σ. The mass position is found to be in agreement among the targets, with the exception of a 2σ shift to lower mass in krypton.
Together with the $f_0(980)$ also the $f_2(1270)$ meson is identified on the hydrogen target with a significance of 4.0σ, with a mass position that is somewhat lower than that quoted in the PDG.

From the comparison of the $f_0(980)$ yield on various targets with different A, no indication is found for a possible attenuation of the produced number of f_0 scalar mesons in heavier gases as compared to lighter ones. Such an attenuation could have been as evidence supporting the proposed $K\bar{K}$-molecule structure of the $f_0(980)$, as suggested in Ref. [39].
The dependence on Q^2, z, P_t^2 and $-t$ of the f_0 and f_2 electroproduction yields has been studied on a hydrogen target and compared to a LUND-model based MC simulation. The MC describes most of the kinematic dependencies fairly well, with slight deviations at high P_t^2 and $-t$ for the f_0 meson, and at low P_t^2 for the f_2 meson. This can be an indication that this type of MC simulation is not fully adequately tuned to describe f_0 and f_2 production in the HERMES kinematic region. However, the MC simulation results are sufficiently adequate to evaluate an acceptance correction for each kinematic bin. In this way multiplicity distributions are obtained with the aim of gaining additional information on the $f_0(980)$ production mechanism. Therefore, a set of model dependent acceptance efficiencies has been calculated for each kinematic dependence. The yields have been corrected, and normalized by the total DIS yield to obtain the multiplicity distributions.
The Q^2 dependence of the f_0 multiplicity distribution suggests a similar fall-off with Q^2 as for DIS direct production mechanism. The z dependence is peaked at $< z > \approx 0.5$, suggesting that the f_0 is likely to be produced in semi-inclusive reactions together with a meson of similar mass. The dependence on the transverse momentum square P_t^2 was parameterized with an exponential function for which the slope parameter was fixed to the value found from the measurements of the NOMAD collaboration. The curve obtained in this way agrees with the P_t^2 dependence of the present data. The dependence on the momentum transfer $-t$ has a similar slope parameter as for diffractive ρ^0 production.
The integrated multiplicities for f_0 and f_2 production as obtained from this analysis are compared to similar values derived from the NOMAD experiment and also to the values of the OPAL experiment. A strong increase of the multiplicity with the center-of-mass energy of the production process is observed.
It is concluded that the $f_0(980)$ scalar meson is observed for the first time in electroproduction at a relatively low center-of-mass energy on various nuclear targets. The study of the A-dependence of the $f_0(980)$ meson does not seem to favor a structure different from a normal $^3P_0$ $q\bar{q}$-meson. Also the study of kinematic dependencies of the $f_0(980)$ production are in agreement with the standard description of this meson as a $q\bar{q}$-object. However, no MC simulations are available for leptoproduction of $f_0(980)$ scalar mesons in the framework of a $qq\bar{q}\bar{q}$ hybrid model, for instance. In the absence of such calculations it is difficult to draw firm conclusions. Moreover, higher statistics are needed to put the conclusions reached on the basis of the present data on a firmer footing.

Appendix A

Extraction of inclusive cross section ratio

In this appendix the details of the extraction of the cross section ratio $\sigma_{\rm A}/\sigma_{\rm D}$ are given, in the particular case of the analysis presented in chapter 5.
Because of the detector misalignment the top and bottom detector halves are treated independently. Two measurements are therefore extracted from the two detectors and need to be combined as independent measurements of the same quantity. For each detector half the measured cross section is evaluated from the yields in gas A and D as:

$$R^{\rm top(bot)} = \left(\frac{\sigma_{\rm A}}{\sigma_{\rm D}}\right)^{\rm top(bot)}_{\rm meas} = \frac{Y_{\rm A}\cdot L^{\rm A}_{acc}}{Y_{\rm D}\cdot L^{\rm D}_{acc}} \tag{A.1}$$

where $Y = \frac{N}{L\cdot l\cdot t}$ (N= number of DIS events, L= luminosity, l= detector live time, t= burst length). L_{acc} is the luminosity monitor acceptance correction calculated to be $L^{\rm Kr}_{acc}$=1.01759 and unity for the other gases.
From the two measurements the weighted mean is extracted according to [63]

$$R_{\rm wgtm} = \left[\frac{R^{\rm top}}{(\delta R^{\rm top})^2} + \frac{R^{\rm bot}}{(\delta R^{\rm bot})^2}\right]\cdot\left[\left(\frac{1}{\delta R^{\rm top}}\right)^2 + \left(\frac{1}{\delta R^{\rm bot}}\right)^2\right]^{-1}, \tag{A.2}$$

$$\delta R_{\rm wgtm} = \left[\left(\frac{1}{\delta R^{\rm top}}\right)^2 + \left(\frac{1}{\delta R^{\rm bot}}\right)^2\right]^{-1/2}. \tag{A.3}$$

For each measurement the χ^2 is given by:

$$\chi^2 = \left(\frac{R_{\rm wgtm} - R^{\rm top}}{\delta R^{\rm top}}\right)^2 + \left(\frac{R_{\rm wgtm} - R^{\rm bot}}{\delta R^{\rm bot}}\right)^2, \tag{A.4}$$

The values of the χ^2 range between 9 and 0.7. Following the method suggested in [63] when averaging independent measurements of the same quantity, if the χ^2 is below or equal to 1 the averaged result is accepted. If the χ^2 is greater than 1, but not too large to motivate the rejection of the result, the average is accepted but the statistical error on is enlarged by a scale factor. In the present case the statistical error on measured cross section as obtained in Eq. (A.3) is enlarged by the square root of the χ^2 calculated from the difference of the top and bottom measurements from the weighted mean (Eq. (A.4)),

$$\delta R'_{\mathrm{wgtm}} = \delta R_{\mathrm{wgtm}} \cdot \sqrt{\chi^2}. \tag{A.5}$$

To obtain the Born cross section ratio the measured ratio, as given by Eq. (A.2), needs to be corrected for radiative corrections and detector efficiencies according to Eq. (5.6), which for clarity can be rewritten specifying all terms:

$$\left(\frac{\sigma_{\mathrm{A}}}{\sigma_{\mathrm{D}}}\right)_{\mathrm{Born}} = \frac{R_{\mathrm{wgtm}}}{\xi^{\mathrm{A}}_{\mathrm{Born}}} \quad [\xi^{\mathrm{D}}_{\mathrm{Born}} + \frac{\xi^{\mathrm{D}}_{\mathrm{elas}}\sigma^{\mathrm{D}}_{\mathrm{elas}} + \xi^{\mathrm{D}}_{\mathrm{qela}}\sigma^{\mathrm{D}}_{\mathrm{qela}} + \xi^{\mathrm{D}}_{\mathrm{inel}}\sigma^{\mathrm{D}}_{\mathrm{inel}}}{\sigma^{\mathrm{D}}_{\mathrm{Born}}} - \frac{\xi^{\mathrm{A}}_{\mathrm{elas}}\sigma^{\mathrm{A}}_{\mathrm{elas}} + \xi^{\mathrm{A}}_{\mathrm{qela}}\sigma^{\mathrm{A}}_{\mathrm{qela}} + \xi^{\mathrm{A}}_{\mathrm{inel}}\sigma^{\mathrm{A}}_{\mathrm{inel}}}{R_{\mathrm{wgtm}}\ \sigma^{\mathrm{D}}_{\mathrm{Born}}}] \tag{A.6}$$

The determination of the reconstruction efficiencies ξ is discussed in section 5.2.1. Note that Eq. (A.6) does not require the absolute knowledge of any efficiency ξ but only of ratios of efficiencies for which some acceptance effects cancel. The radiative corrections contributions are obtained with the TERAD code [81, 82, 83] as described in section 5.2.2[1].
For all targets, the contribution from the radiation of 2 (hard) photons, the so-called α^2 contribution is applied, i.e. each term of the radiative correction is multiplied by a factor[2] f_α. As we do NOT know the reconstruction efficiencies for events with two hard radiated photons (these contributions are not included in the present Monte Carlo simulation), the efficiency do not account for these type of processes. This may not be totally correct but seems to be the best treatment of these contributions.
In the ^{84}Kr case $\sigma^{\mathrm{Kr}}_{\mathrm{elas}}$ has been corrected for processes in which more than one (soft) photon is exchanged with the nucleus. This multi-gamma correction reduces the elastic background

$$\sigma'_{\mathrm{elas}} = \sigma_{\mathrm{elas}}\,(1 - \mu_\gamma), \tag{A.7}$$

with $\mu_\gamma \simeq 0.05 - 0.10$ in the x range $0.01 < x < 0.09$ and zero for larger x.
The statistical error on the Born cross section is obtained by calculating the partial derivatives of Eq. (A.6) with respect to R_{wgtm} and the 8 efficiencies $\xi^{A(D)}_{\mathrm{Born}}, \xi^{A(D)}_{\mathrm{elas}}, \xi^{A(D)}_{\mathrm{qela}}$ and $\xi^{A(D)}_{\mathrm{inel}}$,

[1] In terms of "TERAD language":

$$\begin{aligned} \sigma_{\mathrm{Born}} &= sig1g, \\ \sigma_{\mathrm{elas}} &= ctail \cdot f_\alpha \cdot sig1g/100, \\ \sigma_{\mathrm{qela}} &= qtail \cdot f_\alpha \cdot sig1g/100, \\ \sigma_{\mathrm{\ inel}} &= contin \cdot f_\alpha \cdot sig1g/100. \end{aligned}$$

[2]

$$f_\alpha = \left(1 + \frac{\alpha^2}{qtail + ctail + contin}\right).$$

$$\delta\left(\frac{\sigma_{\rm A}}{\sigma_{\rm D}}\right)_{\rm Born} = (\frac{1}{\epsilon^{\rm A}_{\rm Born}})^2 \times (
$$

$$
\begin{aligned}
&(\xi^{\rm D}_{\rm Born} + \xi^{\rm D}_{\rm elas}\sigma^{\rm D}_{\rm elas}/\sigma^{\rm D}_{\rm Born} + \xi^{\rm D}_{\rm qela}\sigma^{\rm D}_{\rm qela}/\sigma^{\rm D}_{\rm Born} + \xi^{\rm D}_{\rm inel}\sigma^{\rm D}_{\rm inel}/\sigma^{\rm D}_{\rm Born})^2(\delta R'_{\rm wgtm})^2\\
&+R^2_{\rm wgtm}(\delta\xi^{\rm D}_{\rm Born})^2\\
&+(\frac{\sigma^{\rm A}_{\rm Born}}{\sigma^{\rm D}_{\rm Born}})^2(\delta\xi^{\rm A}_{\rm Born})^2\\
&+(\frac{R_{\rm wgtm}}{\sigma^{\rm D}_{\rm Born}})^2\left((\sigma^{\rm D}_{\rm elas}\;\delta\xi^{\rm D}_{\rm elas})^2 + (\sigma^{\rm D}_{\rm qela}\;\delta\xi^{\rm D}_{\rm qela})^2 + (\sigma^{\rm D}_{\rm inel}\;\delta\xi^{\rm D}_{\rm inel})^2\right)\\
&+(\frac{1}{\sigma^{\rm D}_{\rm Born}})^2\left((\sigma^{\rm A}_{\rm elas}\;\delta\xi^{\rm A}_{\rm elas})^2 + (\sigma^{\rm A}_{\rm qela}\;\delta\xi^{\rm A}_{\rm qela})^2 + (\sigma^{\rm A}_{\rm inel}\;\delta\xi^{\rm A}_{\rm inel})^2\right)\\
&\qquad\qquad\qquad\qquad\qquad\qquad\qquad\qquad).
\end{aligned} \tag{A.8}
$$

Finally the extracted $\sigma_{\rm A}/\sigma_{\rm D}$ in (x, Q^2) bins is bin centered to the NMC x value for each x bin (see for instance Fig. 5.12) with a multiplicative factor which also enlarges the statistical error,

$$\left(\frac{\sigma_{\rm A}}{\sigma_{\rm D}}\right)^{\rm bc}_{\rm Born} = \left(\frac{\sigma_{\rm A}}{\sigma_{\rm D}}\right)_{\rm Born} \cdot \frac{R_{\sf NMC}}{R_{\rm fit}}, \tag{A.9}$$

$$\delta\left(\frac{\sigma_{\rm A}}{\sigma_{\rm D}}\right)^{\rm bc}_{\rm Born} = \delta\left(\frac{\sigma_{\rm A}}{\sigma_{\rm D}}\right)_{\rm Born} \cdot \frac{R_{\sf NMC}}{R_{\rm fit}}, \tag{A.10}$$

where $R_{\sf NMC}$ is the value of the parameterization of the NMC data for ^{12}C/D and ^{119}Sn/D calculated at the NMC x and $R_{\rm fit}$ is the value of the same parameterization extracted at the HERMES x for each point. The two parameterizations taken for ^{119}Sn/D and ^{12}C/D respectively are:

^{119}Sn/D: $\quad 0.9697 - 1.433\,x - 0.334\,e^{-54.53\,x} + 1.074\,x^{0.711},$

^{12}C/D: $\quad 0.925 - 0.398\,x - 0.099\,e^{-28.06\,x} + 0.256\,x^{0.246}.$

Appendix B

Tables

In this Appendix the results are listed of the inclusive cross section ratios for ^{3}He, ^{14}N and ^{84}Kr, and of the ratios R_A/R_D, which are obtained according to the analysis described in chapter 5. More complete tables for (x,Q^2) bins can be found in:
http://www.nikhef.nl/∼erikag/Analysis/inclusive.html.

$< x >$	$< Q^2 >$	$\sigma_{\mathrm{Kr}}/\sigma_{\mathrm{D}}$	stat	sys
0.013	0.498	0.829	0.016	0.060
0.018	0.660	0.850	0.020	0.066
0.025	0.872	0.876	0.012	0.039
0.035	1.124	0.937	0.008	0.027
0.045	1.341	0.942	0.009	0.017
0.055	1.527	0.969	0.010	0.018
0.070	1.758	0.989	0.007	0.012
0.090	2.016	1.032	0.009	0.013
0.125	2.342	1.036	0.004	0.015
0.175	2.704	1.040	0.005	0.015
0.250	3.100	1.014	0.004	0.010
0.350	4.138	0.966	0.006	0.017

Table B.1: *Extracted values for $\sigma_{\mathrm{Kr}}/\sigma_{\mathrm{D}}$ in 12 x bins. The 4th column reppresents the relative statistical error while in the 5th is culomn the systematic uncertainty for each point is listed.*

$< x >$	$< Q^2 >$	$\sigma_{\mathrm{N}}/\sigma_{\mathrm{D}}$	stat	sys
0.013	0.497	0.918	0.010	0.032
0.018	0.659	0.930	0.010	0.032
0.025	0.871	0.947	0.007	0.019
0.035	1.123	0.967	0.008	0.021
0.045	1.338	0.978	0.008	0.016
0.055	1.525	0.994	0.008	0.016
0.070	1.753	1.006	0.006	0.013
0.090	2.010	1.018	0.007	0.014
0.125	2.324	1.023	0.003	0.011
0.175	2.674	1.023	0.003	0.012
0.250	3.072	1.010	0.003	0.011
0.350	4.130	0.978	0.004	0.009

Table B.2: *Extracted values for $\sigma_{\mathrm{N}}/\sigma_{\mathrm{D}}$ in 12 x bins. The 4th column reppresents the relative statistical error while in the 5th is culomn the systematic uncertainty for each point is listed.*

$< x >$	$< Q^2 >$	$\sigma_{\mathrm{He}}/\sigma_{\mathrm{D}}$	stat	sys
0.013	0.770	0.910	0.014	0.018
0.018	1.300	0.962	0.012	0.018
0.025	1.800	0.977	0.008	0.011
0.035	2.400	0.971	0.008	0.013
0.045	3.000	0.985	0.009	0.012
0.055	3.800	0.990	0.009	0.013
0.070	4.700	0.996	0.007	0.011
0.090	5.600	1.005	0.008	0.013
0.125	6.300	1.008	0.004	0.010
0.175	7.300	1.017	0.004	0.011
0.250	8.700	1.008	0.004	0.011
0.350	11.000	1.004	0.005	0.010

Table B.3: *Extracted values for $\sigma_{\mathrm{He}}/\sigma_{\mathrm{D}}$ in 12 x bins. The 4th column reppresents the relative statistical error while in the 5th is culomn the systematic uncertainty for each point is listed.*

$< x >$	$< Q^2 >$	F_2^{Kr}/F_2^D	stat	R_{Kr}/R_D	stat	sys
0.013	0.498	1.066	0.139	4.574	2.958	2.393
0.018	0.660	1.011	0.077	3.832	1.887	1.747
0.025	0.872	1.026	0.038	3.465	0.807	1.296
0.035	1.124	0.983	0.020	1.702	0.329	0.525
0.045	1.341	0.989	0.019	1.835	0.342	0.512
0.055	1.527	1.020	0.018	2.063	0.387	0.461
0.070	1.758	1.023	0.013	1.724	0.267	0.334
0.090	2.016	1.049	0.015	1.738	0.394	0.807
0.125	2.342	1.035	0.007	1.180	0.237	0.443
0.175	2.704	1.034	0.007	0.835	0.330	0.545
0.250	3.100	1.016	0.006	2.261	0.911	1.702
0.350	4.138	0.981	0.008	2.730	1.838	0.952
$< x >$	$< Q^2 >$	F_2^N/F_2^D	stat	R_N/R_D	stat	sys
0.013	0.499	1.215	0.163	5.330	3.487	2.502
0.018	0.655	1.011	0.052	1.950	0.674	0.668
0.025	0.903	1.040	0.026	2.263	0.415	0.703
0.035	1.247	0.987	0.019	1.270	0.248	0.348
0.045	1.451	1.007	0.017	1.449	0.245	0.365
0.055	1.579	1.010	0.016	1.266	0.237	0.289
0.070	1.858	1.023	0.011	1.303	0.180	0.255
0.090	2.024	1.024	0.012	1.103	0.204	0.208
0.125	2.437	1.025	0.004	1.092	0.147	0.211
0.175	2.842	1.025	0.004	1.145	0.246	0.252
0.250	3.458	1.008	0.004	0.732	0.291	0.154
0.350	5.151	0.989	0.005	2.543	1.110	1.097
$< x >$	$< Q^2 >$	F_2^{He}/F_2^D	stat	R_{He}/R_D	stat	sys
0.013	0.502	0.815	0.239	0.142	1.952	0.067
0.018	0.655	1.031	0.067	1.763	0.807	0.645
0.025	0.948	1.044	0.031	1.850	0.427	0.601
0.035	1.201	0.999	0.021	1.396	0.289	0.415
0.045	1.404	0.979	0.018	0.902	0.236	0.246
0.055	1.644	1.008	0.018	1.302	0.282	0.328
0.070	1.894	1.013	0.013	1.346	0.229	0.302
0.090	2.078	1.024	0.013	1.455	0.283	0.351
0.125	2.366	1.010	0.005	1.083	0.184	0.322
0.175	2.835	1.024	0.006	1.554	0.358	0.679
0.250	3.353	1.008	0.005	1.118	0.429	0.955

Table B.4: *Extracted values for F_2^A/F_2^D and R_A/R_D obtained in the 2-parameters fit.*

$< x >$	$< Q^2 >$	R_{Kr}/R_D	stat	sys	$< x >$	$< Q^2 >$	R_N/R_D	stat	sys
0.013	0.498	0.985	0.172	1.798	0.013	0.483	1.212	0.107	0.345
0.018	0.660	1.441	0.299	1.847	0.018	0.640	1.270	0.108	0.240
0.025	0.872	1.814	0.183	0.981	0.025	0.846	1.328	0.084	0.246
0.035	1.124	1.510	0.131	0.536	0.035	1.090	1.265	0.102	0.211
0.045	1.341	1.938	0.176	0.433	0.045	1.301	1.345	0.110	0.222
0.055	1.527	1.902	0.206	0.370	0.055	1.482	1.237	0.119	0.185
0.070	1.758	1.746	0.154	0.265	0.070	1.706	1.228	0.101	0.158
0.090	2.016	1.407	0.212	0.295	0.090	1.956	1.105	0.113	0.140
0.125	2.342	1.206	0.165	0.403	0.125	2.271	1.143	0.108	0.111
0.175	2.704	0.714	0.226	0.492	0.175	2.623	1.064	0.179	0.180
0.250	3.100	2.047	0.632	1.146	0.250	3.007	0.765	0.229	0.229
0.350	4.138	0.964	0.898	1.682	0.350	4.014	1.927	0.765	0.766

$< x >$	$< Q^2 >$	R_{He}/R_D	stat	sys
0.013	0.513	1.579	0.163	0.269
0.018	0.680	1.112	0.128	0.158
0.025	0.898	1.080	0.092	0.131
0.035	1.158	1.253	0.113	0.145
0.045	1.381	1.089	0.121	0.144
0.055	1.573	1.207	0.145	0.161
0.070	1.811	1.254	0.125	0.139
0.090	2.077	1.255	0.158	0.165
0.125	2.412	1.210	0.136	0.137
0.175	2.785	1.135	0.236	0.236
0.250	3.193	0.777	0.300	0.300

Table B.5: *Extracted values for R_A/R_D in x bins from HERMES + NMC data with one parameter fit.*

$< x >$	$< Q^2 >$	R_N/R_D	stat	sys
0.013	0.505	2.353	1.139	1.237
0.018	0.678	1.714	0.463	0.632
0.025	0.907	1.537	0.238	0.543
0.035	1.271	1.329	0.186	0.413
0.045	1.442	1.280	0.196	0.362
0.055	1.598	1.299	0.212	0.325
0.070	1.933	1.323	0.160	0.286
0.090	2.188	1.134	0.188	0.228
0.125	2.733	1.045	0.146	0.202
0.175	3.210	1.114	0.253	0.247
0.250	3.876	0.732	0.310	0.153
0.350	5.466	2.585	1.144	0.683
$< x >$	$< Q^2 >$	R_{He}/R_D	stat	sys
0.013	0.535	0.142	1.952	0.075
0.018	0.719	1.763	0.807	0.650
0.025	0.962	1.437	0.336	0.508
0.035	0.347	1.288	0.233	0.400
0.045	1.529	0.946	0.218	0.268
0.055	1.694	1.389	0.265	0.347
0.070	2.049	1.200	0.193	0.259
0.090	2.319	1.347	0.254	0.270
0.125	2.896	1.053	0.183	0.204
0.175	3.402	1.600	0.372	0.354
0.250	4.108	1.102	0.451	0.231

Table B.6: *Extracted values for R_A/R_D in x bins from the Rosenbluth seperation of HERMES + NMC data.*

Bibliography

[1] M. Gell-Mann. *A Schematic model of baryons and mesons*. Phys. Lett., **8**, 1964, pages 214–215.

[2] G. Zweig. *An SU(3) model for strong interaction symmetry and its breaking*. CERN-TH-412.

[3] R.P. Feynman. *Very high-energy collisions of hadrons*. Phys. Rev. Lett., **23**, 1969, pages 1415–1417.

[4] J.I. Friedman and H.W. Kendall. *Deep inelastic electron scattering*. Ann. Rev. Nucl. Part. Sci., **22**, 1972, pages 203–254.

[5] J.D. Bjorken. *Asymptotic sum rules at infinite momentum*. Phys. Rev., **179**, 1969, pages 1547–1553.

[6] Jr. Callan, C.G. and D.J. Gross. *High-energy electroproduction and the constitution of the electric current*. Phys. Rev. Lett., **22**, 1969, pages 156–159.

[7] D.J. Gross and F. Wilczek. *Asymptotically free gauge theories. I*. Phys. Rev., **D8**, 1973, pages 3633–3652.

[8] H.D. Politzer. *Reliable perturbative results for strong interactions?* Phys. Rev. Lett., **30**, 1973, pages 1346–1349.

[9] J.J. Aubert *et al. The ratio of the nucleon structure function $F_2(N)$ for Iron and Deuterium*. Phys. Lett., **B123**, 1983, p. 275.

[10] X.F. Guo and X.N. Wang. *Multiple scattering, parton energy loss and modified fragmentation functions in deeply inelastic eA scattering*. PRL, **85, 3592**, 2000.

[11] L. Lapikas. *Matter density distribution of ^{84}Kr and the attenuation of semi-inclusively produced hadrons*. Internal Report, HERMES 02-030, 2002.

[12] F. Halzen and A.D. Martin. *Quarks & leptons*. Jhon Wiley & sons, 1984.

[13] V.N. Gribov and L.N. Lipatov. *Deep inelastic e p scattering in perturbation theory*. Yad. Fiz., **15**, 1972, pages 781–807.

[14] Yuri L. Dokshitzer. *Calculation of the structure functions for deep inelastic scattering and e^+ e^- annihilation by perturbative theory in quantum chromodynamics. (In Russian)*. Sov. Phys. JETP, **46**, 1977, pages 641–653.

[15] G. Altarelli and G. Parisi. *Asymptotic freedom in parton language*. Nucl. Phys., **B126**, 1977, p. 298.

[16] M. Gluck, E. Reya, M. Stratmann, and W. Vogelsang. *Models for the polarized parton distributions of the nucleon*. Phys. Rev., **D63**, 2001, p. 094005.

[17] A. Airapetian *et al.* *Multiplicity of charged and neutral pions in deep-inelastic scattering of 27.5-GeV positrons on hydrogen*. Eur. Phys. J., **C21**, 2001, pages 599–606.

[18] A. Bialas and T. Chmaj. *Leptoproduction of hadrons from nuclear targets and fragmentation of quarks into hadrons*. Phys. Lett., **B133**, 1983, p. 241.

[19] A. Bialas and M. Gyulassy. *LUND model and an outside - inside aspect of the inside - outside cascade*. Nucl. Phys., **B291**, 1987, p. 793.

[20] A. Airapetian *et al.* *Hadron formation in deep-inelastic positron scattering in a nuclear environment*. Eur. Phys. J., **C20**, 2001, pages 479–486.

[21] K. Gottfried. *Space-time structure of hadronic collisions and nuclear multiple production*. Phys. Rev. Lett., **32**, 1974, p. 957.

[22] B. Kopeliovich, J. Nemchik, and E. Predazzi. *Hadronization in nuclear environment and electroproduction of leading hadrons*. hep-ph/9511214, 1995.

[23] J. Ashman *et al.* *Comparison of forward hadrons produced in muon interactions on nuclear targets and deuterium*. Z. Phys., **C52**, 1991, pages 1–12.

[24] N.Z. Akopov, G.M. Elbakyan, and L.A. Grigoryan. *Nuclear attenuation of charged mesons in deep inelastic scattering*. Internal Report, HERMES 02-004, 2002.

[25] A. Accardi and H.J. Pirner. *Nuclear modifications of fragmentation functions and rescaling models*. nucl-th/0205008, 2002.

[26] A. Accardi, V. Muccifora, and H.-J. Pirner. *Hadron production in deep inelastic lepton nucleus scattering*. nucl-th/0211011, 2002.

[27] R.L. Jaffe, F.E. Close, R.G. Roberts, and G. G. Ross. *On the nuclear dependence of electroproduction*. Phys. Lett., **B134**, 1984, p. 449.

[28] L.S. Osborne *et al.* *Electroproduction of hadrons from nuclei*. Phys. Rev. Lett., **40**, 1978, p. 1624.

[29] B. Kopeliovich. Private Comunications, 2000.

[30] X.N. Wang. *Particle production in high-energy heavy-ion collisions*. hep-ph/0111404, 2001.

[31] R. Baier, Y.L. Dokshitzer, A.H. Mueller, S. Peigne, and D. Schiff. *Radiative energy loss and p_T-broadening of high energy partons in nuclei*. Nucl. Phys., **B484**, 1997, pages 265–282.

[32] U. Thoma. *Scalar mesons and the search for the 0^{++} glueball*. Proceedings of the Quark Nuclear Physics Conference, June 2002, p. Julich (QNP02).

[33] M. Gell-Mann. *Symmetries of baryons and mesons*. Phys. Rev., **125**, 1962, pages 1067–1084.

[34] P. Minkowski and W. Ochs. *The $J^{(PC)} = 0^{++}$ scalar meson nonet and glueball of lowest mass*. hep-ph/9905250, 1999.

[35] K. Hagiwara *et al.* *Review of particle physics*. Phys. Rev., **D66**, 2002, p. 010001.

[36] M.G. Alford and R.L. Jaffe. *Insight into the scalar mesons from a lattice calculation*. Nucl. Phys., **B578**, 2000, pages 367–382.

[37] F.E. Close and A. Kirk. *A glueball q anti-q filter in central hadron production*. Phys. Lett., **B397**, 1997, pages 333–338.

[38] V.N. Gribov and J. Nyiri. *Supercritical charge in bosonic vacuum*. Presented at Perturbative QCD Workshop Mtg., Lund, Sweden, May 21-24, 1991.

[39] F.E. Close, Y.L. Dokshitzer, V.N. Gribov, V.A. Khoze, and M.G. Ryskin. *f_0(975), a_0(980) as eye witnesses of confinement*. Phys. Lett., **B319**, 1993, pages 291–299.

[40] K. Ackerstaff *et al.* *Production of f_0(980), f_2(1270) and Φ(1020) in hadronic Z^0 decay*. Eur. Phys. J., **C4**, 1998, pages 19–28.

[41] P. Astier *et al.* *Inclusive production of ρ^0(770), f_0(980) and f_2(1270) mesons in ν/μ charged current interactions*. Nucl. Phys., **B601**, 2001, pages 3–23.

[42] P. Lebrun. *Observations of the scalar meson $f_0(980)$ in the photoproduction experiment E687 at Fermilab*. Published in the proceedings of 7th International Conference on Hadron Spectroscopy (Hadron 97), Upton, NY, 25-30 Aug 1997.

[43] A. Aloisio *et al.* *Study of the decay* $\Phi \to \pi^0\pi^0\gamma$ *with the KLOE detector*. Phys. Lett., **B537**, 2002, pages 21–27.

[44] A. Aloisio *et al.* *Detection of* $\Phi \to f_0(980)\gamma$, $\Phi \to a_0(980)\gamma$ *into five photons final state with KLOE at DAPHNE*. hep-ex/0107024, 2001.

[45] K. Ackerstaff *et al.* *Flavor Decomposition of the Polarized Quark Distributions in the Nucleon from Inclusive and Semi-Inclusive Deep-inelastic Scattering*. Phys. Lett., **B464**, 1999, pages 123–134.

[46] K. Ackerstaff *et al.* *Exclusive Leptoproduction of* ρ^0 *Mesons on Hydrogen at Intermediate W Values*. Eur. Phys. Jour., **C17**, 2000, pages 389–398.

[47] K. Ackerstaff *et al.* *Hadron Formation in Deep-Inelastic Positron Scattering from* ^{14}N *and* ^{2}H. Eur. Phys. Jour., **C20**, 2001, pages 479–486.

[48] K. Ackerstaff *et al.* *The HERMES experiment*. Nucl. Instrum. Meth., **A417**, 1998, pages 230–265.

[49] C. Baumgarten *et al.* *The Storage Cell of the Polarized H/D Internal Target of the HERMES Experiment at HERA*. Nucl. Instrum. Meth., **A**, 2002.

[50] H. Kolster. *The HERMES Gaseous Internal Polarized Proton target and its use in the HERA Positron Storage Ring*. PhD thesis, Ludwig-Maximilians Univ., M$\ddot{u}$nchen, 1998.

[51] M.C. Simani *et al.* *The gas analyzer of the target of the HERMES experiment*. Submitted to Nucl. Instrum. Meth. A, 2002.

[52] T. Shin. *The Nuclear Dependence of Structure Function Ratios from Unpolarized Deep Inelastic Scattering*. PhD thesis, Hampton University, Massachusetts Institute of Technology, 2000.

[53] N. Akopov and others (The HERMES RICH group). *The HERMES Dual-Radiator Ring Imaging Cerenkov Detector*. Nucl. Instrum. Meth., **A479**, 2002, pages 511–530.

[54] H. Avakian *et al.* *Performance of the Electromagnetic Calorimeter of the HERMES experiment*. Nucl. Instrum. Meth., **A417**, 1998, pages 69–78.

[55] F.M. Menden. *Measurement of the Valence Quark Spin Distributions of the Nucleon Using Deep Inelastic Scattering at HERMES*. PhD thesis, TRIUMF, Vancouver, Canada, 1998.

[56] R. Kaiser. *Likelihood analysis for the RICH IRT method*. Internal Report, HERMES 00-026, 2000.

[57] J. Visser. *Deep inelastic scattering off hydrogen and deuterium*. PhD thesis, Rijksuniversiteit Groningen, Groningen, 2002.

[58] D. Heesbeen. PhD thesis, Rijksuniversiteit Groningen, Groningen, 2003.

[59] A. Reishl. PhD thesis, in preparation, (Amsterdam).

[60] G. Bunce *et al.* *Λ^0 polarization in inclusive production by 300-GeV protons in Berilium*. Phys. Rev. Lett., **36**, 1976, pages 1113–1116.

[61] R.C. Fernow and A.D. Krisch. *High-energy physics with polarized proton beams*. Ann. Rev. Nucl. Sci., **31**, 1981, p. 107.

[62] M. Bockhorst *et al.* *Measurement of $\gamma p \rightarrow K^+\Lambda$ and $\gamma p \rightarrow K^+\Sigma^0$ at photon energies up to 1.47-GeV*. Z. Phys., **C63**, 1994, pages 37–47.

[63] K. Hagiwara *et al.* *Review of Particle Physics*. Physical Review D, **66**, 2002, p. 010001.

[64] R.L. Jaffe. *Polarized Λs in the current fragmentation region*. Phys. Rev., **D54**, 1996, pages 6581–6585.

[65] A. Airapetian *et al.* *Measurement of longitudinal spin transfer to Lambda hyperons in deep-inelastic lepton scattering*. Phys. Rev., **D64**, 2001, p. 112005.

[66] M.P. Alvarez *et al.* *Study of charm photoproduction mechanisms*. Z. Phys., **C60**, 1993, pages 53–62.

[67] S.J. Brodsky, E. Chudakov, P. Hoyer, and J.M. Laget. *Photoproduction of charm near threshold*. Phys. Lett., **B498**, 2001, pages 23–28.

[68] H. Feick. *Radiation Tollerance of Silicon Particle Detecotrs for High-Energy Physics Experiments*. DESY Internel Report, **F35D-97-08**, 1997.

[69] N. Demaria *et al.* *New results on silicon microstrip detectors of CMS tracker*. Nucl. Instrum. Meth., **A447**, 2000, pages 142–150.

[70] M. Moll. *Radiation Damage in Silicon Particle Detectors*. PhD thesis, DESY, Hamburg, 1999.

[71] ATLAS. *Inner Detector Technical Design Report* (atlas-trd-4-5). /CERN/LHCC/97-16 and 17, 1997.

[72] V.A.J. Van Lint. *The physics of radiation damage in particle detectors*. Nucl. Instrum. Meth., **A253**, 1987, pages 453–459.

[73] M.G. van Beuzekom, V. Mexner, S. Mos, R. Reischl, and J.J.M. Steijger. *The HERMES silicon project - the radiation protection system.* Nucl. Instrum. Meth., **A**, 2002.

[74] K. Ackerstaff *et al. Nuclear Effects on $R = \sigma_L/\sigma_T$ in Deep Inelastic Scattering*. Phys. Lett., **B 475**, 2000, pages 386–394.

[75] P. Amaudruz *et al. A Reevaluation of the nuclear structure function ratios for D, He, Li-6, C and Ca*. Nucl. Phys., **B441**, 1995, pages 3–11.

[76] M. Arneodo *et al. The Structure Function ratios F_2^{li}/F_2^D and F_2^C/F_2^D at small x*. Nucl. Phys., **B441**, 1995, pages 12–30.

[77] M. Arneodo *et al. The Q^2 dependence of the structure function ratio F_2^{Sn}/F_2^C and the difference $R_{Sn} - R_C$ in deep inelastic muon scattering*. Nucl. Phys., **B481**, 1996, pages 23–39.

[78] J.J. van Hunen. *Deep-Inelastic Scattering off ^{14}N.* PhD thesis, Universiteit Utrecht, Utrecht, 2000.

[79] M. Arneodo *et al. Accurate measurement of F_2^D/F_2^p and $R_D - R_p$*. Nucl. Phys., **B487**, 1997, pages 3–26.

[80] L.W. Mo and Y.S. Tsai. *Radiative correction to elastic and inelastic e p and μ p scattering*. Rev. Mod. Phys., **41**, 1969, pages 205–235.

[81] A.A. Akhundov, D.Y. Bardin, and N.M. Shumeiko. *Electromagnetic corrections to the deep inelastic μ p scattering at high-energies*. Sov. J. Nucl. Phys., **26**, 1977, p. 660.

[82] D.Y. Bardin and N.M. Shumeiko. *On the weak neutral current and electromagnetic effects on the quantities measures in deed inelastic lepton-N scattering*. Sov. J. Nucl. Phys., **29**, 1979, p. 499.

[83] A.A. Akhundov, D.Y. Bardin, and N.M. Shumeiko. *Electromagnetic corrections to elastic radiative tail in deep inelastic lepton - nucleon scattering*. Sov. J. Nucl. Phys., **44**, 1986, p. 988.

[84] M.P. Locher and A. Svarc. *Deuteron vertex functions including meson exchange corrections*. Fizika, **22**, 1990, pages 549–566.

[85] J.S. Mccarthy, I. Sick, and R.R. Whitney. *Electromagnetic structure of the helium isotopes*. Phys. Rev., **C15**, 1977, pages 1396–1414.

[86] C.W. De Jager, H. De Vries, and C. De Vries. *Nuclear charge and magnetization density distribution parameters from elastic electron scattering*. Atom. Data Nucl. Data Tabl., **14**, 1974, pages 479–508.

[87] T. De Forest and J.D. Walecka. *Electron scattering and nuclear structure*. Adv.in Phys., **15**, 1966, pages 1–109.

[88] M. Gari and W. Krumpelmann. *Semiphenomenological synthesis of meson and quark dynamics and the electromagnetic structure of the nucleon*. Z. Phys., **A322**, 1985, pages 689–693.

[89] J. Bernabeu. *Quasielastic electron and neutrino interactions and the exclusion effects*. Nucl. Phys., **B49**, 1972, pages 186–205.

[90] E.J. Moniz. *Pion electroproduction from nuclei*. Phys. Rev., **184**, 1969, pages 1154–1161.

[91] H. Abramowicz and A. Levy. *The ALLM parameterization of $\sigma_{tot}(\gamma^* p)$: An update*. hep-ph/9712415, 1997.

[92] L.W. Whitlow, S. Rock, A. Bodek, E.M. Riordan, and S. Dasu. *A Precise extraction of $R = \sigma_L/\sigma_T$ from a global analysis of the SLAC deep inelastic e p and e d scattering cross-sections*. Phys. Lett., **B250**, 1990, pages 193–198.

[93] S. Dasu *et al.* *Measurement of kinematic and nuclear dependence of $R = \sigma_L/\sigma_t$ in deep inelastic electron scattering*. Phys. Rev., **D49**, 1994, pages 5641–5670.

[94] S. Stein *et al.* *Electron scattering at 4-degrees with energy of 4.5 GeV - 20 GeV*. Phys. Rev., **D12**, 1975, p. 1884.

[95] K. Kurek. *Contribution of the elastic radiative tail to the deep inelastic muon scattering on heavy targets*. Z. Phys., **C63**, 1994, pages 561–568.

[96] H. Boettcher, Y. Gaerber, and U. Stoesslein. *Results on the Top/Bottom Detector Alignment for the 1997 Data*. Internal Report, HERMES 99-053, 1999.

[97] A. Bruel. Private Comunications.

[98] M. Arneodo *et al.* *Measurement of the proton and the deuteron structure functions, F_2^p and F_2^d*. Phys. Lett., **B364**, 1995, pages 107–115.

[99] S. Platchkov *et al.* *Deuteron A(Q^2) structure function and the neutron electric form-factor*. Nucl. Phys., **A510**, 1990, pages 740–758.

[100] P. Amaudruz *et al.* *Measurements of $R_D - R_p$ and $R_{Ca} - R_C$ in deep inelastic muon scattering*. Phys. Lett., **B294**, 1992, pages 120–126.

[101] K. Abe *et al.* *Measurements of $R = \sigma_L/\sigma_T$ for 0.03 $< x <$ 0.1 and fit to world data*. Phys. Lett., **B452**, 1999, pages 194–200.

[102] M. Arneodo. *Nuclear effects in structure functions*. Phys. Rep., **240**, 1994, pages 301–393.

[103] M. Ericson and S. Kumano. *Nuclear modification of transverse-longitudinal structure function ratio*. **hep-ph/0212001**, 2002.

[104] G.Q. Li, C.H. Lee, and G.E. Brown. *Kaon production in heavy-ion collisions and maximum mass of neutron stars*. Phys. Rev. Lett., **79**, 1997, pages 5214–5217.

[105] G.V. Davidenko and Nikolai N. Nikolaev. *Hadron final states in deep inelastic leptoproduction on nuclei*. Nucl. Phys., **B135**, 1978, pages 333–353.

[106] A. Bialas and E. Bialas. *Determination of quark - nucleon inclusive cross-section from leptoproduction of hadrons in nuclear targets*. Phys. Rev., **D21**, 1980, p. 675.

[107] K. Lipka. *Double-Spin Asymmetries in Diffractive Vector-Meson Production at HERMES*. PhD thesis, Humboldt University, Berlin, 2002.

[108] I. Akushevich, N. Shumeiko, and A. Soroko. *Radiative effects in the processes of hadron electroproduction*. Eur. Phys. J., **C10**, 1999, pages 681–687.

[109] X.N. Wang and X.F. Guo. *Multiple parton scattering in nuclei: Parton energy loss*. Nucl. Phys., **A696**, 2001, pages 788–832.

[110] T. Waas, N. Kaiser, and W. Weise. *Effective kaon masses in dense nuclear and neutron matter*. Phys. Lett., **B379**, 1996, pages 34–38.

[111] E. Friedman *et al.* *K^+ nucleus reaction and total cross-sections: New analysis of transmission experiments*. Phys. Rev., **C55**, 1997, pages 1304–1311.

[112] F. Laue *et al.* *Medium effects in kaon and antikaon production in nuclear collisions at subthreshold beam energies*. Phys. Rev. Lett., **82**, 1999, pages 1640–1643.

[113] N.A. Pavel. *Hadron production in deep inelastic lepton nucleus scattering*. Nucl. Phys., **A532**, 1991, pages 465c–488c.

[114] S. Belostotski, O. Grebenyuk, and Y. Naryshkin. *K_s, Λ and $\bar{\Lambda}$ yields normalized to DIS from different targets*. Internal Note, HERMES, 1998.

[115] L. Lonnblad. Private comunications, 2002.

[116] K. Adcox *et al.* *Suppression of hadrons with large transverse momentum in central $Au + Au$ collisions at $s^{1/2}(NN)$ = 130 GeV*. Phys. Rev. Lett., **88**, 2002, pages 022–301.

[117] E. Wang and X.N. Wang. *Jet tomography of dense and nuclear matter*. Phys. Rev. Lett., **89**, 2002, p. 162301.

[118] G. Ingelman, A. Edin, and J. Rathsman. *LEPTO 6.5 - A Monte Carlo Generator for Deep Inelastic Lepton-Nucleon Scattering*. Comput. Phys. Commun., **101**, 1997, pages 108–134.

[119] Sanjay K. Ghosh and Byron Jennings. *ρ-nucleus bound states in Walecka model*. Phys. Rev., **C61**, 2000, p. 067604.

[120] T. Sjostrand, L. Lonnblad, and S. Mrenna. *PYTHIA 6.2: Physics and manual*. hep-ph/0108264, 2001.

[121] T.H. Bauer, R.D. Spital, D.R. Yennie, and F.M. Pipkin. *The hadronic properties of the photon in high-energy interactions*. Rev. Mod. Phys., **50**, 1978, p. 261.

[122] M. Tytgat. *Diffractive Production of ρ^0 and ω Vector Mesons at HERMES*. PhD thesis, Universiteit Gent, Gent, 2000.

[123] P.B. van der Nat. *Hadronization at 12 GeV*. Master thesis, Vrije Universiteit, Amsterdam, 2002.

Summary

In this thesis the hadronic final state in deep-inelastic positron scattering experiments is studied in order to increase our understanding of non-perturbative (or long-distance) aspects of the theory of strong interactions, Quantum Chromo-Dynamics and hadron structure. More specifically, the time evolution of hadron-formation processes, parton energy-loss mechanisms and the structure of scalar mesons are investigated.
As an experimental tool semi-inclusive deep-inelastic lepton scattering on nuclei is used. In such experiments the atomic nuclei act as a filter for the hadrons produced when a lepton scatters off a quark in one of the nucleons. At the energy scale of the HERMES experiment the hadron-formation processes develop over length scales comparable to the size of the atomic nucleus. Therefore, measurements of the hadron attenuation on various nuclear targets are sensitive to the nature of these processes.
In this thesis, data are presented for the attenuation (or multiplicity) ratios of charged pions, kaons, protons and anti-protons on a krypton target in comparison to deuterium. Using simple phenomenological models it is possible, as it has been shown, to obtain values for the formation times of these particle types. The results indicate that the formation of a proton requires twice as much time as the formation of a pion or kaon. If confirmed with more statistics this observation suggests different formation times for mesons and baryons. In this respect it would be desirable to obtain data on other baryons, like the Λ-hyperon, as well. Such data will become available soon with the larger acceptance for slowly decaying particles provided by the newly installed Lambda Wheels silicon detector[1].
The dependence on z and ν of the multiplicity ratios on krypton have the same behavior as the already published multiplicity ratios on nitrogen. Fast forward (high z) hadrons are more strongly attenuated than non-leading hadrons. Also hadrons produced in events with low energy transfer (low ν) are more strongly attenuated than hadrons produced at high ν. These data demonstrate that the attenuation effects are very prominent in the HERMES energy range, which is different from available EMC data [23]. In this respect, it is interesting to note that data collected at HERMES with a beam energy of 12 GeV will extend the mea-

[1] The main purpose of the Lambda Wheels is in the field of spin physics, however. The study of Λ-hyperon production at $x_F < 0$, for example, gives information on the relative orientation of s and u quarks, while Λ production on transversely polarized targets may give access to the only unmeasured leading-order structure function, i.e. $h_1(x)$.

surements presented in this work to a lower ν region where nuclear attenuation effects are even stronger. A preliminary analysis of these data can be found in Ref. [123].
Essentially two different types of model calculations are available to describe the attenuation of hadron multiplicities: the ones in which the hadron-nucleon rescattering in the medium is the dominant cause of hadron attenuation, and the one in which the entire effect of hadron attenuation is attributed to parton-nucleon rescattering and gluon radiation in a QCD framework. These approaches are both able to describe the kinematic dependencies of the attenuation ratios for both ^{14}N and Kr targets. In an effort to make a distinction between the two approaches the A-dependence of the attenuation ratios has been studied more precisely.
The new data on ^{84}Kr and D presented in this thesis are combined with the published HERMES data on ^{14}N and D to determine the A-dependence of hadron attenuation in nuclei. The data favor (at the 3σ level) the $A^{2/3}$ dependence characteristic of the gluon-quark interference terms (as determined in a QCD framework) over the $A^{1/3}$ dependence predicted by nuclear absorption models. It is not excluded, however that, expecially at low ν where the hadron is more likely to be formed well inside the nucleus, a combination of the two effects is needed. This would be reflected by the observation that the power α (in A^{α}) for data at lower ν is closer to the value 1/3. More data, in particular on other targets with different atomic numbers are needed to better constrain the observed A-dependence. Data at lower energies will be useful to search for possible ν-dependence of the power α.
In order to obtain well normalized data on the hadron multiplicity ratios a thorough study of the inclusive DIS cross section ratio on nuclei was required. The ratio $\sigma_{\mathrm{Kr}}/\sigma_{\mathrm{D}}$ has been extracted from the present data after applying corrections for radiative processes and for a severe detector inefficiency which went previously unnoticed. In the course of these studies previously published data on D, ^{3}He and ^{14}N had to be reanalyzed together with the present data on ^{84}Kr and D. For all target gases the ratio $\sigma_{\mathrm{A}}/\sigma_{\mathrm{D}}$ is found to be in agreement with the existing parameterization of inclusive cross section ratios mostly derived from the NMC experiment. From these inclusive analyses the value of the longitudinal to transverse cross section ratio R as measured on heavier targets has been found to be in agreement with the value obtained on deuterium within 20% in the Q^2 range between 0.5 and 10 GeV^2.
Apart from the study of long lived particles such as pions, kaons and protons, also the study of fast decaying particles can be used to access aspects of the QCD structure of hadrons. In fact, hadron spectroscopy also serves to better understand certain aspects of QCD in the non-perturbative domain. Presently, one of the most important issues in hadron spectroscopy is the search for resonances which are predicted theoretically but not yet observed experimentally, such as glueballs. To be able to identify the lowest mass glueball a very precise knowledge of all the resonances in the mass range between 0.9 and 1.8 GeV is needed, and in particular of the scalar mesons which have the same quantum numbers as the predicted glueball.
In this thesis the $f_0(980)$ scalar meson has been studied, which has been observed for the first time in the present electroproduction data with a significance of about 4σ on various nu-

clear targets. The A-dependence of the yield and the peak position of the $f_0(980)$ have been studied, but no indication was found for an A-dependence of either of these two quantities. Hence, a description of the structure of a $f_0(980)$ in terms of a $K\bar{K}$-molecules, as suggested by some model predictions, is less likely.
Among the four gas targets investigated in this study the hydrogen target gives both a high significance for the $f_0(980)$ signal (of about 4.1) and also offers the possibility to study the $f_2(1270)$ tensor meson which has been observed with a significance of 3.5. The hydrogen data set has therefore been used to further study the properties of $f_0(980)$ electroproduction by investigating various kinematic dependencies of the multiplicity distribution in comparison to those of the $f_2(1270)$ meson. The dependence on Q^2, z, P_t^2 and $-t$ of the f_0 and f_2 yields has been compared to a MC simulation, in which these mesons are assumed to be produced as fragmentation products in deep-inelastic scattering. Within the constraints of such a MC simulation the f_0 and f_2 yields are reproduced adequately, thus providing a model dependent acceptance correction which has been used to evaluate multiplicity distributions for both mesons. A factor ten difference is found when comparing the integrated multiplicity of $f_0(980)$ measured in the present work to the NOMAD findings at a similar center-of-mass energy. From the observed kinematic dependencies of $f_0(980)$ electroproduction it is concluded that the HERMES data are in agreement with a description of this meson as a $q\bar{q}$-object. Though, other models, like the $qq\bar{q}\bar{q}$-hybrid one, cannot be ruled out in the absence of a MC simulation based on such an assumption to compare the data to.
Since the treatment of the background is the largest cause of uncertainty in this analysis, it might be interesting for future studies to exploit the neutral pion decay channel of the $f_0(980)$ meson, in which the background of the ρ^0 peak is not present.

In conclusion it has been shown that semi-inclusive deep-inelastic scattering on nuclei is a useful tool for extracting new insights on non-perturbative QCD and hadron properties. In the present work this tool has been used to obtain information on the hadron-formation and parton energy-loss mechanisms. In addition it has been shown how DIS on nuclei offers a new degree of freedom in the study of the structure of scalar mesons. In the near future the present work can be extended by exploiting new equipment, such as the Lambda Wheels described in chapter 4. Moreover, by collecting new data on other heavy nuclei it will be possible to investigate more precisely the A-dependence of the hadron attenuation, and to put the observation of a $A^{2/3}$ dependence of the nuclear attenuation on a firmer basis. Future high luminosity DIS experiment on nuclei would allow to map the z dependence of hadron attenuation in various ν intervals to identify a possible transition region between different energy loss mechanisms.

Samenvatting

Quantum Chromodynamica (QCD) is de theorie die de sterke wisselwerking tussen elementaire deeltjes beschrijft. Deze theorie is zeer succesvol gebleken zo lang de relatieve energie tussen de deeltjes erg hoog is. Bij lagere energieën is het veel moeilijker om QCD toe te passen, omdat in dit regime de techniek van de storingsrekening niet meer werkt.
In dit proefschrift worden de resultaten van een experimenteel onderzoek beschreven dat gericht is op het vergroten van onze kennis van QCD bij lagere energieën. Daartoe zijn experimenten uitgevoerd waarin positronen van hoge energie verstrooid zijn aan quarks (de bouwstenen van protonen en neutronen) in verschillende atoomkernen. In deze experimenten zijn naast het verstrooide positron ook de geproduceerde hadronen (een verzamelnaam voor uit quarks opgebouwde deeltjes zoals pionen, kaonen en protonen) waargenomen. Door de resultaten verkregen op kleine en grote atoomkernen zoals deuterium en krypton te vergelijken kan informatie worden verkregen over de tijdsduur van het hadron formatieproces (nadat een quark is geraakt), het mechanisme waardoor quarks energie verliezen als ze door de atoomkern bewegen en de structuur van een bijzondere klasse hadronen, de scalaire mesonen.
De metingen zijn verricht bij het HERMES experiment dat opgebouwd is in de oosthal van de electron-protonbotser HERA bij het onderzoekinstituut DESY in Hamburg. Allereerst zijn metingen geanalyseerd waarin alleen naar het verstrooide positron is gekeken. De verhouding van de werkzame doorsnedes voor dit "inclusieve" proces op ^{3}He, ^{14}N en ^{84}Kr ten op zichte van D is vergeleken met metingen die eerder verkregen zijn door het NMC experiment op CERN. Na correctie voor een detectorinefficientie die eerder over het hoofd was gezien is goede overeenstemming gevonden tussen de NMC en HERMES data. Dit resultaat verzekerde dat de normering van de meetgegevens in orde is.
Vervolgens is een analyse uitgevoerd waarin ook de hadronische eindtoestand is bestudeerd. Op basis van deze analyse is de verzwakkingsverhouding (*attenuation ratio*) bepaald van electrisch geladen pionen, kaonen, protonen en antiprotonen, voor krypton t.o.v. deuterium. Met behulp van eenvoudige phenomenologische modellen is het mogelijk gebleken een schatting te geven van de formatietijd van deze deeltjes. De resultaten wijzen erop dat de formatie van een proton twee keer zoveel tijd kost als dat van een pion of een kaon. De afhankelijkheid van de verzwakkingsverhouding van het atoomgetal, A, is eveneens onderzocht, waarbij de nieuwe resultaten voor ^{84}Kr en D, gepresenteerd in dit proefschrift, gecom-

bineerd zijn met de eerder gepubliceerde HERMES data voor ^{14}N en D. Het resultaat hiervan geeft aan dat de verzwakking een $A^{2/3}$ afhankelijkheid vertoont die karakteristiek is voor een gluon-quark interferentie effect voorspeld door QCD. Dit moet vergeleken worden met een $A^{1/3}$ afhankelijkheid, zoals voorspeld door meer klassieke nucleaire absorptiemodellen.
Behalve onderzoek naar langlevende deeltjes, zoals pionen, kaonen en protonen, zijn ook sneller vervallende deeltjes onderzocht om bepaalde aspecten van hun QCD structuur beter te leren begrijpen.
Eén van de belangrijke onderwerpen op het gebied van hadron structuur is de zoektocht naar deeltjes die theoretisch voorspeld zijn, maar nog niet experimenteel zijn waargenomen, zoals *glueballs*. Om dat glueballs dezelfde quantumgetallen hebben als scalaire mesonen is een zeer precieze kennis nodig van alle scalaire mesonen met een massa tussen 0.9 en 1.8 GeV. In dit proefschrift is het scalaire meson $f_0(980)$ onderzocht. Dit meson is voor het eerst waargenomen in het hier beschreven experiment met een significantie van ongeveer 4σ. De resonantie is gezien op 4 verschillende atoomkernen. De A-afhankelijkheid van het aantal gemeten $f_0(980)$ deeltjes en de positie van de $f_0(980)$ resonantie is onderzocht, maar voor geen van beide is een indicatie gevonden die wijst op een A-afhankelijkheid. Deze waarneming maakt het zeer onwaarschijnlijk dat het $f_0(980)$ meson de structuur heeft van een $K\bar{K}$-molecuul zoals wel is voorgesteld. De afhankelijkheid van het aantal gemeten f_0's van Q^2, z, P_t^2 en $-t$ is vergeleken met een Monte Carlo simulatie, waarbij is aangenomen dat deze mesonen ontstaan zijn uit een fragmentatieproces in diep-inelastische vertrooiing. Uit de waargenomen afhankelijkheid van de electroproductie van $f_0(980)$ mesonen van deze kinematische variabelen wordt geconcludeerd dat de HERMES data in overeenstemming zijn met de beschrijving van dit meson als een gebonden toestand van een quark en een antiquark in een $^3P_0$ toestand.
Samenvattend kan gesteld worden dat semi-inclusieve diep-inelastische verstrooiing op atoomkernen een zeer bruikbare methode is om nieuwe inzichten te verkrijgen in niet-perturbatieve QCD en eigenschappen van sommige hadronen. In het hier gepresenteerde onderzoek is van deze methode gebruik gemaakt om informatie te verkrijgen over de hadron formatietijd en om mechanismen te onderzoeken die het energieverlies van quarks en gluonen in atoomkernen beschrijven. Ook is aangetoond hoe diep-inelastische verstrooiing, waarbij gebruik gemaakt wordt van verschillende atoomkernen als trefplaat, een manier biedt om de structuur van scalaire mesonen te onderzoeken. In de nabije toekomst kan het hier gepresenteerde onderzoek uitgebreid worden door gebruik te maken van nieuwe apparatuur, zoals de Lambda Wheels die ook beschreven staan in dit proefschrift. Bovendien zou het wenselijk zijn om de A-afhankelijkheid van de hadron *verzwakking* preciezer te onderzoeken door nieuwe metingen te doen aan andere atoomkernen. Hiermee kan de gevonden $A^{2/3}$-afhankelijkheid met meer nauwkeurigheid vastgesteld worden.

Acknowledgements

To begin I would like to thank my *capo* Gerard for providing the possibility to undertake this long adventure and for his continual support throughout. On the way I have met and worked with many people and would now like to take this opportunity to thank you all!
From the trouble shooting team: Antje your perseverance and determination have taught me the good lesson of ‘never give up’. Andy, Beni, Brendan and Elke our collaboration I found to be both stimulating and instructive and at the end even quite fruitful!
How can I avoid to thank my Italian team? Pasquale and Valeria. I had a lot of fun working on a ‘real’ effect with you. Grazie della collaborazione e della pazienza!
Then Michael another hero of ’pioneering searches’ whom I would like to thank for sharing with me the pain and pleasure of a jump into the obscure scalar land. And I wish him luck with the ’final touches’!
A special thought goes out to Naomi; even though we did not work together directly it has been a real pleasure to be overwhelmed by the enthusiasm and passion that you put into understanding and especially into explaining physics.
Speaking of enthusiasm I want to thank all the guys of the mechanical department of NIKHEF for their pleasant and cheerful co-operation.
Among all the friends who shared with me the joys and stress of this four year enterprise, I want to thank in particular Lara for being ever present, even when far away in the cold and icy land of Alberta. I could not have hoped for a better way to combine laughter and tears; shifts and shopping; cavatelli e ceci! Grazie Larocchia! (e un grazie a tutta la famiglianapoletanestesa!).
I cannot thank yet but I can for sure welcome to life little Erika, I wish you a lot of joy and satisfaction. And I hope you’ll be as lucky as I am to gain from life every day a new smile.
Finally, and not by chance, I want to thank the person from whom I have got the most in all this time, the person who showed me what kind of physicist I want to become. Jos, thank you for all the very precious lessons you taught me, they made the morning coffee much more bearable, thanks for the brackets (I put here just a few for future reference ((( )( )(( )( ))))). Thanks most of all for been always straight and frank, you know your opinion always meant a lot to me!

(For Jos: I knew you were going to count!))